

Supernova remnants: the X-ray perspective

Jacco Vink

Abstract

Supernova remnants are beautiful astronomical objects that are also of high scientific interest, because they provide insights into supernova explosion mechanisms, and because they are the likely sources of Galactic cosmic rays. X-ray observations are an important means to study these objects. And in particular the advances made in X-ray imaging spectroscopy over the last two decades has greatly increased our knowledge about supernova remnants. It has made it possible to map the products of fresh nucleosynthesis, and resulted in the identification of regions near shock fronts that emit X-ray synchrotron radiation. Since X-ray synchrotron radiation requires 10-100 TeV electrons, which lose their energies rapidly, the study of X-ray synchrotron radiation has revealed those regions where active and rapid particle acceleration is taking place.

In this text all the relevant aspects of X-ray emission from supernova remnants are reviewed and put into the context of supernova explosion properties and the physics and evolution of supernova remnants. The first half of this review has a more tutorial style and discusses the basics of supernova remnant physics and X-ray spectroscopy of the hot plasmas they contain. This includes hydrodynamics, shock heating, thermal conduction, radiation processes, non-equilibrium ionization, He-like ion triplet lines, and cosmic ray acceleration. The second half offers a review of the advances made in field of X-ray spectroscopy of supernova remnants during the last 15 year. This period coincides with the availability of X-ray imaging spectrometers. In addition, I discuss the results of high resolution X-ray spectroscopy with the *Chandra* and *XMM-Newton* gratings. Although these instruments are not ideal for studying extended sources, they nevertheless provided interesting results for a limited number of remnants. These results provide a glimpse of what may be achieved with future microcalorimeters that will be available on board future X-ray observatories.

In discussing the results of the last fifteen years I have chosen to discuss a few topics that are of particular interest. These include the properties of Type Ia supernova remnants, which appear to be regularly shaped and have stratified ejecta, in contrast to core collapse supernova remnants, which have patchy ejecta distributions. For core collapse supernova remnants I discuss the spatial distribution of fresh nucleosynthesis products, but also their properties in connection to the neutron stars they contain.

For the mature supernova remnants I focus on the prototypical supernova remnants Vela and the Cygnus Loop. And I discuss the interesting class of mixed-morphology remnants. Many of these mature supernova remnants contain still plasma with enhanced ejecta abundances. Over the last five years it has also become clear that many mixed-morphology remnants contain plasma that is overionized. This is in contrast to most other supernova remnants, which contain underionized plasmas.

This text ends with a review of X-ray synchrotron radiation from shock regions, which has made it clear that some form of magnetic-field amplification is operating near shocks, and is an indication of efficient cosmic-ray acceleration.

Contents

1	Introduction	3
2	Supernovae	4
2.1	Core collapse supernovae	4
2.2	Thermonuclear supernovae	6
3	The classification of supernova remnants	7
4	The hydrodynamic structure and evolution of supernova remnants	9
4.1	Evolutionary phases	9
4.2	Analytical models	9
4.3	Supernova remnants evolving inside wind-blown bubbles	11
5	Collisionless shock heating and particle acceleration	12
5.1	Shock heating	12
5.2	Collisionless shocks	14
5.3	Temperature equilibration	14
5.4	Thermal conduction	16
5.5	Cosmic-ray acceleration by supernova remnant shocks	17
6	X-ray radiation from supernova remnants	19
6.1	Thermal X-ray emission	19
6.2	Line emission associated with radioactivity	23
6.3	Non-thermal emission	25
7	X-ray spectroscopy with <i>Chandra</i>, <i>XMM-Newton</i>, and <i>Suzaku</i>	27
8	Type Ia supernova remnants	30
8.1	X-ray spectroscopy of Type Ia supernova remnants	30
8.2	Evidence for Type Ia progenitor imprints on the circumstellar medium	35
9	Core collapse supernova remnants	36
9.1	Oxygen-rich supernova remnants	36
9.2	The X-ray emission from SN 1987A	41
9.3	Core collapse supernova remnants and neutron stars	44
10	Supernova remnants in or approaching the radiative phase	46
10.1	From non-radiative to radiative shocks	46
10.2	Enhanced metal abundances mature SNRs	48
10.3	Mixed-morphology supernova remnants	49
11	Shock heating and particle acceleration: observations	53
11.1	Electron-ion temperature equilibration	53
11.2	X-ray synchrotron emitting filaments	56
11.3	X-ray based evidence for efficient cosmic-ray acceleration	57
11.4	The relation between X-ray synchrotron and γ -ray emission	60
12	Concluding remarks	62

1 Introduction

Supernovae play a central role in modern astrophysics. They are of prime importance for the chemical evolution of the Universe, and they are one of the most important sources of energy for the interstellar medium (ISM). Part of that energy is in the form of cosmic rays, which have an energy density in the Galaxy of $1\text{--}2\text{ eV cm}^{-3}$, thus constituting about one third of the total energy density of the ISM. Finally, supernovae, in particular Type Ia supernovae (see Sect. 2), play a central role in present day cosmology as their brightness allows them to be detected at high redshifts (up to $z \sim 1.7$, Riess et al., 2007). Their use has led to the recognition that the expansion of the Universe is accelerating instead of decelerating (Perlmutter et al., 1998; Garnavich et al., 1998).

Supernova remnants (SNRs) are an important means to study supernovae. Since supernovae are relatively rare (2-3 per century in a typical spiral galaxy like our own), SNRs provide the best way to study the local population of supernovae. In addition, SNRs can reveal details about the explosions that are difficult to obtain from studying supernovae directly. For example, young SNRs can inform us about nucleosynthesis yields of individual SNRs and about the inherent asymmetries of the explosion itself, as revealed by the spatial and velocity distribution of heavy elements. Moreover, SNRs probe the immediate surroundings of supernovae, which are shaped by their progenitors.

Another aspect of SNRs concerns the interesting physical process that shape their properties. SNR shocks provide the best Galactic examples of high Mach number, collisionless shocks. The physics of these shocks is not well understood, as heating of the atoms occurs collisionless, i.e. shock heating does not operate through particle-particle (Coulomb) interactions, but through electromagnetic fluctuations and plasma waves. The SNR shocks are also thought to be the locations where part of the explosion energy is converted to cosmic-ray energy. This is supported by observations that indicate that GeV and TeV particles are present in SNRs through their radiative signatures: radio to X-ray synchrotron emission from relativistic electrons, and γ -ray emission caused by accelerated electrons and ions.

X-ray observations are one of the most important means to study the many aspects of SNRs. X-ray spectroscopy is essential to obtain abundances of the prime nucleosynthesis products of supernovae, which are the so-called alpha-elements (O, Ne, Mg, Si, S, Ar, Ca) and iron-group elements (chiefly Fe, Ni, and some trace elements with $20 < Z < 28$). All these elements have prominent emission lines in the 0.5-10 keV band for temperatures between 0.2-5 keV, which happens to be the typical electron temperatures of plasma heated by SNR shocks. The hot plasmas of SNRs are also optically thin, so inferring abundances is relatively straightforward. X-ray spectroscopy of SNRs, therefore, provide us with a record of alpha- and iron-group element production by supernovae.

X-ray spectroscopy can also be used to study several as-

pects of SNR shock physics. First of all the line emission provides information about the temperature and ionization state of the plasma, but the absence of lines or weak line emission in young SNRs usually points toward the contribution of X-ray synchrotron radiation. Studying X-ray synchrotron radiation offers a powerful diagnostic tool to study electron cosmic-ray acceleration, as the presence of X-ray synchrotron radiation depends sensitively on the shock acceleration properties. Moreover, the size of the X-ray synchrotron emitting regions can be used to infer magnetic-field strengths.

One of the major advances in X-ray spectroscopy over the last 15-20 years has been the emergence of X-ray imaging spectroscopy. Although presently the spectral resolution offered is limited, it provides a direct way to map the spatial distribution of elements and temperatures in SNRs. For young SNRs it also helps to separate thermal from non-thermal (synchrotron) X-ray emission.

The power of X-ray imaging spectroscopy is illustrated in Fig. 1, which shows Tycho's SNR (the remnant of the historical SN 1572) as observed by *Chandra*. The image shows beautifully the distribution of silicon and iron, but also reveals the synchrotron dominated emission from near the shock front.

Over the last ten years high spectral resolution X-ray spectroscopy has gained in importance, due to the availability of grating spectrometers on board *Chandra* and *XMM-Newton*. These spectrometers are also used to study

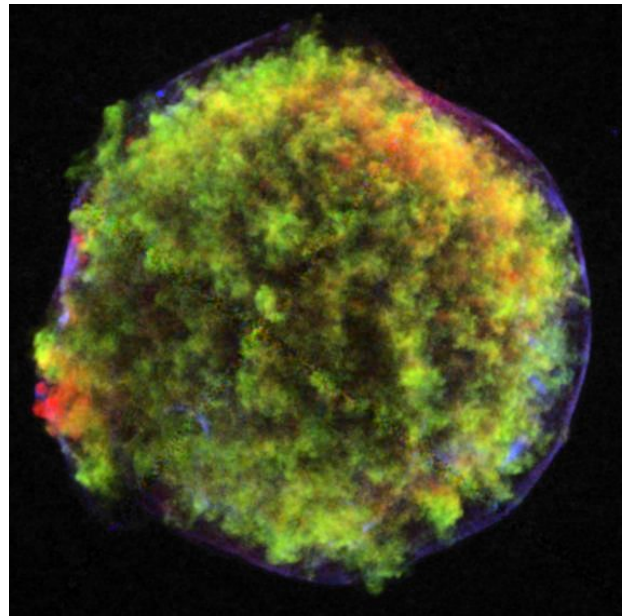


Figure 1: Three-color *Chandra* image of Tycho's SNR (SN1572/G120.1+1.4). The color red shows Fe L-shell emission, green Si XIII, and blue continuum (4-6 keV). Note the very narrow continuum rims near the shock front (blueish/purple in this image), caused by X-ray synchrotron radiation from electrons with energies up to 100 TeV. (Image made by the author from *Chandra* data, see also Hwang et al., 2002; Warren et al., 2005).

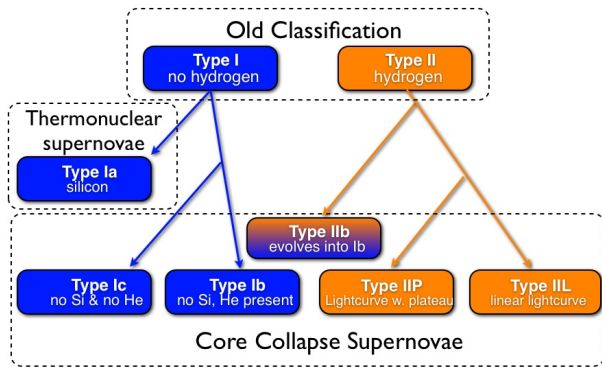


Figure 2: The classification of supernovae, based on optical spectroscopy and light-curve shape.

SNRs, but the contribution of grating spectrometers to our understanding of SNRs has been limited. The reason is that the slitless grating spectrometers are not particularly well suited for extended sources such as SNRs. Nevertheless, some important studies of SNRs with properties that make them suitable for grating spectroscopy have been published. With the emergence of high spectral resolution imaging spectroscopy, as will be possible with the calorimetric spectrometers on board *Astro-H* (Takahashi et al., 2008) and *IXO/ATHENA* (Bookbinder, 2010), high resolution X-ray spectroscopy will become much more prominent.

Here I review the current status of X-ray spectroscopy of SNRs. Since there is a lack of good text books or extended reviews on SNRs in general¹, the first part of this review has a tutorial character, describing our current understanding of the evolution and physics of SNRs. The second half of the review focusses on the X-ray observations themselves, with an emphasis on the achievements obtained with data from the three most recent X-ray observatories: *Chandra*, *XMM-Newton*, and *Suzaku*.

2 Supernovae

Supernovae are divided into two broad categories, reflecting our understanding of the explosion processes: core collapse supernovae and thermonuclear supernovae. In addition an observational classification scheme is used (Fig. 2) that goes back to Minkowski (1941), who observed that some supernovae do not show hydrogen absorption in their spectra (Type I) and others do (Type II).

Type II supernovae are invariably core collapse supernovae, but Type I supernovae can be either core collapse or thermonuclear supernovae. The thermonuclear explosions are associated with spectroscopic class Type Ia (Elias et al., 1985), which have Si absorption lines in their spectra. Type Ib and Ic supernovae are now understood to be explosions of stars that have lost their hydrogen-rich envelope as a result of stellar wind mass loss (e.g. Heger et al.,

¹But see Vink (2006); Reynolds (2008); Badenes (2010) for recent, more topical reviews.

2003), or through binary interaction (e.g. Podsiadlowski et al., 1992). For Type Ic the mass loss seems to have removed even the helium-rich layers of the progenitor. The fact that they are preferentially found in the most luminous regions of galaxies suggests that they are the explosions of the most massive stars (e.g. Kelly et al., 2008). Interestingly, also long duration gamma-ray bursts are associated with Type Ic supernovae (e.g. Galama et al., 1998; Stanek et al., 2003).

The sub-division of the Type II class in Type IIP (plateau), Type IIL (linear light curve) and Type IIb is based on a combination of two observational criteria: optical spectroscopy and light-curve shape (Fig. 2). Type IIP are the most common type of core collapse supernovae, and optical studies of potential progenitor stars confirm that their progenitors have initial masses in the $\sim 8 - 17 M_{\odot}$ range, and that they explode in the red supergiant phase, while still having a substantial hydrogen envelope (see the discussions in Smartt, 2009; Chevalier, 2005). Type IIL progenitors probably have a substantially less massive envelope, either due to stellar wind mass loss, or due to binary interaction. Type IIb supernovae are a class intermediate between Type Ib and Type II, in that their spectra would initially identify them as Type II explosions, but at late times their spectra evolve into Type Ib spectra. Also this can be understood as the result of substantial, but not complete, removal of the hydrogen-rich envelope due to stellar wind mass loss, or binary interaction. The prototypical Type IIb supernova is SN 1993J (Podsiadlowski et al., 1993; Woosley et al., 1994). Interestingly, recent identification and subsequent spectroscopy of the light echo of the supernova that caused the extensively studied SNR Cassiopeia A (Cas A) shows that it is the remnant of a Type IIb supernova, as the spectrum shows both hydrogen and weak helium line absorption (Krause et al., 2008a).

Not listed in Fig. 2 is the Type IIn class. Type IIn supernovae are characterized by narrow hydrogen emission lines, which are thought to come from a dense circumstellar environment, probably caused by substantial mass lost by the progenitor. Its place in the diagram is not quite clear, as at least one Type IIn supernova, SN 2001ic, was observed to be a Type Ia supernova whose spectrum subsequently evolved into a Type IIn supernova (Hamuy et al., 2003).

2.1 Core collapse supernovae

Core collapse supernovae mark the end of the lives of massive stars; that is, those stars with main sequence masses $M \gtrsim 8 M_{\odot}$ (see Woosley and Janka, 2005, for a review). Just prior to collapse the star consists of different layers with the products of the different consecutive burning stages. From the core to the outside one expects: iron-group elements in the core (silicon-burning products), then silicon-group elements (oxygen-burning products), oxygen (a neon burning product), neon and magnesium (carbon-burning products), carbon (a helium-

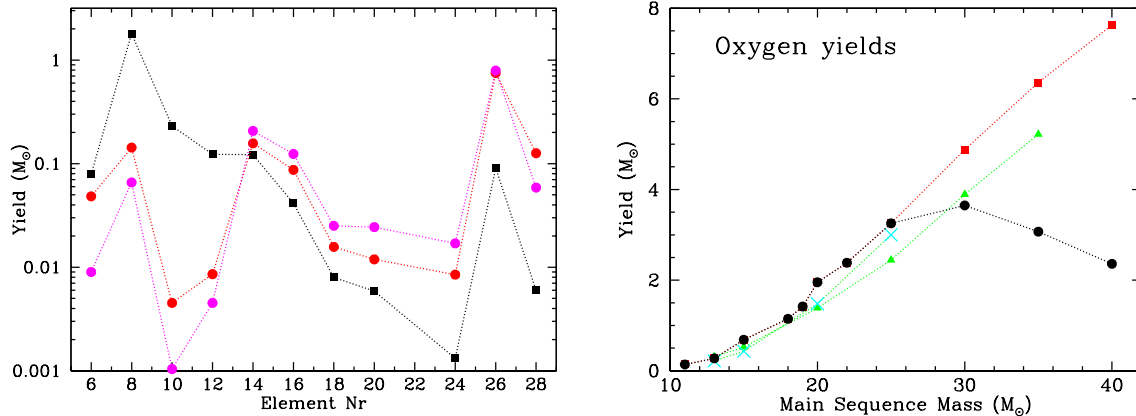


Figure 3: Left: Supernova yields for the most abundant X-ray emitting elements. The squares/black line indicates the mean yield for core collapse supernovae, whereas the circles indicate thermonuclear supernovae (the W7 deflagration model in red and the WDD2 delayed detonation model in magenta). The model yields were taken from Iwamoto et al. (1999). Right: Oxygen yield of core collapse supernovae as a function of main sequence mass. The circles and squares are the predictions of Woosley and Weaver (1995), the triangles are predictions of Chieffi and Limongi (2004), and the crosses of Thielemann et al. (1996). In general the oxygen yields obtained by the various groups are very similar, but above $30 M_{\odot}$ one sees that certain models (Woosley and Weaver, 1995, using 10^{51} erg explosion energies) predict a diminishing oxygen yield. The reason is that above $30 M_{\odot}$ stellar cores may collapse into black holes, and part of the oxygen falls onto the black hole. The amount of fall-back is governed by the explosion energy and the amount of pre-supernova mass loss, but it is also sensitive to the numerical treatment of the explosion.

burning product), helium (a hydrogen-burning product), and, finally, unprocessed hydrogen-rich material.

The creation of the iron-group core, which lasts about a day, is the beginning of the end of the star, as no energy can be gained from nuclear fusion of iron. The core collapses into a proto-neutron star, and for the most massive stars into a black hole. Most of the gravitational energy liberated ($E \sim GM^2/R_{ns} \sim 10^{53}$ erg, with R_{ns} the neutron star radius) is in the form of neutrinos. This has been confirmed with the detection of neutrinos from SN1987A by the Kamiokande (Hirata et al., 1987) and Irvine-Michigan-Brookhaven (Bionta et al., 1987) water Cherenkov neutrino detectors.

The supernova explosion mechanism itself, which requires that $\gtrsim 10^{51}$ erg of energy is deposited in the outer layers, is not well understood. The formation of a proto-neutron star suddenly terminates the collapse, and drives a shock wave through the infalling material. However, numerical simulations show that the shock wave stalls. It is thought that the shock wave may be energized by the absorption of a fraction of the neutrinos escaping the proto-neutron star, but most numerical models involving neutrino absorption are still unsuccessful in reproducing a supernova explosion (Janka et al., 2007). The most recent research, therefore, focusses on the role of accretion instabilities for the supernova explosion, as these instabilities help to enhance the neutrino absorption in certain regions just outside the proto-neutron star. A promising instability is the so called, *non-spherically symmetric standing accretion shock instability* (SASI, Blondin et al., 2003), which may also help to explain pulsar kicks and rotation (Blondin and Mezzacappa, 2007). Alternatively, simula-

tions by Burrows et al. (2007) suggest that acoustic power, generated in the proto-neutron star due to g-mode oscillations, ultimately leads to a successful explosion (but see Weinberg and Quataert, 2008). Finally, there have been suggestions that neutrino deposition is not the most important ingredient for a successful explosion, but that amplification of the stellar magnetic field, due to differential rotation and compression, may lead to magneto-centrifugal jet formation, which drives the explosion (Wheeler et al., 2002).

SASI, acoustic power, and magneto-centrifugal models all predict deviations from spherical symmetry. In the magneto-rotational models one even expects a bipolar symmetry. Another reason why deviations from spherical symmetry has received more attention is that long duration gamma-ray bursts are associated with very energetic Type Ic supernovae (hypernovae). Given the nature of gamma-ray burst these explosions are likely jet driven. This raises the possibility that also more normal core collapse supernovae have jet components (Wheeler et al., 2002). There is indeed evidence, based on optical polarimetry, that core collapse supernovae, especially Type Ib/c, are aspherical (e.g. Wang et al., 2001). In Sect. 9.1 I will discuss evidence that also the remnants of core collapse supernovae show deviations from spherical symmetry.

The ejecta of core collapse supernovae consist primarily of stellar material, except for the innermost ejecta, which consist of explosive nucleosynthesis products, mostly Fe and Si-group elements. These elements are synthesized from protons and alpha-particles, which are the remains of the heavy elements that have disintegrated in the intense heat in the innermost regions surrounding to the

collapsing core (Arnett, 1996). Some of the explosive nucleosynthesis products are radioactive, such as ^{56}Ni , and ^{44}Ti . In particular the energy generated by the decay of ^{56}Ni into ^{56}Co , and finally ^{56}Fe , heats the ejecta, which leaves a major imprint on the evolution of the supernova light curve. The yields of these elements depend sensitively on the details of the explosion, such as the mass cut (the boundary between material that accretes on the neutron star and material that is ejected), explosion energy, and explosion asymmetry. Since the mass of the neutron star/black hole, the location of energy deposition and the presence of asymmetries are not well constrained, the expected yields of these elements are uncertain, and vary substantially from one set of models to the other (Fig. 3, Woosley and Weaver, 1995; Thielemann et al., 1996; Chieffi and Limongi, 2004).

Overall the yields of core collapse supernovae are dominated by carbon, oxygen, neon and magnesium, which are products of the various stellar burning phases (e.g. Woosley and Weaver, 1995; Thielemann et al., 1996; Chieffi and Limongi, 2004). These yields are a function of the initial mass of the progenitor (Fig. 3). It is for this reason that oxygen-rich SNRs (Sect. 9.1) are considered to be the remnants of the most massive stars.

2.2 Thermonuclear supernovae

Type Ia supernovae are generally thought to be thermonuclear explosions of C/O white dwarfs, i.e. the explosion energy originates from explosive nuclear burning, rather than from gravitational energy liberated during the collapse of a stellar core.

Although there is some variation in peak brightness of Type Ia supernovae, the variation is much less than that of Type II supernovae. This is in line with the idea that all Type Ia supernovae are explosions of similar objects: C/O white dwarfs with masses close to the Chandrasekhar limit ($1.38 M_{\odot}$). Moreover, an empirical relation exists between their peak brightness and the post peak decline rate of the light curve (Phillips et al., 1992), which can be used to calibrate the absolute peak brightness of each event. This makes Type Ia supernovae excellent distance indicators, on which much of the evidence rests that the expansion of the Universe is accelerating (Perlmutter et al., 1998; Garnavich et al., 1998; Riess et al., 2007).

There is no direct observational evidence that Type Ia progenitors are white dwarfs, but the fact that only Type Ia supernovae can occur among old stellar populations indicates that massive stars cannot be their progenitors. Their relative uniformity can be best explained by assuming a progenitor type with a narrow mass range (Mazzali et al., 2007). Moreover, C/O white dwarfs close to the Chandrasekhar mass limit are very likely Type Ia progenitors, since their high density makes for an ideal “nuclear fusion bomb” (Arnett, 1996): Once a nuclear reaction in the core is triggered, it will result in an explosion. The trigger mechanism itself is, however, not well understood.

A more serious problem is that we do not know what

the most likely progenitor systems are. It is clear that C/O white dwarfs have to accrete matter in order to reach the Chandrasekhar limit, so thermonuclear supernovae must occur in a binary system. However, this still leaves several possibilities for the progenitor systems: double degenerate systems (two white dwarfs), or white dwarfs with either a main sequence star, or an evolved companion (i.e. single degenerate). Only a limited range of mass transfer rates, $\sim 4 \times 10^{-8} - 7 \times 10^{-7} M_{\odot} \text{ yr}^{-1}$, lead to stable growth of the white dwarf (Nomoto, 1982; Shen and Bildsten, 2007). Novae, for instance, are relatively slow accretors, which are thought to blow off more mass than they accrete. The only stable white dwarf accretors seem to be supersoft sources², but their population seems too small to account for the observed supernova rate (e.g. Ruiter et al., 2009). Depending on the progenitor evolution and accretion scenarios, the progenitor binary system may affect its circumstellar medium. For example, in the case of wind accretion, not all the mass lost from the donor will end up on the white dwarf. Hachisu et al. (1996, 1999) proposed a scenario in which Roche-lobe overflow from the donor star is stabilized through a fast, optically thick, wind from the white dwarf, which will also affect the immediate surroundings of the SNR.

For some time it was thought that Type Ia supernovae were associated with population II stars, in which case they must evolve on time scales $\gtrsim 10^9$ yr, but it has recently been established that also a short “channel” exists, with an evolutionary time scale of $\sim 10^8$ yr (e.g. Mannucci et al., 2006; Aubourg et al., 2008).

Models for thermonuclear explosions come in three classes: detonation, deflagration, and delayed detonation models. In detonation models the explosive nucleosynthesis occurs due the compression and heating of the plasma by a shock wave moving through the star. In deflagration models the burning front proceeds slower than the local sound speed. The nuclear fusion in the burning front is sustained by convective motions that mixes unburnt material into the hot burning zone. The classical deflagration model is the W7 of Nomoto et al. (1984).

Pure detonation models predict that almost all of the white dwarf matter will be transformed into iron-group elements, whereas optical spectroscopy of Type Ia supernovae show that the ejecta contain significant amount of intermediate mass elements (Branch et al., 1982). On the other hand, the pure deflagration models overpredict the production of ^{54}Fe with respect to ^{56}Fe and predict too narrow a velocity range for the intermediate mass elements compared to observations. For these reasons, the currently most popular model for Type Ia supernovae are the delayed detonation (DDT) models (Khokhlov, 1991), in which the explosion starts as a deflagration, but changes to a detonation wave burning the remainder of the white dwarf into intermediate mass elements (IMEs), such as silicon. There is observational evidence that the fraction of

²Soft X-ray point sources that are thought to be white dwarfs that stably accrete material from a companion (Kahabka and van den Heuvel, 1997).

C/O that is burned is roughly constant $M = 1.1 M_{\odot}$, but that the variation in peak brightness is either caused by the ratio of iron-group elements over IME products (Mazali et al., 2007), or by the ratio of stable iron over ^{56}Ni (Woosley et al., 2007). ^{56}Ni decays into ^{56}Fe , and the heat that this generates determines the brightness of a Type Ia supernova (see Sect. 6.2).

Figure 3 shows the predicted overall abundance pattern of deflagration and DDT models. Compared to core collapse supernovae, thermonuclear supernovae produce much more iron-group elements ($\sim 0.6 M_{\odot}$). The explosion energy, E , of thermonuclear explosions is determined by the mass of their burning products (Woosley et al., 2007):

$$E_{51} = 1.56M_{\text{Ni}} + 1.74M_{\text{Fe}} + 1.24M_{\text{IME}} - 0.46, \quad (1)$$

with the E_{51} the final kinetic energy in units of 10^{51} erg, and the masses of stable Fe, ^{56}Ni and IME in solar units.

3 The classification of supernova remnants

Given the fact that supernovae can be broadly classified in core collapse and thermonuclear/Type Ia supernovae, one would hope that SNRs would be classified as core collapse or Type Ia SNRs. Although it is possible now to determine the supernova origin of a given SNR using X-ray spectroscopy (see Sect. 7 and 8), for many old SNRs, whose emission is mainly coming from swept-up gas, one has to rely on secondary indicators for determining their supernova origin. The most reliable indicator is of course the presence of a neutron star inside the SNR, which makes it clear that the SNR must have a core collapse origin. But even here one has to be aware of chance alignments (Kaspi, 1998), in particular for SNRs with large angular diameters. A secondary indicator for a SNR to originate from a core collapse event is whether a SNR is located in a star forming region or inside an OB association (e.g Westlund, 1969). But this does not constitute proof for such an origin. In contrast, a position of a SNR high above the Galactic plane can be taken as supporting evidence for a Type Ia origin. Such is the case for, for example, SN 1006 (Stephenson and Green, 2002).

Because the supernova origin of SNRs is often difficult to establish, SNRs have a classification of their own, which is mostly based on their morphology. Traditionally, this classification recognized three classes: *shell type* SNRs, *plerions*, and *composite SNRs*. As the blast wave sweeps through the interstellar medium (Sect. 4) a shell of shock heated plasma is created. Therefore, in many cases the morphology of a SNR is characterized by a limb brightened shell, which classifies the SNR as a shell-type SNR.

However, in case of a core collapse one may expect the presence of a rapidly rotating neutron star. It loses energy with a rate of $\dot{E} = I\Omega\dot{\Omega} = 4\pi^2 I\dot{P}/P^3$, with Ω , the angular frequency, P the rotational period and $I \approx 10^{45}$ g cm²

the moment of inertia. This energy loss produces a wind of relativistic electrons and positrons, which terminates in a shock, where the electrons/positrons are accelerated to ultra-relativistic energies. These particles advect and diffuse away from the shock creating a nebula of relativistic electron/positrons which emit synchrotron radiation from the radio to the soft γ -ray bands, and inverse Compton scattering from soft γ -ray to the TeV band (Gaensler and Slane, 2006, for a review). Such a nebula is aptly named a *pulsar wind nebula*. The most famous pulsar wind nebula is the Crab Nebula (also known as M1 or Taurus A), which is powered by the pulsar B0531+21. This nebula is associated with the historical supernova of 1054 (Stephenson and Green, 2002). As a result the Crab Nebula, but also similar objects like 3C58, have the status of a SNR. Since the nebula has a morphology that is bright in the center, and does not show a shell, they are called *filled center* SNRs or *plerions*, with the name plerion derived from the Greek word for "full", *pleres* (Weiler and Panagia, 1978).

It is arbitrary whether one should call the Crab-nebula and related objects plerions or pulsar wind nebula. The radio and X-ray emission from plerions is powered by the pulsar wind, not by the supernova explosion, and as such the nebula should not really be referred to as a SNR. To complicate matters, the Crab nebula does show optical line emission from supernova ejecta, which could be referred to as a SNR. Pulsar wind nebulae can be found around both young and old pulsars, even a few millisecond pulsars have small nebulae around them (Kargaltsev and Pavlov, 2008). Since these older pulsars do not have a connection with recent supernova activity, one should not call them plerions. So the name pulsar wind nebula is more generic and informative than plerion, and is, therefore, preferable.

Energetic pulsars with ages less than $\sim 20,000$ yr are expected to have blown a pulsar nebula while they are still surrounded by the SNR shell. One expects then a radio and X-ray morphology that consists of a pulsar wind nebula surrounded by a shell. Indeed a few SNRs have this characteristic (Fig. 4c) and are classified as *composite SNRs*. In fact, it is still puzzling why a young object like the Crab Nebula does not show a SNR shell (see Hester, 2008, for a discussion).

Since the 1980s the SNR classification has become broader. Due to the imaging capabilities of X-ray satellites like *Einstein* and *ROSAT* it became clear that there are many SNRs that display a shell-type morphology in radio emission, but whose X-ray emission mainly comes from the center of the SNR (White and Long, 1991; Rho and Petre, 1998), as illustrated in Fig. 4d. In general, these SNRs are relatively old, and are associated with dense interstellar medium. The X-ray emission from the center of these SNRs was not powered by a pulsar, but consisted of thermal emission from a hot plasma. These SNRs are referred to as *mixed-morphology SNRs* (Rho and Petre, 1998) or as *thermal-composite SNRs* (Shelton et al., 1999). I will discuss their properties in Sect. 10.3.

X-ray spectroscopy has greatly enhanced our ability



Figure 4: The SNR morphological classification illustrated with examples. From top left to bottom right: a) The Cygnus Loop, a shell-type SNR with a diameter of 3° , as observed by the *ROSAT* PSPC instrument (Levenson et al., 1998), red is very soft emission from ~ 0.1 - 0.4 keV, green $\sim 0.5 - 1.2$ keV, and blue $\sim 1.2 - 2.2$ keV. b) 3C58, a plerion/pulsar wind nebula, as observed by *Chandra* (Slane et al., 2004). The long axis of this object is $\sim 7'$. c) The composite SNR Kes 75 as observed by *Chandra* (Helfand et al., 2003) with the inner pulsar wind nebula, which has a hard X-ray spectrum, powered by the pulsar J1846-0258. The partial shell has a radius of $\sim 1.4'$. The colors indicate 1-1.7 keV (red, Ne and Mg emission), 1.7-2.5 keV (green, Si/S), and 2.5-5 keV (blue, mostly continuum emission from the pulsar wind nebula). d) The “thermal-composite” SNR W28 as observed in X-rays by the *ROSAT* PSPC (blue) and in radio by the VLA (Dubner et al., 2000). (Image credit: Chandra press office, <http://chandra.harvard.edu/photo/2008/w28/more.html>)

to derive the origin of SNRs (Sect. 7 and 8). So one now also encounters classifications such as *Type Ia SNR*. Other SNRs show optical and X-ray evidence for enhanced oxygen abundances; these so-called *oxygen-rich SNRs* (Sect. 9.1) are likely the remnants of the most massive stars. Depending on the context these designations are often more helpful than the morphological classifications.

Note that these new classifications are not mutually exclusive with the traditional morphological classifications. For example oxygen-rich SNRs such as G292.0+1.8 and the Large Magellanic Cloud SNR B0540-69.3, also harbor a pulsar wind nebulae. They can therefore be classified both as composite SNRs and as oxygen-rich SNRs.

4 The hydrodynamic structure and evolution of supernova remnants

4.1 Evolutionary phases

The evolution of SNRs is usually divided in four phases (Woltjer, 1972): I) the ejecta dominated phase, in which the mass of the supernova ejecta, M_{ej} , dominates over the swept-up mass, M_{sw} ; II) the Sedov-Taylor phase, for which $M_{\text{sw}} > M_{\text{ej}}$, but for which radiative losses are not energetically important; III) the pressure-driven, or “snow-plough” phase, in which radiative cooling has become energetically important; the evolution of the shock radius is now best described by using momentum conservation; IV) the merging phase, in which the shock velocity and temperature behind the shock become comparable to, respectively, the turbulent velocity and temperature of the interstellar medium.

Although these discrete phases provide a useful framework to think of SNRs, it should be kept in mind that it is an oversimplification, and the phase of an individual SNR is not always that easily labeled. Moreover, different parts of a SNR may be in different phases. For example, a remnant like RCW 86 has radiative shocks in the southwest (phase III), whereas in the northeast it has very fast, non-radiative, shocks (phase I). This is the result of the complexity of the medium it is involving in, which is probably shaped by the stellar wind of the progenitor that created a cavity, surrounded by a dense shell, with which part of the shock wave is interacting (e.g. Rosado et al., 1994; Vink et al., 1997).

Phase I is sometimes called the free-expansion phase, and phase II the adiabatic phase. Both names are somewhat misleading. Free expansion suggests that the shock velocity is described by $V_s = R_s/t$, with R_s , the radius of the outer shock, and t the age of the SNR. However, as described below, even in phase I one has $V_s < R_s/t$. Since energy losses are according to standard models not important in both phase I and II, it is also misleading to call exclusively phase II the adiabatic phase. Moreover, in the very early evolution of SNRs (almost the supernova phase) SNRs may go through a short radiative loss phase (e.g. Truelove and McKee, 1999; Sorokina et al., 2004).

Also escaping cosmic rays may add to the energy losses in phase I and II (see Sect. 5.1). Despite these shortcomings, the labels have proven to be of some value, as they provide some framework to characterize the evolutionary phase of a given SNR.

In the literature one also often finds designations for SNRs like “young”, “mature” and “old” (Jones et al., 1998). These designations do not have a very precise meaning, but a general guideline is that young SNRs are less than $\sim 1000 - 2000$ yr old, and are in phase I or early in phase II, mature SNRs are in late phase II, or early phase III, whereas the label old SNRs is usually given to the very extended structures associated with SNRs in phase IV. These old SNRs hardly produce X-ray emissions, so in this review we will only encounter young and mature SNRs.

4.2 Analytical models

Several analytical models for the shock evolution of SNRs exist. The most widely used is the Sedov-Taylor self-similar solution (Sedov, 1959; Taylor, 1950). It assumes that the explosion energy E is instantaneously injected into a uniform medium with uniform density ρ_0 (i.e. a point explosion), and that no energy losses occur. In that case the shock radius R_s and velocity V_s will develop as

$$R_s = \left(\xi \frac{Et^2}{\rho_0} \right)^{1/5}, \quad (2)$$

$$V_s = \frac{dR_s}{dt} = \frac{2}{5} \left(\xi \frac{E}{\rho_0} \right)^{1/5} t^{-3/5} = \frac{2}{5} \frac{R_s}{t}. \quad (3)$$

The dimensionless constant ξ depends on the adiabatic index; $\xi = 2.026$ for a non-relativistic, monatomic gas ($\gamma = 5/3$). An analytical solution exists for the density, pressure, and velocity profiles inside the shocked medium, which is shown in Fig. 5. The Sedov-Taylor solution can be generalized to a gas medium with a power-law density profile $\rho(r) \propto r^{-s}$: $R_s \propto t^\beta$, $V_s = \beta R_s/t$, with $\beta = 2/(5-s)$, the expansion parameter. An astrophysically relevant case is $s = 2$, corresponding to a SNR shock moving through the progenitor’s stellar wind (see below); a situation that likely applies to the young Galactic SNR Cas A (e.g. van Veelen et al., 2009). This gives $\beta = 2/3$, which should be compared to the experimental value found for Cas A based on the expansion found in X-rays: $\beta = 0.63 \pm 0.02$ (Vink et al., 1998; Delaney and Rudnick, 2003; Patnaude and Fesen, 2009).

The Sedov-Taylor solutions do not take into the account structure of the supernova ejecta itself. This is a good approximation once the swept-up mass exceeds the ejecta mass. However, in the early phase, only the outer layers of the supernova transfer their energy to the surrounding medium. As time progresses, more energy is transferred from the freely expanding ejecta to the SNR shell. This takes place at a shock separating hot ejecta from freely expanding (cold) ejecta, the so-called reverse shock (McKee, 1974).

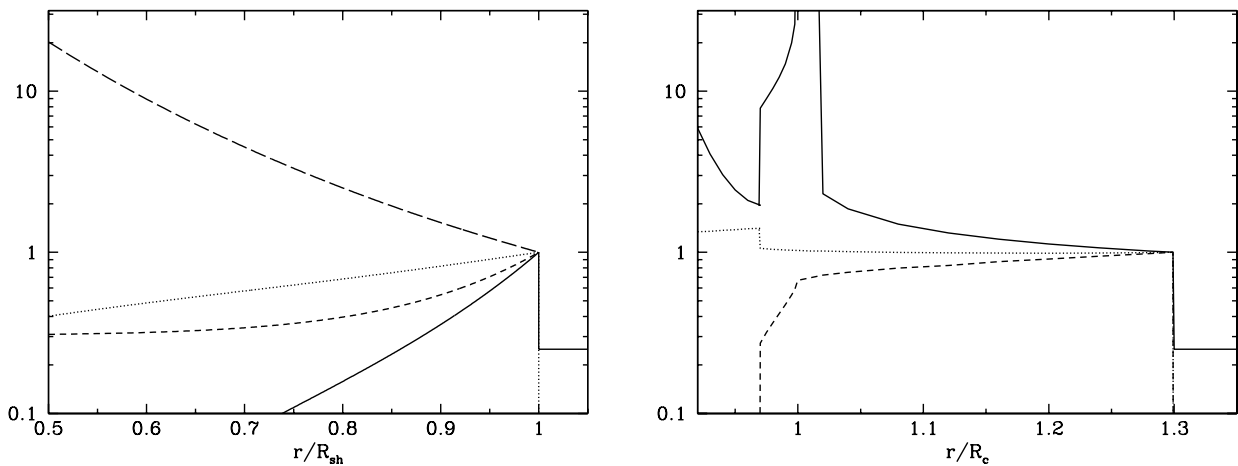


Figure 5: The structure of a SNR as given by the self-similar models of Sedov (1959) (left) and Chevalier (1982) ($n = 7, s = 2$). The values for the parameters have been normalized to the values immediately behind the forward shock. For the Sedov model the radius is expressed in units of the shock radius, for the Chevalier model in units of the contact discontinuity R_c , the border between swept-up and ejecta material. The solid lines show the density, the dotted lines the velocity, and the short-dashed lines the pressure profiles. For the Sedov model also the temperature is indicated (long-dashed line). For this model the temperature goes to infinity toward the center. For the Chevalier model the density goes to infinity for $r = R_c$. Note that in the observer frame the velocity drops at the reverse shock.

Two analytical models exist to describe the structure and evolution of SNRs taking into account the initial velocity structure of the ejecta. The first one, by Chevalier (1982), describes the early evolution of SNRs, in which the freely expanding ejecta have approximately a power-law density distribution $\rho_{ej} \propto v_{ej}^{-n}$. This is a reasonable approximation for the outer ejecta structure as found in numerical models of supernova explosions, with $n = 7$ a situation that describes reasonably well the ejecta structure of Type Ia supernovae, whereas $n = 9 - 12$ is a valid approximation for the density structure of core collapse supernovae.

As shown by Chevalier (1982) the SNR evolution can be described by a self-similar solution of the form:

$$R_s \propto t^\beta, \quad (4)$$

with β the expansion parameter given by³

$$\beta = \frac{n-3}{n-s}. \quad (5)$$

For $s = 0, n = 7$ this gives $\beta = 0.57$, and for $n = 9, s = 2$ this gives $\beta = 0.86$. The models describe a self-similar velocity, pressure, and density structure. I will not reproduce them here, but show as an example the density, pressure, and velocity structure of a $n = 7, s = 2$ model (Fig. 5). It is important to realize that the Chevalier solutions describe the early evolution of SNRs, when the reverse shock has not yet reached the inner most ejecta. Once the inner ejecta are reached by the reverse shock the expansion param-

³The expansion parameter is often, but not uniformly, indicated with the symbol m , but since the characters i, \dots, n have an integer connotation, I opt here for β . Note that Truelove and McKee (1999) use η (but this conflicts with its use in acceleration theory, Sect. 5.5), and Chevalier (1982) uses $1/\lambda$.

eter will evolve toward the Sedov solution (thus the expansion parameter evolves from $\beta = (n-3)/(n-s)$ to $\beta = 2/(5-s)$). It is clear from the Chevalier solutions that from a very early stage on $\beta < 1$. There is also observational evidence for this. For example, the initial expansion parameter of SN 1993J in the galaxy M81 has recently been determined to be $\beta = 0.85$ (Marcaide et al., 2009); assuming an interaction of the shock with a circumstellar wind ($s = 2$) this implies $n \approx 8.5$.

An analytical model that takes into account the smooth transition from phase I to phase II was obtained by Truelove and McKee (1999). Their models employ the following characteristic length, time and mass scales:

$$\begin{aligned} R_{ch} &\equiv M_{ej}^{1/3} \rho_0^{-1/3}, \\ t_{ch} &\equiv E^{-1/2} M_{ej}^{5/6} \rho_0^{-1/3}, \\ M_{ch} &\equiv M_{ej}, \end{aligned} \quad (6)$$

with M_{ej} the ejected mass, E the explosion energy, and ρ_0 the circumstellar medium density. These numbers can be used to construct a set of solutions, which now only depend on n and s , and the dimensionless variables $R^* = R/R_{ch}$ and $t^* = t/t_{ch}$. The models are continuous, but consist of two parts; one for the evolution in the ejecta dominated phase and one for the Sedov-Taylor phase, with t_{ST} the dimensionless transition age. For example, the blast wave trajectory in the $n = 7, s = 0$ model is $R_s^* 1.06 = t^{*4/7}$ for $t^* < t_{ST}$ and $R_s^* = (1.42t^* - 0.312)^{2/5}$ for $t^* > t_{ST}$, with $t_{ST} = 0.732$. These solutions show that initially the expansion parameter is identical to the one derived by Chevalier (1982) (Eq. 5), while it asymptotically approaches the Sedov-Taylor solution, $\beta = 2/5$.

Fig. 6 illustrates the evolution of SNR shocks as given

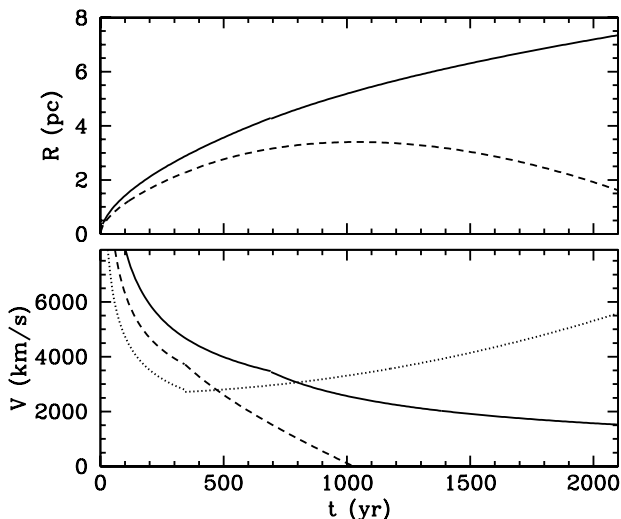


Figure 6: Shock radii and shock velocities as a function of time according to the Truelove-McKee $n = 7, s = 0$ model (Truelove and McKee, 1999). The solid line represents the forward shock, whereas the dashed line represents the reverse shock. In the bottom panel the reverse shock velocity in the frame of the ejecta is shown as a dotted line. The dimensionless model was adjusted to fit the properties of Kepler’s SNR (Vink, 2008c).

by one of the Truelove & McKee solutions. It shows that the reverse shock initially expands outward, despite its name, with $\beta = (n - 3)/(n - s)$. But as soon as the shock heated shell has more pressure than the ram pressure of the freely expanding ejecta, the reverse shock will move toward the center; i.e. its velocity in the observers frame will become negative. For the plasma temperature the shock velocity in the frame of the freely expanding ejecta is important (Sect. 5.1). This is given by

$$V_{\text{rev,phys}} = \frac{R_{\text{rev}}}{t} - V_{\text{rev,obs}}, \quad (7)$$

with R_{rev}/t the velocity of the freely expanding ejecta just before entering the reverse shock, and $V_{\text{rev,obs}} = dR_{\text{rev}}/dt$, the reverse shock velocity in the frame of the observer. Fig. 6 shows that initially $|V_{\text{rev,phys}}| < V_s$, in which case one expects the shocked ambient medium to be hotter than the shocked ejecta. In later phases this situation reverses, as $|V_{\text{rev,phys}}| > V_s$, resulting in a hot core enclosed by a cooler shell. Once the reverse shock has reached the center of the SNR, it consists of a hot shell surrounding an even hotter, but very tenuous interior.

It is worth mentioning that efficient cosmic-ray acceleration (Sect. 5.5) may alter the hydrodynamics of SNRs, because it alters the equation of state, and because escaping cosmic rays may result in energy losses. This can result in a reverse shock radius at any given time that is closer to the outer shock than indicated by models like that of Truelove & McKee (Decourchelle et al., 2000). I will discuss in Sect. 11.3 the observational evidence for this.

In phase III, the momentum conservation or “snow-plough” phase, radiative energy losses have become dy-

namically important. Instead of energy conservation, the radial expansion is governed by momentum conservation, $MV_s = 4\pi/3 R_s^3 \rho_0 dR_s/dt = \text{constant}$. For the constant one can take the momentum at the time t_{rad} , for which radiative losses have become important: $t_{\text{rad}} = 4\pi R_{\text{rad}}^3 / 3\rho_0 V_{\text{rad}}$. Integration yields the following expression for the age, t , of the SNR as a function of radius (e.g. Toledo-Roy et al., 2009):

$$t = t_{\text{rad}} + \frac{R_{\text{rad}}}{4V_{\text{rad}}} \left[\left(\frac{R}{R_{\text{rad}}} \right)^4 - 1 \right]. \quad (8)$$

As can be seen, the expansion parameter in this phase is $\beta \approx 1/4$. Generally speaking, radiative losses become important when the post-shock temperature falls below $\sim 5 \times 10^5$ K, in which case oxygen line emission becomes an important coolant (e.g. Schure et al., 2009). This occurs when the shock velocity is $V_s = V_{\text{rad}} = 200 \text{ km s}^{-1}$ (Wolter, 1972, see also Sect. 5.1). One can use the Sedov self-similar solution (Eq. 2 and 3) to calculate when $V_s = V_{\text{rad}}$, thereby estimating R_{rad} and t_{rad} . Eq. 3 leads to expression for t_{rad} in terms of R_{rad} : $t_{\text{rad}} = R_{\text{rad}}/V_{\text{rad}} = 2.0 \times 10^{-8} R_{\text{rad}}$ s. Eq. 2, then provides the following estimate for the age and radius at which the SNR becomes radiative:

$$t_{\text{rad}} = 1.5 \times 10^{-13} \left(\frac{\xi E}{\rho_0} \right)^{1/3} = \quad (9)$$

$$1.4 \times 10^{12} \left(\frac{E_{51}}{n_{\text{H}}} \right)^{1/3} \text{ s} \approx 44,600 \left(\frac{E_{51}}{n_{\text{H}}} \right)^{1/3} \text{ yr}$$

$$R_{\text{rad}} = 7.0 \times 10^{19} \left(\frac{E_{51}}{n_{\text{H}}} \right)^{1/3} \text{ cm} \approx 23 \left(\frac{E_{51}}{n_{\text{H}}} \right)^{1/3} \text{ pc}, \quad (10)$$

with n_{H} the pre-shock hydrogen density, $\xi = 2.026$, and E_{51} the explosion energy E in units of 10^{51} erg.

4.3 Supernova remnants evolving inside wind-blown bubbles

The structure of the circumstellar medium is usually not as simple as used by the analytical solutions discussed above. The interstellar medium itself is not homogeneous, but also stellar winds from the supernova progenitors impose a specific structure on the ambient media. For example, a massive O-star will spend $\sim 90\%$ of its life on the main sequence, during which it blows a fast, tenuous wind with velocity $v_w \approx 1500 - 3000 \text{ km s}^{-1}$, with $\dot{M} \approx 5 \times 10^{-7} - 10^{-5} M_{\odot} \text{ yr}^{-1}$ (e.g. Mokiem et al., 2007). This wind carves a low density region into the interstellar medium, surrounded by a shock heated shell containing the swept-up interstellar medium and wind material.

In the subsequent red supergiant (RSG) phase the mass loss rate increases to as much as $\dot{M} \approx 10^{-4} M_{\odot} \text{ yr}^{-1}$ (e.g. van Loon et al., 2005), which, together with a much slower wind velocity $v_w \sim 10 \text{ km s}^{-1}$, results in a very dense wind, with a density at radius r given by

$$\rho_w(r) = \frac{\dot{M}}{4\pi r^2 v_w}, \quad (11)$$

a relation that follows from mass conservation. Stars more massive than $60 M_{\odot}$ can even have extremely high

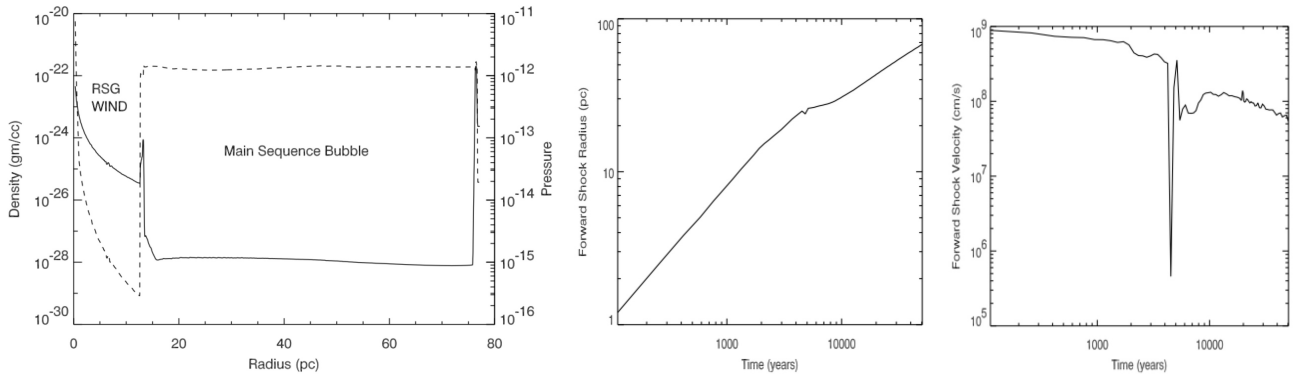


Figure 7: Left: The density (solid line) and pressure (dashed line) of the circumstellar medium around a red supergiant. Middle and right: The evolution of the shock radius and velocity for a SNR in a wind-blown cavity, surrounded by a dense, swept-up shell. All figures taken from Dwarkadas (2005).

mass loss rates, often accompanied by violent bursts of mass loss. These are so-called Luminous Blue Variables (LBVs). An example is Eta Carinae (Davidson and Humphreys, 1997).

Most massive stars will explode in the RSG phase, but the highest mass stars may enter the Wolf-Rayet star phase. In this phase the stars have lost all of their hydrogen envelopes. Their mass loss rates are high, $\dot{M} \approx 10^{-5} - 10^{-4} M_{\odot} \text{ yr}^{-1}$, with a high wind velocity $1000 - 2000 \text{ km s}^{-1}$ (Nugis and Lamers, 2000). This results in a tenuous wind, which will sweep up the RSG wind into a dense shell. It is not clear whether LBVs will become Wolf-Rayet stars, or whether they are the last stage of the stellar evolution.

Progenitors that were part of a binary system may even have had more complicated mass loss histories. In some cases a common envelope phase may have existed, which could also have lead to a stellar merger. In these case the circumstellar medium structure may be rather complex. See for example the binary evolution model that can explain some of the features of the circumstellar medium of SN 1987A (Morris and Podsiadlowski, 2007, Sect. 9.2).

So core collapse supernovae are, even in the simplest cases, surrounded by regions with different densities and temperatures, created and shock heated during the various wind phases (Weaver et al., 1977; Dwarkadas, 2005, Fig. 7). As long as the SNR shock moves through the unshocked stellar wind of the progenitor, the analytical models are valid, but if this is not the case, then the evolutionary path may differ quite substantially from the standard SNR evolutionary models discussed above.

These more complicated situations have been studied with numerical simulations. See for example Tenorio-Tagle et al. (1991), Dwarkadas (2005) and Fig. 7. In the case that the shell swept up by the wind has a mass that is higher than the ejecta mass, the shock wave will first move through the low density region without much deceleration ($\beta = 0.87$, for an $n = 9$ ejecta density profile, Eq. 5). In this phase the X-ray emission from the SNR is low, because of the low density inside the stellar wind. Once the shock

reaches the dense shell, transmitted and reflected shocks develop. The transmitted shock heats the shell and pushes it outward, whereas the reflected shock further heats the interior of the SNR. In this phase, the X-ray luminosity increases rapidly by a factor ten to hundred, due to the high density in the shell (Dwarkadas, 2005).

5 Collisionless shock heating and particle acceleration

5.1 Shock heating

Shock waves transform part of bulk kinetic energy into thermal energy. Astrophysical shocks are characterized by low densities, which makes that the actual heating process cannot be established by particle-particle interaction (Sect. 5.2). For SNRs part of the kinetic energy may not only be used for shock heating the plasma, but also for cosmic-ray acceleration.

Irrespective of the microphysical details of particle heating and acceleration, the collisionless shocks still have to obey the conservation of mass, momentum, and energy flux across the shock (e.g. Zel'dovich and Raizer, 1966; McKee and Hollenbach, 1980). However, one should realize that SNR shocks are not the idealized, infinitely narrow temperature transition zones treated in standard physics textbooks. Instead, collisionless heating, and cosmic-ray acceleration imply that there is a broad transition zone from the unshocked medium (or upstream) to the shocked (downstream) region. In the case of efficient cosmic-ray acceleration (Sect. 5.5), this transition zone, the so-called *cosmic-ray shock precursor*, has a width of approximately the diffusion length scale of the cosmic rays with energies near the peak in the energy spectrum (e.g. Blasi et al., 2005; Vladimirov et al., 2008).

Irrespective of whether cosmic-ray acceleration is important, mass conservation across the shock remains valid,

and for a plane parallel case implies:

$$\rho_0 v_0 = \rho_2 v_2 \leftrightarrow \rho_2 = \frac{v_0}{v_2} \rho_0 \equiv \chi \rho_0, \quad (12)$$

with χ the shock compression ratio, and v_0 and v_2 taken to be in the frame of the shock. The subscript 2 refers to the downstream plasma, and the subscript 0 the (far) upstream medium, thereby symbolically ignoring “region 1”, the transition zone containing the cosmic-ray shock precursor.

Cosmic-ray acceleration also hardly affects the conservation of momentum flux:

$$P_2 + \rho_2 v_2^2 = P_0 + \rho_0 v_0^2 \leftrightarrow P_2 = P_0 + \left(1 - \frac{1}{\chi}\right) \rho_0 V_s^2, \quad (13)$$

with the second part following from substituting Eq. 12, and relating v_0 to the shock velocity, $v_0 = -V_s$. For high Mach number shock waves the pressure far upstream can be neglected ($P_0 = 0$). And if we make the assumption that the downstream plasma pressure consists of a thermal and a non-thermal (cosmic-ray) part, with the parameter w giving the non-thermal (NT) pressure contribution,

$$w \equiv \frac{P_{2,NT}}{P_{2,T} + P_{2,NT}}, \quad (14)$$

we find from Eq. 13 and 14 that the post-shock plasma must have a temperature

$$kT_2 = (1-w) \frac{1}{\chi} \left(1 - \frac{1}{\chi}\right) \mu m_p V_s^2. \quad (15)$$

One of the consequences of efficient cosmic ray acceleration is that the highest energy cosmic rays may escape far upstream (i.e. into the unshocked medium), whereas downstream (in the shock-heated plasma) the dominant flux of cosmic-ray energy is through plasma transport. This means that conservation of energy flux is not necessarily valid. A similar situation holds for so-called *radiative shocks*, for which radiative energy losses are important, a situation that can occur for shocks with $V_s \lesssim 200 \text{ km s}^{-1}$.

We can take into account of the energy flux losses, F_{esc} , by introducing (Berezhko and Ellison, 1999): $\varepsilon_{esc} \equiv \frac{F_{esc}}{\rho_0 v_0^3}$. With this equation the conservation of energy flux can be written as

$$(u_2 + P_2 + \frac{1}{2} \rho_2 v_2^2) v_2 = (1 - \varepsilon_{esc}) \frac{1}{2} \rho_0 v_0^2 v_0, \quad (16)$$

with $u = \frac{1}{\gamma-1} P$, the internal energy, and γ the adiabatic index. Taking for the non-thermal (cosmic ray) contribution $\gamma = 4/3$ and for the thermal plasma $\gamma = 5/3$ we obtain

$$u_2 + P_2 = \left(\frac{3}{2} w + \frac{5}{2}\right) P_2 \equiv \Gamma P_2. \quad (17)$$

Using Eq. 13, we can rewrite Eq. 16 as

$$2\Gamma \left(1 - \frac{1}{\chi}\right) + \frac{1}{\chi} = (1 - \varepsilon_{esc}) \chi, \quad (18)$$

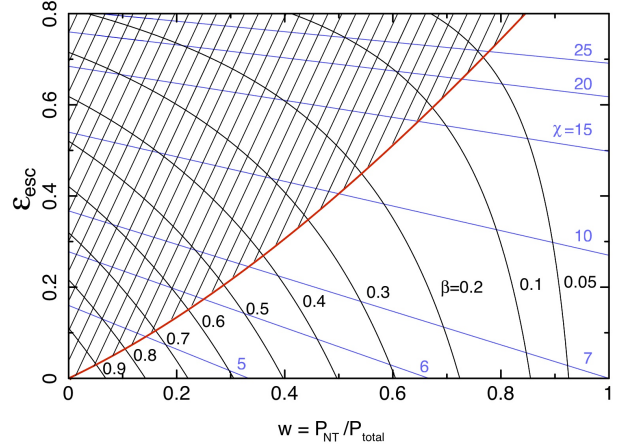


Figure 8: The impact of the partial pressure by non-thermal components (cosmic rays) and the fraction of energy flux escaping as cosmic rays (Vink, 2008a; Helder et al., 2009). The black lines indicate constant values of temperature (Eq. 15), given as a correction factor with respect to post-shock temperature for the standard case (i.e. $w = 0, \varepsilon_{esc} = 0$, Eq. 20): $\beta \equiv \overline{kT} / (\frac{3}{16} \mu m_p V_s^2)$. Also indicated are lines of constant post-shock compression ratio χ . The red line depicts the solution cosmic-ray acceleration with the highest possible efficiency (Helder et al., 2009; Vink et al., 2010); the combination of w and ε_{esc} to the left of this line are considered unphysical.

which has the non-trivial root (e.g. Berezhko and Ellison, 1999; Vink, 2008a):

$$\chi = \frac{\Gamma + \sqrt{\Gamma^2 - (1 - \varepsilon_{esc})(2\Gamma - 1)}}{1 - \varepsilon_{esc}}. \quad (19)$$

In most textbooks only the case of a single fluid gas without energy losses is considered. This corresponds to $w = 0$ and $\varepsilon_{esc} = 0$. This gives a compression ratio of $\chi = 4$. Substituting this in Eq 15 gives

$$\overline{kT} = \frac{3}{16} \mu m_p V_s^2 \approx 1.2 \left(\frac{V_s}{1000 \text{ km s}^{-1}}\right)^2 \text{ keV}, \quad (20)$$

with μ the average particle mass ($\mu \approx 0.6$ for a plasma with solar abundances).

I used here \overline{kT} in order to indicate that this refers to the average temperature, as different particle species can have different temperatures. The reason is that for collisionless shocks it is not quite clear whether the microphysics that governs the actual heating results in temperature equilibration among different, or whether different species will have different temperatures proportional to their mass: $kT_i \propto m_i V_s^2$ (Sect. 5.2). The latter can be expected if heating is predominantly governed by scattering isotropization of the incoming particles by plasma waves in the shock region.

Finally, if cosmic-rays contribute substantially to the post-shock pressure ($w \neq 0$) and, if cosmic-ray escape plays an important role, then the compression ratios can be much higher than $\chi = 4$. In this so-called *non-linear*

cosmic-ray acceleration case, there is no longer a unique value for kT and χ , but a range of values is possible. The possible values of the compression ratio and post-shock plasma temperature as a function of post-shock cosmic-ray pressure fraction, and escape flux are summarized in Fig. 8. In this figure the mean plasma temperature \overline{kT} is expressed in terms of the temperature for the $w = 0/\varepsilon_{esc} = 0$ case, using $\beta \equiv \overline{kT}/(3\mu m_p V_s^2/16)$.

In all cases non-linear cosmic ray acceleration leads to lower plasma temperatures, in the most extreme cases perhaps even quenching thermal X-ray emission (Drury et al., 2009). On a macroscopic level this can be understood by considering that part of the incoming energy flux is used for particle acceleration. On a more detailed level it can be understood by considering that directly upstream of the shock the cosmic rays provide a non-negligible pressure, which pre-compresses and pre-heats the plasma. The presence of the cosmic-ray precursor results therefore in a lower Mach number gas-shock.⁴ For a more thorough treatment of the shock equations, including a cosmic ray precursor, see Vink et al. (2010) for an analytical treatment, or Vladimirov et al. (2008); Caprioli et al. (2008) for a kinetic approach. In the latter two references also the effects of non-adiabatic precursor heating is taken into account.

5.2 Collisionless shocks

Shock waves in the interstellar medium (ISM) are characterized by very low densities, typically $n \sim 1 \text{ cm}^{-3}$. In high density shocks, such as in the earth's atmosphere, the shock heating process is accomplished by particle-particle interactions. However, the mean free paths for particle-particle interactions in shocks in the ISM are long compared to the typical sizes of SNRs. This can be illustrated as follows. For charged particles the energy exchange is governed by Coulomb interactions. A particle is deflected by 90° in the center of mass frame, if the following condition for the impact parameter b is met:

$$\frac{1}{2} \frac{m_1 m_2}{m_1 + m_2} v^2 = \frac{Z_1 Z_2 e^2}{b}, \quad (21)$$

with m_1, m_2 the masses of the two particles, $Z_1 e, Z_2 e$ their charges, and v their relative velocity. The cross section for such a deflection by a single scattering is ($\sigma_{\text{Coulomb}} = \pi b^2$):

$$\sigma_{\text{Coulomb}} \approx 4\pi \frac{Z_1^2 Z_2^2 e^4}{v^4} \left(\frac{m_1 + m_2}{m_1 m_2} \right)^2. \quad (22)$$

The corresponding collision time scale is $\tau_{\text{Coulomb}} = 1/(n\sigma v) \propto v^{-3} \propto E^{-3/2}$. Inserting for the m_1 and m_2 the proton mass and a typical velocity of $v = 1000 \text{ km s}^{-1}$, one finds for proton-proton collisions $\tau_{\text{pp}} \approx 10^{12} n_p^{-1} \text{ s}$ (about $32,000 n_p^{-1} \text{ yr}$), and a mean free path $\lambda_p \approx 10^{20} n_p^{-1} \text{ cm}$ (32 pc). These are much larger than the ages

⁴This is the actual shock that heats the plasma, but it is often called *sub-shock* in order to set it apart from the overall shock structure that includes both the precursor and the gas-/sub-shock.

and radii of young SNRs. As these young SNRs clearly do have shocks and hot, X-ray emitting, plasma, as beautifully shown by Fig. 1, the formation of the shock and the plasma heating cannot be the result of Coulomb interactions. Instead “collective interactions”, occurring through fluctuating electric and magnetic fields, must be responsible for the plasma heating. Simulations (e.g. Bennett and Ellison, 1995) show that the heating in such shocks takes place over a distance of typically 10-100 times c/ω_{pe} , with $\omega_{pe} = (4\pi e^2 n_e/m_e)^{1/2}$ the plasma frequency. This corresponds to a shock thickness of roughly $\Delta x = 10^7 n_e^{-1/2} \text{ cm}$, thirteen orders of magnitude smaller than the range over which Coulomb collisions operate. For this reason SNR shocks and shocks in other low density media, such as the interplanetary medium, are called *collisionless shocks*.

The heating mechanism is somewhat analogous to the process of “violent relaxation” (Lynden-Bell, 1967) in the formation of bound gravitational systems, such as galaxies and clusters of galaxies; i.e. large scale gravitational potential fluctuations rather than two-body interactions are important for the relaxation of the system.

5.3 Temperature equilibration

It is not a priori clear, whether collisionless shocks will result in temperature equilibration of all types of particles immediately behind the shock front (see Bykov et al., 2008a, for a review). The two opposite cases are a) complete equilibration, in which all different particle populations (electrons, protons, other ions) have the same temperature, which for a strong shock without cosmic-ray acceleration would mean $T \propto \mu m_p V_s^2$ (Eq. 15), or b) full non-equilibration, in which case each particle species thermalizes the bulk kinetic energy independently and one expects $T_i \propto m_i V_s^2$ (corresponding to replacing μm_p with m_i in Eq. 15 and 20).⁵ There are many plasma instabilities that act to equilibrate the energies of different plasma constituents. Both hybrid simulations (Cargill and Papadopoulos, 1988) and particle in cell (PIC) simulations (e.g. Shimada and Hoshino, 2000) show that high Mach number shocks may substantially heat the electrons, but not completely up to the same temperature as the protons. So one may expect $m_e/m_p \ll T_e/T_p < 1$. For example, Shimada and Hoshino (2000) report $T_e/T_p \approx 17\%$. Optical spectroscopy of SNR shocks show mixed results with indications that full equilibration is important for $V_s < 500 \text{ km s}^{-1}$, and non-equilibration for higher velocities (Ghavamian et al., 2007; Helder et al., 2011). In Sect. 11.1 I discuss the implications for X-ray spectroscopy.

Note that these simulations have several limitations. For example, PIC simulations often have $m_p/m_e \approx 0.01 - 1$,

⁵The latter case corresponds to a velocity distribution that is independent of the particle mass. This is again similar to the outcome of violent relaxation for bound gravitational systems. For example, in galaxy clusters the velocity distribution is similar for massive and dwarf galaxies (with the exception of the giant ellipticals that reside in a large fraction of cluster centers). Also in this case the kinetic energy (“temperature”) distribution is proportional to the mass of the galaxy.

for computational reasons. In contrast, hybrid simulations treat the electrons as a massless fluid. Moreover, the amount of equilibration of electron/proton temperatures may depend on the initial conditions, such as Mach number, the ratio of magnetic over kinetic pressure and the magnetic-field orientation. This means that some variation in shock equilibration can be expected in SNRs.

An important ingredient that affects electron heating, and one that is difficult to model, is cosmic-ray acceleration (see Sect. 5.5), because the process of acceleration to high energies takes place on a longer time scale than the formation of strong shocks, and longer than the typical time scales that can be modeled with PIC simulations.

Nevertheless, hybrid and PIC simulations (e.g. Bennett and Ellison, 1995; Dieckmann and Bret, 2009) do show evidence for the initial stages of particle acceleration: often the particle distribution has non-thermal components, i.e. the particles have roughly a Maxwellian energy distribution at low energies, but a non-thermal, quasi-power-law distribution at high energies. This non-thermal tail, may be the first stage of particle acceleration, but part of this non-thermal distribution, may disappear again further behind the shock, as the particles are slowed down through Coulomb interactions. This is especially relevant for the low energy part of the non-thermal electron distribution (Sect. 6.3.2, Vink, 2008b), and amounts to a source of late time electron heating.

At the shock front plasma wave coupling between electrons and accelerated ions may also result in heating of the electrons (Rakowski et al., 2008). Finally, very efficient particle acceleration by the Fermi process may alter the shock structure altogether, as it results in the formation of a cosmic-ray shock precursor that may pre-heat both electrons and protons before they enter the main shock (see Sect. 5.5 and Sect. 5.1). In Sect. 11.1 I review the observational measurements concerning electron/ion equilibration.

If the shock heating does not immediately lead to equal electron and ion temperatures, Coulomb interactions will slowly equilibrate them. It turns out that Eq. 22 is not a good approximation for the relevant cross sections, as it ignores the contributions for long range interactions. These result in less energy exchange per encounter, but they occur much more frequently. The relevant expressions for energy exchange between charged particles of various mass ratios can be found in Huba (2002), which gives for the temperature equilibration rate (see also Zel'dovich and Raizer, 1966; Itoh, 1984):

$$\frac{dkT_1}{dt} = 1.8 \times 10^{-19} \times \sum_i \frac{(m_1 m_i)^{1/2} Z_1^2 Z_i^2 e^4 n_i \ln \Lambda_{1i}}{(m_i kT_1 + m_1 kT_i)^{3/2}} (kT_i - kT_1) \text{ eV s}^{-1}, \quad (23)$$

with label 1 for the particle species of interest, i for all the other species, and kT measured in units of eV. $\ln \Lambda$ is the Coulomb logarithm, which is roughly similar for electron

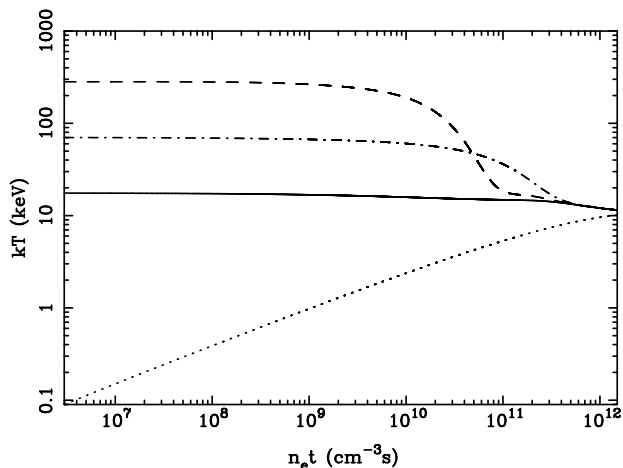


Figure 9: An illustration of the effect of temperature non-equilibration at the shock front for a shock velocity of $V_s = 3000 \text{ km s}^{-1}$. Shown is the temperature of electrons (dotted), protons (solid), helium (dashed-dotted) and oxygen ions (dashed) as a function of $n_e t$, assuming that heating at the shock front is proportional to the mass of the particle (Sect. 5.1). The oxygen-proton equilibration is faster than the helium-proton equilibration, as the cross sections scale linearly with particle mass, but quadratically with charge (Eq. 22). (Figure previously published in Vink (2006).)

proton interactions and for electron-electron interactions:

$$\ln \Lambda = 30.9 - \ln \left[n_e^{1/2} \left(\frac{kT_e}{1 \text{ keV}} \right)^{-1} \right]. \quad (24)$$

For electron-proton equilibration Eq. 23 implies an equilibration time scale:

$$\tau_{ep} \approx 3.1 \times 10^{11} n_p^{-1} \left(\frac{kT}{1 \text{ keV}} \right)^{3/2} \left(\frac{\ln \Lambda}{30.9} \right)^{-1} \text{ s}, \quad (25)$$

with T the mean temperature. Similarly, the electron self-equilibration time, which determines how fast the electrons can establish a Maxwellian distribution, is

$$\tau_{ee} \approx 4.9 \times 10^8 n_e^{-1} \left(\frac{kT}{1 \text{ keV}} \right)^{3/2} \left(\frac{\ln \Lambda}{30.9} \right)^{-1} \text{ s}. \quad (26)$$

Eq. 25 shows that it can easily take 10,000 years for electrons and protons to equilibrate, much longer than the ages of many of the young SNRs that will be discussed in the second part of this review. Note that the equilibration time is roughly inversely proportional to n_p ($\approx n_e$). A relevant parameter is, therefore, not so much the age of the SNR, but the average $n_e t$, a parameter that will resurface in Sect. 6.1.2, where non-equilibrium ionization is discussed. In fact, X-ray spectroscopy provides a direct way of measuring $n_e t$, thereby providing the means to estimate whether non-equilibration of temperatures could be important.

The possible absence of full equilibration has important consequences for the interpretation of X-ray observations (see Itoh, 1978, for an early discussion), because

in general the X-ray spectra reveal the electron temperature (Sect. 6.1), and not the mean plasma temperature. The mean plasma temperature is energetically the relevant parameter. It is for example directly related to the shock velocity (Sect. 5.1). Using the electron temperature, as an estimate for the mean temperature may lead to a serious underestimation of the shock velocity. But, as shown in Sect. 5.1, efficient cosmic-ray acceleration will lead to lower mean temperatures. So even having a good estimate of both the electron and ion temperatures may not be sufficient to estimate the shock velocity.

Fig. 9 illustrates the effects of non-equilibration of temperatures at the shock front. The equilibration time depends on the density, the mass ratio and the square of the charge of the particles (Eq. 23). The ion-ion equilibration, therefore, proceeds faster than electron-ion equilibration. Interestingly, iron-proton equilibration proceeds faster than proton-helium equilibration, due to the charge dependence. This becomes important for $n_e t > 10^9 \text{ cm}^{-3} \text{ s}$, when iron has become stripped of all m-shell electrons. Broadly speaking one can recognize three phases:

1. *Full non-equilibration*; all species have different temperatures ($n_e t \lesssim 5 \times 10^{10} \text{ cm}^{-3} \text{ s}$),
2. *Partial non-equilibration*; all ions are equilibrated, but without electron-ion equilibration ($5 \times 10^{10} \lesssim n_e t \lesssim 10^{12} \text{ cm}^{-3} \text{ s}$),
3. *Full equilibration* ($n_e t \gtrsim 10^{12} \text{ cm}^{-3} \text{ s}$).

It is worth noting that non-equilibration of electron-ion temperatures may also be caused by ionization (Itoh, 1984): Due to the fact that the cross sections for ionization peak near the ionization energy, the electrons originating from post-shock ionization will start relatively cool. The electron-electron equilibration is relatively fast, so this results in a relatively cool electron population, even if the free electrons that entered the shock were equilibrated with the ions. This may be an important effect in metal-rich plasmas, which have been shock heated by the reverse shocks in young SNRs (Sect. 4), since in that case most of the electrons will originate from ionizations, rather than from entering the shock as free electrons.

5.4 Thermal conduction

Thermal conduction is a topic that every now and then enters the discussion of SNRs, as significant thermal conduction may alter the temperature and density structures of SNRs (see for example Cui and Cox, 1992, and Sect. 10.3).

The role of thermal conduction in SNR structure and evolution, like that of temperature non-equilibration, has never been satisfactorily resolved. The reason is that thermal conduction in a plasma is likely to be anisotropic due to the inhibiting effects of magnetic fields. Note that the processes of thermal conduction and temperature equilibration are related, because thermal conduction is a combination of transport and exchange of heat. Without mag-

netic fields, or along magnetic fields, thermal conduction is usually mediated through electrons, because they have higher thermal speeds and are more strongly coupled to each other. Across magnetic-field lines the particles with the largest gyroradius, i.e. the ions, will dominate thermal conduction.

The process of thermal conduction is described by Fourier's law:

$$\mathbf{F}_{\text{heat}} = -\kappa \nabla T. \quad (27)$$

In the absence of magnetic fields, or along magnetic field lines, the coefficient κ depends on the typical mean free path for energy exchange, $\lambda \approx \tau_{ee} v_{\text{th}}$, with $v_{\text{th}} = \sqrt{kT_e/m_e}$ and τ_{ee} the self-equilibration time (Eq. 26). Numerically, $\lambda \approx 0.2(kT/1 \text{ keV})^2 \text{ pc}$. The amount of heat being transported relates to the energy density $u = 3/2 n_e kT_e$ and the transport velocity v_{th} , so that approximately $\kappa/k \approx 3/2 n_e kT \lambda v_{\text{th}} = 3/2 n_e kT \tau_{ee} v_{\text{th}}^2$. This is correct up to a small factor that is needed to ensure zero electric current (e.g. Spitzer, 1965). Taking this into account one obtains (Huba, 2002)⁶:

$$\kappa_{\parallel}/k = 2.3 \frac{n_e kT_e \tau_{ee}}{m_e} = 2.0 \times 10^{27} \left(\frac{kT_e}{1 \text{ keV}} \right)^{5/2} \text{ cm}^{-1} \text{ s}^{-1}. \quad (28)$$

This shows that thermal conduction is strongly temperature dependent.

Eq. 27 is only valid when the temperature scale height is larger than the mean free path for energy exchange. If this is not the case then the heat flux is described by the so-called saturated heat flux (Cowie and McKee, 1977) is

$$F_{\text{sat}} = 0.4 \left(\frac{2kT_e}{\pi m_e} \right)^{1/2} n_e kT_e. \quad (29)$$

In this case heat is transported by electrons streaming away from hot regions, but heat exchange between electrons is not taken into account, i.e. the electron distribution will not be Maxwellian. The factor 0.4 takes into account that the heat flux should be electrically neutral, reducing the heat flow. Unlike the classical heat flux, the saturated heat flux is density dependent. The ratio of the classical over saturated heat flow, involving a temperature scale height parameter R_s is (c.f. Cowie and McKee, 1977):

$$\sigma \equiv \frac{7.2 \tau_{ee} \sqrt{kT_e/m_e}}{R_s} = 1.5 n_e^{-1} \left(\frac{R_s}{1 \text{ pc}} \right)^{-1} \left(\frac{kT_e}{1 \text{ keV}} \right)^2 \left(\frac{\ln \Lambda}{30.9} \right)^{-1}. \quad (30)$$

The saturated heat flux is, therefore, dominant for small scale sizes ($R_s \ll 1 \text{ pc}$).

The thermal conduction across field lines, which is predominantly mediated by ions (protons), is (Spitzer, 1965; Huba, 2002):

$$\kappa_{\perp}/k = \frac{2.8 n_p kT_p}{m_p \omega_{cp}^2 \tau_{pp}} = 1.4 \times 10^7 \left(\frac{B}{10 \mu\text{G}} \right) \text{ cm}^{-1} \text{ s}^{-1}, \quad (31)$$

with $\omega_{cp} = eB/(m_p c)$ the proton gyrofrequency, and τ_{pp} the proton self-equilibration time scale. This shows that

⁶Correcting for a slightly different definition of τ_{ee} .

there is a very large difference in conduction parallel and across field lines. Only for $B \sim 10^{-15}$ G does the perpendicular and parallel conduction become comparable (for $n = 1 \text{ cm}^{-3}$).

To get an order of magnitude estimate for the importance of thermal conduction one should compare the advective enthalpy flux $F_E = v \frac{5}{2} nkT$ (c.f. Eq 16) with the thermal conduction flux, approximating the temperature gradient with kT/R_s and assuming a typical flow speed v :

$$\frac{F_E}{F_{\text{heat}}} \approx \frac{5nRv}{2\kappa} = 0.4n \left(\frac{R_s}{1 \text{ pc}} \right) \left(\frac{v}{1000 \text{ km s}^{-1}} \right) \left(\frac{kT_e}{1 \text{ keV}} \right)^{-5/2}, \quad (32)$$

where for κ the value along the magnetic field has been used. The fact that the numerical value is around one suggests that in SNRs the issue of thermal conduction is critical. This in turn makes the regularity of the magnetic field a crucial parameter. Note that the advected over conductive heat flow ratio (Eq 32) is proportional to $(kT)^{-5/2}$, if in addition one assumes $v \propto \sqrt{kT}$, this ratio will be proportional to $(kT)^2$. This means that thermal conduction is more important for hotter plasmas. However, there are indications that the magnetic fields in young SNRs, which have hotter plasmas, are more turbulent (Sect. 11.3), reducing the thermal conductivity. On the other hand little is known about the magnetic fields in the ejecta components of SNRs. This may, as we see be of interest for the interior components of some mature SNRs (Sect. 10.3).

5.5 Cosmic-ray acceleration by supernova remnant shocks

SNRs are considered to be the prime candidate sources for cosmic rays (e.g. Ginzburg and Syrovatskii, 1969), at least for energies up to 3×10^{15} eV, at which energy the cosmic-ray spectrum steepens from a power law with slope -2.7 to a slope of -3.1. This spectral feature is often referred to as the “knee”. There is evidence that around the “knee” the composition changes (Hörandel, 2008, for a review), suggesting a rigidity⁷ dependent maximum cosmic-ray energy at the source, with more massive particles having their spectral breaks at higher energies. It is thought that only cosmic rays above $\sim 10^{18}$ eV may have an extragalactic origin.

The main reason to consider SNRs as the dominant sources of Galactic cosmic rays is that the inferred Galactic cosmic-ray energy density ($\sim 1 - 2 \text{ eV cm}^{-3}$, Webber, 1998), combined with the inferred time an average cosmic ray spends in the Galaxy, requires a Galactic cosmic-ray production with a total power of about $10^{41} \text{ erg s}^{-1}$ (e.g. Ginzburg and Syrovatskij, 1967). Supernovae are the only sources known to provide such a power: with their average explosion energy of $\sim 10^{51} \text{ erg}$ and an inferred Galactic supernova rate of 2-3 per century, they provide a

⁷The rigidity of a particle is $R \equiv p/q$, with p the momentum and $q = Ze$ the charge. Massive particles, having a higher charge, will have a smaller gyroradius, and will therefore less easily diffuse away from the shock.

total power of $\sim 10^{42} \text{ erg s}^{-1}$. This requires that on average about 10% of the initial explosion energy is used for accelerating cosmic rays. Note, however, that the cosmic-ray energy density is very much dependent on the lowest energy part of the cosmic-ray spectrum, of which is little known, as low energy cosmic rays are shielded from the solar system by the solar wind.

Although supernovae are the most likely energy source for cosmic-ray acceleration, there is a debate on how and when their kinetic energy is used to accelerate cosmic rays. The general view is that cosmic rays are mostly accelerated in the (early) SNR stage. An alternative view is that the collective effects of multiple SNR and stellar wind shocks inside star-forming regions are responsible for most of the Galactic cosmic-ray acceleration, and that this provides a mechanism to accelerate cosmic rays up to energies of 10^{18} eV (e.g. Bykov and Fleishman, 1992; Parizot et al., 2004).

A long standing argument to consider the SNRs as the main source of Galactic cosmic rays is that non-thermal radio emission from SNRs provides clear evidence for particle acceleration, although strictly speaking this only provides evidence for electron acceleration, whereas the cosmic-ray spectrum observed on Earth consists for 99% of protons and other ions. Over the last 10-15 years the evidence for cosmic-ray acceleration in SNRs has been reinforced by the detection of X-ray synchrotron radiation (discussed in Sect. 11.2), and TeV γ -rays from several SNRs. See Sect. 11.4 and the reviews by Hinton and Hofmann (2009) and Reynolds (2008).

The acceleration of particles in SNRs is likely the result of the so-called first order Fermi process, also often referred to as *diffusive shock acceleration* (Axford et al., 1977; Bell, 1978a; Blandford and Ostriker, 1978; Krymskii, 1977). In this process some charged particles repeatedly scatter back and forth across the shock front. On either side of the shock the particles scatter elastically, due to the presence of a turbulent magnetic field. After each crossing the particles will be pushed along with the plasma, resulting in a net energy gain given by

$$\frac{\Delta E}{E} \approx \frac{4}{3} \frac{v_0 - v_2}{c} = \frac{4}{3} \left(\frac{\chi - 1}{\chi} \right) \frac{V_s}{c}, \quad (33)$$

with v_0 and v_2 the plasma velocities upstream and downstream⁸, seen in the frame of the shock, and $v_1 = V_s = \chi v_2$ (Eq. 12). The particles downstream will be advected away from the shock by the plasma with a rate $n_{CR} v_2 = n_{CR} V_s / \chi$, but the rate at which particles scatter back into the upstream medium is $\frac{1}{4} n_{CR} c$ for an isotropic particle distribution,⁹ with c the velocity of the particle. The ratio of these two rates gives the chance that the particles escape

⁸To be more precise: if there is a cosmic-ray precursor one should write $v(x) - v_2$ with $v(x)$ the velocity at coordinate x within the precursor, and $v_0 < v(x) < v_1$, with subscripts as defined in Sect. 5.1. So particles of a given energy may not sample the total change in shock velocity over the shock structure, but only a fraction of it.

⁹ $1/4c$ is the projected velocity to the shock normal for particles diffusing upstream.

downstream:

$$P_{\text{esc}} = \frac{n_{\text{CR}} v_2}{\frac{1}{4} n_{\text{CR}} c} = 4 \frac{v_2}{c} = 4 \frac{V_s}{c\chi}. \quad (34)$$

The chance that a particle will be scattered up and down at least k -times is $P(n \geq k) = (1 - P_{\text{esc}})^k$. A particle that has crossed the shock k time will on average have an energy $E \approx E_0(1 + \Delta E/E)^k$. Eliminating k gives

$$\ln P(n \geq k) = \frac{\ln(E/E_0)}{\ln(1 + \Delta E/E)} \ln(1 - P_{\text{esc}}) \quad (35)$$

The *integrated* probability function is therefore a power law with slope $-q + 1$:

$$\begin{aligned} -q + 1 &= \frac{d \ln P}{d \ln E} = \frac{\ln(1 - P_{\text{esc}})}{\ln(1 + \Delta E/E)} \\ &\approx -\frac{4V_s/(c\chi)}{4/3(\chi - 1)/\chi V_s/c} = -\frac{3}{\chi - 1}. \end{aligned} \quad (36)$$

The *differential* distribution function is then

$$n(E)dE \propto E^{-q}dE, \quad q = \frac{\chi + 2}{\chi - 1}. \quad (37)$$

In order to give an idea about how many shock crossings are needed to reach 10^{15} eV, assume that a proton is accelerated by a shock with $V_s = 5000 \text{ km s}^{-1}$, starting with an initial energy of 100 keV, and assuming a shock compression ratio of $\chi = 4$. According to Eq. 33 the gain per shock crossing is 1.7%, therefore the number of scatterings is $\log(10^{15} \text{ eV}/10^5 \text{ eV})/\log(1.017) \approx 1400$.

One of the outstanding uncertainties is how charged particles are injected into the Fermi acceleration process, i.e. how do they reach sufficient velocity to make it back to the unshocked medium. It is often assumed that these are the particles in the high velocity tail of the Maxwellian distribution, but computer simulations show that immediately behind the shock a non-thermal distribution of particles is present that may act as seed particles for further acceleration by the Fermi process (e.g. Bykov and Uvarov, 1999; Riquelme and Spitkovsky, 2011, for the case of electrons).

The typical time accelerate a particle from an initial momentum p_i to a final momentum p_f is (e.g. Malkov and Drury, 2001)

$$t_{\text{acc}} = \frac{3}{v_2 - v_0} \int_{p_i}^{p_f} \left(\frac{D_0}{v_0} + \frac{D_2}{v_2} \right), \quad (38)$$

with p the momentum ($E = pc$ for ultra-relativistic particles), D the diffusion coefficient, and v the plasma velocity, with subscripts 0 and 2 referring to the upstream and downstream regions. The diffusion coefficients are usually parameterized in terms of the so-called Bohm-diffusion coefficient, for which the particle mean free path corresponds to the gyroradius:

$$D = \eta \frac{Ec}{3eB}, \quad (39)$$

with η expressing the deviation from Bohm diffusion.

This suggests a typical acceleration time scale of (Parizot et al., 2006)

$$\begin{aligned} \tau_{\text{acc}} &\approx 1.83 \frac{D_2}{V_s^2} \frac{3\chi^2}{\chi - 1} \\ &= 124 \eta B_{-4}^{-1} \left(\frac{V_s}{5000 \text{ km s}^{-1}} \right)^{-2} \left(\frac{E}{100 \text{ TeV}} \right) \frac{\chi_4^2}{\chi_4 - \frac{1}{4}} \text{ yr}, \end{aligned} \quad (40)$$

with B_{-4} the downstream magnetic field in units of $100 \mu\text{G}$ and χ_4 the overall compression ratio in units of 4. The factor 1.83 comes from taking into account the difference in diffusion coefficient between the upstream (ahead) and downstream (post-shock) region, under the assumption that upstream the magnetic field is highly turbulent and isotropic, whereas the downstream magnetic field is determined solely by the compression of the magnetic-field component perpendicular to the shock normal. Note that a higher compression ratio corresponds to a longer acceleration time, but that a high compression ratio itself is a result of efficient acceleration (Sect. 5.1).

The typical length scale over which diffusion dominates over advection¹⁰ is given by $l_{\text{diff}} \approx 2D/v$, which for the downstream (post-shock) region becomes

$$\begin{aligned} l_{\text{diff}} &\approx 2 \frac{D_2 \chi}{V_s} \\ &= 5.3 \times 10^{17} B_{-4}^{-1} \eta \chi_4 \left(\frac{V_s}{5000 \text{ km s}^{-1}} \right)^{-1} \left(\frac{E}{100 \text{ TeV}} \right) \text{ cm}. \end{aligned} \quad (41)$$

The diffusion length scale gives approximately the region from which particles situated in the downstream (shock-heated) region are still able to cross the shock front.

Eq.37 shows that a compression ratio of 4 corresponds to a particle index of $q = 2$. Note that this result is independent of the diffusion properties (slow or fast) as long as the diffusion is isotropic. This slope is close to what is needed to explain the cosmic-ray spectrum observed on Earth ($q = 2.7$), provided one takes into account that cosmic rays with higher energies escape faster out of the Galaxy than low energy cosmic rays. Note that for $q = 2$ each decade in particle energy contributes the same amount of energy to the overall cosmic-ray energy budget. For $q < 2$ the highest energy particles contain most energy, whereas for $q > 2$ the lowest energy particles contain most of the energy. For the lower energy limit one can take the particle's rest mass energy, as around that energy a break in the cosmic-ray spectrum is expected (Bell, 1978b).

Diffusive shock acceleration becomes more complicated when particle acceleration becomes very efficient and the accelerated particles contribute a significant fraction to the overall pressure. This situation is usually referred to as *non-linear cosmic-ray acceleration*. As explained in Sect. 5.1 this results in a lower downstream plasma temperature and an overall compression ratio $\chi_{\text{tot}} > 4$. The main shock (subshock) will have a compression ratio $\chi_{\text{gas}} \leq 4$. The compression ratio sampled

¹⁰ To see this consider that the length scale associated with diffusion over a time t is $l_{\text{diff}} = \sqrt{2D_2 t}$, whereas for advection $l_{\text{adv}} = v_2 t$. These two are equal for $l = 2D_2/v_2 = 2D_2\chi/V_s$.

by a diffusing particle may therefore depend on its energy/diffusion length scale. The highest energy particles experience a compression ratio of χ_{tot} and the low energy particles χ_{gas} . As a result the spectrum at low energies is steep, with $q > 2$ and flattens at higher energies. For very efficient acceleration Eq. 37 is not valid, but instead the spectrum approaches the limit $q = 1.5$ (Malkov, 1997).

There is observational evidence that the particle spectrum is indeed steeper at low energies than at high energies (Sect. 11.2). However, there is no proof yet that the spectrum at high energies becomes as flat as $q = 1.5$. Some physical processes may prevent that, such as a possible tendency for Alfvén waves to move away from the shock, reducing the velocity gradient that the particles experience (Zirakashvili and Ptuskin, 2008). Alternatively, an additional pressure term in the precursor, for example caused by amplified magnetic fields and cosmic ray induced heating, may prevent very high compression ratios in the precursor, thereby limiting the overall compression ratio to $\chi \approx 4 - 7$ (Morlino et al., 2007).

6 X-ray radiation from supernova remnants

6.1 Thermal X-ray emission

The hot, X-ray emitting, plasmas created by SNR shocks have two characteristic properties: they are to a very good approximation optically thin, and the ionization distribution of atoms is often out of equilibrium.

Optically thin, X-ray emitting, plasmas are also found in a clusters of galaxies (Böhringer and Werner, 2009), colliding stellar winds, and the coronae of cool stars like our sun (hence the name coronal plasmas, see Mewe, 1999, for details on emission processes). In some cases, when the lines are not too much broadened by thermal or turbulent motion, line emission may be affected by optical depth effects, caused by resonant line scattering (Kaastra and Mewe, 1995). The overall spectrum will not be affected by this process, as resonant line scattering does not destroy photons, but merely changes the direction of photons. In coronal plasma's excitations and ionizations are caused predominantly by the electrons colliding with the ions. Most of the spectral characteristics of the thermal emission (continuum shape, emission line ratios) are determined by the *electron temperature*, which, as explained in Sect. 5.2 is not necessarily the same as the proton/ion temperature. The most important spectroscopic effect of the *ion* temperature is thermal line broadening, which is difficult to measure with the current generation of X-ray spectroscopic instruments (but see Sect. 11.1).

Because SNR plasmas are optically thin for X-rays, X-ray spectroscopy is a powerful tool for measuring abundances in SNRs, as no detailed radiative transfer models are needed. For old SNRs this can be used to reliably measure the abundances of the interstellar medium (e.g. Hughes et al., 1998), whereas for young SNRs X-ray spec-

troscopy is an important tool for measuring abundances, and connect them to supernova ejecta yields for the various types of supernova. Here I discuss the basic radiation mechanisms. In depth reviews of thermal X-ray emission are provided by Mewe (1999); Kaastra et al. (2008).

6.1.1 Thermal continuum emission

Thermal X-ray spectra consist of continuum emission caused by bremsstrahlung (free-free emission), recombination continuum (free-bound emission), and two-photon emission, the latter caused by the radiative electron transition from a meta-stable quantum level. For a Maxwellian energy distribution of the electrons, the emissivity is given by

$$\epsilon_{\text{ff}} = \frac{2^5 \pi e^6}{3 m_e c^3} \left(\frac{2\pi}{3 k m_e} \right)^{1/2} g_{\text{ff}}(T_e) T_e^{-1/2} \exp\left(-\frac{h\nu}{kT_e}\right) \quad (42)$$

$$\times n_e \sum_i n_i Z_i^2 \text{ erg s}^{-1} \text{ cm}^{-3} \text{ Hz}^{-1},$$

with $g_{\text{ff}} \approx 1$, the gaunt-factor, which has a frequency dependence (e.g. Rybicki and Lightman, 1979). The subscript i denotes the various ion species, each with charge eZ_i . The emissivity at a given temperature is therefore determined by the factor $n_e \sum_i n_i Z_i^2$. For solar or sub-solar abundances, bremsstrahlung is dominated by electrons colliding with protons and helium ions. In spectral codes one therefore usually parametrizes the normalization factor in Eq. 43 ($n_e \sum_i n_i Z_i^2$) with $n_e n_{\text{H}}$ or n_e^2 . Since one observes the emission from plasma of a given volume, spectral fitting codes usually use as a normalization factor for the plasma $\int n_e n_{\text{H}} dV$ or $\int n_e^2 dV$. This quantity is called the *emission measure* or *EM*. Of course one should also take into account the distance, in order to convert to flux units. A popular X-ray spectral fitting code like *xspec* uses the normalization factor $\int n_e n_{\text{H}} dV / (4\pi d^2)$.

Using this type of normalization is valid as long as the helium to proton ratio is close to the cosmic ratio, and the continuum contribution for elements beyond $Z = 2$ can be neglected. However, for shocked supernova *ejecta* electrons colliding with heavy ions can also be an important or even dominant source of continuum radiation. If one does not take this into account one can derive erroneous density and mass estimates from the bremsstrahlung emissivities (e.g. Vink et al., 1996). Note that the higher emissivity of a metal-rich plasma is not only caused by the factor Z_i^2 , but also by the effect that ionized metals produce more free electrons. For example, each hydrogen atom contributes only 1 electron, whereas fully ionized oxygen produces 8 electrons.

Free-bound and two-photon emission are not always mentioned as sources of continuum radiation, but they can be a dominant source of continuum emission (Kaastra et al., 2008), in particular for the metal-rich plasmas in young SNRs. Free-bound emission arises as an electron is captured into one of the atomic shells. The energy of the emitted photon is then $h\nu_n = E_e + \chi_n$, with E_e the energy of the free electron, and χ_n the ionization potential

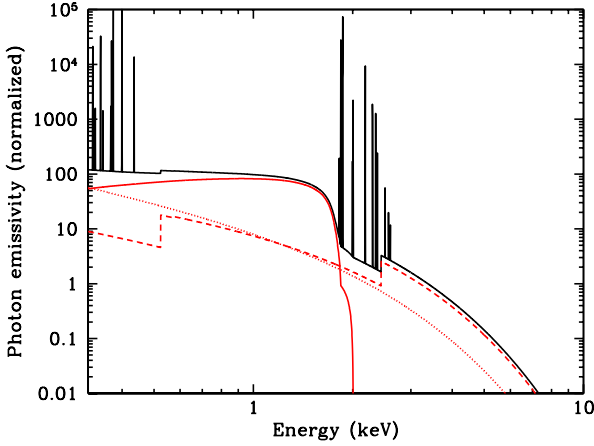


Figure 10: The emissivity of a pure silicon plasma out of ionization equilibrium ($kT_e = 1$ keV, $n_e t = 5 \times 10^{10} \text{ cm}^{-3} \text{ s}$). Shown are the contributions of two-photon emission (red solid line), free-bound continuum (red dashed line) and bremsstrahlung (free-free emission, red dotted line). The total emissivity is also shown, including Si-L and Si-K shell line emission (based on calculations made with the spectral code *SPEX*, Kaastra et al., 2003).

for an electron in level n . An electron is more likely to be captured in a shell with high principal quantum number n , due to the high statistical weights of these shells. As the energy difference for levels with high n are small, free-bound emission shows a sharp edge near the series limits. For a given energy level the emissivity is given by

$$\begin{aligned} \epsilon_{\text{fb}} = & \left(\frac{2}{\pi}\right)^{1/2} n_e n_{z+1} \frac{g_i}{g_{i+1}} \times \\ & c \sigma(h\nu) \left(\frac{h\nu}{\chi_n}\right) \left(\frac{\chi_n^2}{m_e c^2 kT}\right)^{3/2} \\ & \times \exp\left(-\frac{h\nu - \chi_n}{kT_e}\right) \text{ erg s}^{-1} \text{ cm}^{-3} \text{ Hz}^{-1}, \end{aligned} \quad (43)$$

with n_{z+1} the density of a ion with charge $z + 1$, g_{z+1}, g_z the statistical weights of the ion before and after recombination, and $\sigma(h\nu)$ the photo-ionization cross section of the ion in its final state. Since $\sigma(h\nu) \propto \nu^{-3}$, the spectral shape for $h\nu \gg \chi_n$ resembles that of thermal bremsstrahlung. However, if $kT \ll h\nu$, a situation that will occur in photo-ionized or overionized plasmas, free-bound emission results in narrow emission peaks near the series limits of lines. These line-resembling continua, which is usually shortened to RRCs. RRCs have recently been identified in the X-ray spectra of a few mature SNRs, suggesting the presence of overionized plasmas (Sect. 10.3).

Two-photon emission results from electrons in metastable states, such as the $2s$ state of a hydrogen-like atom. Since decay to the $1s$ level is forbidden (because $\Delta s = 0$), it can either be collisionally de-excited (unlikely in the rarified plasmas of SNRs), or it can de-excite by emitting two photons, with the associated energy distributed over two photons.

The different types of thermal continuum processes are illustrated in Fig. 10 for the case of a silicon-rich plasma out of equilibrium with $kT_e = 1$ keV.

6.1.2 Non-equilibrium ionization

The discussion of thermal emission so far pertains to all coronal plasmas, whether they are found in clusters of galaxies, SNRs, or cool stars, with the additional complication that young SNRs can have very metal-rich plasmas. But there is another important difference between the optical emission from SNRs and other hot astrophysical plasmas: SNR plasmas are often out of ionization equilibrium. This is usually indicated with the term *non-equilibrium ionization*, or *NEI*. The plasmas of cool stars and clusters of galaxies are referred to as *collisional ionization equilibrium*, or *CIE*.

The reason that SNR plasmas are in NEI is simply that, for the low densities involved, not enough time has passed since the plasma was shocked, and per ion only a few ionizing collisions have occurred for any given atom (Itoh, 1977).

The number fraction of atoms in a given ionization state F_i is governed by the following differential equation:

$$\frac{1}{n_e} \frac{dF_i}{dt} = \alpha_{i-1}(T) F_{i-1} - [\alpha_i(T) + R_{i-1}(T)] F_i + R_i(T) F_{i+1}, \quad (44)$$

with $\alpha_i(T)$ being the ionization rate for a given temperature, and ion i , and R_i the recombination rate.¹¹

For CIE the ion fraction of a given state remains constant, thus $dF_i/dt = 0$. For NEI $dF_i/dt \neq 0$, and the ionization fractions have to be solved using the coupled differential equations of all ion species i as a function of time, or as indicated by Eq. 44 as a function of $n_e t$. To complicate matters, in reality neither kT_e , nor n_e are expected to be constant in time. The parameter $n_e t$ is often referred to as the *ionization age* of the plasma.

Equation 44 can be solved by direct integration, but this is CPU intensive and not very practical when it comes to fitting X-ray spectral data. A faster approach (Hughes and Helfand, 1985; Kaastra and Jansen, 1993; Smith and Hughes, 2010) is to rewrite Eq. 44 in matrix notation,

$$\frac{1}{n_e} \frac{d\mathbf{F}}{dt} = \mathbf{A} \cdot \mathbf{F}, \quad (45)$$

determine the eigenvalues and eigenvectors of \mathbf{A} and then solve for the uncoupled equations

$$\frac{1}{n_e} \frac{d\mathbf{F}'}{dt} = \lambda \cdot \mathbf{F}', \quad (46)$$

with λ the diagonal matrix containing the eigenvalue, and $\mathbf{F}' = \mathbf{V}^{-1} \mathbf{F}$, with \mathbf{V} containing the eigenvectors.

¹¹For this equation it is assumed that the fractions only increase by ionization from a lower ionization state or recombination from a higher ionization state. This may not be strictly true, if one takes into account inner shell ionizations, which may result in multiple electrons being liberated.

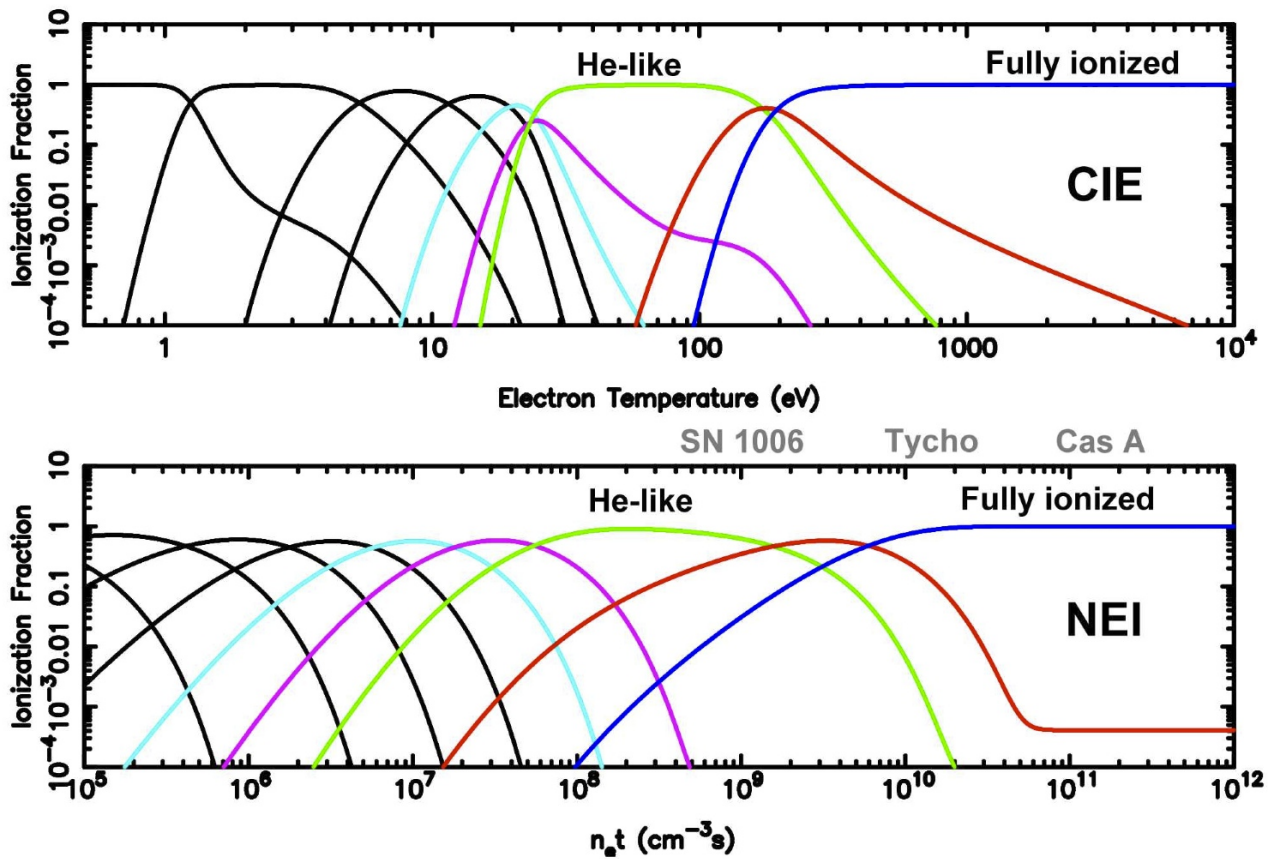


Figure 11: The effects of non-equilibrium ionization (NEI) illustrated for oxygen. Both panels look very similar, but the top panel shows the oxygen ionization fraction as a function of electron *temperature* for collisional ionization equilibrium (CIE), whereas the bottom panel shows the ionization fraction as function of $n_e t$, and for a fixed temperature of $kT_e = 1.5$ keV (ionization/recombination rates based on Shull and van Steenberg, 1982). Approximate, mean $n_e t$ values for the plasma in the young SNRs Cas A, Tycho and SN 1006 are indicated. (Figure earlier published in Vink, 2006)

The main effect of NEI in young SNRs is that the ionization states at a given temperature are lower than in the CIE situation. In Fig. 11 the effect of NEI in young SNRs is illustrated. As an example consider the presence of O VIII in Fig. 11a, which peaks in CIE at $kT_e = 0.2$ keV. Seeing a plasma in a SNR with most of the oxygen in O VIII may lead to the conclusion that the plasma is relatively cool. However, as Fig. 11b shows, the temperature may very well be $kT_e = 1$ keV, but with a low ionization parameter of $n_e t \approx 8 \times 10^9 \text{ cm}^{-3} \text{ s}$. For temperatures relevant for young SNRs ($kT_e = 0.5 - 4$ keV) the time needed to reach CIE is around $n_e t \approx 10^{12} \text{ eV}$. Typical values for $n_e t$ in SNRs are between $10^9 - 5 \times 10^{12} \text{ cm}^{-3} \text{ s}$, i.e. the plasmas of most SNRs are not in CIE. Note that the relevant time scales for reaching CIE is similar to that for reaching electron-proton temperature equilibration (Sect. 5.3).

Once a plasma has reached CIE one can have a reversal of the NEI situation; i.e. the plasma can become *overionized* instead of underionized, if the cooling rate is faster than the recombination rate. This will be discussed in connection to mixed-morphology SNRs in Sect. 10.3.

NEI models as found in X-ray spectral codes can have various levels of refinement, both concerning the atomic data (a strong point of the SPEX NEI code Kaastra et al., 2003), or in the additional physics taken into account, such as non-equilibration of electron and ion temperatures (Sect. 5.2), and the ensuing gradients in the electron temperature behind the shock front (e.g. the *vps shock* model in XSPEC, Borkowski et al., 2001a). Some models (e.g. Hamilton et al., 1983; Kaastra and Jansen, 1993; Borkowski et al., 2001a) also take into account the temperature structure within a SNR in the Sedov-Taylor phase of its evolution (Sect. 4).

6.1.3 Line emission diagnostics

In SNRs line emission results from collisional excitation of ions, a process dominated by electron-ion collisions. This is either direct excitation or through recombination, which usually results in an ion in an excited energy level. Since the density is very low, most ions can be assumed to be in the ground state; and, once an excitation occurs, collisional de-excitation or further excitation or ionization can be neglected. This also means that the ionization balance can be treated independently of the line emission properties (see Mewe, 1999, for a full treatment).

An important aspect of line emission that is characteristic for NEI plasma (and under certain circumstances photo-ionized plasmas: Liedahl, 1999; Kallman et al., 2004) is inner shell ionization. In this process an electron from an inner shell, for example the K-shell ($n = 1$) is removed, whereas higher level atomic shells (L- or M-shells, $n = 2, n = 3$) are still filled. This results in an ion with a hole in the K-shell, but plenty of electrons around from L, or M shells. The ion can then either de-excite without radiation, by filling the hole, and using the energy from that transition for further ionization (called Auger transitions), or it can adjust radiatively, which is called fluorescence.

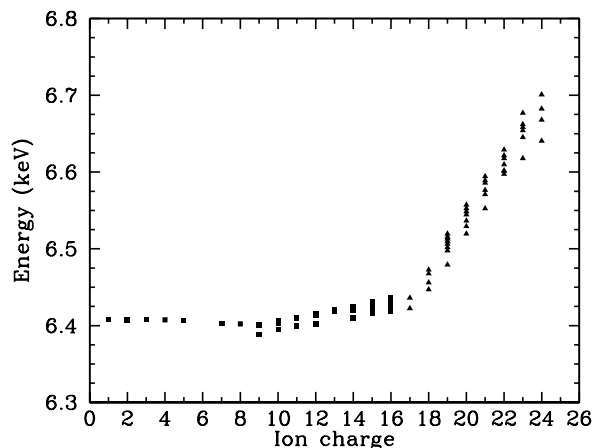


Figure 12: Fe-K shell line emission energies, as determined theoretically (squares, Fe II-Fe XVII, Palmeri et al., 2003; Mendoza et al., 2004) and observationally (triangles, Fe XVIII-Fe XXV, Beiersdorfer et al., 1993).

The likelihood for a radiative transition is called the *fluorescence yield*, and is higher for atoms with larger nuclear charge. For example the fluorescence yield for a K-shell ionization of neutral iron (Fe I) for a K-shell transition is 34%, for neutral silicon it is 5% and for neutral oxygen it is only 0.8% (Krause, 1979; Kallman et al., 2004). Because the radiative transition occurs in the presence of L-shell and M-shell electrons, the effective charge of the nucleus is reduced as compared to a K-shell transition in the helium-like state. As a result the $K\alpha$ line energy is smaller, and rises slowly as a function of ionization state (Fig. 12).

Iron line emission is an important diagnostic tool for the state of a SNR plasma, i.e. the average electron temperature and ionization age, $n_e t$. This is even true for medium energy resolution spectroscopy as provided with the CCD instruments on board *Chandra*, *XMM-Newton*, and *Suzaku*. Because of its high fluorescence yield and high abundance, Fe K-shell emission can be observed for all ionization states of iron, provided that the electron temperature is high enough ($kT_e \gtrsim 2$ keV). The average line energy of the Fe-K shell emission provides information about the dominant ionization state (Fig. 12). For ionization states from Fe I to Fe XVII the average Fe-K shell line is close to 6.4 keV.

Fe has also prominent Fe-L-shell transitions in the 0.7-1.12 keV range. These transitions occur for ionization states with electrons present in the L-shell ($n = 2$), i.e. Fe XVII to Fe XXIV, with each ionization state having its own specific line transitions, which increase on average in line energy for higher ionization states. Fe-L-line emission occurs for lower temperatures/ionization ages than Fe-K, i.e. $kT_e \gtrsim 0.15$ keV. Taken together, Fe-L- and Fe-K-shell emission can be used to accurately determine the ionization state of the plasma. For example, Fe-K emission around 6.4 keV could be caused by Fe XVII-XIX, or by lower ionization states, but in the latter case no

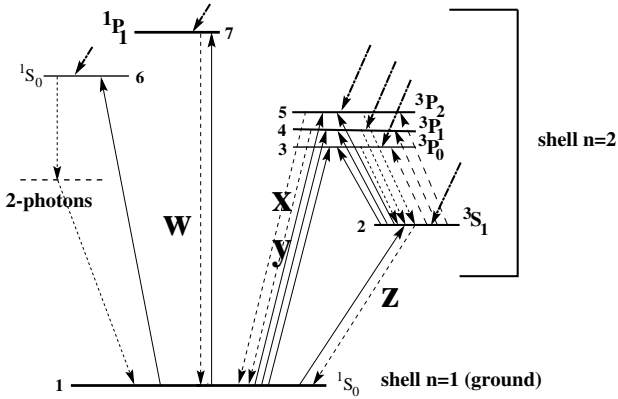


Figure 13: Simplified Grotrian diagram of He-like ions, with the transitions from an excited $n = 2$ state to the ground state (taken from Porquet et al., 2001). The triplet consists of the resonant line r or w , the intercombination line, $i = x + y$, and the forbidden line f or z .

Fe-L emission should be present. The presence of Fe-K-line emission around 6.7 keV indicates the presence of Fe XXV (He-like Fe), and around 6.96 keV Fe XXVI (H-like). High resolution X-ray spectroscopy greatly improves the value of Fe-line diagnostics, as it allows one to resolve the Fe-L shell emission in individual lines. And for Fe-K shell emission it is possible to detect different ionization stage individually instead of relying line emission centroids.

It is worth mentioning that $K\alpha$ line emission from low ionization states of iron can be the result of dust grains embedded in hot SNR plasmas (Borkowski and Szymkowiak, 1997). Hot electrons can penetrate dust grains, giving rise to inner shell ionizations inside the grains, whereas the emitted photon can escape from small grains. In addition, dust grains are slowly destroyed in hot plasmas due to dust sputtering, on a time scale of $\sim 10^{13}/n_e$ s. This results in a slow release of near neutral iron into the hot plasma. This should give rise to the presence of a broad range of ionization stages of Fe inside the plasma.

Another line diagnostic, available for high resolution spectroscopy ($E/\Delta E \gtrsim 200$), is provided by the “triplet” line emission from He-like ions, consisting of three prominent (blended) lines designated w (resonance), $x + y$ (intercombination), and z (forbidden) (Fig. 13, see Gabriel and Jordan, 1969; Mewe, 1999; Liedahl, 1999; Porquet et al., 2010).¹² The ratio $G \equiv (z + x + y)/w = (f + i)/r$ is of interest for SNRs, as it is sensitive to the temperature and ionization state of the plasma (Mewe and Schrijver, 1978; Liedahl, 1999). For example, inner shell ionization of the Li-like state, which has ground state configuration $1s^2 2s$, will result in an excited He-like ion in the $1s 2s^3 S_1$ state. Since de-excitation to the ground state is forbidden for electric dipole radiation ($\Delta l = 0$), this gives rise to forbidden, magnetic dipole, radiation. Thus, inner shell excitation enhances the forbidden line transition, and

¹² The word “triplet” denotes here the presence of three closely spaced lines, and is not used in the usual sense indicating a mixed quantum state.

acts as a measure for the fraction of Li-like ions. This can be seen in Fig. 13, showing that the G -ratio is high for $n_e t < 3 \times 10^9 \text{ cm}^{-3} \text{ s}$ for oxygen and $n_e t < 2 \times 10^{10} \text{ cm}^{-3} \text{ s}$ for silicon. This figure also shows that for higher $n_e t$ values G -ratio may fall below the CIE values. The reason is that Li-like ions are no longer present, but at the same time the recombination rate to the He-like state is low, because the atoms are still underionized, and collisions are more likely to result in ionizations than recombinations. Only when $n_e t \gtrsim 10^{11} \text{ cm}^{-3} \text{ s}$ are the G -ratios similar to those for CIE at the same temperature.

Another potential influence on the G -ratio is resonant line scattering. Resonant line scattering only influences the intensity of the resonant line, as it scatters the resonant photon out of the line of sight. A very high G -ratio (i.e. relatively strong forbidden line emission) may therefore help to diagnose resonant line scattering, and its importance can be estimated, if $n_e t$ and kT_e can be estimated independently from the G -ratio. Note that, since resonant line scattering does not destroy the photon, from the other parts of the SNR, in particular from the edges, there may be enhanced resonant line emission.

The ratio $R \equiv z/(x + y) = f/i$ is for CIE plasmas a sensitive diagnostic tool to measure electron densities, if the densities are in the range $n_e = 10^8 - 10^{13} \text{ cm}^{-3}$, which is much higher than encountered in SNRs. For SNRs it is of more interest that the R -ratio is also sensitive to the ionization age, and to a lesser extent on temperature (Fig. 14, right). The reason is that the R -ratio in SNRs is mainly determined by inner shell ionization, which enhances the forbidden line emission for low $n_e t$. Once the fraction of Li-like ions is negligible, and inner shell ionizations are therefore no longer important, the R -ratio becomes relatively flat. Note that the R -ratio may help to disentangle resonant line scattering effects from pure NEI effects; resonant line scattering does not influence the R -ratio.

6.2 Line emission associated with radioactivity

Apart from collisional processes one may also have line emission caused by radioactivity. Radioactive elements are produced during the lifetime of stars, and, of particular interest here, during the supernova explosion. The most important radioactive element is ^{56}Ni , which decays in 8.8 days¹³ into ^{56}Co , which subsequently decays into ^{56}Fe (see Table 6.2 for the details, and Diehl and Timmes, 1998, for a review). This decay chain forms the dominant source of energy for the expanding supernova ejecta during the first year after the explosion. It has a significant imprint on the light curves of supernovae. Moreover, its final product, ^{56}Fe , is the most abundant Fe isotope in the Universe. A large part of the production comes from Type Ia supernovae (Sect. 2.2), which produce typically $0.6 M_\odot$ per explosion.

¹³The decay time τ is the e -folding time, as opposed to the half-life $\tau_{1/2} = \tau \ln 2$.

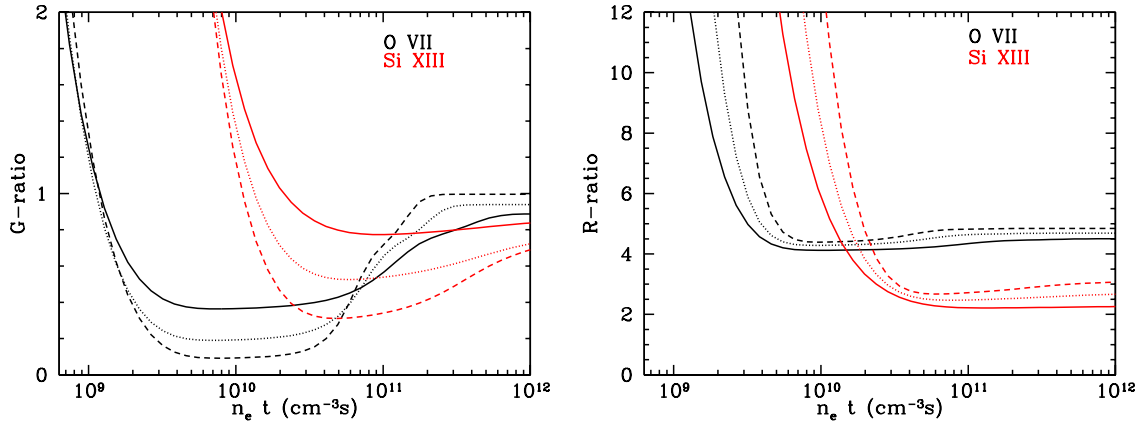


Figure 14: Left: The G-ratios $G = (f + i)/r$ for He-like oxygen and silicon. Three different temperatures are shown: 0.5 keV (solid line), 1 keV (dotted) and 2 keV (dashed). Right: Idem, but now for the R-ratios $R = f/i$. Note that these ratios are based on pure He-like ion lines only, in reality some blends may occur with L-like satellite lines (e.g. Vink et al., 2003), which tend to increase the G-ratio at low $n_e t$ values. In these figures the effects of blends with line emission from Li-like ions are not taken into account. These enhance the G-ratio and R-ratio at low $n_e t$. (This figure is based on calculations by the author using the *SPEX* code, Kaastra et al., 2003).

An element that is less abundantly produced is ^{44}Ti , with typical expected yields in core collapse supernovae of $10^{-5} - 10^{-4} M_{\odot}$ (e.g. Prantzos, 2011). Type Ia supernovae probably produce less, unless the explosion is triggered by an explosion at the surface of the white dwarf (the so-called double detonation sub-Chandrasekhar model, e.g. Fink et al., 2010). ^{44}Ti has a much longer decay time than ^{56}Ni , namely 85 yr (Ahmad et al., 2006). This makes it of interest also for the SNR phase. ^{44}Ti is an alpha-rich freeze-out product, which means that its yield is determined by the amount of α -particles left over after the initial stages of explosive nuclear burning (Arnett, 1996). It is therefore sensitive to the speed of expansion of the inner layers of the ejecta, as this determines how rapidly the density drops, which prevents further build up to more massive elements like ^{56}Ni . In addition, the ^{44}Ti yield is sensitive to the mass cut (the boundary between what is accreted onto the proto-neutron star and what will be ejected) and explosion asymmetries (Nagataki et al., 1998). This sensitivity to explosion conditions explains the astrophysical interest in ^{44}Ti .

The most unambiguous, direct signature of radioactivity are the γ -ray lines associated with their decay (as predicted by Clayton and Silk, 1969). The daughter products of radioactive elements are usually not in their nuclear ground states, but rapid de-excitation occurs through the emission of γ -ray lines (Table 6.2). The nuclear decay lines of ^{56}Co at 847 keV and 1238 keV have been detected from SN 1987A by several balloon and satellite experiments (Cook et al., 1988; Mahoney et al., 1988; Sandie et al., 1988; Teegarden et al., 1989, see also Sect. 9.2). Kurfess et al. (1992) later report the detection of 122 keV line emission from ^{57}Co by the Oriented Scintillation Spectrometer Experiment (*CGRO-OSSE*) on board the Compton Gamma Ray Observatory (*CGRO*). No supernova Type Ia has exploded near enough in modern times to

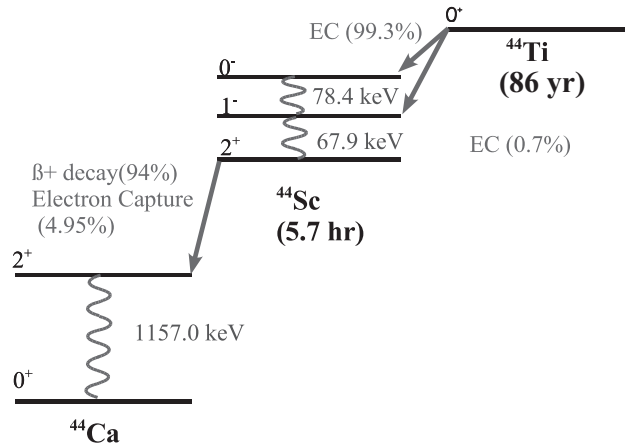


Figure 15: The decay chain of ^{44}Ti with the indicated channels, electron capture (EC) and beta-decay.

firmly detect γ -ray lines, but there was a hint of ^{56}Co emission in *CGRO-Comptel* observations of the bright Type Ia supernova SN1991T (Morris et al., 1997), which had a distance of about 13.5 Mpc.

Apart from γ -ray line emission, the decay chain of ^{44}Ti also results in hard X-ray line emission at 67.9 keV and 78.4 keV, which are caused by the nuclear de-excitation of ^{44}Sc (Fig. 15). This line emission, and the the 1157 keV γ -ray line of ^{44}Ca , have been detected for the young SNR Cas A (Sect. 9.1) with the *CGRO-Comptel*, *Beppo-SAX-PDS*, and *INTEGRAL-IBIS* instruments (respectively, Iyudin et al., 1994; Vink et al., 2001; Renaud et al., 2006b). The flux per line of $(2.5 \pm 0.3) \cdot 10^{-5} \text{ cm s}^{-1} \text{ cm}^{-3}$ implies a rather large ^{44}Ti yield of $(1.6 \pm 0.3) \cdot 10^{-4} M_{\odot}$ (Renaud et al., 2006b). This yield is comparable to what has been inferred for SN 1987A, based on the late time light curve of SN 1987A (Jerkstrand et al.,

Table 1: Decay chains of the most important radioactive explosive nucleosynthesis products and some of their hard X-ray and γ -ray signatures.

		Decay time	Process	Lines (keV)
$^{56}\text{Ni} \rightarrow$		8.8 d	EC	158, 812
	$^{56}\text{Co} \rightarrow$ ^{56}Fe	111.3 d	EC, e^+ (19%)	847, 1238
$^{57}\text{Ni} \rightarrow$		52 hr	EC	1370
	$^{57}\text{Co} \rightarrow$ ^{57}Fe	390 d	EC	122
$^{44}\text{Ti} \rightarrow$		86.0 yr	EC	67.9, 78.4
	$^{44}\text{Sc} \rightarrow$ ^{44}Ca	5.7 hr	e^+ , EC (1%)	1157

2011). A ^{44}Ti detection was also reported for the SNR RX J0852-4622 (“Vela jr”), based on measurements of the 1157 keV line with *CGRO-Comptel* (Iyudin et al., 1998). But *INTEGRAL-IBIS* measurements of the 68 keV and 78 keV lines are inconsistent with this detection (Renaud et al., 2006a).

The radioactive processes in the decay chains of ^{56}Ni , ^{57}Ni and ^{44}Ti are electron capture (EC) or beta-decay (e^+ in Table 6.2). The beta-decay process is a source of positrons and may be partially responsible for the 511 keV electron-positron annihilation line emission from the Galaxy (Prantzos et al., 2011). Most of the positrons released by the decay of ^{56}Co probably do not survive the supernova phase, but in the subsequent SNR phase not many positrons may annihilate due to the low densities and high plasma temperature. No 511 keV line emission has yet been detected from a SNR (Kalemci et al., 2006; Martin et al., 2010).

Apart from *nuclear* decay line emission, radioactivity also gives rise to X-ray line emission. The reason is that electron-captures results in a daughter product with a vacancy in the K-shell. This vacancy may result in a K-shell transition that could be detected using more sensitive future X-ray telescopes such as *IXO/ATHENA* (Bookbinder, 2010). Leising (2001) lists in total 17 radioactive elements, but the most promising of them are ^{55}Fe ($\rightarrow^{55}\text{Mn}$, $\tau = 3.9$ yr, $K\alpha$ energy 5.888 & 5.899 keV), ^{44}Ti ($\rightarrow^{44}\text{Sc}$, $\tau = 85$ yr, 4.086 & 4.091 keV), ^{59}Ni ($\rightarrow^{59}\text{Co}$, $\tau = 108$ kyr, 6.915 & 6.930 keV), and ^{53}Mn ($\rightarrow^{53}\text{Cr}$, $\tau = 5.4$ Myr, 5.405 & 5.415 keV).

For SNRs, $K\alpha$ line emission of ^{44}Ti and ^{59}Ni is of particular interest, since the decay times are compatible with the lifetimes of SNRs. For ^{44}Ti the K-shell transitions form a complement to the nuclear decay line emission. The advantage of the K-shell transition measurements is that the spatial resolution of soft X-ray telescopes is in general superior to hard X-ray or γ -ray telescopes. But it should be noted that the line transitions are not unique. In principle, other Sc isotopes may also produce the K-shell lines. But stable Sc is not a very abundant element. A more severe problem is that the K-shell transitions are also a function of the ionization state of the atom (Sect. 6.1.3), which may not be a priori known, complicating the search for line emission. Nevertheless, future more sensitive tele-

scopes are expected to detect these lines (Leising, 2001; Hughes et al., 2009). And one may then be able to determine the ionization state of the radioactive elements, which allows one to position the ^{44}Ti in the shocked or unshocked parts of the ejecta.

Borkowski et al. (2010) reported the detection of velocity broadened $K\alpha$ line emission from ^{44}Ti (or technically speaking from its daughter product Sc) for the youngest known Galactic SNR G1.9+0.3 (~ 100 yr Carlton et al., 2011). The measured flux of $(0.35 - 2.4) \times 10^{-6}$ ph $\text{cm}^{-2} \text{s}^{-1}$ implies a ^{44}Ti production of $(1 - 7) \times 10^{-5} M_{\odot}$. G1.9+0.3 is possibly a Type Ia SNR (Sect. 8), but the ^{44}Ti yield is consistent with either a core collapse or Type Ia origin. A search for ^{44}Ti associated $K\alpha$ line emission from Cas A (Theiling and Leising, 2006) and SN 1987A (Leising, 2006) did not yet result in detections.

6.3 Non-thermal emission

6.3.1 X-ray synchrotron radiation

Relativistic electrons gyrating in a magnetic field emit synchrotron radiation (Ginzburg and Syrovatskij, 1967).¹⁴ In most cases encountered in astrophysics, synchrotron radiation is caused by a *non-thermal* population of electrons, which often well approximated over a large energy range by a power-law distribution, certainly if first order Fermi acceleration is responsible for the production of the relativistic electron populations.

Sources of synchrotron radiation usually produce this radiation over a very wide range in frequency, from the low frequency radio bands (~ 10 MHz) up to X-rays ($\sim 10^{18}$ Hz). Most SNRs are radio synchrotron sources, with synchrotron radiation coming from the SNR shell, but for composite SNRs also from the embedded pulsar wind nebulae¹⁵. X-ray synchrotron emission from SNRs was traditionally associated with the presence of a pulsar wind nebula, but only relatively recently has X-ray

¹⁴For more massive charged particles synchrotron radiation is still emitted, but at a much lower efficiency.

¹⁵See for example the catalogue by Green D. A., 2009, ‘A Catalogue of Galactic Supernova Remnants’, Astrophysics Group, Cavendish Laboratory, Cambridge, United Kingdom (available at <http://www.mrao.cam.ac.uk/surveys/snrs/>)

synchrotron emission from young SNR shells been established (Koyama et al., 1995, see Sect. 11.2).

A relativistic electron with energy E moving in a magnetic field with strength B will emit synchrotron radiation with a maximum emission at the characteristic frequency ν_{ch} given by (Ginzburg and Syrovatskii, 1965)

$$\begin{aligned} \nu_{\text{ch}} &= 1.8 \times 10^{18} B_{\perp} \left(\frac{E}{1 \text{ erg}} \right)^2 \text{ Hz}, \\ h\nu_{\text{ch}} &= 13.9 \left(\frac{B_{\perp}}{100 \mu\text{G}} \right) \left(\frac{E}{100 \text{ TeV}} \right)^2 \text{ keV}, \end{aligned} \quad (47)$$

with $B_{\perp} \approx \sqrt{2/3}B$ the magnetic-field component perpendicular to the motion of the electron. For the typical magnetic fields inside SNRs, $B = 10 - 500 \mu\text{G}$, the emitting electrons have energies of 10-100 TeV. These electrons may therefore also be responsible for many of the detected TeV gamma-ray emission (e.g. Aharonian et al., 2001, 2004). However, pion production by high energy ions also gives rise to TeV gamma-ray emission, and there is an on going debate on which radiation mechanism dominates the TeV emission from SNRs (see Sect. 11.4, and Hinton and Hofmann, 2009, for a review).

An electron emitting synchrotron radiation suffers radiative losses with a rate:

$$\begin{aligned} \frac{dE}{dt} &= -\frac{4}{3} \sigma_{\text{T}} c \left(\frac{E}{m_e c^2} \right)^2 \frac{B_{\perp}^2}{8\pi} \\ &= -4.05 \times 10^{-7} \left(\frac{E}{100 \text{ TeV}} \right)^2 \left(\frac{B_{\perp}}{100 \mu\text{G}} \right)^2 \text{ erg s}^{-1}, \end{aligned} \quad (48)$$

with σ_{T} the Thomson cross section. Usually one includes into B_{\perp} a term to include the effect of losses due to inverse Compton scattering, replacing B_{\perp} by $B_{\text{eff}}^2 = B_{\text{rad}}^2 + B_{\perp}^2$, with $B_{\text{rad}} = 3.3 \mu\text{G}$, the value for which the magnetic-field energy density equals the radiation energy density of the cosmic microwave background.¹⁶ This corresponds to a synchrotron loss time scale of

$$\tau_{\text{syn}} = \frac{E}{dE/dt} = 12.5 \left(\frac{E}{100 \text{ TeV}} \right)^{-1} \left(\frac{B_{\text{eff}}}{100 \mu\text{G}} \right)^{-2} \text{ yr}. \quad (49)$$

For a population of relativistic electrons with a power-law energy distribution, the spectral index, α , of the synchrotron flux density spectrum is related to the spectral index of the electron energy distribution, q , as $\alpha = (q - 1)/2$. The typical spectral radio index of young SNRs is $\alpha \approx 0.6$, indicating that electrons have an energy distribution with $q \approx 2.2$, close to the predictions from first order Fermi acceleration (Sect. 5.5). For X-ray emission it is more common to use the photon index, $\Gamma = \alpha + 1$.

Typically, X-ray synchrotron spectra of young SNRs have rather steep indices, $\Gamma = 2 - 3.5$, indicating a rather steep underlying electron energy distribution. This steepness indicates that the synchrotron X-ray emission is caused by electrons close to the maximum energy of the relativistic electron distribution. This maximum is usually for energies at which acceleration gains are comparable

to the radiative losses, the so-called *loss-limited case*. Alternatively, the electron energy spectrum breaks off, because the shock acceleration process has not acted for long enough time for the electrons to reach higher energies. This is the so-called *age-limited case* (Reynolds, 1998). In the age-limited case the underlying electron spectrum has an exponential cut-off in energy $\propto \exp(-E/E_{\text{max}})$, whereas in the loss-limited case the cut-off is expected to be steeper $\propto \exp(-\{E/E_{\text{max}}\}^2)$ (Zirakashvili and Aharonian, 2007). Because the synchrotron emissivity function for a given electron energy has a rather broad spectral profile (Ginzburg and Syrovatskii, 1965), the rather steep cut-off in electron energies results in a much more gradual roll over of the synchrotron spectrum:

$$n(h\nu) \propto (h\nu)^{-\Gamma} \exp\left\{-\left(\frac{h\nu}{h\nu_{\text{cut-off}}}\right)^{1/2}\right\}. \quad (50)$$

The cut-off photon energy for the loss-limited case can be calculated by combining Eq. 41 and Eq. 49, which gives

$$\begin{aligned} \frac{E_{\text{max}}}{100 \text{ TeV}} &\approx 0.32 \eta^{-1/2} \left(\frac{B_{\text{eff}}}{100 \mu\text{G}} \right)^{-1/2} \\ &\times \left(\frac{V_s}{5000 \text{ km s}^{-1}} \right) \left(\frac{\chi_4 - \frac{1}{4}}{\chi_4^2} \right)^{1/2}. \end{aligned} \quad (51)$$

Inserting this in Eq. 47 shows that the cut-off photon energy, $h\nu_{\text{cut-off}}$, is independent of the magnetic field (Aharonian and Atoyan, 1999):

$$h\nu_{\text{cut-off}} = 1.4 \eta^{-1} \left(\frac{\chi_4 - \frac{1}{4}}{\chi_4^2} \right) \left(\frac{V_s}{5000 \text{ km s}^{-1}} \right)^2 \text{ keV}. \quad (52)$$

See Zirakashvili and Aharonian (2007) for a more detailed derivation. This equation indicates that X-ray synchrotron emission requires the relatively high shock velocities ($\gtrsim 2000 \text{ km s}^{-1}$) only encountered in young SNRs. Moreover, the detection of X-ray synchrotron emission from SNR shells suggests that the diffusion coefficients cannot be too large compared to the Bohm-diffusion case (Sect. 5.5), i.e. $\eta \lesssim 10$.

6.3.2 Non-thermal bremsstrahlung

Apart from synchrotron radiation, non-thermal X-ray emission can also result from lower energy electrons through bremsstrahlung and inverse Compton scattering. Inverse Compton scattering is for SNRs important in GeV-TeV γ -ray band (Hinton and Hofmann, 2009), but for the magnetic fields inside SNRs, $B \approx 5 - 500 \mu\text{G}$, it is generally not expected to be important in the soft X-ray band.

Bremsstrahlung caused by the presence of a non-thermal electron distribution has been considered as a possible source of X-ray continuum emission for some time (e.g. Asvarov et al., 1990; Vink et al., 1997; Bleeker et al., 2001; Laming, 2001b). Since the electrons that produce X-ray bremsstrahlung have non-relativistic, to mildly relativistic energies, identifying non-thermal bremsstrahlung

¹⁶ $B_{\text{rad}}^2/(8\pi) = u_{\text{CMB}} = 4.2 \times 10^{-13} \text{ erg cm}^{-3}$.

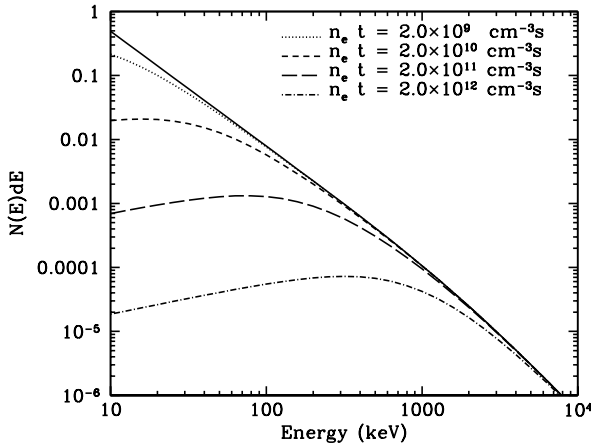


Figure 16: The fate of a suprathermal electron distribution exchanging energy with thermal electrons through Coulomb collisions, as a function of $n_e t$ (Vink, 2008b).

would help to obtain information about the low energy end of the electron cosmic-ray distribution. This relates to the poorly known electron cosmic-ray injection process (Sect. 5.5). However, it is unlikely that non-thermal bremsstrahlung contributes enough radiation to identify it with the current generation of hard X-ray telescopes. The reason is that the Coulomb interactions between thermal and non-thermal electrons thermalizes the low energy tail of the electrons on a relatively short timescale, $n_e t \sim 10^{10} \text{ cm}^{-3} \text{ s}$, so that non-thermal bremsstrahlung can only be expected in a narrow region close the shock front (Fig. 16 Vink, 2008b), or for those SNRs that have an overall low ionization age. Such a low ionization age is for example encountered in SN 1006, but here the X-ray continuum is overwhelmed by synchrotron radiation (Sect. 11.2). The low ionization age is caused by a low density of the plasma, which also makes that the bremsstrahlung emissivity is not very large (Eq. 43).

7 X-ray spectroscopy with *Chandra*, *XMM-Newton*, and *Suzaku*

Before reviewing the most recent results obtained by the current generation of X-ray missions capable of either high resolution spectroscopy and/or imaging spectroscopy, *Chandra*, *XMM-Newton*, and *Suzaku*, I describe some of the characteristics of these telescopes and their instruments in the context of studying SNRs.

All the aforementioned X-ray telescopes have multiple instruments on board, with the CCD-detectors being the work horses for all three missions. X-ray detecting CCDs were first used by the Broad Band X-ray Telescope (BBXRT, Petre et al., 1993), flown for ten days on the space shuttle Columbia, but only with the launch of the *ASCA* satellite (Tanaka et al., 1994) did the results of CCDs imaging spectroscopy become available to the broad community of X-ray astronomers. X-

ray CCD-detectors are suitable for imaging spectroscopy with medium spectral resolution ($R = E/\Delta E \approx 10 - 43$ FWHM for 0.5-6 keV) and imaging resolution close to the telescope resolution.¹⁷ The *Chandra* telescope provides the highest spatial resolution, which is slightly undersampled by the CCD pixel size of $0.49''$. The CCDs themselves come in various types, even within one instrument. The CCD-detectors used in current observatories go by the names ACIS (AXAF CCD Imaging Spectrometer) on board *Chandra*, EPIC (European Photon Imaging Camera) behind the *XMM-Newton* telescopes, with EPIC-MOS (Turner et al., 2001) behind two of the telescopes, and EPIC-pn behind the third (Strüder et al., 2001), and XIS (X-ray Imaging Spectrometer) for *Suzaku*. XIS consists also of four separate detectors behind four independent telescopes.

CCD-detectors are excellent for studying the spatial distribution of elemental abundances inside SNRs, or identifying regions with likely synchrotron radiation contributions. They cannot be used to resolve Fe-L complexes, or the He-like triplets (Sect. 6.1.3), which offer more precise diagnostic power to measure temperatures and ionization parameters. They are also not good enough to measure Doppler shifts for velocities below a few thousand km s^{-1} .

In addition to CCD camera's, *Chandra* and *XMM-Newton* carry grating spectrometers¹⁸, which give high spectral resolution for point sources, but, compared to the CCD instruments, have a smaller effective area.

XMM-Newton has a Reflection Grating Spectrometer (RGS, den Herder et al., 2001), consisting of two gratings behind two of the X-ray three telescopes. It covers the soft part of the X-ray spectrum from 6-38 Å (0.32-2 keV). About 50% of the X-rays go through the gratings, and the remaining fall on the EPIC-MOS instruments. As a consequence, the RGS gathers data simultaneous with EPIC. The spectral reflection angle for the RGS is large ($\sim 4.8^\circ$) compared to those of the transmission spectrometers of *Chandra*. As a result an extended source in a monochromatic line gets distorted (squeezed) in one direction. The design of the RGS is such that the spectrum is stretched over a large detecting area, with the spectrum being detected by nine CCDs for both RGS1 and RGS2.¹⁹ The CCDs' intrinsic energy resolution are used to separate spectra of different spectral orders. The large physical size of the spectral extraction region has as a disadvantage that the background induced by energetic particles is relatively large. But it has the advantage that the RGS is less sensitive to the source extent, with the additional line width

¹⁷ A predecessor of the CCD-detectors was the Solid State Spectrometer (SSS) on board the Einstein satellite, which did not provide spatial information, but an energy resolution similar to present day CCD-detectors (Joyce et al., 1978).

¹⁸ *Suzaku* has another high resolution X-ray spectrometer on board, XRS, which is based on the calorimetric detection method. Unfortunately this instrument failed shortly after the launch of *Suzaku*.

¹⁹ Both for RGS1 and RGS2 there is one CCD not working, luckily intended to cover different wavelengths. So the current number of CCDs is 8 per grating.

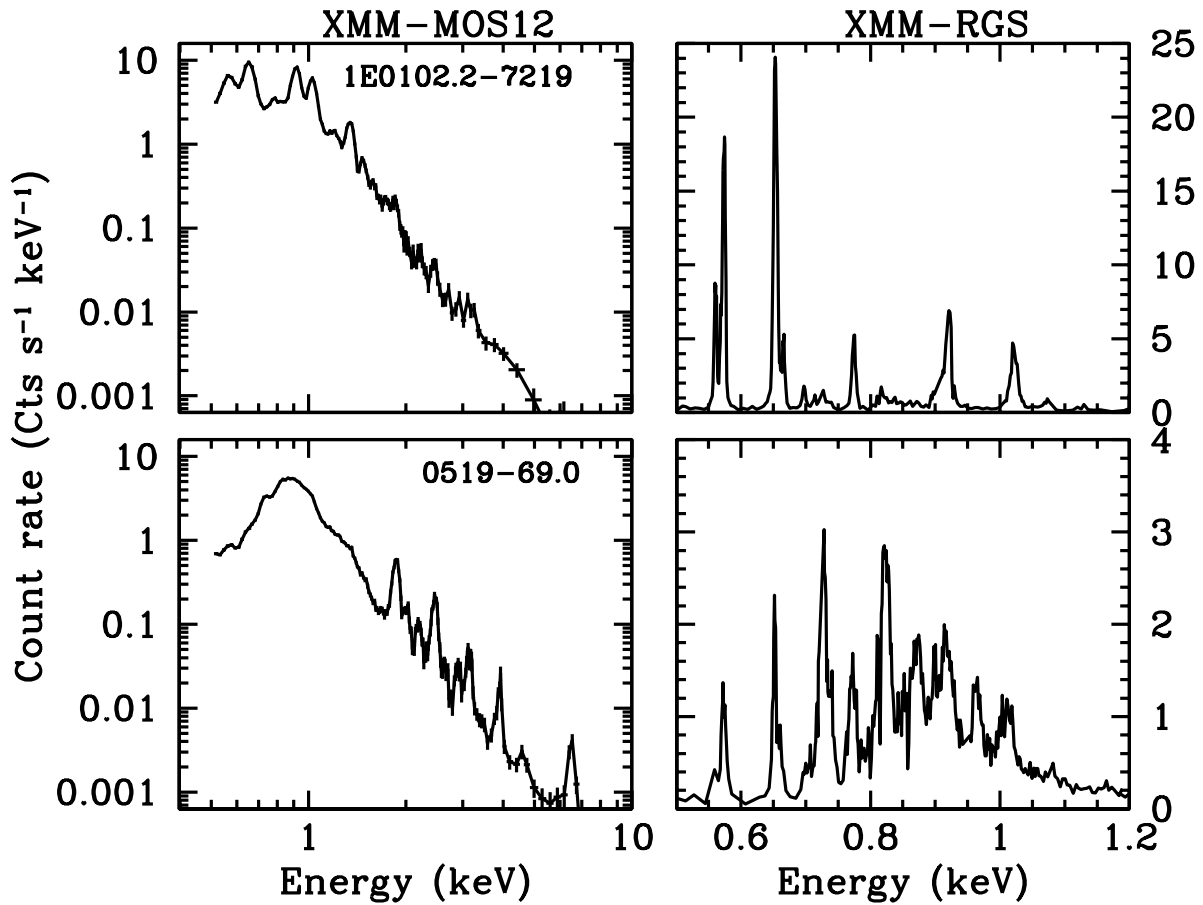


Figure 17: CCD (*XMM-Newton*-MOS) and Reflective Grating Spectrometer (*XMM-Newton*-RGS) spectra of an oxygen-rich (1E0102.2-7219) and a Type Ia SNR (0519-69.0). The figure illustrates the gain in spectral resolution of the RGS instrument over CCD-detectors, even for mildly extended objects; both SNRs have an extent of about $30''$. The figure also illustrates the differences between Type Ia spectra and core collapse SNR spectra, with the former Type Ia SNR being dominated by Fe-L emission (see Sect. 8 and 9.1).

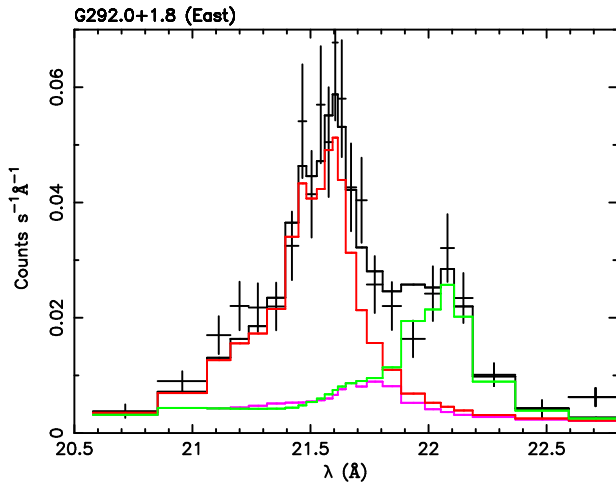


Figure 18: The O VII triplet (Sect. 6.1.3) as observed with the *XMM-Newton* RGS in the oxygen-rich SNR G292.0+1.8 (Sect. 9.1). The RGS still offers a good resolution despite the fact that G292.0+1.8 has an angular size of nearly $8'$. In this case the presence of a bright, narrow, bar-like feature helped to obtain a good spectral resolution. The red line indicates the emission from the resonance line, magenta the intercombination line, and green the forbidden line. (Figure first produced in Vink, Bleeker, Kaastra, and Rasmussen (2004).)

caused by source extent, $\Delta\phi$, given by

$$\Delta\lambda = 0.124(\Delta\phi/1') \text{ \AA}. \quad (53)$$

So RGS spectra from typical young SNRs in the Magellanic Clouds, which have $\Delta\phi \approx 0.5'$, are only mildly deteriorated compared to those of point sources with an additional broadening of $\Delta\lambda = 0.06 \text{ \AA}$. This is comparable to the intrinsic resolution of the RGS, $\Delta\lambda = 0.06 \text{ \AA}$. Adding these numbers quadratically shows that the spectral resolution for those SNRs is $\lambda/\Delta\lambda = E/\Delta E \approx 265$ at $\lambda = 22.5 \text{ \AA}$ (i.e. around the O VII triplet, Sect. 6.1.3). Even for a source extent of $4'$, one still obtains a spectral resolution of 40, outperforming CCDs at long wavelengths and comparable to the spectral resolution of CCD-detectors at 6 keV. If the extended object is dominated by some particularly bright regions, the spectral resolution may be very good, as illustrated with the O VII triplet line emission of SNR G292.0+1.8 in Fig. 18. The gain in spectral resolution obtained by using the RGS compared to the CCD data is illustrated in Fig. 17.

The *Chandra* transmission gratings come in two varieties, the High Energy Transmission Grating Spectrometer (HETGS, Canizares et al., 2005) and the Low Energy Transmission Grating Spectrometer (LETGS), which provide spectral coverage in the range 1.5–30 \AA (HETGS) and 1.2–175 \AA (LETGS). The gratings for both instruments can be put into the optical path of the mirror assembly. The HETGS consists of two grating arrays, a Medium Energy Grating (MEG) and High Energy Grating (HEG), placed at a small angle with respect to another. This results in an X-shaped dispersion pattern on the detectors, with the zero

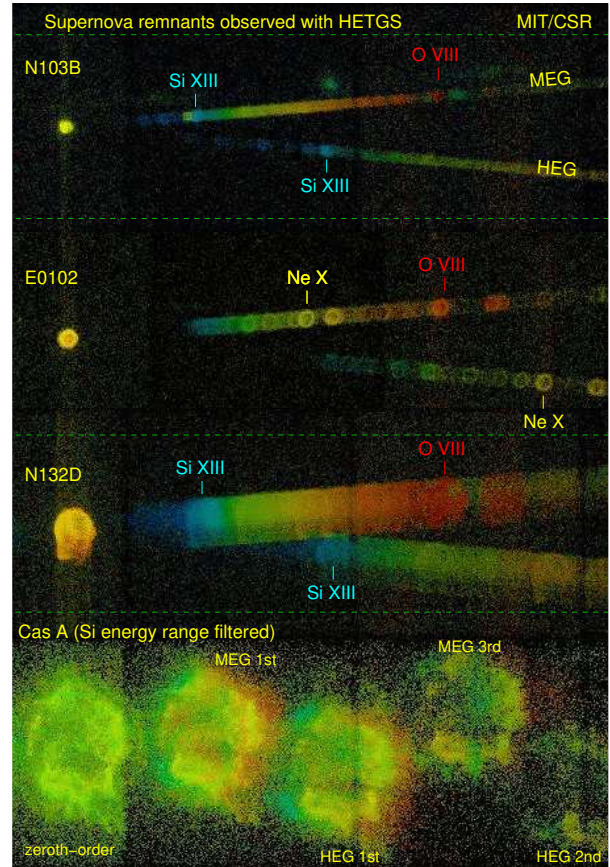


Figure 19: An overview of *Chandra* high energy gratings observations of SNRs (Dewey, 2002). (Figure kindly provided by D. Dewey.)

order image in the center of the X. Since they are transmission gratings, the HETGS and LETGS have plus and minus order spectra. Only one order is shown in Fig. 19. The detectors onto which the spectra are dispersed are the normal imaging detectors of *Chandra*, i.e. either the ACIS (CCD) instrument or the High Resolution Camera (HRC), a microchannel plate detector. For the HETGS the ACIS-S is the instrument of choice as it allows for the separation of different spectral orders. The LETGS is either used with the ACIS-S array, if the long wavelength range is not of interest, or with the HRC, which offers a longer wavelength range and smaller pixel size, but does not offer an intrinsic energy resolution and has lower quantum efficiency.

The dispersion angles of the HETGS and LETGS are much smaller than those of the *XMM-Newton*-RGS. As a result lines are much more narrowly spaced on the detector, with smaller detector pixels to match. However, for extended sources this means that the monochromatic image of a source in a given line will easily start overlapping with the images from nearby lines. This is even true for moderately extended sources, such as the already mentioned Magellanic Cloud SNRs. In numbers: the degradation in spectral resolution is (Eq. 53) $0.67\text{\AA}'$, $1.33\text{\AA}'$, and $3.33\text{\AA}'$ for the HEG, MEG and LETGS, respectively (Dewey, 2002). The effect of source extent on the spectra

is illustrated for the HETGS in Fig. 19, which gives an impression of the challenges faced when analyzing HETGS SNR data. Note that the complications are more severe for Type Ia SNRs (Sect. 8), because they have bright Fe-L lines, which, due to the richness of the line emission, easily blend together for extended sources. This is illustrated for N103B in Fig. 19 (see also Dewey, 2002). The situation is much better for the spectrum of the core collapse SNR 1E0102.2-7219, whose intrinsic spectrum is less complex (Fig. 17).

Given that small SNRs are already difficult to analyze, one would assume that the situation is almost hopeless for large SNRs. However, HETGS observations of a large SNR like Cas A (5') still provide important results. But instead of obtaining high resolution spectra of the SNR as a whole, one can obtain spectral properties of small, X-ray bright spots, embedded in a background of diffuse emission from other parts of the SNR (Dewey et al., 2007). In general, for extended sources, the RGS performs better for obtaining high resolution spectra of the SNR as a whole, whereas the HETGS will provide spectral information that relates to spectral properties in localized regions of the SNR.

The problems of obtaining high resolution X-ray spectra of extended sources will be over once the next generation of spectrometers will be put into space. These will in all likelihood be based on the calorimetric principle; an X-ray photon heats a small metal element, and the increase and subsequent decrease in temperature is measured with high sensitivity, using, for example, Transition Edge Sensors (TESs). TESs are superconducting devices operated near the critical temperature, where a small change in temperature leads to a strong response in conductivity. The spectral resolution can be as good as $\Delta E = 2$ eV at 6 keV. The small elements can be built into arrays, thereby allowing for imaging, high resolution spectroscopy. Currently, microcalorimeters are planned for the Japanese/US Astro-H mission (Takahashi et al., 2008) and the proposed ESA mission Athena²⁰.

8 Type Ia supernova remnants

8.1 X-ray spectroscopy of Type Ia supernova remnants

As discussed in Sect. 2.2, thermonuclear or Type Ia SNRs produce about a factor ten more mass in Fe-group elements than core collapse supernovae. This is the reason that Type Ia SNRs are often characterized by strong Fe-L shell emission, which cannot be resolved with CCD instruments, but it can be partially resolved by the current grating instruments (Sect. 7, Fig. 17, and Hughes et al., 1995). Many SNRs are now identified as Type Ia remnants based on the prominence of the Fe-L emission (see Table 2 for a list of likely Type Ia SNRs and relevant references). In

the case of two SNRs, Tycho/SN1572 (Fig. 1) and SNR B0509-67.5 the Type Ia identification has been confirmed by optical spectra of the light echoes (Krause et al., 2008b; Rest et al., 2008, truly spectacular results).

Not all Type Ia SNRs display prominent Fe emission. For example the X-ray spectra of SN 1006 show hardly any evidence for Fe-L emission (Vink et al., 2003), although recently Fe-K emission has been reported based on *Suzaku* observations (Yamaguchi et al., 2007, 2008). For SN 1006 the lack of Fe-L emission is partially due to the low ionization age ($n_e t \approx 2 \times 10^9$ cm⁻³s, e.g. Vink et al., 2003), which makes that the dominant Fe ionization stage is below that of Fe XVII. In that case hardly any Fe-L line emission is produced, but some Fe-K fluorescence line emission is still to be expected (Sect. 6.1.3). However, optical/UV spectroscopy of a bright UV star behind SN 1006 also shows a lack of absorption features from cool, unshocked, Fe (Hamilton et al., 2007). This is somewhat disconcerting, but it may indicate that SN 1006 produced a relatively large amount of intermediate mass elements and relatively small amounts of iron-group elements. This would still fit in with the optical results for Type Ia supernovae of Mazzali et al. (2007), which allows for the occurrence of fainter, Fe/Ni-poor supernovae. It is, however, more difficult to explain the lack of Fe with the models of Woosley et al. (2007) that suggest that the total mass of all Fe-group elements does not vary much among Type Ia SNe, but that there is only a variation in the relative amounts of radioactive ⁵⁶Ni and stable Fe. This is clearly of interest, and both models and the observational data should be scrutinized further.

Another reason why a Type Ia SNR may not be very bright in Fe-L or Fe-K line emission is that the Fe-rich layers has not yet been completely shock heated by the reverse shock. For example, Tycho/SN 1572, although far from devoid of Fe-L and Fe-K emission, shows less Fe-L emission with respect to Si XIII emission than most other Type Ia SNRs (Hwang and Gotthelf, 1997; Decourchelle et al., 2001; Hughes et al., 1995).

The effects of the progression of the reverse shock into the ejecta is nicely illustrated using the Large Magellanic Cloud (LMC) Type Ia SNRs in Fig. 20. For SNR B0509-67.5 (Warren and Hughes, 2004; Kosenko et al., 2008; Badenes et al., 2008b) the Fe-L emission is confined to a small, partial shell that is most pronounced in the west. This is the youngest LMC remnant (Rest et al., 2005), and the one with the largest X-ray line Doppler broadening, $\sigma_V \approx 5000$ km s⁻¹, as measured using *XMM-Newton*-RGS high resolution spectra (Kosenko et al., 2008). These spectra also indicate that the Fe-L emission is mainly coming from Fe XVII. In SNR B0519-69.0 (Kosenko et al., 2010) and N103B (Lewis et al., 2003; van der Heyden et al., 2002b) the Fe-L line emitting shell is more pronounced. The *XMM-Newton*-RGS spectra of B0519-69.0 show less line broadening, $\sigma_V \approx 1900$ km s⁻¹, and Fe-L emission is now also coming from the higher Fe ionization stages Fe XVII-Fe XXI. The *Chandra* data show that the lower Fe ionization stage, Fe XVII, is located closer to

²⁰Athena is a simplified version of the International X-ray Observatory (IXO, Bookbinder, 2010)

Table 2: Likely Type Ia supernova remnants

Name	Location	Distance (kpc)	Radius (pc)	High Res. Spec.	Other studies
G1.9+1.3 ^a	MW	8 (?)	2	(1,2,3)	
Kepler (SN 1604/G4.5+6.8)	MW	6 (4,5,6)	3		(7,8,9,10,5)
Tycho (SN 1572/G120.1+1.4)	MW	3	3.8	(11,12)	(13,14,15,16,12)
SN 1006 (G327.6+14.6)	MW	2.0 (17)	9.3	(18,19)	(20,21,22,23,24,25)
B0509-67.5	LMC	50 (25)	3.6	(27)	(28,29)
N103B	LMC	50	3.6	(30)	(31)
B0519-69.0	LMC	50	3.9	(32)	
DEM L 71	LMC	50	8.6	(33)	(34)
B0548-70.4	LMC	50	12.5		(35)
DEM L316A ^c	LMC	50	15		(36,37)
B0534-69.9	LMC	50	16		(35)
DEM L238	LMC	50	21		(38)
DEM L249	LMC	50	23		(38)
B0454-67.2	LMC	50	27		(39)
IKT 5 (B0047-73.5)	SMC	60 (26)	15 ^b		(40)
IKT 25 (B0104-72.3)	SMC	60	18		(40,41)
DEM S 128 (B0103-72.4)	SMC	60	26		(38)

MW=Milky Way, LMC=Large Magellanic Cloud, SMC=Small Small Magellanic Cloud.

References: 1) Reynolds et al. (2008); 2) Borkowski et al. (2010); 3) Carlton et al. (2011); 4) Sankrit et al. (2005); 5) Vink (2008c); 6) Chiotellis et al. (2011); 7) Kinugasa and Tsunemi (1999); 8) Cassam-Chenaï et al. (2004); 9) Badenes et al. (2007); 10) Reynolds et al. (2007); 11) Ghavamian et al. (2001); 12) Hayato et al. (2010); 13) Hwang and Gotthelf (1997); 14) Decourchelle et al. (2001); 15) Hwang et al. (2002); 16) Tamagawa et al. (2009); 17) Ghavamian et al. (2002); 18) Vink et al. (2003); 19) Vink (2004a); 20) Long et al. (2003); 21) Yamaguchi et al. (2007); 22) Acero et al. (2007); 23) Yamaguchi et al. (2008); 24) Katsuda et al. (2009); 25) Miceli et al. (2009); 26) Schaefer (2008); 27) Kosenko et al. (2008); 28) Warren and Hughes (2004); 29) Badenes et al. (2008b); 30) van der Heyden et al. (2002a); 31) Lewis et al. (2003); 32) Kosenko et al. (2010); 33) van der Heyden et al. (2003); 34) Hughes et al. (2003a); 35) Hendrick et al. (2003); 36) Nishiuchi et al. (2001); 37) Williams and Chu (2005); 38) Borkowski et al. (2006); 39) Seward et al. (2006); 40) van der Heyden et al. (2004); 41) Lee et al. (2011)

Notes:

^a Type Ia origin debatable, and largely based on morphology (Borkowski et al., 2010).

^b Only the Fe-L emitting interior is visible in X-rays, so the radius is not necessarily the shock radius for IKT 5.

^c DEM L316A is part of two associated SNRs. Shell A is given its Fe abundance most likely a Type Ia SNRs, whereas B is most likely a core collapse SNR (Williams and Chu, 2005). The two shells are likely not physically connected (Toledo-Roy et al., 2009).

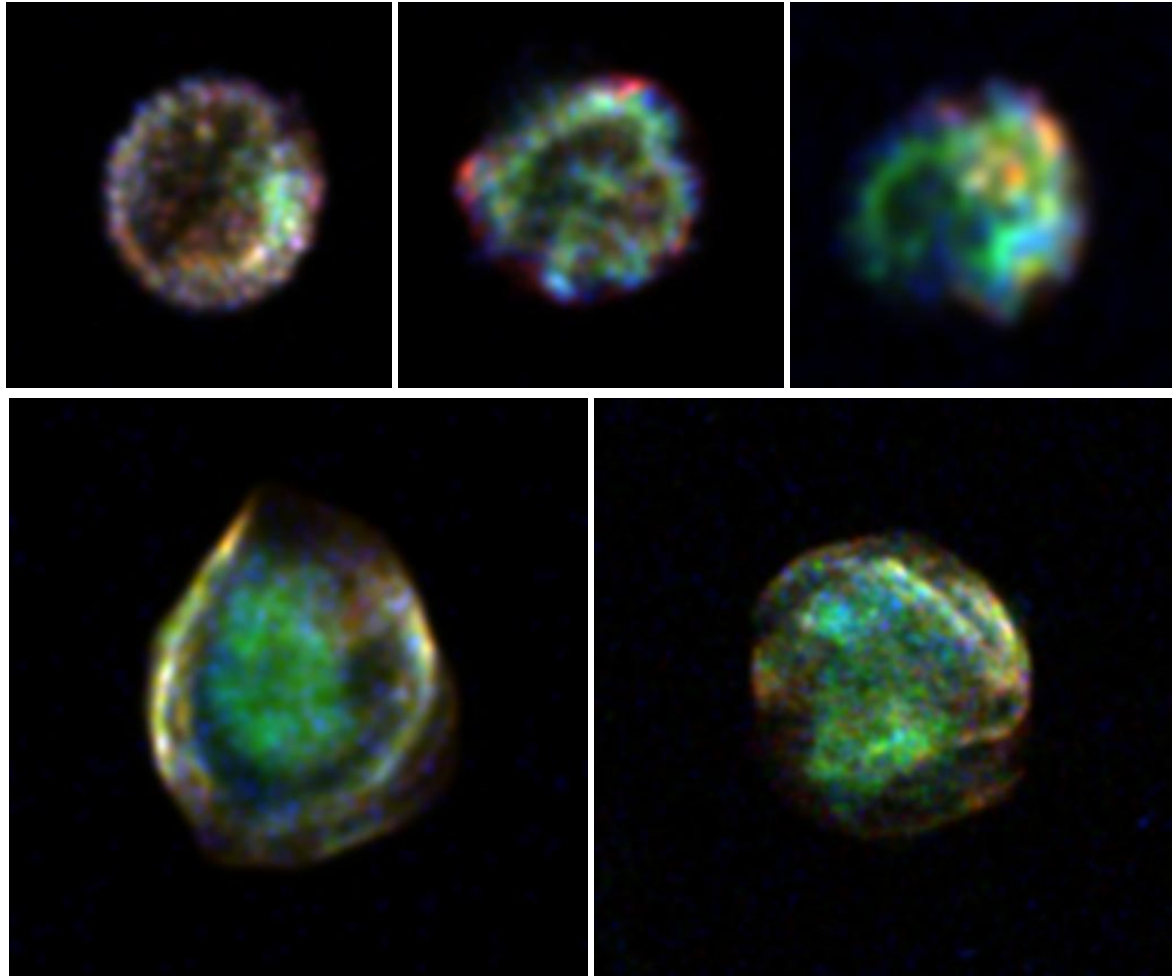


Figure 20: *Chandra* X-ray images of LMC Type Ia SNRs. These are three-color images, and in all cases red represents the O VII/O VIII band (0.5-0.7 keV), the color green represents Fe-L emission line (~ 1 keV). From left to right, top to bottom: B0509-67.5 (Warren and Hughes, 2004), B0519-69.0 (Kosenko et al., 2010), N103B (Lewis et al., 2003), Dem L 71 (Hughes et al., 2003a), and B0534-699 (Hendrick et al., 2003). The order of the figures is approximately indicative of the relative dynamical age. (Images generated by the author using the *Chandra* archive.)

the center. This is expected, because this is the location of the most recently shock-heated Fe (Kosenko et al., 2010, see Fig. 21).

Concerning the more mature SNRs Dem L71 (Hughes et al., 2003a; van der Heyden et al., 2003) and B0534-69.9 (Hendrick et al., 2003), one observes that Fe-L emission is coming from the whole center of the SNR, indicating that (almost) all ejecta have been shock-heated. There is a clear indication from recent X-ray data from both Galactic and LMC SNRs that the shocked ejecta of Type Ia remnants are well stratified; from the outside in one first encounters oxygen, then a silicon-rich layer, and finally the iron-group elements (Fig. 21), testifying of a more or less spherically symmetric explosion. This is clearly the case in SNR B0519-69.0 (Kosenko et al., 2010) and in the southwestern region of Kepler's SNR (Cassam-Chenaï et al., 2004), whereas the more mature SNR Dem L71 has an Fe-rich core (van der Heyden et al., 2002b; Hughes et al., 2003a). Only Tycho's SNR seems less stratified (Decourchelle et al., 2001). Note that the radial X-ray line emission is also influenced by ionization age differences in different layers, as indicated by *ASCA* and *XMM-Newton* observations of Tycho (Hwang and Gotthelf, 1997; Decourchelle et al., 2001), Kepler (Cassam-Chenaï et al., 2004), and the already discussed SNR B0519-69.0.

The more or less layered structure is unlike that of core collapse SNRs (Sect. 9.1), where in some cases plasma with more massive elements seems to have overtaken plasma with less massive elements. In addition, the morphologies of Type Ia SNRs are more symmetric than those of core collapse remnants (more on this in Sect. sec:orich). The reason for this may be a more spherically symmetric explosion and that the circumstellar medium (CSM) has been less disturbed, possibly because Type Ia SNe occur more frequently outside turbulent starforming regions. Nevertheless some imprints of CSM interaction can be found in Type Ia SNR (see next section).

Both for core collapse and for Type Ia SNRs the variation of elemental abundances inside the remnant poses a problem in modeling the overall X-ray spectra of SNRs. The reason is that one cannot realistically expect to fit the spectra with one or two NEI (Sect. 6.1.2) plasma models. On the other hand, adding many more NEI components leads to unconstrained results. Imaging spectroscopy offers some help, as one can extract spectra from distinct regions and apply single or double NEI components to these individual spectra. But projections effects play a role as well. Recently Kosenko et al. (2010) stretched the capabilities of multi-component fitting of SNR B0519-69.0 to the maximum, by using seven NEI components, each corresponding to a layer that could also be identified in the stratification inferred from narrow band *Chandra* imaging (Fig. 21): an O-rich layer, a Si/S-rich layer, a Ar/Ca layer, a low ionized Fe layer, and a highly ionized Fe layer. The continuum component was constrained by setting the abundance pattern to that of the LMC. Such a procedure works better for the radially stratified Type Ia SNRs than

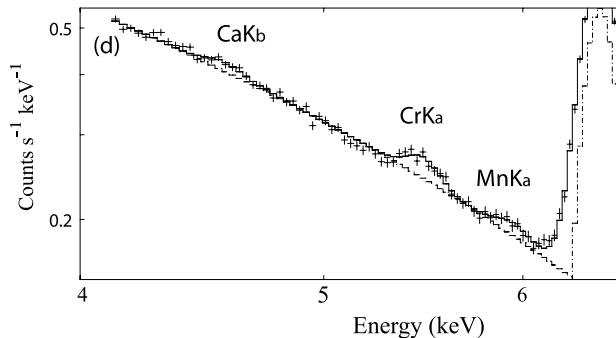


Figure 23: Detail of the *Suzaku* spectrum of Tycho/SN1572, showing $K\alpha$ emission from Cr, Mn and Fe (reprinted from Tamagawa et al., 2009).

for the more chaotic spatial abundance distribution of core collapse SNRs.

An alternative method that has already given interesting results is to model the whole hydrodynamical evolution of the SNR, from the explosion to the SNR phase, including the temperature/ionization evolution and X-ray emission, using the theoretically predicted initial stratification and velocity distribution of the ejecta (Badenes et al., 2003, 2005, 2008b; Sorokina et al., 2004; Kosenko, 2006; Kosenko et al., 2008, 2011). This procedure works relatively well for Type Ia SNRs, because the explosion properties of thermonuclear supernovae are much better constrained and allow for less variation than for core collapse supernovae. The grid of explosion models for Type Ia SNe is, therefore, much more limited. The method has been applied to Tycho/SN 1572 (Fig. 22 Badenes et al., 2006; Kosenko, 2006) and SNR B0519-69.0 (Badenes et al., 2006; Kosenko, 2006). For the latter, Badenes et al. (2008b) found that the most energetic Type Ia explosion models, which synthesize more Fe, fit the data best. Kosenko et al. (2008) reported for this SNR a very high plasma velocity based on the Doppler broadening measured with the *XMM-Newton*-RGS instrument. In addition, the RGS detected N VII line emission, which helps to constrain the amount of shocked CSM, because nitrogen is not a Type Ia nucleosynthesis product. In this case the inferred circumstellar density is $n_H = 0.4 - 0.8 \text{ cm}^{-3}$.

An uncertainty in modeling the combined hydrodynamics/X-ray emission from Type Ia SNRs is the influence of efficient cosmic-ray acceleration, as discussed in Sect. 4 and 5.5. Kosenko et al. (2008) incorporated the cosmic-ray acceleration effects by altering the equation of state of the shocked plasma, which gave a good fit to the *XMM-Newton* (EPIC-MOS) spectra for a cosmic-ray energy density that is about 40% of the gas density (see also Decourchelle et al., 2000; Kosenko et al., 2011).

Abundance studies of SNRs in X-ray are usually confined to the alpha-elements (C, O, Ne, Mg, Si, S, Ar, Ca) and Fe-group elements (Fe/Ni). These elements are the most abundant elements in the Galaxy, and are the dominant nucleosynthesis products of supernovae (Sect. 2),

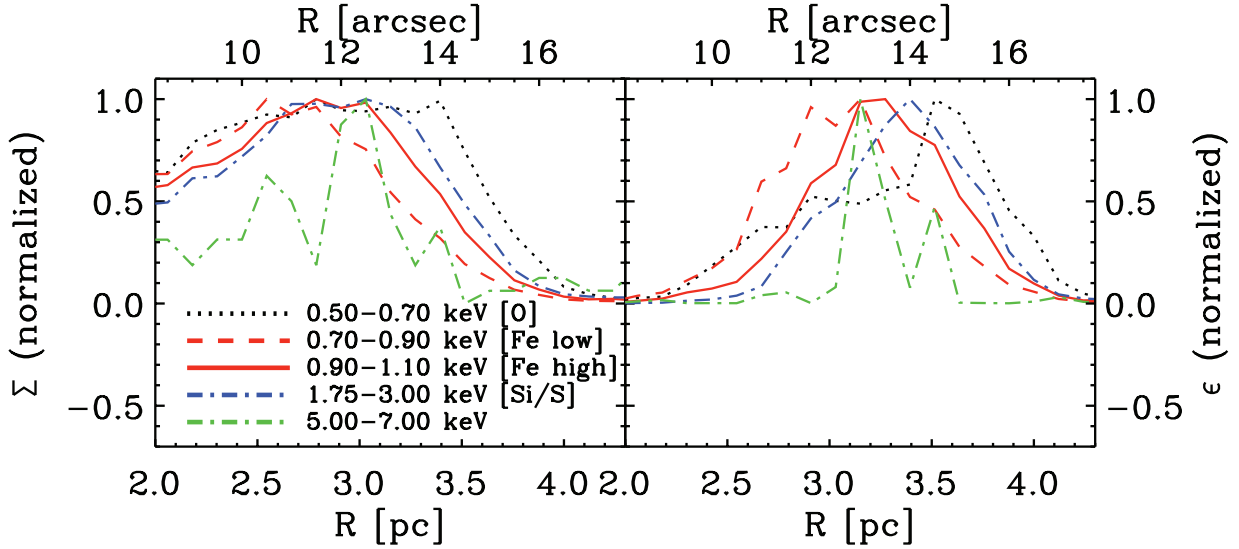


Figure 21: The stratification of O VII-VIII, Si XII, and Fe XVII-XVIII (Fe low), Fe XIX-XXI (Fe high) in SNR B0519-69.0, based on *Chandra* data. The left panel shows the radial surface emission profile, whereas the right panel shows the deprojected (emissivity) profile. (Figure taken from Kosenko et al., 2010).

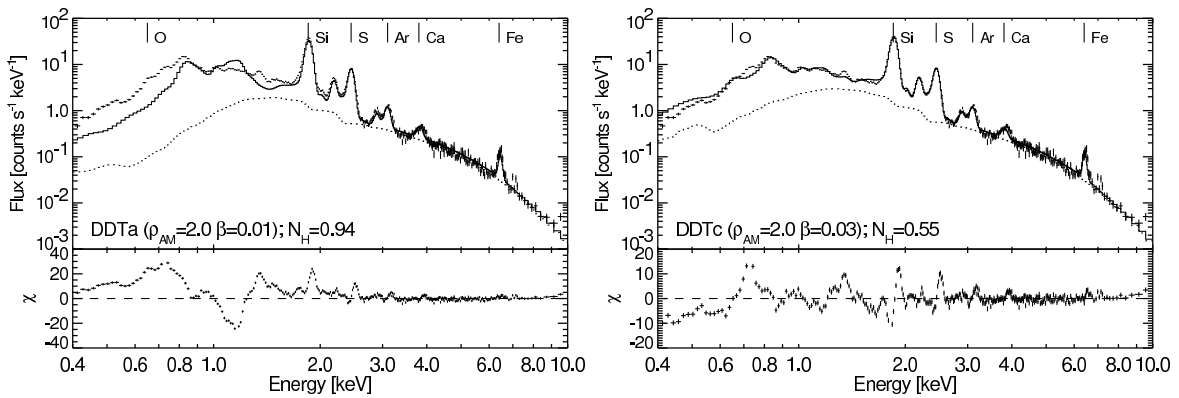


Figure 22: *XMM-Newton* MOS1 spectrum of western part of Tycho/SN 1572. The two panels show two models (solid lines) from an extensive grid of Type Ia models (Badenes et al., 2006). The model characteristics are indicated: the explosion model (here DDTa and DDTc), the circumstellar density, ρ_{AM} in units of 10^{-24} g cm $^{-3}$ and absorption column density, N_H in units of 10^{21} cm $^{-2}$. (Courtesy C. Badenes)

and all have prominent line transitions in the X-ray band. Other elements, for example those with uneven atom number, are usually too rare to detect in X-rays. However, recently Tamagawa et al. (2009) reported the detection of chromium (Cr, $Z = 24$) and manganese (Mn, $Z = 25$) K- α line emission from Tycho's SNR using *Suzaku* data (Fig. 23, see also Yang et al., 2009). The nucleosynthesis of Mn is influenced by the presence of the neutron rich element ^{22}Ne , whose abundance is determined by the metallicity of the white dwarf progenitor. An explanation for the relatively high flux ratio of Mn/Cr is, therefore, that SN1572 had a white dwarf progenitor that started as a main sequence star with solar or supersolar metallicity (Badenes et al., 2008a). In other words, SN 1572 was not the explosion of a Population II star.

8.2 Evidence for Type Ia progenitor imprints on the circumstellar medium

As explained in Sect. 2.2, there is little doubt that Type Ia supernovae are thermonuclear explosions of white dwarfs, but there is much uncertainty about the binary system that leads to the growth of a C/O white dwarf close to the Chandrasekhar limit. The mass transfer from the companion of the white dwarf can occur during various phases in the evolution of the companion; during the main sequence, red giant (RG), or asymptotic giant branch (AGB) phase, or when the companion itself is a white dwarf. The mode by which the mass transfer occurs may shape the CSM of the system. For example, Roche-lobe overflow is considered to lead to unstable mass transfer, but it may be stabilized by a fast, $\sim 1000 \text{ km s}^{-1}$, wind emanating from the white dwarf (Hachisu et al., 1996, 1999). This fast wind will create a large ($> 10 \text{ pc}$), low density bubble surrounded by a dense shell. Evolved stars, like RG and AGB stars, have slow winds ($\sim 10 \text{ km s}^{-1}$) which result in a rather dense CSM with a density profile scaling as r^{-2} (Sect. 4).

The specific characteristics of the binary are, therefore, expected to have an important imprint on the CSM, and, as a result, on the evolution, morphology and X-ray spectra of the SNR. Models for Type Ia usually ignore the possible effects of pre-supernova evolution, and instead assume a uniform CSM (i.e. an $s = 0$ model, in the notation of Chevalier (1982), see Sect. 4).

One important constraint on the progenitor system provided by SNRs comes from optical observations. These show that many of the SNRs mentioned in Table 2 have so-called Balmer-dominated shocks (e.g. Smith et al., 1991; Sankrit et al., 2005). Optical spectra from their shock regions show $\text{H}\alpha$ line emission, without [NII] line. This is caused by collisional excitation of neutral hydrogen entering the shock region. In addition, broad $\text{H}\alpha$ emission arises from charge transfer of neutral hydrogen with shock heated ions (Chevalier et al., 1980; van Adelsberg et al., 2008). The presence of Balmer-dominated shocks is only possible when the neutral fraction in the CSM is relatively high. It is therefore of interest that most of the SNRs with

Balmer-dominated shocks are Type Ia SNRs.²¹ The reason for this is that progenitors of core collapse supernovae create large Strömgenspheres ($> 10 \text{ pc}$ Chevalier, 1990). And even if they explode as red supergiants the bright flash of ionizing photons when the shock reaches the surface, creates a large ionized region (Chevalier, 2005). Type Ia supernovae, on the other, do not produce a UV flash at shock break-out bright enough to ionize a large region.

The presence of neutral hydrogen within a couple of parsecs from the explosion, therefore, is easy to explain for Type Ia SNR, *provided that the progenitor itself was not a powerful source of ionizing photons*. This excludes, therefore, an important class of Type Ia candidate progenitors, namely the so-called *supersoft sources*. These are soft X-ray sources that probably consist of a white dwarf accreting material from a companion at a rate close to the Eddington limit, and burn the accreted material in stable way at the surface (Li and van den Heuvel, 1997). But because supersoft sources are luminous UV/X-ray sources, $10^{37} - 10^{38} \text{ erg s}^{-1}$, they will easily ionize a region of 30 pc in radius. Many of the Balmer-dominated Type Ia SNRs, including Tycho, Kepler, B0509-67.5, B0519-69, DEML 71, can, therefore, not have had supersoft sources as progenitors (Ghavamian et al., 2003).

There are several other recent studies that cast a light on the structure of Type Ia SNRs. In one of them Badenes et al. (2007) investigates whether Galactic and LMC Type Ia SNRs show any evidence for having evolved inside large, tenuous cavities, as implied by the fast-wind model of Hachisu et al. (1996). This study shows that this is not the case, as the radii of the SNRs are too small and their ionization age, n_{et} , too large compared to model predictions that incorporate the effects of fast progenitor winds. Possible exceptions are SN 1006 and RCW 86. However, SN 1006 is located high above the Galactic plane, where the density is expected to be low irrespective of the progenitor model, and RCW 86 is not a bona fide Type Ia SNR, as it is located in an OB association (Westerlund, 1969), in a region with a high star forming rate, as indicated by outbreaks of gas from the Galactic plane region (Matsunaga et al., 2001).²²

Another study that may be revealing something about Type Ia progenitor systems concerns an analysis of *Chandra/XMM-Newton* of two old, $\sim 10^4 \text{ yr}$, LMC SNRs, DEM L238 and DEM L249 by Borkowski et al. (2006). These two SNRs are rather faint in X-rays, but are both characterized by a relatively bright interior dominated by Fe-L emission, somewhat similar to DEM L71 and SNR B0534-699 displayed in Fig. 20. The most surprising result of the analysis is that of the spectra from the interior indicate high values for the ionisation parameter, n_{et} ,

²¹The only exceptions are the large SNRs the ‘‘Cygnus Loop’’ and RCW 86, which are both likely core collapse SNRs (Ghavamian et al., 2001), but see Williams et al. (2011) for an alternative view on RCW 86.

²²However, recently Williams et al. (2011) argued, nevertheless, for a Type Ia origin, because there is no evidence for a neutron star inside the SNR, and there is evidence for large amounts of Fe.

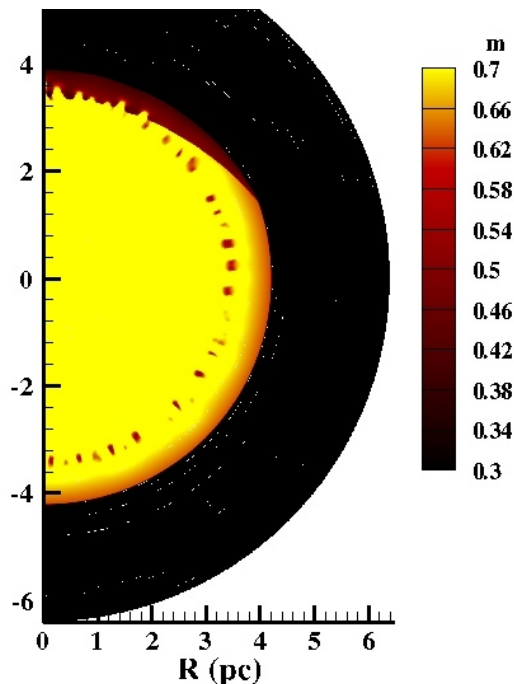


Figure 25: Results of the hydrodynamical study of Kepler’s SNR Chiotellis et al. (2011), showing the expansion parameter in the SNR for a model in which the progenitor systems moved with respect to the interstellar medium, and created a one side shell due to interaction of the progenitor wind and the ISM. The expansion parameter in the densest regions of the shell are as low as $\beta = 0.35$, comparable to observations (Dickel et al., 1988; Vink, 2008c; Katsuda et al., 2008c). (Figure provided by A. Chiotellis.)

$\sim 10^{12}\text{cm}^{-3}\text{s}$ for DEM L238 and $\sim 4 \times 10^{11}\text{cm}^{-3}\text{s}$ for DEM L249. Such high values require relatively high densities in the interior. This is in contrast to the low densities implied by the X-ray spectra of the shell, and, indeed, the overall faintness of these SNRs in X-rays. Borkowski et al. (2006) argue that in order to account for the high central density the blast wave must have encountered a high density CSM early during the SNR evolution. Such a dense medium is usually a signature of a slow wind outflow, instead of the fast winds implied by the models of Hachisu et al. (1999), or a simple, uniform density medium.

Finally, evidence that winds from Type Ia progenitors affect the CSM is provided by the historical SNR of SN 1604 (also known as Kepler’s SNR, or Kepler for short). Kepler is located high above the Galactic plane, with latitude $b = 6.8^\circ$, which translates to 446 pc for a distance of 4 kpc (Sankrit et al., 2005).²³ This high latitude would make Kepler an obvious Type Ia SNR, if it were not for the presence of dense, nitrogen-rich material, mostly in the northern part of the remnant, which indicates the presence of a circumstellar shell (van den Bergh and Kamper,

²³Or 670 pc for a distance of 6 kpc, the distance preferred based on modeling the explosion, if the kinetic energy is $> 10^{51}$ erg (Aharonian et al., 2008a; Vink, 2008c; Chiotellis et al., 2011).

1977; Bandiera, 1987). During the 1990s a core collapse origin for SN 1604, was therefore preferred. X-ray spectroscopy, first with ASCA (Kinugasa and Tsunemi, 1999) and later with *XMM-Newton* (Cassam-Chenaï et al., 2004) and *Chandra* (Reynolds et al., 2007), revealed that the spectrum is dominated by Fe-L emission around 1 keV, and bright Fe-K shell emission around 6.7 keV, characteristic for Type Ia SNRs. Additional evidence for a Type Ia origin is the low oxygen content, and the lack of an obvious X-ray point source that may be the neutron star that should in most cases result from a core collapse supernova (Reynolds et al., 2007).

The idea that the SNR encounters a dense shell in the north is reinforced by two recent X-ray studies (Vink, 2008c; Katsuda et al., 2008c), which confirm an earlier radio measurement (Dickel et al., 1988) that the expansion of this SNR in the north is relatively slow with a small value for the expansion parameter (Eq. 5) of $\beta \approx 0.35$, whereas the average value is ≈ 0.5 . The value for the north is unusual in that it falls below the value 0.4 for a SNR in the Sedov phase of its evolution. On the basis of expansion measurements, Vink (2008c) estimated that the mass in the swept-up, nitrogen-rich shell must have been $\sim 1 M_\odot$.

This result, and the morphology of Kepler, resembling a bow shock in the north (Fig. 24 and Fig. 25 for a model), is used by Chiotellis et al. (2011) to argue that the progenitor system was a binary consisting of a C/O white dwarf with an asymptotic giant branch (AGB) star as a companion. Such a system would be labeled as a symbiotic binary. Part of the slow wind ($\sim 15 \text{ km s}^{-1}$) of the AGB star was accreted onto the white dwarf, until it exploded. In order to account for the nitrogen enrichment of the shell one has to assume a main sequence mass for the secondary star of 4-5 M_\odot . The bow-shock shape of Kepler, and its height above the Galactic plane ($\sim 400 - 700$ pc), can be explained by a proper motion of the system with about 250 km s^{-1} (c.f. Bandiera and van den Bergh, 1991; Borkowski et al., 1994). Nevertheless, within a Type Ia scenario, it is not quite clear, why a binary system was ejected with such a high velocity, as usually interaction of two binaries leads to the ejection of fast single stars (Leonard and Duncan, 1990). But it does occur, see for example the relatively high velocity ($\sim 130 \text{ km s}^{-1}$) of the AGB star Mira A and its companion (Martin et al., 2007).

9 Core collapse supernova remnants

9.1 Oxygen-rich supernova remnants

As explained in Sect. 2, the nucleosynthesis yields of core collapse supernovae peaks for the element oxygen. The oxygen yield itself is strongly correlated with the main sequence mass of the progenitor, although for masses $\gtrsim 30 M_\odot$ the poorly known fraction of material that falls back onto the central object (neutron star or black hole) may reverse this trend. An important class of SNRs are the so-called oxygen-rich SNRs (Table 3). As the name

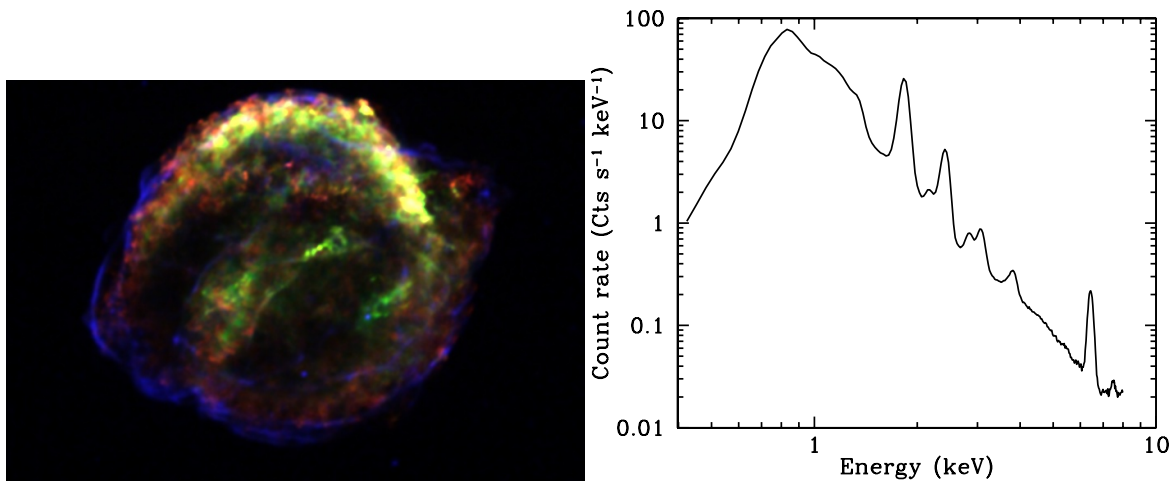


Figure 24: Left: *Chandra* image of Kepler's SNR, with red indicating Si-K α emission (1.75-1.95 keV), green Fe-L emission (0.8-1.6 keV), and blue continuum emission (4-6 keV). The image is based on a deep, 750 ks, *Chandra* observation (Reynolds et al., 2007). Right: raw count rate spectrum from Kepler's SNR, based on the same observation. Note the dominant Fe-L emission between 0.7-1.5 keV (c.f. Fig. 17c).

Table 3: Oxygen-rich supernova remnants

Name	Location	Distance (kpc)	Radius (pc)	High Res. Spec.	Other studies
Cas A (G111.7-2.1)	MW	3.4 (1)	2.6 (2)	(3,4)	(5,6,7,8,9)
MSH 11-54 (G292.0+1.8)	MW	$\gtrsim 6$ (10)	$\gtrsim 7.5$	(11)	(12,13)
Puppis A (G260.43.4)	MW	2.2 (14)	17.6	(15)	(16,17)
B0540-69.3	LMC	50 (18)	8.4	(19)	(20,21)
N132D	LMC	50	11	(22,23)	(24)
1E 0102.2-7219 (IKT 22)	SMC	60 (18)	5.9	(25,26)	(27)
B0049-73.6 (IKT 6)	SMC	60	21.2		(28,29)
B0103-72.6 (IKT 23)	SMC	60	26.1	(28)	(30)

MW=Milky Way, LMC=Large Magellanic Cloud, SMC=Small Small Magellanic Cloud.

Selected references:

1) Reed et al. (1995); 2) Gotthelf et al. (2001); 3) Bleeker et al. (2001); 4) Lazendic et al. (2006); 5) Willingale et al. (2002); 6) Hwang and Laming (2003); 7) Hwang et al. (2004); 8) Maeda et al. (2009); 9) DeLaney et al. (2010); 10) Gaensler and Wallace (2003); 11) Vink et al. (2004); 12) Gonzalez and Safi-Harb (2003); 13) Park et al. (2007); 14) Reynoso et al. (1995); 15) Winkler et al. (1981); 16) Hwang et al. (2008); 17) Katsuda et al. (2008a); 18) Schaefer (2008); 19) van der Heyden et al. (2001); 20) Hwang et al. (2001); 21) Park et al. (2010); 22) Behar et al. (2001); 23) Canizares et al. (2001); 24) Borkowski et al. (2007); 25) Rasmussen et al. (2001); 26) Flanagan et al. (2004); 27) Gaetz et al. (2000); 28) van der Heyden et al. (2004); 29) Hendrick et al. (2005); 30) Park et al. (2003)

suggests, these SNRs show large overabundances of oxygen, indicating that these are remnants of the most massive stars ($M_{MS} \gtrsim 18 M_{\odot}$). Initially these sources were mainly identified based on their optical oxygen-line emission properties ([OIII], e.g. Goss et al., 1979; Mathewson et al., 1980; Lasker, 1979; Dopita et al., 1981), but in many cases the X-ray spectral properties confirm the elevated oxygen abundances, in particular for young remnants like Cas A (Vink et al., 1996; Willingale et al., 2002), 1E 0102.2-7219 (Hughes and Singh, 1994; Gaetz et al., 2000; Rasmussen et al., 2001; Flanagan et al., 2004), and G292.0+1.8 (MSH 11-54, e.g. Park et al., 2007). Even for some of the more mature oxygen-rich SNRs, like N132D and Puppis A, it is still possible to identify regions with oxygen-rich ejecta (Behar et al., 2001; Borkowski et al., 2007; Katsuda et al., 2008a).

The neon and magnesium yields of core collapse supernovae trace the oxygen yield (Fig. 3), one therefore expects also that the Ne and Mg abundances of oxygen-rich SNRs are high. This appears to be indeed the case for young oxygen-rich SNRs like 1E 0102.2-7219 (Rasmussen et al., 2001; Gaetz et al., 2000, Fig. 17, 26, 28) and G292.0+1.8 (Hughes et al., 2001; Gonzalez and Safi-Harb, 2003; Park et al., 2007; Vink et al., 2004). But an important exception to this rule is Cas A, which has Ne/Mg abundances a factor 5-10 below the expected values (Vink et al., 1996). In general, the most striking feature of the X-ray spectrum of Cas A is the very bright silicon and sulphur emission. It is usually assumed that the Cas A ejecta are dominated by oxygen, which is almost fully ionized (Vink et al., 1996; Hwang and Laming, 2003), but Dewey et al. (2007) has argued that the most abundant element in the ejecta is silicon.

If the ejecta indeed are almost devoid of hydrogen, this greatly affects the ejecta mass estimates (Sect. 6.1, Eq. 43). For example, for Cas A it implies a rather low ejecta mass of 2-4 M_{\odot} , with about 1-2 M_{\odot} of oxygen (Vink et al., 1996; Willingale et al., 2003). This oxygen mass is consistent with a progenitor main sequence mass of $18 \pm 2 M_{\odot}$. This led Chevalier and Oishi (2003) to the conclusion that Cas A must have been a Type IIb SNR, given the similarity between the apparent mass loss and main sequence mass of the Type IIb supernova SN1993J and Cas A. This conclusion has been spectacularly confirmed by the optical light echo spectrum of the Cas A supernova (Krause et al., 2008a).

Another property of Cas A is the strong bipolarity of the silicon/sulphur-rich ejecta, as indicated by optical (Fesen et al., 2006), X-ray (Vink, 2004b; Hwang et al., 2004), and infrared observation (Hines et al., 2004). These observations show the presence of Si/S-rich material outside the radius of the main shock in the northeast and southwest. The presence of ejecta outside the shock in the northeast was already known for a long time, and its optical feature has long been referred to as “the jet”. In X-rays the presence of two opposite jets is best shown by mapping the ratio of Si XIII over Mg XI $K\alpha$ emission (Vink, 2004b; Hwang et al., 2004, Fig. 26b), or the equivalent width

of the Si XIII emission (Hwang et al., 2000; Yang et al., 2008).

The hydrodynamical simulations by Schure et al. (2008) show that these jets cannot have survived the interaction with a circumstellar shell. Such a shell would be present if there has been a fast Wolf-Rayet star wind ploughing through a red super giant wind (Sect. 4.3). This strongly suggests that the Cas A progenitor exploded while in the red supergiant phase. This is consistent with a main sequence mass below $\sim 25 M_{\odot}$, for which stars do not go through a Wolf-Rayet star phase. Since there was likely no high mass loss Wolf-Rayet star phase, the low ejecta mass is best explained with a binary star scenario, in which a high mass loss is caused by a common envelope phase (Young et al., 2006; van Veelen et al., 2009). A similar scenario was proposed for the Type IIb supernova 1993J (Woosley et al., 1994), whose optical spectrum closely resembles that of the light echo spectrum of Cas A (Krause et al., 2008a). There is no candidate secondary star in Cas A, so the common envelope phase may have led to a merger of the cores of the two stars.

The apparent bipolarity of the Cas A explosion may be related to the mass loss history of the progenitor, which may have included a common envelope phase. It is not clear whether all core collapse supernovae develop strong bipolarities either due to the accretion process onto the collapsing core, or perhaps due to rapid rotation (Sect. 2). In more massive progenitors, these bipolarities may be smothered while the explosion ploughs through the extended envelope of the star. Indeed, for supernovae the amount of asphericity indicated by optical polarimetry seems to depend on how much of the hydrogen-rich envelope was removed (Wheeler et al., 2002). It may also be related with the common envelope merger, as it may have increased the rotation of the stellar core.

A puzzling property of the jets in Cas A is their silicon richness. If the jets really come from the core one expects the jets to contain more iron-rich plasma. Cas A does contain many iron-rich knots, but not so much in the jets, as well as at the outer edge of the southeastern part of the main shell (Hughes et al., 2000; Hwang and Laming, 2003); see the blueish colored regions in Fig. 26a. The projected radius of these iron knots, together with the inferred age of Cas A ~ 330 yr (Thorstensen et al., 2001), indicate that the mean velocity of these iron knots are higher than 7000 km s^{-1} . This is very high indeed, as core collapse simulations by Kifonidis et al. (2006) show iron-group elements with velocities only up to 3300 km s^{-1} .

The morphology of Cas A as seen in Fe-line emission does not have an obvious axis of symmetry. As Fig. 26a shows iron-rich regions can be found in the southeast, the north, inside the silicon-rich shell, and in the west. Although in the northern part the Fe-rich ejecta seem to be on the inside of the Si-rich shell, Doppler measurements using *XMM-Newton* EPIC-MOS data show that in this region the velocity of iron is higher, $\sim 2500 \text{ km s}^{-1}$, than that of silicon, $\sim 2000 \text{ km s}^{-1}$ (Willingale et al., 2002). It is therefore likely that also in the northern part the Fe-

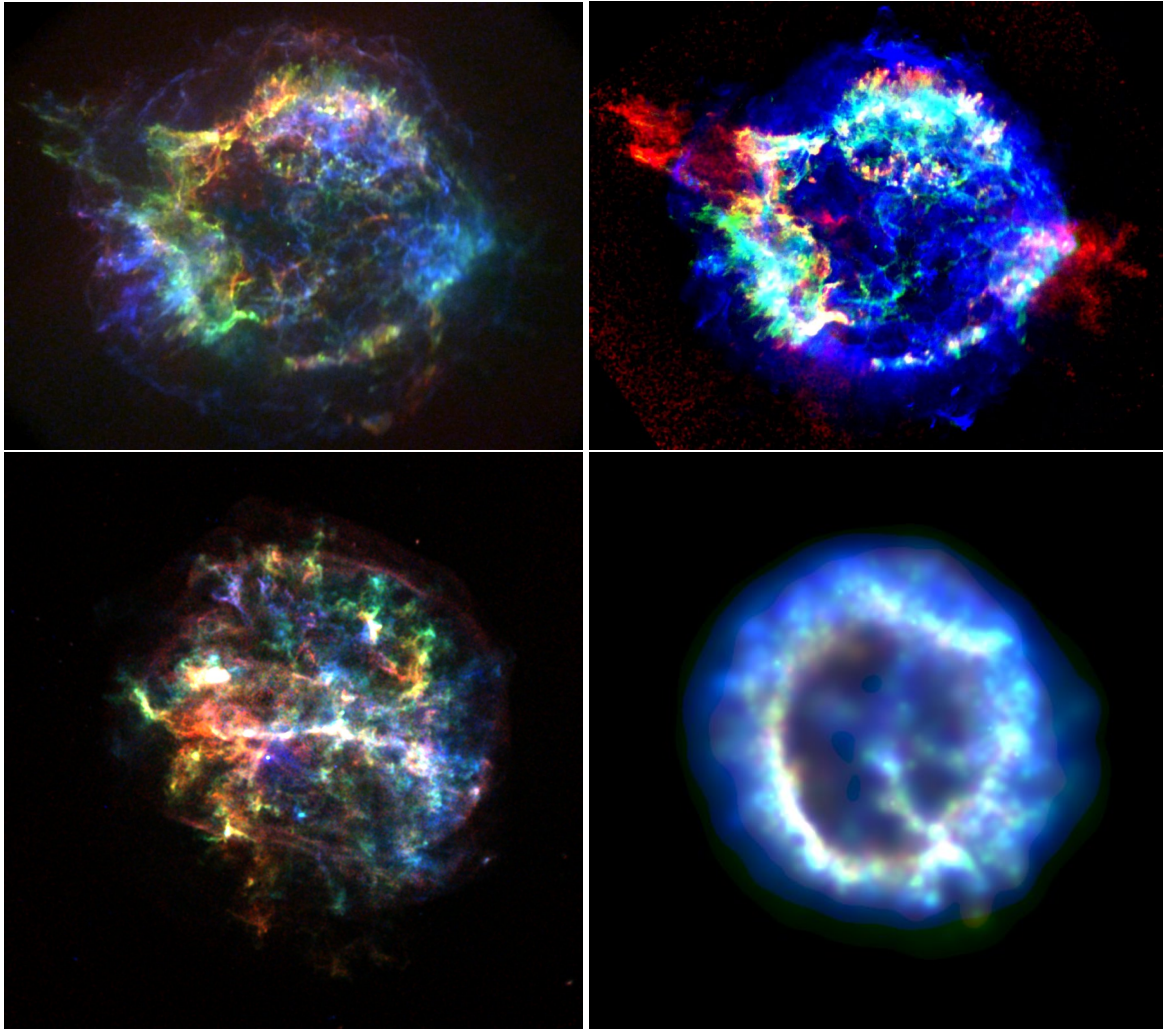


Figure 26: Multi-color *Chandra* X-ray images of four oxygen-rich SNRs (see Table 3 for the sizes). Top left: Cas A, with red indicating O VIII Ly- β emission, green Si XIII He α , and blue Fe XXVI He α (based on the 1 Ms observation Hwang et al., 2004). Top right: A different view of Cas A, based on a combination of radio (blue), X-ray Si XIII emission (green), and the ratio of Si XIII over Mg XI emission (red). The latter brings out the jet-counter-jet system, which protrudes the radio/X-ray shell in the northeast-southwest region (Vink, 2004b; Hwang et al., 2004; Schure et al., 2008). Bottom left: G292.0+1.8, with red O VIII Ly- α emission, green is Ne X Ly α , and blue Si XIII HE α emission. Image based on a 516 ks long observation (Park et al., 2007). Bottom right: The Small Magellanic Cloud SNR 1E 0102.2-7219, with red O VII and O VIII emission, green Ne IX and Ne X emission, and blue emission above 1.27 keV, which includes Mg XI, Mg XII, and Si XVIII emission (see also Fig. 17 and 28).

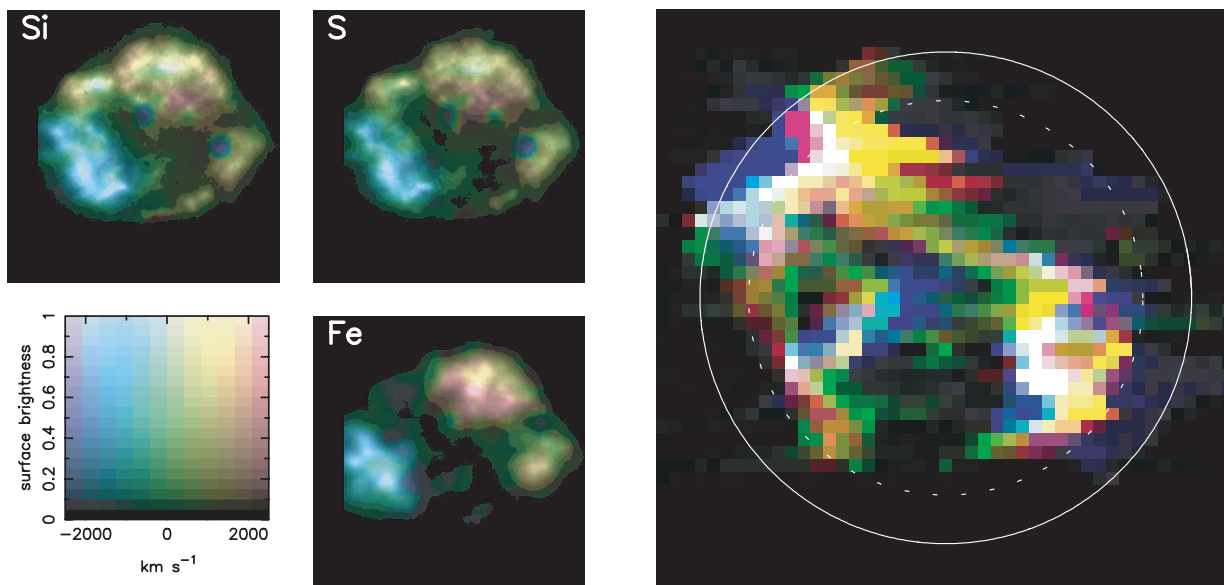


Figure 27: Left: Doppler maps of Cas A in the bands of He-like silicon, sulphur and iron, based on *XMM-Newton*-MOS data. Right: Reconstructed “side view” of Cas A, based on the Doppler maps, using a combination of north-south position and Doppler velocity to reconstruct the third dimension. Red represent silicon, green silicon, and blue iron. Note that in the North iron is in front of the silicon-rich layer. Both figures are based on figures from Willingale et al. (2003).

rich ejecta are outside the Si-rich shell. The study by Willingale et al. (2002) also showed, by combining Doppler information with the spatial structure, that the overall morphology of the Si-rich resembles more closely a donut-like structure than a spherical shell (Fig. 27), as already suggested by Einstein Focal Plane Crystal Spectrometer data (Markert et al., 1983) and ASCA data (Holt et al., 1994).

Finally, it is worth pointing out that Cas A is special in the sense that the detection of ^{44}Ti γ -ray and hard X-ray lines from this SNR suggest a rather large production of this element ($1.6 \times 10^{-4} M_{\odot}$, see also Sect. 6.2, Renaud et al., 2006b). This is much higher than model predictions, but consistent with what has been inferred for SN 1987A. This higher than expected yield may be related to the fact that the Cas A explosion was asymmetric (Nagataki et al., 1998). Something that may also apply to SN 1987A. On the other hand, Prantzos (2011) shows that the solar ratio of $^{44}\text{Ca}/^{56}\text{Fe}$, the stable products of, respectively, ^{44}Ti and ^{56}Ni , is more consistent with the inferred yields for Cas A and SN 1987A than with model predictions. This suggests that asymmetric explosions are more common than assumed, or that the production processes of these elements is not yet well understood.

High resolution X-ray spectroscopy with the *Chandra* HETGS suggest that the SMC SNR 1E 0102.2-7219, has a similar, “donut-like” structure (Flanagan et al., 2004). This has been established using a special property of transmission gratings, namely that the plus and minus orders are each others mirrors in terms of wavelengths, whereas the projection of the object in a single wavelength is not mirrored between the plus and minus orders. If for example one side of the object has on average a redshift and the other side a blueshift, this results in the blueshifted

side to be shifted toward the center (zeroth order) and the redshifted side to be shifted away from the center. The monochromatic images in the plus or minus orders are, therefore, squeezed in one order and stretched in the opposite order. 1E 0102.2-7219 shows exactly this behavior as shown in Fig. 28 for the Ne Ly- α line.

If we now turn the attention to another well studied oxygen-rich SNR G292.0+1.8 (MSH 11-54) one also sees a non-spherical distribution of elements (Park et al., 2002, 2007, Fig. 26c). There is the enigmatic bar, running from east to west, first seen in X-ray images taken with the Einstein satellite (Tuohy et al., 1982). The origin of this structure is not so clear, but may be a pre-existing feature in the CSM that was overtaken by the forward shock. The idea that the bar is of CSM origin is supported by the lack of evidence for enhanced metal abundances, as determined by *Chandra* X-ray imaging spectroscopy (Park et al., 2002). The overall metal abundance distribution shows a striking asymmetry between the northwest, which contains more Si-group elements, and the southwest, which contains more oxygen, neon, magnesium. There is no evidence that this asymmetry is caused by an asymmetry in the CSM. Thus an asymmetric explosion seems to have taken place (Park et al., 2007). Gonzalez and Safi-Harb (2003) analyzed *Chandra* X-ray spectra and came to the conclusion that the abundance pattern matches that of a star with a main sequence mass of 30-40 M_{\odot} .

If there is one thing that one that can be concluded from X-ray observations of core-collapse SNRs, it is that their explosions are very irregular, with their SNRs showing large deviations from spherical symmetry and a lack of elemental stratification. Material from the core (Fe-group elements) can be ejected with speeds in excess of those

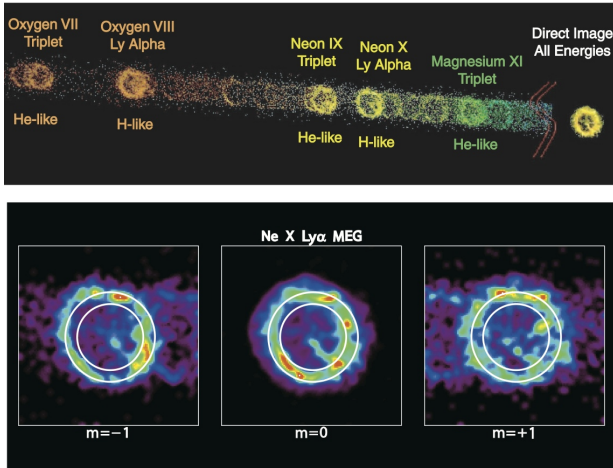


Figure 28: *Chandra*-HETGS spectrum of the oxygen-rich SNR 1E 0102.2-7219. The top panel shows part of the spectrum in the negative order ($m = -1$) as seen with the Medium Energy Grating of the HETGS. The SNR in individual emission lines shows up as images ordered by wavelength. Bottom panel: a comparison between Ne X Ly α images in the negative, zeroth order, and positive order. Differences in radial velocities over the face of the SNR result in distortions of the image with respect to the zeroth order images. Deviations from spherical symmetry show up as distortions of the images that are different in the negative and positive orders, as can be clearly seen here. (Figure taken from Flanagan et al. (2004).)

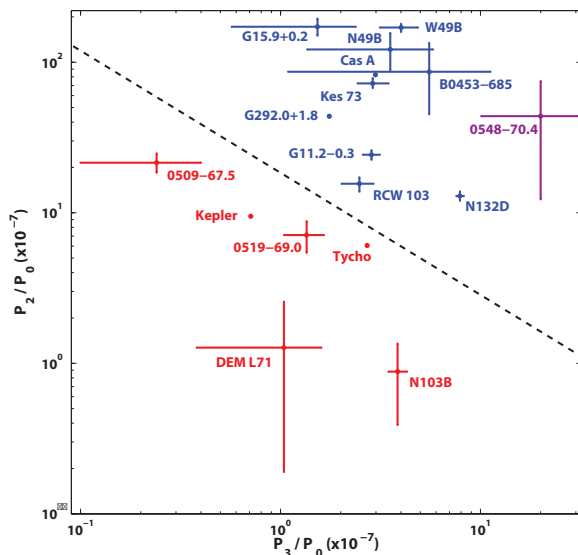


Figure 29: Results from a statistical analysis of the Si XIII emission images (around 1.85 keV) as observed with the *Chandra*-ACIS instrument. The numbers P_0, P_2, P_3 are linked to different symmetry properties of the SNR emissivity distribution, with P_3 indicating an overall deviation from circular symmetry, whereas P_2 is sensitive to mirror-symmetry. Type Ia SNRs (red) clearly occupy a different region of the diagram than core-collapse SNRs (blue). (Figure taken from Lopez et al. (2009).)

of layers higher up in the star. This behavior is markedly different from that of the well stratified Type Ia SNRs.

Recently, Lopez et al. (2009, 2011) made a quantitative analysis of the morphological differences between core collapse and Type Ia SNRs, using a multipole statistical analysis of the X-ray surface brightness distribution of SNRs. Deviations from circular symmetry show up as large values for P_3/P_0 (normalized third moment), whereas a mirror symmetry gives large values for P_2/P_0 . As Fig. 29 shows, Type Ia SNRs are on average rather more spherical than core-collapse SNRs; their mean values for both P_2/P_0 and P_3/P_0 are smaller. In addition, there is the trend that if an individual Type Ia SNR shows deviations from spherical symmetry (large P_3/P_0) it tends to have less mirror symmetry. These difference makes that Type Ia and core-collapse SNRs occupy different areas in the P_3/P_0 versus P_2/P_0 diagram.

That there is a structural difference between core-collapse and Type Ia SNRs is not too surprising, since the energy of Type Ia SNRs comes from explosive nucleosynthesis, and requires a regular burning front to propagate through the white dwarf. Core-collapse supernovae are driven by the gravitational energy from the collapsing core, and much of that energy is deposited in the inner regions. Irregularities will not impair the explosion of the rest of the star.

However, there are some signs of aspherical structures that may reveal us something about the explosion process: there are the donut-like morphologies of Cas A and 1E0102.2-7219, and, in particular, the bipolar Si-rich jets in Cas A. Currently there is no theory to explain these features, but it is tempting to relate the jets of Cas A to those of long duration gamma-ray bursts. In fact, the less energetic gamma-ray bursts, the X-ray flashes, have properties rather similar to what has been inferred for Cas A. For example, for the X-ray flash SN 2006aj (Mazzali et al., 2007; Laming et al., 2006) the inferred explosion energy is 2×10^{51} erg, and the inferred main sequence mass is $\sim 20 M_\odot$ with an ejecta mass of $\sim 2 M_\odot$.

9.2 The X-ray emission from SN 1987A

The Type II supernova SN 1987A was discovered on February 23, 1987 in the LMC. Due its proximity, it remains, to date, the best studied supernova. The detection of ~ 20 neutrinos during a short interval of ~ 13 s by Kamiokande II (Hirata et al., 1987) and IMB (Bionta et al., 1987) confirmed beautifully the theory that Type II supernovae are the result of the collapse of a stellar core into a neutron star, and that most of the energy is released through a cooling population of neutrinos. The detection of neutrinos also meant that the collapse of the core was very accurately timed, and that the core collapse preceded the optical detections by about 3 hr (see Arnett et al., 1989, for a review).

In many respects SN 1987A was a peculiar supernova. Its maximum luminosity was unusually low, corresponding to $M_B = -15.5$, compared to ~ -18 for typical Type

II supernovae. This low luminosity is the result of the compactness of the progenitor star at the moment of explosion: the progenitor was not a red supergiant, but a B3 I supergiant, identified as the star Sanduleak -69°202. Such an evolved, blue giant is expected to have a fast, tenuous wind, creating a low density cavity within a red supergiant wind of a previous mass loss phase. Instead, optical spectroscopy (Fransson et al., 1989) provided evidence for dense ($n_e \sim 3 \times 10^4 \text{ cm}^{-3}$) circumstellar material enriched in nitrogen. Later optical imaging revealed the presence of three rings (Crotts et al., 1989; Wampler et al., 1990), which was later confirmed by a, now iconic, *Hubble Space Telescope* image (Burrows et al., 1995). The fact that the progenitor exploded as a blue supergiant, the chemical abundances (Podsiadlowski, 1992), and the triple-ring system may be explained by the merging of a 15-20 M_\odot star with a 5 M_\odot star, about 20,000 yr prior to explosion; see the hydrodynamical simulations of Morris and Podsiadlowski (2007, 2009).

SN 1987A is of great importance, since it is the first supernova for which one has been able to follow the evolution from supernova to SNR. Moreover, our knowledge about the supernova type and progenitor is much more detailed than for any other SNR. One can say that the supernova stage has given way to the SNR stage, when the emission is no longer dominated by radiation from the cooling ejecta, but by radiation from shock-heated CSM/ejecta.²⁴

A few months after the explosion SN 1987A was detected in hard X-rays (Sunyaev et al., 1987; Dotani et al., 1987). The hard X-ray emission was probably the result of multiple Compton scatterings of γ -rays generated by the decay of radioactive material. Nuclear decay-line emission from ^{56}Co was detected surprisingly early on, indicating considerable mixing of inner ejecta toward the surface of the supernova envelope (e.g. Leising and Share, 1990, and references therein). Moreover, the nuclear decay lines were redshifted (Sandie et al., 1988; Teegarden et al., 1989; Tueller et al., 1990). This is an indication for an asymmetric explosion, bringing to mind the evidence for an asymmetric explosion of the Cas A supernova in the form of jets and high velocity iron knots (Sect. 9.1).

The onset of the SNR stage of SN1987A, as far as the X-ray emission is concerned, was marked by the gradual increase of the soft X-ray emission as seen early on by ROSAT, starting in February 1991 (Hasinger et al., 1996). Since then all major X-ray observatories have observed SN 1987A on a regular basis, following the X-ray evolution of the SNR in considerable detail (Fig. 30).

The X-ray observations show that after an initial phase, in which the outer shock wave was moving through the, relatively tenuous, medium associated with the progenitor's fast wind, between 1995-1999 the shock wave started to interact with the central dense ring seen in the optical. This ring has a size of 1.7'' by 1.2'', consistent with a ring of radius 0.19 pc seen under an angle of $\sim 45^\circ$. The dense

ring itself has considerable small-scale structure, with regions of different densities, and fingers sticking inward (McCray, 2007, Fig. 31). As a result the ring is not lighting up all at once, but several "hot spots" turned on; first in the northeast (Burrows et al., 2000), later also in other regions. By now all along the ring one can find X-ray emitting regions (Racusin et al., 2009, see Fig. 31).

The complexity of the interaction of the blast wave with the dense inner ring do not fit into the simplified description of SNR hydrodynamics as sketched in Sect. 4 (Borkowski and Szymkowiak, 1997; Michael et al., 2002; McCray, 2007). The basic structure of a blast wave heating the CSM, and a reverse shock heating of the ejecta is still valid. But a range of shock velocities must be considered, as the encounter of the blast wave with the density enhancements in the ring and its protrusions lead to a system of transmitted and reflected shocks. The transmitted shocks heat the material of the ring, whereas the reflected shocks go back into the plasma behind the blast wave. These reflected shocks are low Mach number shocks, as they go through already shock-heated plasma, and result in additional heating and compression of the already hot plasma. The transmitted shocks will have a range of velocities, depending on the density of the material and the obliquity with which the blast wave hits the protrusions. The slowest transmitted shocks ($V_S \lesssim 200 \text{ km s}^{-1}$) become radiative (Sect. 4.1), resulting in the bright optical radiation that accounts for the bright knots that lie as beads all along the optical ring as observed by the *Hubble Space Telescope* (Kirshner, 2007, Fig. 31).

Because the blast wave reached the ring in about 5-10 yr, the average blast wave velocity was initially $\sim 15,000 - 30,000 \text{ km s}^{-1}$. In contrast, recent expansion measurements indicate an expansion velocity of $\sim 4000 \text{ km s}^{-1}$ in the radio (Ng et al., 2008) and $1800 \pm 600 \text{ km s}^{-1}$ in X-rays (Racusin et al., 2009). Until 2004 (6000 days after the supernova) the expansion velocity in X-rays was similar to that in the radio, indicating that the blast wave reached the denser region of the inner rings around that time. The X-ray emission also became brighter around that time (Park et al., 2005). Currently, the light curve has flattened again (Racusin et al., 2009, see Fig. 30). The strong deceleration of the blast wave from $15,000-30,000 \text{ km s}^{-1}$ to $1800-5000 \text{ km s}^{-1}$ means that a strong reverse shock must have developed with shock velocities in the frame of the ejecta of $\sim 10,000 \text{ km s}^{-1}$. Note that the difference between the radio and X-ray expansion may be partially due to the fact that the X-ray emission depends on density as $\propto n_e^2$ (Sect. 6.1), whereas the radio synchrotron emission scales probably as $\propto n_e$ (with some uncertainty, because synchrotron radiation also depends on the electron acceleration properties of the shock and on the magnetic-field strength, see also the discussion in Zhekov et al., 2010). The X-ray expansion may, therefore, be more skewed toward higher density regions, than the radio expansion measurements.

From 2000 to 2010 SN 1987A was observed several times with both the CCD and grating spectrometers on

²⁴ Note that strictly speaking this means that radio supernovae (Weiler et al., 2009), should be considered SNRs, as their radio emission is due to interaction of the ejecta with the dense CSM.

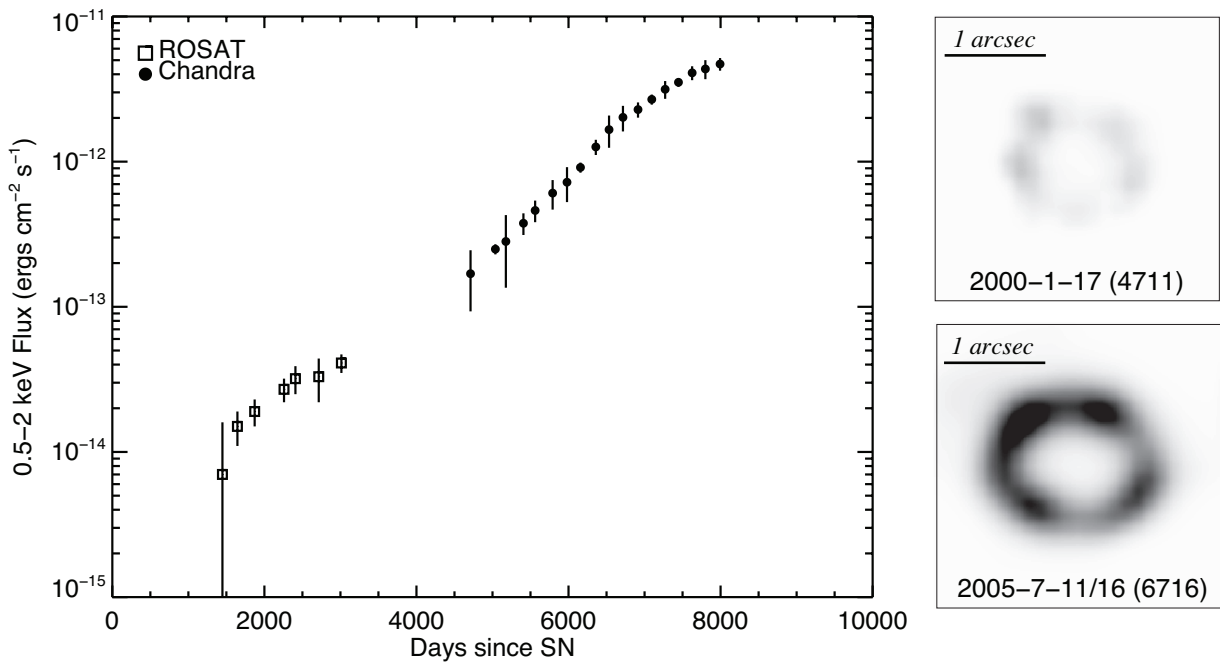


Figure 30: Left: The evolution of the X-ray flux of SN 1987A (Racusin et al., 2009). Right: Two frames taken from Fig. 1 of Park et al. (2006), showing *Chandra* images of the SN1987A, which indicate that it did not only substantially brighten, but also changed morphology as the shock heated more parts of the circumstellar ring. The first regions to be heated were in the northeast, but by 2009 most of the ring is lit up in X-rays, although the brightest region is still the northeast. In addition the radius of X-ray bright torus has increased from $0.6''$ to $0.78''$ (Racusin et al., 2009).

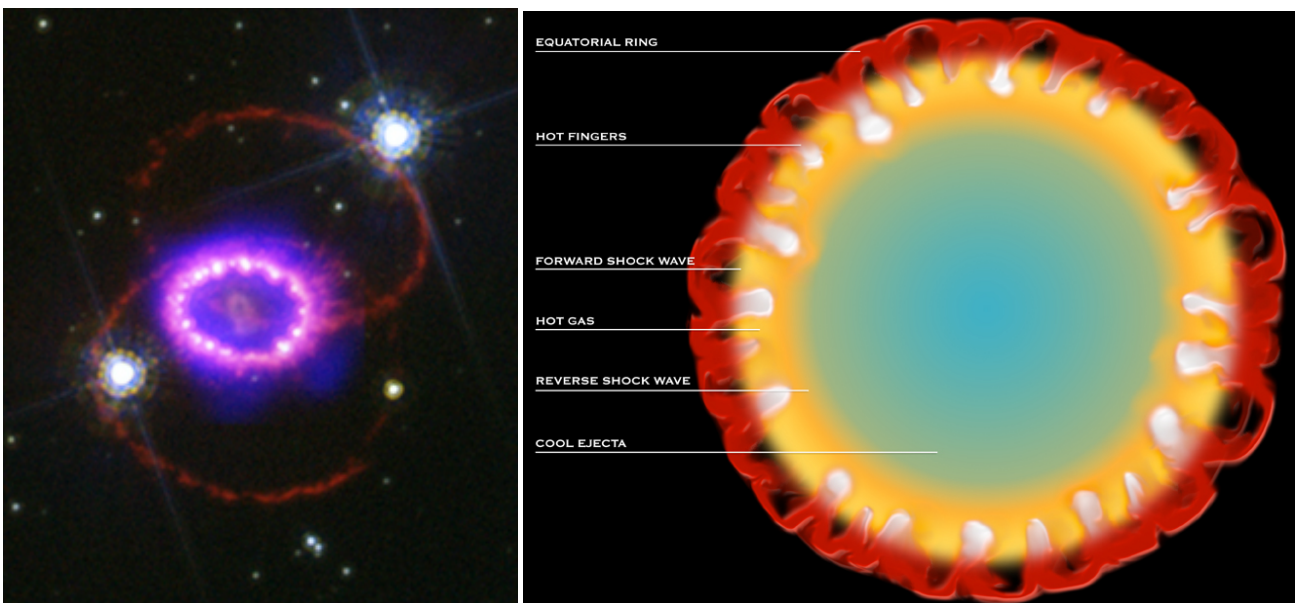


Figure 31: Left: Composite optical/X-ray image (Credit: X-ray: NASA/CXC/PSU/S.Park & D.Burrows.; Optical: NASA/STScI/CfA/P.Challis). Right: Illustration of the interaction of the blast wave of SN1987A with the circumstellar ring. The blast wave shock heats the “fingers” on the inside of the ring, and as a result both in X-rays and in the optical the emission comes from discrete bright spots rather than smooth structures. (Source: NASA/CXO/M.Weiss)

board *Chandra* and *XMM-Newton*. The CCD spectra are well fitted with a two component model, a soft component with $kT_e = 0.2 - 0.3$ keV, which is close to CIE, and a harder component with $kT_e = 2 - 3.5$ keV and $n_e t \approx 3 \times 10^{11} \text{ cm}^{-3} \text{ s}$ (Park et al., 2006; Zhekov et al., 2010). The soft CIE component is associated with the densest regions, heated by the transmitted shock, whereas the hotter, NEI component is generally attributed to the plasma heated by reflected shocks (Park et al., 2006; Zhekov et al., 2010). However, it is not clear whether also reverse shock heated plasma is responsible for some of the harder X-ray emission.

Note that even the reflected/reverse shock heated plasma must be relatively dense as the ionization parameter indicates $n_e \approx 950 t_{10}^{-1} \text{ cm}^{-3}$, with t_{10} the time since the plasma was shocked in units of 10 yr. As the SNR ages, the low temperature component is becoming hotter ($kT_e \approx 0.2$ keV in 1999 versus $kT_e \approx 0.3$ keV in 2005), whereas the high temperature component is becoming cooler ($kT_e \approx 3.3$ keV and $kT_e \approx 2.3$ keV, respectively), see Park et al. (2006); Zhekov et al. (2009, 2010).

SN 1987A is an ideal target for the grating spectrometers of *Chandra*, due to its small angular extent and its brightness (Burrows et al., 2000; Michael et al., 2002; Dewey et al., 2008; Zhekov et al., 2009, Fig. 32), which allows for resolving the He-like triplets (Sect. 6.1.3). The earliest high resolution spectrum, taken with the *Chandra* HETGS, dates from 1999 (Burrows et al., 2000). It reveals prominent emission lines from H-like and He-like transitions of O, Ne, Mg, and Si, and line widths consistent with an expansion of $\sim 4000 \text{ km s}^{-1}$. Recent HETGS and LETGS spectra indicate a line broadening ranging from $1000\text{-}5000 \text{ km s}^{-1}$ (FWHM), but with a bulk velocity that is surprisingly low, $\sim 100 - 200 \text{ km s}^{-1}$, consistent with the radial velocity of the LMC (Dewey et al., 2008; Zhekov et al., 2009). This is a strong indication that the hottest component is not due to the main blast wave, for which the plasma velocity should move with $\frac{3}{4}V_s$, but must result from either reflected shock (Zhekov et al., 2009) or from the reverse shock heated plasma. This would reconcile the large line widths and hot temperatures, indicating large shock velocities, with a relative low velocity in the observers frame (see Sect. 4 and Sect. 5.1).

X-ray spectra taken with different instruments do not agree in all details. For example the *Chandra* CCD spectra indicate a cool component consistent with CIE (Park et al., 2006), whereas the high spectral resolution HETGS/LETGS spectra indicate a plasma with a higher electron temperature, 0.55 keV, and out of ionization equilibrium, with $n_e t = 4 \times 10^{11} \text{ cm}^{-3} \text{ s}$ (Zhekov et al., 2009). The best fit RGS model gives a solution that lies somewhere in between $n_e t \approx 8 \times 10^{11} \text{ cm}^{-3} \text{ s}$ (Heng et al., 2008).

In reality a range of temperatures and $n_e t$ values are expected, given the complexity of the ring structure. Even the lowest $n_e t$ values reported, imply densities in excess of $n_e \approx 2000 \text{ cm}^{-3}$. Nevertheless, these differences in fit parameters may also result in differences in abundance determinations. In general the abundance determi-

nations from various studies are in good agreement (Heng et al., 2008; Zhekov et al., 2009), indicating LMC abundances except for oxygen, which seems underabundant, and nitrogen, which is mildly overabundant. The RGS and LETGS/HETGS mainly disagree on the iron abundance, which is underabundant according to fits to the RGS data (Heng et al., 2008).

SN 1987A will remain an important object for X-ray astronomy in the coming decennia. It will brighten in the coming years as the transmitted shock will penetrate deeper and deeper into the ring. The main blast wave, which will pass around the ring, will at some point encounter the shell that separates the tenuous wind of the progenitor from the dense red supergiant wind. This shell is likely to have a complicated shape, as indicated by the triple-ring system seen in the optical, and the hydrodynamical simulations of Morris and Podsiadlowski (2007). The SNR will brighten as a result of encountering the shell, first just outside the equatorial region, later also in the polar regions. As the reverse shock penetrates deeper into the ejecta one will be able to probe the composition of the inner ejecta of SN 1987A.

The evolution of SN 1987A has already shown us that the early evolution of SNRs can be much more complicated than described by the standard evolutionary models described in Sect. 4. SN 1987A may be a special case, with its triple-ring system and the possibility that its progenitor was the result of a recent common envelope merging of a binary system. However, such mergers are far from unique; even for the text-book shell-type SNR Cas A it has been argued that its progenitor was a merger product (Sect. 9.1).

9.3 Core collapse supernova remnants and neutron stars

Core collapse SNRs are apart from their abundance patterns, also distinguished by the presence of a neutron star. In the past it was assumed that this would automatically imply the presence of a pulsar wind nebula (PWN, see Helfand and Becker, 1984, for an early review on neutron stars in SNRs), but over the last 20 years it has become clear that not all neutron stars manifest themselves through the creation of a PWN (Gaensler and Slane, 2006, for a review).

There is good evidence that 5-10% of all neutron stars are born as magnetars, neutron stars with very high magnetic fields ($10^{14} - 10^{15}$ G), which emit predominantly in the soft and hard X-ray bands (Mereghetti, 2008, for a review), and whose emission is not powered by pulsar spin-down, but by magnetic-field decay. These magnetars rotate slowly ($P = 2 - 12$ s), presumably due to a very rapid initial spin-down. As a result, their spin-down power is currently too low to drive the creation of a PWN.²⁵

²⁵There is evidence that the most rapidly spinning magnetar (1E1547.0-5408 $P = 2$), located inside a faint SNR (G327.24-0.13 Gelfand and Gaensler, 2007) is surrounded by a faint PWN (Vink and Bamba, 2009), but this is disputed by Olausen et al. (2011).

tial spin period $P_0 \ll P$, and if the spectral braking index is $n = 3$,²⁶ which is the value for braking due to a rotating magnetic dipole. The presence of neutron stars in SNRs helps to verify these assumptions as τ_c can be compared with age estimates of the SNR. This helped establish that for the neutron star in Puppis A $P_0 \approx P$ (Gotthelf and Halpern, 2009).

The presence of a SNR surrounding a PWN can also be used to constrain the initial period in another way, namely by considering the pressure confinement of the PWN by the shock heated SNR shell (van der Swaluw and Wu, 2001; Chevalier, 2005). The total pressure inside the PWN is determined by the integrated energy loss of the pulsar, which in itself is mostly determined by the initial spin period. A surprising result of these studies is that there is a large range in initial spin periods, which is theoretically not well understood (e.g. Ott et al., 2006). Moreover, and this brings us to the above formulated question a), there is no clear relation between the initial period of a neutron star and the type of supernova as determined from the SNR characteristics (Chevalier, 2005).²⁷

The same conclusion can be drawn when also considering the other classes of neutron stars, CCOs and magnetars. First of all, the discovery of these neutron stars owe much to the fact that unresolved X-ray sources were discovered in SNRs. Most CCOs and magnetars that are more than a million year old are very difficult to discover. The CCO will not be surrounded by a SNR anymore (and hence no longer deserve their name), and will have cooled substantially. Magnetic field decay makes that old magnetars become radio-quiet dim X-ray sources. Neutron stars in SNRs are therefore important to estimate the the neutron star birthrate, especially of radio-quiet neutron stars, and to estimate the initial spin-period and magnetic-field distributions.

As for the characteristics of the SNRs with CCOs and magnetars. At least two CCOs are found in oxygen-rich SNRs (Sect. 9.1), the remnants of the most massive stars. For one of them (in Puppis A) we know that the neutron star has a low magnetic field. For the other one (Cas A), no pulsation has yet been found, and its nature is still unclear. For magnetars, there is so far only circumstantial evidence linking them to the core collapse of the most massive stars. There is also evidence that a perfectly normal neutron star can be created from a very massive star: The oxygen-rich SNR G292.0+1.8, has a pulsar with $P \approx 0.135$ s (Hughes et al., 2003b), and $B \approx 10^{13}$ G (Chevalier, 2005). So the conclusion must be that the most massive stars make neutron stars with any type of magnetic field (low, normal, or magnetar-like).

This SNR/neutron star combination of G292.0+1.8 (Fig. 26, Sect. 9.1) stands out for another reason as well. Its X-ray spectrum has been used to determine an abundance pattern that suggests that G292.0+1.8 is the result of the explosion of a star with an initial mass of $M = 30 - 40 M_\odot$ (Gonzalez and Safi-Harb, 2003). This is the

mass range for which theorists have argued that core collapse should lead to the creation of a black hole, instead of a neutron star. Clearly this is important for our understanding of neutron star and black hole formation, but the evidence needs to be further studied.

In contrast, no neutron star has yet been found in the Cygnus Loop (Fig. 4, see Sect. 10.1). If this means that the event did not produce a neutron star but a black hole, we have an example of a less massive core collapse event ($M_{\text{MS}} \approx 15 M_\odot$, Sect. 10.2) that did not produce a neutron star. But the Cygnus Loop is very big and perhaps a neutron star is inside or in the vicinity of the SNR and has not yet been identified.

As for magnetars, the origin of their magnetic fields is not clear. An interesting hypothesis is that the magnetic fields result from a dynamo mechanism in rapidly rotating proto-neutron stars (Duncan and Thompson, 1992). This requires rather short initial spin period of $P_0 \approx 1 - 3$ ms. Since the rotational energy of such a rapidly rotating neutron star is $E_{\text{rot}} = \frac{1}{2} I \Omega^2 \approx 3 \times 10^{52} \left(\frac{P}{1 \text{ ms}}\right)^{-2}$ erg, one expects that a large part of the rotational energy will power the supernova (Arons, 2003; Allen and Horvath, 2004). But an X-ray study of SNRs with magnetars by Vink and Kuiper (2006) shows that the SNRs are consistent with typical explosion energies of 10^{51} erg. This is more consistent with the alternative hypothesis concerning the origin of magnetar fields, namely that magnetars are born from the core collapse of stars with very large magnetic fields (the fossile field hypothesis Ferrario and Wickramasinghe, 2006). There is another, albeit non-conclusive, argument against the idea that magnetars are born rapidly rotating. As explained above, there is a large spread in initial spin periods of normal neutron stars. In fact there is very little evidence for pulsars born with periods $P_0 < 10$ ms (van der Swaluw and Wu, 2001; Chevalier, 2005). How likely is it then that 5-10% of the neutron stars are born with extremely short periods, $P_0 \sim 1 - 5$ ms?

The debate on the origin of magnetar magnetic fields has not yet settled, but it is clear that SNRs play an important role in this debate (e.g. Durant and van Kerkwijk, 2006; Horvath and Allen, 2011).

10 Supernova remnants in or approaching the radiative phase

10.1 From non-radiative to radiative shocks

A couple of thousand years after the explosion SNRs have swept up considerably more mass than the supernova ejected. SNRs in this phase of their evolution are often referred to as ‘‘mature SNRs’’ (Sect. 4). Once their shocks have slowed down to below $V_s < 200 \text{ km s}^{-1}$, the shocks are becoming radiative, and the SNR evolution can no longer be described by the Sedov-model (Eq. 2). Slowing down even more results in a post-shock region that is too cool to emit substantially in X-rays. Nevertheless, some SNRs with slow shocks have bright interior X-ray

²⁶ n is defined as $\dot{\Omega} = -k\Omega^n$

²⁷ See also Chevalier (2010).

emission, as will be discussed in Sect. 10.3.

The prototypical “mature” SNRs are the Cygnus Loop (Fig. 4a) and the Vela SNR, which are on the border between phase II and phase III (Sect. 4). They are both considered to be core collapse SNRs, as I will describe below. They have earned their prototypical status predominantly by being *nearby examples* of mature SNRs. Their small distance also means that their X-ray emission can be studied on very small physical length scales. And because the absorption column is low, one can also study their soft X-ray and UV emission.

The Cygnus Loop is at a distance of 540 ± 100 pc (Blair, 2005), and has an angular radius of 1.4° , corresponding to 13 pc, with a break-out region in the south. Its age has been estimated to be 8,000 to 14,000 yr (Levenson et al., 1998, 2002; Katsuda et al., 2008c), and its shocks have velocities in the range of $150\text{--}400$ km s⁻¹ (Levenson et al., 1998, 2002; Blair, 2005; Salvesen et al., 2009). This range in shock velocities indicates that the Cygnus Loop has both radiative and non-radiative shocks. In fact, the Cygnus Loop derives part of its fame from the beautiful optical nebula associated with the radiative shocks, the so-called Veil Nebula. The large contrasts in shock properties are best explained by the idea that the Cygnus Loop is evolving in a wind-blown cavity (McCray and Snow, 1979; Charles et al., 1985; Levenson et al., 1998; Miyata and Tsunemi, 1999). Earlier in its evolution the SNR must have expanded rapidly within the tenuous medium inside the wind-blown bubble. But currently most of the shock is interacting with the dense shell swept up by the progenitor’s wind (see also Sect. 4). In such a case parts of the shock may reach the radiative phase at a relatively young age. Another example is the probably even younger SNR RCW 86 (probably SN 185, Stephenson and Green, 2002), which also shows a mixture of radiative and non-radiative shocks (e.g. Smith, 1997; Ghavamian et al., 2001), and whose plasma ionization ages and emission measures testify of large density contrasts (Vink et al., 1997; Bamba et al., 2000; Bocchino et al., 2000; Rho et al., 2002; Vink et al., 2006). As a “cavity SNR” the Cygnus Loop may therefore not deserve its status as a prototypical mature SNR. On the other hand, all SNRs when investigated in detail appear to have some unique features.

X-ray spectroscopy of the Cygnus Loop has provided some peculiar results. One example is that imaging spectroscopy with *ASCA*, *Suzaku*, *Chandra* and *XMM-Newton* has revealed that the abundances of the bright X-ray shell are sub-solar, with typical depletion factors of ~ 5 (Miyata et al., 1994, 2007; Katsuda et al., 2008b; Nemes et al., 2008).²⁸ The low abundance of the inert element Ne shows that this is not due to dust depletion. In contrast, Katsuda et al. (2008b) found that near the rim of the bright shell there are abundance enhancements of about a factor 2. The same team later attributed these enhanced abundances at the very edge of the SNR to charge exchange reactions between unshocked neutral hydrogen and shock

ionized O VIII (Katsuda et al., 2011). However, as they point out, further investigation is clarify the possible role of resonant-line scattering on the line equivalent widths. As discussed in Sect. 6.1.3, this process results in scattering of photons with energies corresponding to resonant lines out of the line of sight. As the photons will eventually escape the SNR, it will result in enhanced line emission at the edges of emission regions, and an attenuation of resonant line emission from the regions projected toward the interior. Indeed, there is some evidence for resonant line scattering (Miyata et al., 2008), but currently it is not clear whether charge exchange and/or resonant line scattering can explain the X-ray line emission from the rim of the Cygnus Loop, or whether the metallicity of the plasma is really depleted. Future high resolution X-ray spectroscopy may be needed to clarify this issue, as it is needed to resolve the resonant lines from forbidden lines. Resonant line scattering will boost the G-ratio toward the center of the SNR, and lower it at the edge of the rim. Charge exchange will only enhance the G-ratio at the edge of the rim, but without affecting the G-ratio in the rest of the shell. In Sect. 10.2 I will discuss the X-ray spectroscopic results of inner regions of the Cygnus Loop.

One striking feature of mature SNRs like the Cygnus Loop is the complexity of the emission, which is caused by the interactions of the shocks with density inhomogeneities (clouds, or cloudlets), and by a variety of shock velocities giving rise to both radiative and non-radiative shocks. Moreover, these shock-cloud interactions lead to the creation of reflected and transmitted shocks (Levenson et al., 1996; Patnaude et al., 2002), not unlike the situation described in connection with SN 1987A (Sect. 9.2).

A SNR that has been used quite extensively to investigate the interaction of the blast with the inhomogeneous CSM is the Vela SNR. The Vela SNR contains a pulsar with a rotational period of 89 ms, which is surrounded by a pulsar wind nebula (Helfand et al., 2001). Its characteristic age is $\sim 11,000$ yr. The actual age of the pulsar and SNR may be older, $\sim 20,000$ yr (Aschenbach et al., 1995). VLBI parallax measurements of the pulsar show that its distance is 287 ± 19 pc (Dodson et al., 2003), at which distance the angular size of the SNR, 4° , corresponds to a physical radius of 20 pc. The SNR is located in a complex, starforming region, which also contains the γ^2 -Velorum massive stellar binary. Both of them are embedded within the hot bubble/HII region that is known as the Gum-nebula (Aschenbach et al., 1995; Sushch et al., 2011).

ROSAT and *XMM-Newton* X-ray imaging spectroscopy of isolated regions, in combination with optical narrow filter imaging show a complex structure (Bocchino et al., 2000; Lu and Aschenbach, 2000; Miceli et al., 2005) that is best described in terms of three components: 1) a tenuous inter-cloud medium, which is difficult to characterize in X-rays due to its diffuse nature and low surface brightness, 2) soft X-ray emission from cloud cores, heated by slow transmitted shocks, and with temperatures around $kT \approx 0.1$ keV, and 3) hotter regions surrounding the clouds, consisting perhaps of plasma evaporated from

²⁸ Although this is not confirmed by Levenson et al. (2002), who only analyzed a small portion of the SNR with *Chandra*.

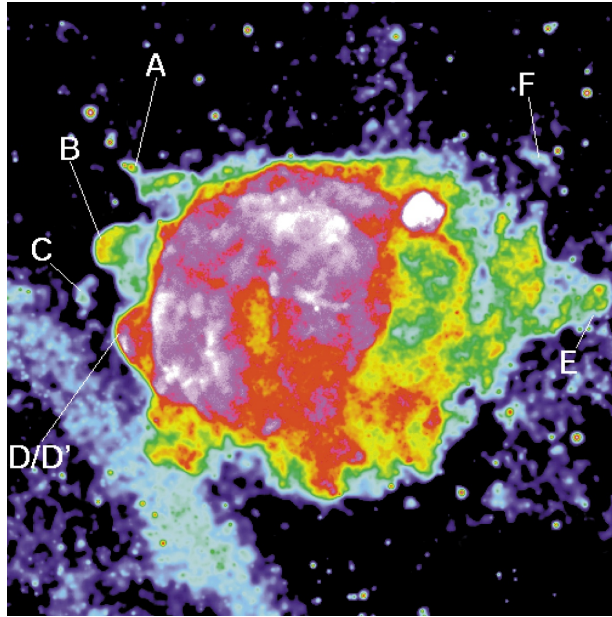


Figure 33: False color map of the Vela SNR as observed in X-rays with *ROSAT* (Aschenbach et al., 1995). The figure points out the location of the “shrapnels” and their designations. (Source: Max-Planck-Institut für extraterrestrische Physik (<http://www.mpe.mpg.de>).

the clouds (see also Kahn et al., 1985); this plasma could be heated by thermal conduction from the hot intercloud medium, but may otherwise cool by radiation and thermal conduction with the cool cloud cores. The cloud cores have a moderately high densities of $n \approx 5 \text{ cm}^{-3}$.

10.2 Enhanced metal abundances mature SNRs

One striking result of imaging X-ray spectroscopy of mature SNRs has been the identification of metal-rich plasmas even within mature SNRs. In Sect. 8 and Sect. 9.1 a few mature SNRs were mentioned that could be identified as Type Ia (e.g. Dem L71) or core collapse/oxygen-rich SNRs (e.g. N132D and Puppis A) based on their abundances. However, even older SNRs such as Vela and the Cygnus Loop have regions with high metal abundances.

Despite its large angular size, a significant fraction of the Cygnus Loop has now been mapped with *Suzaku* and *XMM-Newton* CCD-detectors (Uchida et al., 2009). This has revealed that metal-rich plasma is associated with the low surface brightness interior of the SNR, which has a temperature that is considerably hotter ($kT \approx 0.6 \text{ keV}$, Tsunemi et al., 2007) than the bright shell ($kT \approx 0.2 \text{ keV}$). Even within this hotter region there is some variation in abundance patterns, with O, Ne, and Mg, more abundant in the outer regions, and Si, S, and Fe more abundant in the central region (Fig. 34, Tsunemi et al., 2007; Uchida et al., 2008). Recently also the detection of Ar lines was reported, indicating high Ar abundances (8-9 times solar, Uchida et al., 2011). This suggests a layered explosion, with the more massive elements situated in the center. This is in contrast to Cas A, for which the Fe-rich ejecta has

(partially) overtaken the Si-rich ejecta (Sect. 9.1).

The overall abundance pattern of the inside of the Cygnus Loop is consistent with that expected from a core collapse supernova with an initial progenitor mass of $M \approx 15 M_{\odot}$, but with 5-10 times more Fe than predicted by supernova explosion models (Tsunemi et al., 2007). As noted in Sect. 2 the predicted Fe yield has considerable uncertainty. The idea that the Cygnus Loop progenitor was not a very massive star ($M > 20 M_{\odot}$) is also consistent with the radius of the stellar wind bubble of 13 pc, which is more in line with an early type B-star than with an early type O-star (Chevalier, 1990).

It is tempting to speculate that the more layered metallicity structure of the Cygnus Loop, as opposed to the more radially mixed metallicity of Cas A, has to do with the different progenitor types. The Cygnus Loop progenitor, with its relatively low initial mass, probably exploded as a red supergiant, but may still have had a significant fraction of the hydrogen envelope at the time of explosion. The Cas A progenitor was almost completely stripped of its hydrogen envelope at the time of explosion (Sect. 9.1), which made it perhaps easier for convective motions inside the supernova explosion to affect the layering of the ejecta. Indeed the simulations of Kifonidis et al. (2003) show a qualitative difference in core ejecta velocities between Type II and Type Ib (i.e. stripped progenitor) supernovae.

The metal-rich plasma in the Vela SNR is not associated with the interior, but rather with a number of protruding plasma clouds, usually referred to as the Vela “bullets” or “shrapnels” (Fig. 33, Aschenbach et al., 1995; Strom et al., 1995). The name shrapnels is justified by their high abundances (Tsunemi et al., 1999), which indeed suggest that the clouds consist of supernova ejecta. Although it is not

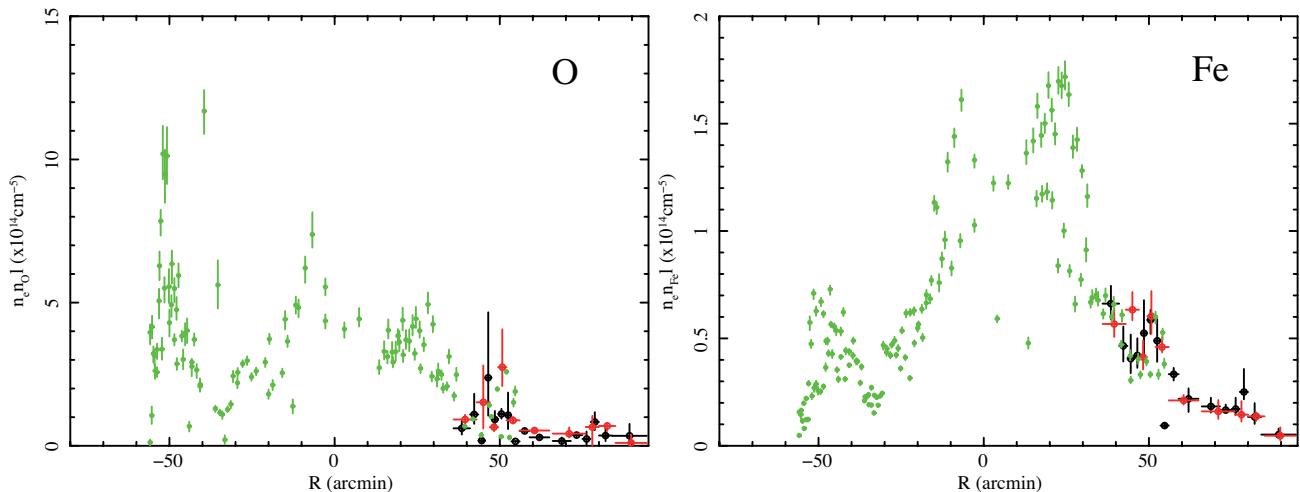


Figure 34: The emission pattern of oxygen (left) and iron line emission (right) from the Cygnus Loop as a function of position within the SNR, following a track from roughly northeast to southwest. The green symbols are taken from Tsunemi et al. (2007) and black and red points were determined by Uchida et al. (2008). (Figure from Uchida et al., 2008)

clear whether this also means that the clouds were ejected as such by the supernova, or whether they were formed due to some hydrodynamical instabilities at the contact discontinuity in the early SNR phase. The morphology of the SNRs are suggestive of clouds surrounded by bowshocks, whose opening angles indicate Mach numbers $M \approx 3 - 4$. For the hot, tenuous environment of the Vela SNR ($n \sim 0.01 \text{ cm}^{-3}$ Strom et al., 1995), this corresponds to velocities of $V \approx 300 - 700 \text{ km s}^{-1}$. The average shrapnel densities are $n_e \approx 0.1 - 1 \text{ cm}^{-3}$ with masses for shrapnel A and D of, respectively, $0.005 M_{\odot}$ and $0.1 M_{\odot}$ (Katsuda and Tsunemi, 2005, 2006).

Given their projected distance from the main shell of $\sim 1^{\circ}$, corresponding to $l \approx 5 \text{ pc}$, the shrapnels must have survived passage through the hot bubble for quite some time. Even for a mean average velocity difference between shock and shrapnels of $\Delta v \approx 1000 \text{ km s}^{-1}$, the travel time is $t_{\text{trav}} \sim l/\Delta v \sim 5000 \text{ yr}$. This should be compared to the typical cloud-crushing time t_{cc} (Klein et al., 1994):

$$t_{\text{cc}} = \frac{\chi^{1/2} R}{v_b} = 980 \left(\frac{\chi}{100} \right)^{1/2} \left(\frac{v_b}{1000 \text{ km s}^{-1}} \right)^{-1} \left(\frac{R}{1 \text{ pc}} \right) \text{ yr}, \quad (55)$$

with χ the density contrast between the shrapnel and its ambient medium. Comparison of these time scales, assuming $v_b \sim \Delta v$, shows that the apparent survival of the shrapnels indicates that the density contrast between the shrapnels and the ambient medium must be high $\chi \sim 1000$. A higher average velocity does not help, as it lowers both the travel time and the destruction time. A higher density contrast could either mean that the initial density of the knots was higher than it is now, or that the ambient density is lower, $\sim 0.001 \text{ cm}^{-3}$. Either way, the Vela shrapnels may owe their survival to the low density of the ambient medium and a fortuitous timing concerning the phase in which we happen to observe the Vela SNR. There is some morphological evidence for hydrodynamical instabilities

occurring in shrapnel D (Katsuda and Tsunemi, 2005), which will lead to the destruction of this cloud.

As already indicated, imaging spectroscopy with *ASCA* (Tsunemi et al., 1999), *Chandra* (Miyata et al., 2001), and *XMM-Newton* (Katsuda and Tsunemi, 2005, 2006) have shown that the clouds represent supernova ejecta. These studies also indicate that the shrapnels originate from different layers inside the supernova, with Shrapnel A being more rich in the oxygen-burning product Si, and shrapnel D more rich in Ne and the carbon-burning products O, Ne, Mg (with enhanced abundances by a factor 5-10 with respect to solar). The shrapnels are apparent due to their projected distance from the Vela SNR. However, more shrapnels may be projected unto the main SNR shell. Indeed, Miceli et al. (2008) found various regions observed by *XMM-Newton* that have overabundances of O, Ne, Mg and Fe, which may be either indicative of other shrapnels, or which may be regions containing the remains of destroyed shrapnels.

10.3 Mixed-morphology supernova remnants

Among the mature SNRs, one class of objects sticks out: the mixed-morphology (or thermal-composite) SNRs (Sect. 3). They are characterized by centrally dominated, thermal X-ray emission, whereas their radio morphology is shell-like. But apart from the curious radio/X-ray morphology they have a number of other characteristics in common (e.g. Cox et al., 1999). They tend to be older SNRs ($\gtrsim 20,000 \text{ yr}$) and are associated with the denser parts of the ISM. Many of them are associated with OH masers, which is an indication of interactions between the SNR shocks and molecular clouds (e.g. Claussen et al., 1997; Frail and Mitchell, 1998, Table 4). Several of them are also sources of GeV and even TeV γ -ray emission (Ta-

ble 4), which likely arises from cosmic ray *nuclei*²⁹ interacting with dense gas in the SNR shell, or from escaping cosmic rays interacting with unshocked parts of molecular clouds. These interactions produce pions, of which the neutral pions decay into γ -ray photons. Finally, imaging X-ray spectroscopy of mixed-morphology SNRs shows that their X-ray emitting plasmas have more or less homogeneous temperatures.

The morphology of these SNRs is difficult to explain with standard SNR evolution models (Sect. 4). There have been several models to explain both the centrally enhanced X-ray emission, which contrasts with their shell-type radio appearances (Fig. 4d). The model of White and Long (1991) assumes that the central thermal emission is caused by dense cloudlets that have survived the passage of the forward shock, but are slowly evaporating inside the hot medium due to saturated thermal conduction. They found a self-similar analytical model for the evolution of thermal-composite SNRs, which in addition to the Sedov solutions (Sect. 4) has two additional parameters, namely C , the ratio between the mass in the clouds and the mass in the intercloud medium, and τ , the ratio between the evaporation time of the clouds and the SNR age.

An alternative model proposed by Cox et al. (1999) concentrates on the contrast between the radio and X-ray morphology. According to their model the SNRs evolve inside medium density CSM. The forward shock has decelerated to velocities below $\sim 200 \text{ km s}^{-1}$, resulting in a strongly cooling shell that is too cool to emit X-ray emission. Because the shocks are radiative, the shock compression factors are large, giving rise to strongly compressed magnetic fields, and enhanced cosmic-ray electron densities. As a result the radio synchrotron emission from the shells is strongly enhanced.³⁰ The electrons are either accelerated by the SNR, or are simply ambient relativistic electrons swept up by the radiative shock. The X-ray emission from the interior has a homogeneous temperature due to thermal conduction (Cui and Cox, 1992) and turbulent mixing (Shelton et al., 2004a). Numerical hydrodynamical models based on the model of Cox et al. (1999) indeed show centrally enhanced X-ray morphologies (Shelton et al., 1999; Velázquez et al., 2004).

Although the nature of mixed-morphology SNRs is still debated, there has been considerable progress in our knowledge of them over the last ten years. Shelton et al. (2004b) showed that SNR G65.2+5.7, which is clearly in the radiative evolutionary stage³¹, shows an X-ray filled

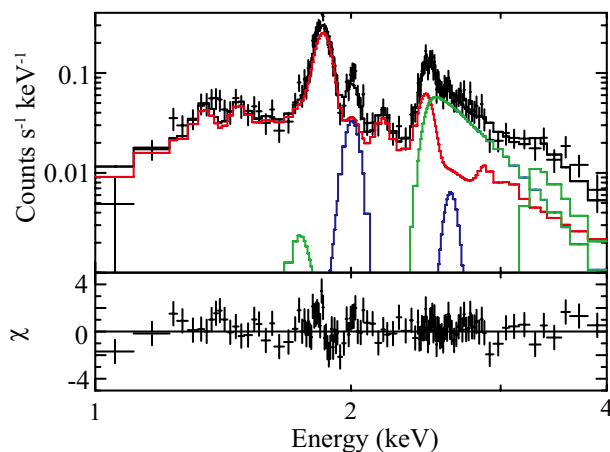


Figure 35: Suzaku SIS spectrum of G359.1-05 (Ohnishi et al., 2011), showing in green the Si and S Ly α line and in blue the radiative-recombination continua.

morphology. Due to the low absorption column toward this SNR, *ROSAT* was also able to reveal a shell-like outer part in X-ray emission below 0.3 keV. These two characteristics are in qualitative agreement with the explanation for mixed-morphology remnants by Cox et al. (1999).

Due to progress in X-ray imaging spectroscopy over the last 15 years, several other clues about the nature of mixed-morphology SNRs have appeared. Many of the mixed-morphology SNRs show evidence for metal-rich plasmas in the interior: Lazendic and Slane (2006) list 10 out of a sample of 23 thermal-composite SNRs with enhanced abundances. Examples are W44 (Shelton et al., 2004a), HB 21, CTB 1 and HB 3 (Lazendic and Slane, 2006; Pannuti et al., 2010b), IC 433 (Troja et al., 2008) and Kes 27 (Chen et al., 2008). Kawasaki et al. (2005) noted another feature that may be generic for this class of SNRs: their ionization state is close to ionization equilibrium (Sect. 6.1.2), unlike young SNRs and old SNRs like the Cygnus Loop. Moreover, the thermal-composite SNRs IC 443 (Kawasaki et al., 2002; Yamaguchi et al., 2009), W49B (Ozawa et al., 2009)³², and G359.1-0.5 (Ohnishi et al., 2011) show signs of overionization, in the form of radiative-recombination continua (RRCs, Sect. 6.1.2) associated with metals like Si, S, and Fe (Fig. 35).

It is not clear whether metal-richness is a generic feature of mixed-morphology SNRs, but it seems at least to be a common feature. There are several ways in which metal-richness helps to explain the characteristics of thermal-composite SNRs. Firstly, the uniform temperatures in their interiors are often attributed to thermal conduction (e.g. Cox et al., 1999). A problem for this explanation is that magnetic fields limit thermal conduction across field lines (Sect. 5.4). However, if the interiors consist predominantly

²⁹As opposed to electrons. See also the discussion in Sect. 11.2

³⁰This explanation for synchrotron emission from SNRs is called the Van der Laan mechanism (van der Laan, 1962). Uchiyama and Aharonian (2008) recently proposed that the radio emission may be additionally enhanced by the presence of secondary electrons/positrons, i.e. the electrons/positrons products left over from the decay of charged pions, created due to cosmic ray nuclei colliding with the background plasma. The presence of secondary electrons/positrons may also explain the flat spectral radio indices α_R in Table 4. Finally, Bykov et al. (2000) discusses the possibility of electron acceleration by magnetohydrodynamic turbulence behind high density shocks.

³¹See for example the well defined shell in optical [OIII] emission (Boumis et al., 2004)

³²W49B is a young ejecta dominated SNR, and it is not clear whether it belongs to the class of thermal-composite SNRs. However, apart from its age it has three characteristics of thermal-composite SNRs: a high ambient density, centrally enhanced X-ray emission (Rho and Petre, 1998), and γ -ray emission (Abdo et al., 2010d).

Table 4: Mixed morphology SNRs.

SNR	Name	Size	F_R	α_R	Dist	Enh. metals	RRC	GeV	TeV	OH Maser
		arcmin	Jy		kpc					
G0.0+0.0	Sgr A East	3.5×2.5	100?	0.8?	8	X		?	?	X (v)
G6.40.1	W28	48	310	0.3	1.9			X (c)	X (g)	X (n)
G31.9+0.0	3C391	7×5	24	0.49	8.5			X (k)		X (n)
G33.6+0.1	Kes 79	10	22	0.5	7.8					
G34.70.4	W44	35×27	230	0.37		X		X (e)		X (n)
G41.10.3	3C397	4.5×2.5	22	0.48	7.5	X				
G43.30.2	W49B	4	38	0.48	10	X	X (s)	X (d)	X (j)	
G49.20.7	W51C	30	160	0.3	6			X (a)	X (y)	X (o)
G53.62.2	3C400.2	33×28	8	0.75	2.8					
G65.3+5.7	G65.3+5.7	310×240	52?	0.6?	0.8					
G82.2+5.0	W63	95×65	120	0.35		X				
G89.0+4.7	HB21	120×90	220	0.48	0.8	X				
G93.70.2	CTB 104A	80	65	0.65	1.5					
G116.9+0.2	CTB1	34	8	0.61		X				
G132.7+1.3	HB3	80	45	0.6	2.2	X		X (b)?		
G156.2+5.7	G156.2+5.7	110	5	0.5		X				
G160.9+2.6	HB9	140×120	110	0.64	< 4					
G166.0+4.3	VRO 42.05.01	55×35	7	0.37	4.5	X (i)				
G189.1+3.0	IC 443	45	160	0.36	1	X (i)	X (x)	X (f)	X (h)	X (m)
G272.2-3.2	G272.2-3.2	15?	0.4	0.6	2?	X (t)?				
G290.1-0.8	MSH 11-61A	19×14	42	0.4	7	X		X (b)?		
G327.4+0.4	Kes 27	21	30	0.5	5	X (l)				
G357.1-0.1	Tornado	8×3	37	0.4	> 8					
G359.1-0.5	G359.1-0.5	24	14	0.4		X	X (r)			X (q)

This list is based on the list by Lazendic and Slane (2006). Sizes, distances, and radio properties (radio flux F_R , and spectral index α_R) were obtained from Green D. A., 2009, "A Catalogue of Galactic Supernova Remnants (2009 March version)", Astrophysics Group, Cavendish Laboratory, Cambridge, United Kingdom (available at <http://www.mrao.cam.ac.uk/surveys/snrns/>). The column names indicate: Enh. metals, the presence of plasma with overabundances (Lazendic and Slane, 2006, unless indicated otherwise); RRC, the presence of radiative recombination line continua; GeV, the detection in the GeV band (*Fermi*); TeV the detection of associated sources in the TeV band with Cherenkov telescopes; OH Maser, the detection of associated OH masers. The letters in parentheses refer to the following references:

a) Abdo et al. (2009); b) Abdo et al. (2010a); c) Abdo et al. (2010b); d) Abdo et al. (2010d); e) Abdo et al. (2010e); f) Abdo et al. (2010f); g) Aharonian et al. (2008b); h) Albert et al. (2007a); i) Bocchino et al. (2009); j) Brun et al. (2011); k) Castro and Slane (2010); l) Chen et al. (2008) m) Claussen et al. (1997); n) Frail et al. (1996) ; o) Green et al. (1997) p) Koralesky et al. (1998a); q) Lazendic et al. (2002); r) Ohnishi et al. (2011); s) Ozawa et al. (2009); t) Park et al. (2009); u) Yusef-Zadeh et al. (1995); v) Yusef-Zadeh et al. (1996); w) Yusef-Zadeh et al. (1999); x) Yamaguchi et al. (2009); y) Feinstein et al. (2009); Krause et al. (2011).

of supernova ejecta, then the magnetic fields may be very low, simply because the stellar magnetic field has been diluted by the expansion. Magnetic flux conservation gives $B = B_*(R_*/R)^2$, with R_* the stellar radius, and R the radius of the SNR interior. Taking typical values of $R_* \approx 10^{13}$ cm, $R \approx 10^{20}$ cm, $B_* = 1$ G, shows that the interior magnetic field may be as low as 10^{-14} G, approaching the value where conduction across field lines becomes comparable to conduction along field lines. Hence, the conditions are optimal for thermal conduction, but only up to the boundary between ejecta dominated and swept-up matter, where Rayleigh-Taylor instabilities at the contact discontinuity may have enhanced the magnetic-field strengths and may have made the magnetic fields more tangled, preventing strong thermal conduction across the contact discontinuity.

Secondly, metal-rich plasma emits more X-ray emission, further increasing the contrast in X-ray emission between metal-rich interior and the cool shell of swept-up matter. An important additional aspect to consider here is whether the interiors consist of enhanced metal abundances, i.e. a mix of ejecta and swept-up matter, or of pure ejecta. For SNR W49B, a rather young member of the mixed-morphology class, a pure metal abundance seems likely, but for older SNRs the plasma is probably best described by hydrogen/helium dominated plasma with enhanced abundances. One can illustrate the key features of the cool-shell/hot-interior scenario for mixed-morphology SNRs with some simple numerical calculations, ignoring for the sake of argument the more rigorous analytical treatment of the SNR evolution by Cox et al. (1999).

Firstly, most mixed-morphology SNRs appear to be in the snowplough phase of their evolution, with $V_s < 200$ km s⁻¹, which results in cool, X-ray dim, but optical/UV bright regions immediately behind the shock front. The interior, presumably consisting of supernova ejecta, is more or less homogeneous in temperature and, because of pressure equilibrium also reasonably homogeneous in density. Given the age of the SNR and the relatively high sound speed in the interior, one can assume approximate equilibrium between the ram pressure at the forward shock and the interior (c.f. Cui and Cox, 1992). This gives:

$$n_{\text{interior}} k T_{\text{interior}} \approx \rho_0 V_s^2, \quad (56)$$

with n_{interior} the total interior plasma density. If we use the values for W44 listed by Cox et al. (1999), $V_s = 150$ km s⁻¹, $k T_{\text{interior}} = 0.6$ keV and $\rho_0 = 1.0 \times 10^{-23}$ g cm⁻³, we find a density of $n_{\text{interior}} \approx 2.3$ cm⁻³, which translates into an electron density of $n_e \approx 0.8$ cm⁻³, in rough agreement with X-ray measurements (Cox et al., 1999). W44 has a radius of $R \approx 10$ pc, for an estimated distance of 2.5 kpc, but the X-ray emitting interior has a radius of $R_{\text{interior}} \approx 6$ pc, corresponding to an interior volume of $V_{\text{interior}} \approx 2.7 \times 10^{58}$ cm⁻³. This means that the total internal energy is $U = n k T V_{\text{interior}} \approx 0.9 \times 10^{50}$ erg (about 10% of the explosion energy). The X-ray emitting mass is $M_{\text{interior}} \approx 28 M_{\odot}$; somewhat higher than the expected ejecta mass of a Type II supernova, but not too far

off, given the crudeness of the approximation. At least it suggests that a substantial fraction of the interior plasma consists of ejecta, and that the interior magnetic field may be low due to large expansion of the ejecta material, or early shocked swept-up material.

Note that if we assume that the interior consists of metals only, this does not lead to a consistent result. For example, if we assume O VII to be the dominant ion, then we have $n_{\text{OVII}} = n/8 \approx 0.29$ cm⁻³ and $M_{\text{interior}} \approx 100 M_{\odot}$. This is clearly much more oxygen than a massive star can produce. So pure metal abundances seem unlikely, although perhaps there are some regions in the interior that have unmixed ejecta. For a discussion on the metal abundances in W44, see Shelton et al. (2004a).

A SNR will reach the snowplough phase when its age is larger than $t_{\text{rad}} \approx 44,6000(E_{51}/n_H)^{1/3}$ yr. For W44 ($n_H = 6$ cm⁻³), this corresponds to $\sim 25,000$ yr. Hence, an ionization age of 4×10^{11} cm⁻³s is expected (Sect. 6.1.2). This is relatively high, but below the ionization age for ionization equilibrium (10^{12} cm⁻³s). However, the situation is more complex, as the interior density and temperature may have been higher in the past, and, therefore, the degree of ionization may be higher than indicated by the simple multiplication of the present day age and electron density. This could explain the observation by Kawasaki et al. (2005) that most mixed-morphology SNRs are near ionization equilibrium. Note that the high density in the interior of W44 and other mixed-morphology SNRs is a direct consequence of the high ISM density (Eq. 56) and the thermal conduction, which results in a more uniform interior density with medium hot temperatures, rather than very high temperatures with very low interior densities.

In the context of mixed-morphology SNRs, it is of interest to show why some old SNRs are expected to have RRCs. As noted by Ohnishi et al. (2011), one may expect RRCs whenever the plasma cools faster than the recombination time, for example due to thermal conduction (Kawasaki et al., 2002) or adiabatic expansion (Itoh and Masai, 1989; Yamaguchi et al., 2009). Yamaguchi et al. (2009) calculated that the time scale for cooling by conduction is too long, so adiabatic expansion is probably the appropriate explanation. The time scale for adiabatic expansion can be calculated from the thermodynamic relation $TV^{\gamma-1} = \text{constant}$, which means that the adiabatic cooling time scale is given by (Broersen et al., 2011):

$$\tau_{\text{ad}} = -\left(\frac{T}{\dot{T}}\right)_{\text{ad}} = -\frac{1}{1-\gamma} \frac{V}{\dot{V}} = -\frac{1}{3(1-\gamma)} \frac{R}{\dot{R}} = \frac{1}{2} \frac{R}{\dot{R}} = \frac{1}{2} \beta^{-1} t, \quad (57)$$

with β the expansion parameter (Sect. 4.2), $\gamma = 5/3$, and t the age of the SNR. For SNRs in the snowplough phase we can use $\beta = 0.25$ (Eq 8). This suggests that $\tau_{\text{ad}} \approx t/8$. For overionization to occur it is first required that the ionization age of the plasma must be large enough (otherwise there could underionization). The second condition is that the timescale for recombination is longer than the adia-

batic cooling time scale:

$$\tau_{\text{ad}} < \tau_{\text{rec}} = \frac{1}{\alpha_{\text{rec}} n_{\text{e}}}, \quad (58)$$

with α_{rec} the recombination rate. The mixed-morphology SNRs show evidence for overionization of Si XIII, for temperatures around $kT = 0.2 - 0.7$ keV. For these temperatures the recombination rate for Si XIV to Si XIII is approximately $\alpha_{\text{rec}} = 5.9 \times 10^{-14} \text{ cm}^3 \text{ s}^{-1}$ (Shull and van Steenberg, 1982). Using now that $n_{\text{e}} = 0.5 n_{\text{interior}}$ and Eq. 56 the condition for overionization in mixed-morphology SNR is:

$$t < \frac{8}{\alpha_{\text{rec}} n_{\text{e}}} = \frac{8kT_{\text{interior}}}{0.5\alpha_{\text{rec}}\rho_0 V_s^2} = \quad (59)$$

$$2 \times 10^6 n_{\text{H}}^{-1} \left(\frac{V_s}{150 \text{ km s}^{-1}} \right)^{-2} \left(\frac{kT_{\text{interior}}}{0.5 \text{ keV}} \right)$$

$$\times \left(\frac{\alpha_{\text{rec}}}{6 \times 10^{-14} \text{ cm}^3 \text{ s}^{-1}} \right)^{-1} \text{ yr},$$

with n_{H} the pre-shock density. This equation shows that overionization should be common, as most SNRs are much younger than a few million year. More important is whether the average plasma ever reached ionization equilibrium, i.e. whether $\int n_{\text{e}} dt \gtrsim 10^{12} \text{ cm}^{-3} \text{ s}$. The discovery of RRCs in mixed-morphology SNRs has been relatively recent. Given Eq. 59, one expects that many more SNRs, with relatively dense interior plasmas, should have RRCs in their X-ray spectra.

Finally, some word of caution considering the interpretation of mixed-morphology SNRs. The explanation of their properties sketched above is relatively simple, but nature is often not that simple. For example, one may ask how it comes that SNRs with maser emission, and which are interacting with molecular clouds, have densities of only $n_{\text{H}} = 5 \text{ cm}^{-3}$. This is relatively high, but not nearly as high as the dense molecular clouds usually associated with maser emission, $n_{\text{H}} > 1000 \text{ cm}^{-3}$ (Frail and Mitchell, 1998). But in fact, millimeter-wave and near infrared observations of W44 and W28 by Reach et al. (2005) reveal the presence of dense molecular gas. However, this dense gas has only a small filling factor. Reach et al. (2005) even note that some of the dense clumps may survive the shock passage, which brings us back to the scenario proposed by White and Long (1991). The interclump densities, which applies to 90% of the volume are, however, consistent with the estimates of Cox et al. (1999), $n_{\text{H}} \approx 5 \text{ cm}^{-3}$. These infrared observations show that old SNRs have a complex structure, which, for a proper understanding, requires multi-wavelength observations.

11 Shock heating and particle acceleration: observations

11.1 Electron-ion temperature equilibration

As explained in Sect. 5.3, from a theoretical point of view collisionless shocks do not naturally lead to equilibration of electron and ion temperatures in the immediate post-shock region. The degree of post-shock temperature equilibration by SNR shocks is therefore an important observational issue. Unfortunately, X-ray measurements of plasma temperatures usually refer only to the *electron* temperature, as it is the electron temperature that determines X-ray line ratios (Sect. 6.1.3), and the shape of the thermal X-ray continuum (Sect. 6.1).

A first indication that the electron temperature is not equal to proton temperature, or at least that Eq. 20 (Sect. 5.1) does not hold for young SNRs, is the fact that for young SNR no X-ray temperatures above $kT_{\text{e}} \approx 5$ keV have been reported.³³ This is in contrast to the expected temperatures for some young SNRs with high shock velocities. For example, Cas A and Tycho have shock velocities of, respectively, $V_s \approx 5100 \text{ km s}^{-1}$ (Vink et al., 1998; Koralesky et al., 1998b; Delaney and Rudnick, 2003; Patnaude and Fesen, 2009) and $V_s \approx 4000 \text{ km s}^{-1}$ (Reynoso et al., 1997; Katsuda et al., 2010a). They should, according to Eq. 20, have plasma components with $kT_{\text{e}} > 19$ keV. Even though part of the X-ray continuum of those two SNRs is due to X-ray synchrotron emission (Sect. 11.2), plasmas as hot as 20 keV should easily be detectable as they give rise to relatively flat spectra with power-law indices around 1.5. In contrast, the observed spectral indices in the 4-6 keV continuum dominated band are typically ≈ 3 (e.g. Helder and Vink, 2008). Also the hard X-ray spectra do not show signs of thermal X-ray emission from plasmas with $kT \gtrsim 5$ keV (Allen et al., 1997; Favata et al., 1997; Allen et al., 1999; Vink et al., 2001; Renaud et al., 2006b).

Apart from non-equilibration of electron-ion temperatures there may be another reason for the low electron temperatures in young SNRs: non-linear cosmic-ray acceleration may be so efficient that the overall plasma temperatures are very low (Sect. 5.1, Drury et al., 2009; Helder et al., 2009; Vink et al., 2010).

In order to estimate the *proton* or *ion* temperature, as opposed to the electron temperature, one needs to measure the thermal Doppler broadening. Thermal Doppler broadening gives rise to a Gaussian line profile with line width³⁴:

$$\sigma_{\text{E}} = \left(\frac{E_0}{c} \right) \sqrt{\left(\frac{kT_{\text{i}}}{m_{\text{i}}} \right)}. \quad (60)$$

³³ One of the highest temperatures reported is $kT_{\text{e}} = 4.3$ keV for the SNR IC 131 in M33 (Tüllmann et al., 2009).

³⁴ The lack of a factor 2 in the equation may be confusing. Note that Rybicki and Lightman (1979) show that the profile is proportional to $\exp[-m_{\text{i}}c^2(E - E_0)^2/(2E_0kT_{\text{i}})]$. Comparing this to a gaussian $\exp[-(x - x_0)^2/(2\sigma^2)]$ shows the correctness of Eq. 60.

The line width is often given in terms of Doppler velocities, in which case $\sigma_v = \sqrt{kT_i/m_i}$. In order to measure the thermal Doppler broadening one best uses a spectrum of a region that is expected to be devoid of bulk line of sight motions. This is expected at the edges of SNRs, where the expansion of the shell only results in velocities in the plane of the sky.

Most measurements of thermal Doppler broadening are based on optical and UV observations of Balmer and Lyman lines of hydrogen. A comprehensive list of these measurements is given by Ghavamian et al. (2007). Balmer and Lyman emission lines from SNR shocks require that the shocks move through (partially) neutral gas. As the neutral hydrogen penetrates the shock heated region the neutral atom may get excited, giving rise to narrow line emission in the optical/UV. In addition to excitations also charge transfer reactions may occur, i.e. a shock heated proton may pick up an electron from a neutral particle. This process gives rise to thermally broadened Balmer or Lyman line emission (e.g. Chevalier et al., 1980; Heng, 2010) from which the hydrogen temperature immediately behind the shock can be measured (van Adelsberg et al., 2008). The ratio between the narrow and broad line emission is a function of shock velocity and the degree of electron-proton temperature equilibration.

Ghavamian et al. (2007) presented evidence that for low shock velocities the proton and electron temperatures are equilibrated, whereas for shock speeds above $\sim 500 \text{ km s}^{-1}$ the temperatures become increasingly non-equilibrated, with a rough dependency of $T_e/T_p \propto 1/V_s^2$. The work by van Adelsberg et al. (2008) and Helder et al. (2011) does not corroborate the dependency, but does confirm that slow shocks produce thermally equilibrated plasmas, whereas fast shocks do, in general, not. Note that the work of Helder et al. (2011), and earlier work of Rakowski et al. (2003), is based on electron temperatures measured using X-ray spectroscopy, whereas proton temperatures were measured from broad $H\alpha$ line emission. Helder et al. (2011) used the SNR RCW 86, which has large density and shock velocity contrasts (Vink, 2006; Helder et al., 2009), and may be efficient in accelerating cosmic rays (Helder et al., 2009; Aharonian et al., 2009). Rakowski et al. (2003) measured temperature equilibration in the LMC SNR DEM L71 with inferred shock velocities of 500-1000 km s^{-1} . For DEM L71 the $T_e/T_p \propto 1/V_s^2$ relation seems to be valid.

In addition to the hydrogen lines, also lines from other ions can be used to measure ion temperatures. A noteworthy example is the UV line emission from the north-western region of SN 1006 as measured by the *Hopkinson Ultraviolet Telescope (HUT)*, which shows that the lines from H I, He II, C IV, N V, and O VI all have the same width of $\sim 2300 \text{ km s}^{-1}$ (FWHM Raymond et al., 1995). This indicates that the ions are not equilibrated, since there is no dependency of the line width on the mass of the ion (see Eq. 60).

Thermal Doppler broadening measurements in X-rays are rare, as one needs high resolution spectroscopy of a

region very close to the shock front, and the current grating spectrometers do not easily allow to isolate particular regions of an extended object. But Vink et al. (2003) measured the line broadening of the O VII $\text{He}\alpha$ line emission from a bright knot that stands out at the northeastern rim of SN 1006. The size of the knot is approximately $1'$. This measurement was possible for SN1006, because this remnant is rather large for a young SNR ($30'$). As a result only a small amount of the overall X-ray emission from the rest of the SNR is contaminating the *XMM-Newton* RGS spectrum. The expected line profile for a narrow line consists of a sharp rise, as for a normal point source, but it has a long tail, caused by emission from the interior of SN 1006 (Fig. 36). The shape of the short wavelength side of the line profile is, therefore, sensitive to the thermal line broadening. Vink et al. (2003) reported a line profile with a width of $\sigma = 3.4 \pm 0.5 \text{ eV}$, corresponding to $\sigma_v = 1777 \text{ km s}^{-1}$. Using Eq. 60, this translates into a temperature for O VII of $kT_{\text{OVII}} = 528 \pm 150 \text{ keV}$. This seems extremely hot, but using Eq. 20, with $m_i = 16m_p$ instead of μm_p , shows that it corresponds to a shock velocity of $\sim 4000 \text{ km s}^{-1}$, provided that oxygen has not been equilibrated with protons. The high O VII temperature should be compared to the electron temperature as measured with the EPIC instruments on board *XMM-Newton*, $kT_e \approx 1.5 \text{ keV}$. This is a clear indication that in this electrons and oxygen ions are not equilibrated.

The nature of the X-ray emitting knot in SN 1006 is not quite clear. It seems to have enhanced O and Si abundances, and may therefore be an ejecta knot, in which case it was heated by the reverse shock. Another important issue is whether non-thermal components, such as accelerated particles may have influenced the thermal balance of the shock, as discussed in Sect. 5.1. The northeastern part of SN 1006 seems, in that sense, a relatively good place to measure equilibration processes in the absence of cosmic rays, as this region shows no evidence for X-ray synchrotron emission (see also Sect. 11.2).

Although the RGS observations of SN 1006 are perhaps the most direct measurements of thermal Doppler broadening in X-rays, thermal Doppler broadening is important to take into account when using the overall line broadening of SNRs. An example is the Doppler line broadening of LMC SNRs like 0509-67.5 (Kosenko et al., 2008) and 0519-69.0 (Kosenko et al., 2010) as measured with the *XMM-Newton* RGS. Thermal line broadening may even affect the line width as measured with CCD instruments. Furuzawa et al. (2009) reported that Fe-K line broadening of X-ray line emission from Tycho's SNR, and its spatial distribution, cannot be easily modeled with bulk velocities alone, but that thermal Doppler broadening is needed as well. From this they infer an iron temperature of $(1-3)10^{10} \text{ K}$ (860-2600 keV)! So there are several pieces of evidence that electrons and ions may indeed have different temperatures. In X-rays, however, the evidence seems at the moment to pertain to plasma heated by the *reverse* shock. The evidence for non-equilibration of temperatures of plasma heated by the forward shock is mostly based on

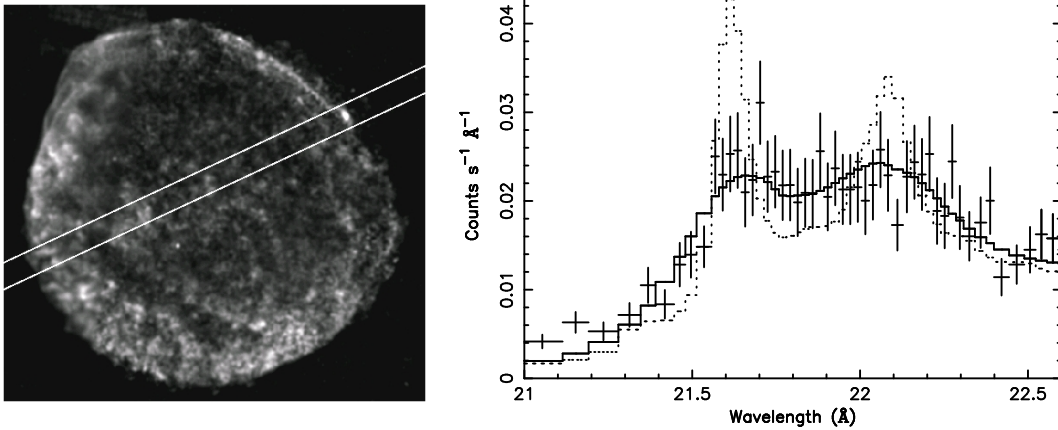


Figure 36: Left: Map of O VII emission made from several *Chandra*-ACIS observations (see also Fig. 37). The lines indicate the region observed by the *XMM-Newton* RGS instrument. The target was the bright knot in the northeast inside the RGS region. Right: Detail of the RGS1 spectrum of the northeastern knot, showing O VII He α line emission. The dotted line is the best fit model without line broadening, whereas the solid line shows the model including thermal line broadening (adapted from Vink et al., 2003).

H α measurements. For these measurements the amount of equilibration is based on the narrow to broad line flux ratio, but the interpretation is model dependent and does not always give consistent results (van Adelsberg et al., 2008). Moreover, current models do not take into account the effects of cosmic-ray precursor physics, which is likely important for the correct interpretation of the line ratios (van Adelsberg et al., 2008; Rakowski et al., 2008; Helder et al., 2011; Raymond et al., 2011).

It could be that the dichotomy between equilibrated shocks below 500 km s^{-1} , and unequilibrated shocks above 500 km s^{-1} , is somehow related to cosmic-ray acceleration, possibly due to an increased role of plasma waves (e.g. Rakowski et al., 2008). However, this different equilibration behavior between slow and fast shocks may also have another origin: as pointed out by Bykov (2004), electrons have thermal velocities larger than the shock velocity for Mach numbers $M < \sqrt{m_p/m_e} = 43$. The velocity with which the electrons are therefore scattered behind the shock is largely determined by the pre-shock temperature rather than by the shock velocity. This may lead to additional electron heating mechanisms. A Mach number of ~ 43 corresponds, for a typical sound speed of 10 km s^{-1} , to a shock velocity of 400 km s^{-1} . Interestingly, low Mach numbers may also occur for high shock speeds in the presence of cosmic rays. This happens when the cosmic-ray precursor significantly preheats the incoming plasma. The different equilibration properties of the TeV source RCW 86 (Helder et al., 2011) and DEM L71 (Rakowski et al., 2003) may be explained by the more prominent role of cosmic-ray acceleration in RCW 86. This is suggestive of an intimate relation between cosmic-ray acceleration and temperature equilibration at the shock.

In the future, with the availability of microcalorimeter spectrometers on *Astro-H* and *IXO*, it will be possible to routinely obtain line broadening measurements from re-

gions close to SNR shock fronts. The advantage that X-ray measurements have over H α measurements is that no neutral hydrogen is needed upstream of the shock. Right now the sample of young SNRs with thermal Doppler broadening measurements is skewed toward Type Ia SNRs, as they seem to be more likely to have H α emission from the shock region (Sect. 8). The problem with this is that the presence of a large fraction of neutral atoms may dampen Alfvén waves. This may result in different shock-heating properties and may also quench efficient cosmic-ray acceleration (Drury et al., 1996). X-ray measurements of ion temperature, therefore, provides a more unbiased probe of shock-heating properties. The disadvantage is that on average the X-ray emission comes from further behind the shock front than H α emission.

High resolution X-ray spectroscopy may also be used to gather information on the post-shock equilibration process itself, because different plasma ionization ages should also correspond to different degrees of equilibration (i.e. full/partial non-equilibration and equilibration, see Sect. 5.2).

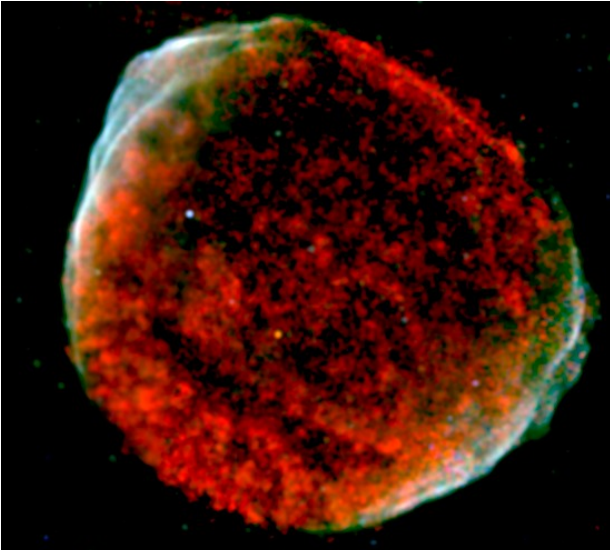


Figure 37: *Chandra* image of SN 1006 based on a mosaic of several observations. The three colors correspond to the 0.5-0.6 keV band (O VII He- α , red), 1-1.7 keV (continuum with some Mg XI emission, green), and 2-5 keV (continuum dominated, blue). SN 1006 was the first SNR for which imaging spectroscopy with the *ASCA* showed a clear spatial separation of continuum emission, identified as synchrotron emission mostly from near the rims of the SNR, and thermal emission (dominated by O VII), which dominates the emission from the interior (Koyama et al., 1995).

11.2 X-ray synchrotron emitting filaments

Although SNRs are thought to be the main sources of Galactic cosmic rays (Sect. 5.5), until 1995 the observational evidence for this consisted mostly of the detection of radio synchrotron radiation from SNRs. The electrons responsible for radio emission have energies in the GeV range. So radio synchrotron radiation informs us that SNRs can accelerate electrons, but does not prove that they can accelerate particles to energies comparable to the “knee” in the cosmic ray spectrum ($\sim 3 \times 10^{15}$ eV).

In 1995 it was for the first time convincingly demonstrated that a SNR, SN 1006, emitted X-ray synchrotron radiation (Koyama et al., 1995). That the X-ray spectrum of this source was unusual was already clear from observations with the solid-state spectrometer on board the *Einstein* X-ray observatory (Becker et al., 1980). The spectrum appeared featureless, and was completely different from the line-rich X-ray spectra of a young SNRs like Tycho or Cas A. This was interpreted by Reynolds and Chevalier (1981) as the result of synchrotron emission from shock accelerated electrons. However, Hamilton et al. (1986) proposed an ingenious interpretation in which most of the emission was coming from carbon-rich, shocked ejecta, which would provide a large thermal bremsstrahlung emissivity (Eq. 43) without much line radiation in the 0.5-7 keV range. The case for X-ray

synchrotron radiation by Koyama et al. (1995) was settled thanks to the spectral-imaging capabilities of *ASCA*, which established that thermal radiation was being emitted from all over the face of SN 1006, but that the thermal emission was overwhelmed by non-thermal continuum emission coming from two regions close to the forward shock (Fig. 37). This had important consequences for the idea that SNRs can accelerate particles, as X-ray synchrotron emission implies that electrons are accelerated up to energies of 10 – 100 TeV. This requires rather small diffusion coefficients (see Eq. 52 for the loss-limited case). If indeed maximum electron energies are limited by radiative losses, then ions can in principle be accelerated to even higher energies, possibly even beyond 10^{15} eV. But the X-ray synchrotron radiation does not prove that this is the case.

Around the same time that X-ray synchrotron radiation from SN 1006 was established non-thermal hard X-ray emission was detected from the young SNR Cas A by the *CGRO*-OSSE (The et al., 1996), *RXTE*-HEXTE (Allen et al., 1997) and *Beppo-SAX*-PDF (Favata et al., 1997) instruments. This hard X-ray emission is likely caused by synchrotron radiation as well, although other explanations have been proposed (e.g. Allen et al., 1997; Vink et al., 1999; Laming, 2001a; Vink, 2008b; Helder and Vink, 2008). Moreover, *ASCA* observations also established that two newly discovered SNRs RX J1713.7-3946 (G347.3-0.5, Pfeffermann and Aschenbach, 1996) and RX J0852.0-4622 (G266.2-1.2, Aschenbach, 1998) were similar to SN 1006 in that their X-ray emission was completely dominated by synchrotron emission (Koyama et al., 1997; Slane et al., 1999, 2001). In fact, no thermal X-ray emission from these SNRs has yet been detected (e.g. Hiraga et al., 2005; Acero et al., 2009; Slane et al., 2001; Pannuti et al., 2010a).

The spatial resolution of *Chandra* helped to establish that not only rather large SNRs are source of X-ray synchrotron radiation (SN 1006, RX J1713.7-3946, and RX J0852.0-4622 are all larger than $30'$). Also Cas A (Gotthelf et al., 2001), Tycho (Hwang et al., 2002) and Kepler (Reynolds et al., 2007) have regions close to the shock front that are continuum dominated. These regions are, however, very thin ($1-2''$). It was soon shown that the narrowness of these filaments must be the result of relatively large magnetic fields ($\sim 100 - 600 \mu\text{G}$, Vink and Laming, 2003; Berezhko et al., 2003; Bamba et al., 2004, 2005; Völk et al., 2005; Ballet, 2006; Parizot et al., 2006).

Vink and Laming (2003) determined a high magnetic field for Cas A by assuming the width of the filament is determined by the radiative loss time of X-ray synchrotron emitting electrons. As the plasma is advected away from the shock front, a radiative loss time also corresponds to a physical length scale. The plasma velocity with respect to the shock front is given by $v_2 = V_s/\chi$ (c.f. Eq. 12), whereas the synchrotron loss time is given by Eq. 49. The synchrotron loss time, therefore, corresponds to an advect-

tion length scale of

$$l_{\text{adv}} = v_2 \tau_{\text{syn}} = \frac{V_s \tau_{\text{syn}}}{\chi}. \quad (61)$$

Since τ_{syn} depends on both the magnetic field and electron energy ($\tau_{\text{syn}} \propto B^{-2} E^{-1}$), one needs additional information to determine B and E separately. For that one can use the dependence of the typical photon energy on the magnetic-field strength and electron energy ($\propto E^2 B$, Eq. 47). This is graphically depicted in Fig. 38, showing that for Cas A $B \sim 100 \mu\text{G}$ near the shock front. This method is not the only way to determine the magnetic field. One can also assume that the width of the synchrotron emitting filaments are equal to the diffusion length scale ($l_{\text{diff}} \propto B^{-1} E$, Eq. 42) appropriate for the energies of the synchrotron emitting electrons (Berezhko et al., 2003).

Both methods give roughly the same magnetic-field estimates (Ballet, 2006). In principle, the X-ray synchrotron rims should be always wider than, or comparable to, the diffusion length scale, as this is the width of the region from which electrons are actively being accelerated (indicated by the shaded region in Fig. 38b). But the diffusion length scale is always comparable to the advection length scale for electrons with energies close to the maximum energy (Parizot et al., 2006; Vink et al., 2006). This is easily demonstrated using the basic condition for determining the maximum electron energy, i.e. the acceleration time equals the synchrotron cooling time, $\tau_{\text{acc}} \approx \tau_{\text{syn}}$ (Eq. 51). The acceleration time scale is within an order of magnitude given by $\tau_{\text{acc}} \approx D/v_2^2$ (c.f. Eq. 41). Using Eq. 61 one can rewrite the condition for reaching the maximum electron energy, $\tau_{\text{acc}} \approx \tau_{\text{syn}}$, in $\tau_{\text{acc}} \approx l_{\text{adv}}/v_2$. Eq. 42 shows that $l_{\text{diff}} \approx D/v_2 \approx \tau_{\text{acc}} v_2$. Hence, the condition $\tau_{\text{acc}} \approx \tau_{\text{syn}}$ also implies $l_{\text{diff}} \approx l_{\text{adv}}$.

By combining Eq. 49 and Eq. 51 one obtains a relation between the typical width of the X-ray synchrotron emitting region, assumed to be l_{adv} , and the magnetic-field strength, under the assumption that we observe synchrotron emission from electrons near the cut-off energy (c.f. Parizot et al., 2006; Vink et al., 2006):

$$B_2 \approx 26 \left(\frac{l_{\text{adv}}}{1.0 \times 10^{18} \text{cm}} \right)^{-2/3} \eta^{1/3} \left(\chi_4 - \frac{1}{4} \right)^{-1/3} \mu\text{G}, \quad (62)$$

with B_2 the average magnetic field in the shocked plasma, χ_4 the total shock compression ratio in units of 4, and η as defined in Eq. 39. Note that this magnetic field estimate is independent of the shock velocity and depends only weakly on the shock compression ratio and η . Since the actual width is determined by a combination of diffusion and advection the actual observed width is larger than either l_{adv} or l_{diff} , and one can take $l_{\text{obs}} \approx \sqrt{2} l_{\text{adv}}$.

It is worth mentioning that not all X-ray synchrotron radiation may come from loss-limited spectra. For large SNRs like RX J1713.7-3946, with a rather broad X-ray synchrotron emitting shell, one may wonder if the magnetic field is not so large that the X-ray synchrotron spectrum is age limited. Also for the youngest known Galactic SNR, G1.9+0.3 (Reynolds et al., 2008; Borkowski et al.,

2010), it is not clear whether the X-ray synchrotron emission is age or loss limited. One possible way to test this is to monitor the non-thermal X-ray emission for some time. For example, recently it has been shown that the X-ray synchrotron brightness of Cas A has declined between 2000 and 2010. At the same time the spectrum has softened (Patnaude et al., 2011). This can be understood assuming a loss-limited spectrum, as the exponential cut-off energy depends solely on V_s^2 (Eq. 52). Since the shock is decelerating the cut-off energy will decrease, thereby making the spectral index larger (corresponding to a softer spectrum) and the brightness smaller. For an age-limited synchrotron spectrum the cut-off photon energy depend on the age of the SNR. Thus the cut-off energy will increase with time. Depending on the magnetic-field evolution in the shock region this could in principle make the X-ray synchrotron spectrum harder (Carlton et al., 2011). The secular evolution of the X-ray synchrotron emission does, however, also depend on other variables, such as the number of electrons accelerated as a function of age, but the evolution of the exponential cut-off is likely to be the dominant contribution to the spectral evolution (Patnaude et al., 2011; Katsuda et al., 2010b).

11.3 X-ray based evidence for efficient cosmic-ray acceleration

One of the surprises that came out of the magnetic-field determination was that the magnetic fields were typically 100 – 600 μG , larger than might be expected, if they were merely caused by the compression of the interstellar magnetic field ($B_{\text{ISM}} \approx 5 \mu\text{G}$). Additional evidence for these high magnetic fields is that the X-ray synchrotron emitting regions seem to vary on time scales of several months to years, which may be indicative of the synchrotron cooling time scales, and, hence high magnetic fields (Patnaude and Fesen, 2007; Uchiyama et al., 2007; Uchiyama and Aharonian, 2008).³⁵ The high magnetic fields suggest that some magnetic-field amplification mechanism is operating near the shocks of young SNRs.

There are several theories that link magnetic-field amplification to efficient cosmic-ray acceleration. A particular promising mechanism is that discovered by Bell (2004), in which cosmic rays streaming outward result in an electron return current. These electrons are then deflected by the magnetic field, thereby creating a very turbulent, amplified magnetic field. This mechanism is expected to give $u_B \approx V_s u_{\text{cr}} \propto \rho V_s^3$, with u_B and u_{cr} respectively the magnetic field and cosmic-ray energy density, and ρ_0 the ambient plasma density.

Combining the magnetic-field estimates of several young SNRs shows that there is indeed a clear trend that SNRs evolving in low density environments seem to have lower magnetic fields than those evolving in high density media (Bamba et al., 2005; Völck et al., 2005; Ballet, 2006; Vink, 2008a). This also explains the trend that the wider

³⁵However, an alternative explanation may be varying magnetic fields due to passages of large scale plasma waves (Bykov et al., 2008b).

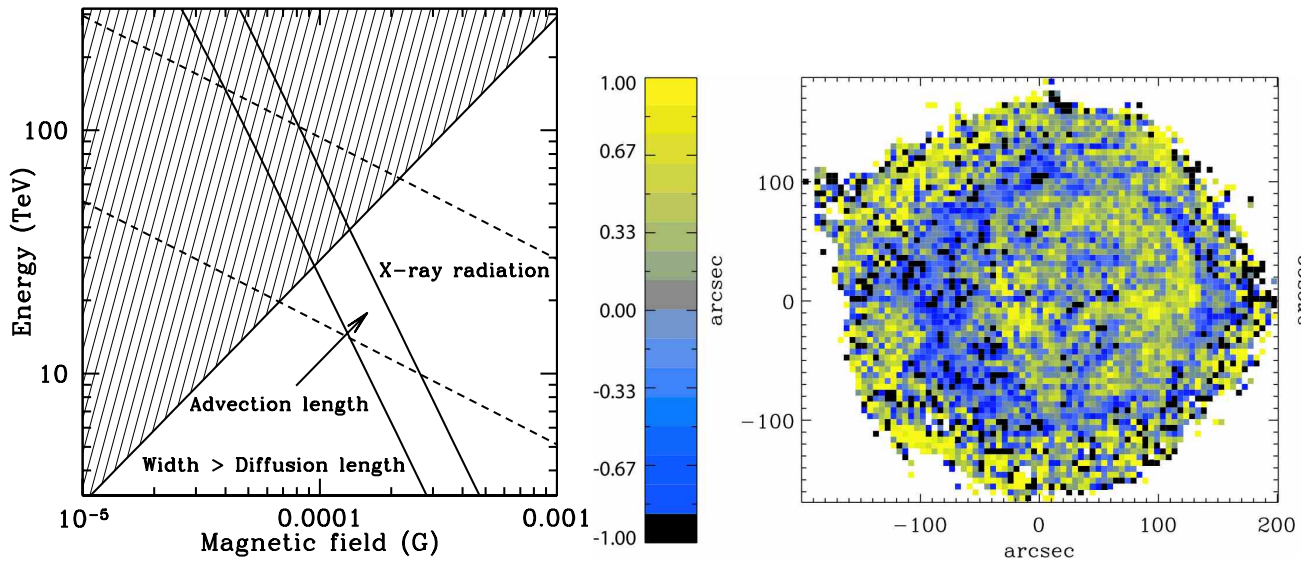


Figure 38: Left: The maximum cosmic-ray electron energy versus magnetic-field strength for the region just downstream of Cas A's shock front, as determined from the thickness of the filaments (Vink and Laming, 2003). The shaded area is excluded, because the filament width cannot be smaller than the minimum possible diffusion length (c.f. Vink and Laming, 2003). (These figures were published before in (Vink, 2006).) Right: The power slope of the X-ray continuum in the 4-6 keV band based on the 1 MS *Chandra* observation of Cas A (Helder and Vink, 2008). The color scale indicates the slope difference with respect to the mean slope of $\Gamma = 3.2$. Brighter color mean harder spectra, and signify a larger contribution of synchrotron radiation. Note that there seem to be two general regions of synchrotron radiation, the outer edge and the inner region near the reverse shock. A high resolution *Chandra* X-ray image of Cas A is shown in Fig. 26, where the X-ray synchrotron can be seen as a faint blue wisp at the edge of the SNR.

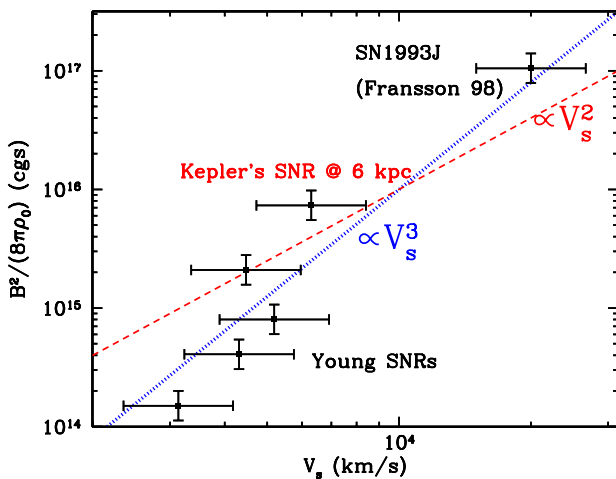


Figure 39: The dependence of the post-shock magnetic field energy density $B^2/(8\pi)$ on the shock velocity V_s . The dashed line shows a V_s^2 dependency and the dotted line a V_s^3 dependency. The input values can be found in (Vink, 2006), except for SN1993J (Fransson and Björnsson, 1998) and Kepler's SNR, for which the shock velocity in the southwest was taken from (Vink, 2008c) and the density from (Cassam-Chenaï et al., 2004).

X-ray synchrotron emitting regions, hence lower magnetic fields, are found in larger SNRs: these SNRs have a combination of high shock velocity and large radius, because they evolve in a low density region (Ueno et al., 2006).

The relation between magnetic-field energy density and shock velocity is less clear. The reason is that for X-ray synchrotron emitting SNRs the dynamic range in velocity is relatively small ($\sim 2000 - 6000 \text{ km s}^{-1}$). Völk et al. (2005) find that $B^2 \propto \rho_0 V_s^2$, but they used an outdated measurement of the shock velocity of Cas A ($\sim 2500 \text{ km s}^{-1}$). Vink (2008a) instead favors a dependency of $B^2/(8\pi) \propto \rho_0 V_s^3$, but noted that the dynamic range makes the dependency on V_s uncertain. Including the magnetic-field determination for SN 1993J ($V_s \approx 20,000 \text{ km s}^{-1}$, and $B \approx 64 \text{ G}$, Fransson and Björnsson, 1998; Tatischeff, 2009) indicates that $B^2 \propto V_s^3$ seems more likely (Fig. 39). But it should be noted that it is not quite clear whether the magnetic-field amplification mechanism in SN1993J has a similar origin as in young SNRs.

There has been some concern that amplified, turbulent magnetic fields dampen rapidly, even to the point that the width of the narrow X-ray synchrotron filaments in young SNRs may not be determined by the advection or diffusion length scale, but by the magnetic-field damping time scale (Pohl et al., 2005). However, this would affect the radio and X-ray synchrotron profile similarly, and this does not appear to be the case (Cassam-Chenaï et al., 2007; Gotthelf et al., 2001).

The X-ray synchrotron emission from SN 1006 has another characteristic that may be of importance for a better understanding of cosmic-ray acceleration: it appears that the synchrotron radiation is coming from just two regions of the SNR, i.e. there seems to be very little synchrotron

emission from the center of the SNR (Willingale et al., 1996; Rothenflug et al., 2004; Cassam-Chenaï et al., 2008). A likely explanation is that this is due to initial the magnetic field configuration. Given the inferred polar geometry, the implication is that X-ray synchrotron radiation is favored by a magnetic field that is parallel to the shock normal. On the other hand, the presence of X-ray synchrotron radiation requires a turbulent magnetic field. This seems a contradiction, but the two conditions can be combined by assuming that efficient cosmic-ray acceleration favors a parallel magnetic field to start, but once it has started it creates its own turbulent magnetic field (Völk et al., 2003). SN 1006 may be special in that its background magnetic field was much more regular than that of other X-ray synchrotron emitting SNRs.

One question that may be raised is whether the magnetic fields in young SNRs are caused by amplification, or that even creation of magnetic fields is possible. There is at least some indication for magnetic-field creation, because Helder and Vink (2008) showed, on the basis of a spectral analysis of *Chandra* X-ray data (Fig. 38b), that most of the X-ray synchrotron emitting filaments are not associated with the forward shock, but with the reverse shock (see also Uchiyama and Aharonian, 2008). Since these filaments are also narrow, the local magnetic fields must be of the order of 100 – 500 μ G. A problem with this is that the ejecta, due to their large expansion must have very low magnetic fields. So this suggests that Bell’s mechanism, or any other amplification mechanism, even operates for very low seed magnetic fields, or perhaps does not even require a seed magnetic field. Alternatively, cosmic rays diffusing from the forward shock to the reverse shock may have provided a seed population of cosmic rays that resulted in magnetic-field amplification through Bell’s mechanism (Schure et al., 2010). Note that there are also suggestions that the reverse shock regions of RCW 86 (Rho et al., 2002) and RX J1713.7-3946 (Zirakashvili and Aharonian, 2010) are sources of X-ray synchrotron radiation.

Irrespective of the exact magnetic-field dependence on shock velocity, the evidence for magnetic-field amplification in young SNRs has important consequences. The presence of amplified magnetic fields imply large cosmic-ray energy densities. This makes it likely that cosmic rays are indeed being efficiently accelerated, i.e. a large fraction of the shock energy may be transferred to cosmic rays. This in turn suggests that the post-shock temperatures are expected to be low and the shock compression ratios should be larger than four (Sect. 5.1).

As argued in Sect. 11.1, the lack of very hot electron temperatures in young SNRs may be caused either by a lack of electron-proton temperature equilibration, or by efficient acceleration. Proton temperatures are less affected by equilibration effects, and can be determined from $H\alpha$ line widths. Using this technique Helder et al. (2009) showed that in the northeastern part of RCW 86 the proton temperature is $kT \approx 2$ keV, much lower than the expected $kT > 10$ keV. They derived from this a post-shock cosmic-ray pressure contribution of > 50 %. Note that

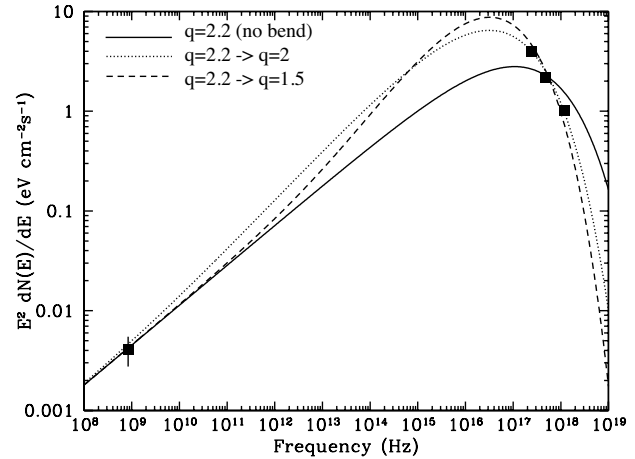


Figure 40: Radio to X-ray synchrotron spectrum of the northeastern part of RCW 86 (Vink et al., 2006). The models show that a curved synchrotron spectrum is needed. A simple synchrotron spectrum with a spectral radio index $\alpha = 0.6$ (corresponding to an electron particle index of $q = 2.2$, Sect. 11.2) and an exponential cut-off in electron energy cannot simultaneously fit both the radio and X-ray data points.

RCW 86 is a TeV source (Aharonian et al., 2009) and that the northeastern part emits X-ray synchrotron radiation (Bamba et al., 2000; Borkowski et al., 2001b; Vink et al., 2006). A similar study of the rapidly expanding LMC SNR B0509-67.5 (Sect. 8) indicates that there in the southwest the post-shock pressure is for $> 20\%$ provided by cosmic rays (Helder et al., 2010). This method can also be employed using X-ray spectroscopy once high resolution, non-dispersive, spectrometers will be available

Another effect of efficient cosmic-ray acceleration is high shock compression ratios (Sect. 5.1). There is indeed evidence for high shock compression ratios in Tycho (Warren et al., 2005; Cassam-Chenaï et al., 2007) and SN 1006 (Cassam-Chenaï et al., 2008). Although the compression ratio cannot be measured directly, X-ray imaging spectroscopy of both SNRs shows that the ejecta that are located very close to the forward shock, which is an observational consequence of a high compression ratio (Decourchelle et al., 2000).

Efficient acceleration should also lead to a curvature of the relativistic electron spectrum. The reason is that particles of different energies experience different compression ratios during the acceleration process, depending on whether they experience the overall shock compression ratio, the gas-shock (sub-shock) compression ratio, or something in between (see Sect. 5.5). Radio spectra of a few SNRs do indeed show evidence for spectral hardening with increasing frequencies (Reynolds and Ellison, 1992). For X-ray spectroscopy the consequence of spectral curvature is that the X-ray synchrotron brightness cannot be simply estimated from an extrapolation of the radio synchrotron spectrum, but it should be brighter than ex-

pected. This has indeed been demonstrated to be the case for the northeastern rim of RCW 86 (Vink et al., 2006, see Fig. 40) and SN 1006 (Allen et al., 2008).

11.4 The relation between X-ray synchrotron and γ -ray emission

The field of GeV and TeV γ -ray astronomy has made tremendous progress over the last decade, thanks to technical progress in building sensitive TeV Cherenkov telescopes (see Hinton and Hofmann, 2009, for a review) and, very recently the launch of the NASA *Fermi* satellite, which is sensitive to $\sim 0.1 - 100$ GeV γ -rays. Together these telescopes have greatly expanded the number of γ -ray sources, and, over the last decade have resulted in the first firm detections of continuum γ -ray emission from shell-type SNRs. The first such detection in the TeV band was Cas A with *HEGRA* (Aharonian et al., 2001), but the list of TeV detected telescopes has greatly expanded since then.³⁶

The 0.1 – 100 GeV band was sampled by γ -ray satellites since the 1970ies, but the first evidence for associations between GeV γ -ray sources and SNRs were found with *CGRO-EGRET*, and concerned mature SNRs interacting with molecular clouds (Esposito et al., 1996). *Fermi* has confirmed these early associations, and greatly enhanced the number of γ -ray sources among mature SNRs interacting with molecular clouds (Sect. 10.3). In addition, also a number of younger SNRs have now been detected. The first catalog of *Fermi* listed 41 sources as possibly associated with SNRs (Abdo et al., 2010a) and this list is still expanding.³⁷

The great importance of GeV and TeV γ -ray astronomy is that it can give us a direct view of the accelerated cosmic-ray nuclei³⁸, which make up 99% of the cosmic rays observed on earth. These nuclei produce γ -ray emission if they collide with atomic nuclei, thereby creating, among others, neutral pions, which decay in two γ -ray photons. However, two other important γ -ray radiation processes originate from relativistic electrons: interactions with background photons result in inverse Compton up-scattering, whereas interactions with ions in the SNR result in bremsstrahlung. X-ray observations are crucial for disentangling all these contributions. The thermal X-ray emission is important for determining the local plasma density, which determines the γ -ray non-thermal bremsstrahlung and pion-decay contributions. The X-ray synchrotron emission can be used to determine the local magnetic field. The combination of magnetic field and radio and X-ray synchrotron flux can then be used to infer the inverse Compton contribution to the γ -ray emission.

³⁶At the moment of writing 13 shell-type SNRs are now claimed to be TeV sources, see <http://tevcat.uchicago.edu>.

³⁷Note that the γ -ray may not necessarily come from the SNR shell, but in some cases from an embedded pulsar wind nebula.

³⁸Protons and other ions. These are often named "hadronic cosmic rays", as opposed to leptonic cosmic rays, which are mostly electrons and positrons.

Although X-ray observations seem to indicate that cosmic-ray acceleration is efficient in young SNRs, the recent observations of SNRs in GeV and TeV γ -rays provide a more ambiguous story. Although many SNRs have been detected in TeV γ -rays with TeV telescopes like *HEGRA* (Aharonian et al., 2001), *HESS* (e.g. Aharonian et al., 2004), *MAGIC* (Albert et al., 2007b) and *Veritas* (e.g. Acciari et al., 2011) and the *Fermi* satellite, the γ -ray observations do not provide clear evidence that cosmic rays are being accelerated *efficiently*, nor that they SNRs accelerate ions to beyond "the knee".

There has been a strong debate about the nature of TeV emission X-ray synchrotron radiation dominated SNRs. A central role in this debate concerns the brightest TeV emitting SNR, RX J1713.7-3946. For example Berezhko and Völk (2010) advocates a dominant pion-decay contribution to the TeV γ -ray emission, whereas Katz and Waxman (2008) and Ellison et al. (2010) argue that the γ -ray emission is dominated by inverse Compton scattering. The lack of thermal X-ray emission is an important ingredient in this debate, as to some it indicates low densities, and hence low pion-decay luminosities, whereas others (notably Drury et al., 2009) have argued that it could be the result of extremely low temperatures caused by efficient cosmic-ray acceleration (see Sect. 5.1). An argument in favor of an electron origin for the γ -ray emission of RX J1713.7-3946 is the close resemblance between the TeV γ -ray and X-ray brightness distribution, which suggests that both originate from the same population of particles: electrons (Fig. 41, Acero et al., 2009).

However, there are two arguments in favor of pion decay. Namely the relatively hard spectrum in TeV, which extends up to 100 TeV, and the inferred high magnetic field in the SNR, $> \text{mG}$ (Uchiyama et al., 2007). Higher magnetic fields imply lower relativistic electron densities for a given X-ray synchrotron flux. Hence, the electron contribution to the TeV flux is expected to be low, and pion decay becomes the most likely dominant source of TeV γ -rays. The high magnetic-field estimates are based on the the observation of rapid X-ray flux changes and comparing them to the synchrotron loss time scales (see Eq. 49). But the fluctuations may also originate from fluctuations of due to long wavelength Alfvén waves (Bykov et al., 2008b). Another argument in favor of relatively high magnetic fields are the small widths of the X-ray synchrotron rims (Sect. 11.2). But for this measurement the problem is what region one should measure the width of: the whole shell or just a bright filament? For example, one can take the overall shell size of RX J1713.7-3946 to be the size of the filament (since for this SNR the whole shell seems to emit synchrotron emission), or use some filamentary substructures. This problem is illustrated in (Fig. 42). If one takes the whole shell region, at best one comes up with a length scale of $100''$ corresponding to $25 - 30 \mu\text{G}$.

The most serious challenge to the pion-decay model for RX J1713.7-3946 comes from recent observations by *Fermi* (Abdo and Fermi LAT Collaboration, 2011), which show that the shape of the broad band γ -ray spectrum

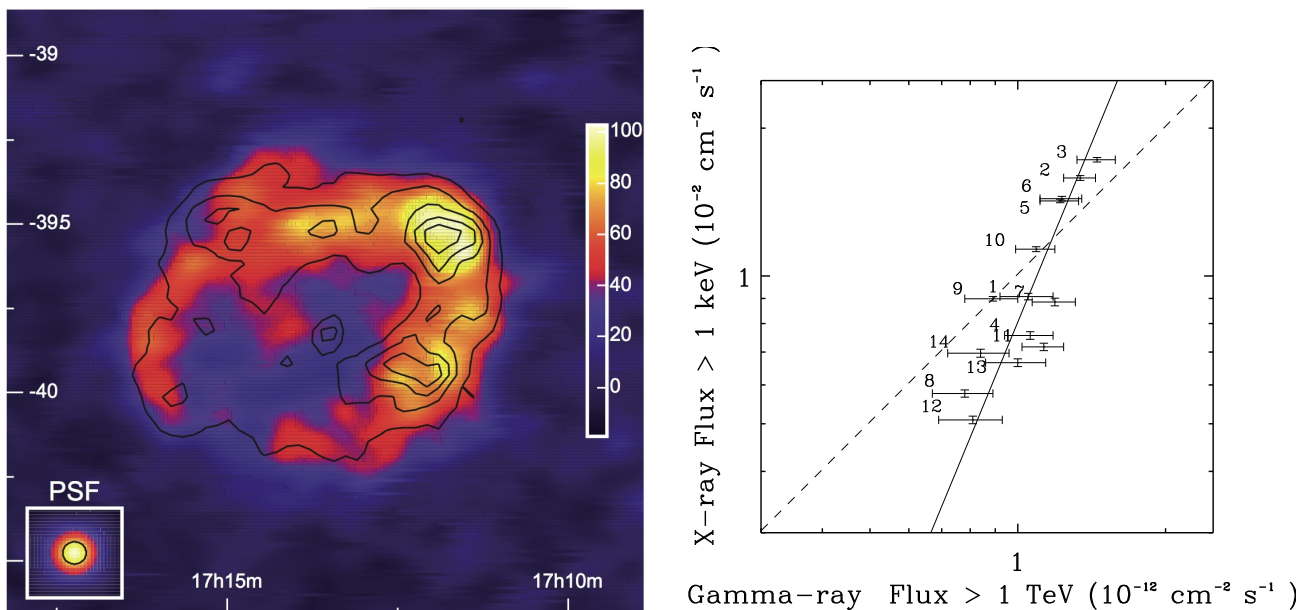


Figure 41: Left: γ -ray excess count map of RX J1713.7-3946 as observed by *HESS*. Overlaid are 1-3 keV X-ray (*ASCA*) intensity contours (Aharonian et al., 2007). Right: A comparison of the X-ray flux (1-10 keV, *XMM-Newton*) and *HESS* γ -ray integrated flux (1-10 TeV band, Figure taken from Acero et al., 2009).

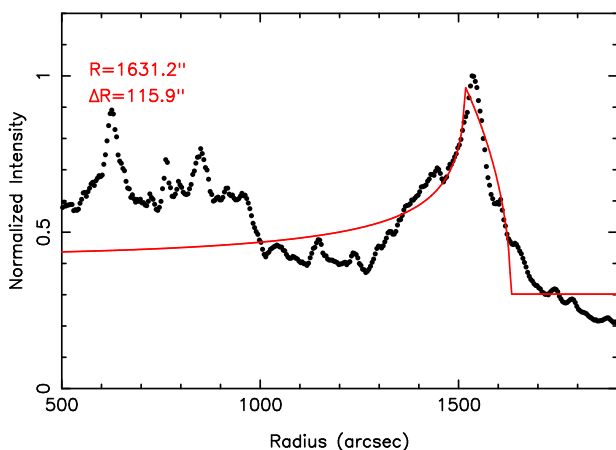


Figure 42: X-ray emission profile of the southeastern part of RX J1713.7-3846 (extracted by the author from the *XMM-Newton* image reduced by Acero et al., 2009). It illustrates the difficulty in determining for this SNR what the width of the X-ray synchrotron emitting region is. The red line indicates a simple model of a projected sphere with a uniform emissivity with a shell width of $116''$. For a distance of 1 kpc this corresponds, according to Eq. 62, to $25 \mu\text{G}$.

is more consistent with inverse Compton scattering than pion decay. The implication of this result is surprising, because RX J1713.7-3946 was often used as a key object in the argument that SNRs can accelerate ions to very high energies.

An important result of *Fermi* (Abdo et al., 2010c) is the detection of GeV γ -ray emission from Cas A, which indicates that the total cosmic-ray energy content is less than

4% of the total explosion energy. This is disappointing if one thinks that young SNRs should be able to accelerate cosmic rays efficiently, and convert $> 10\%$ of the explosion energy to cosmic rays (Sect. 5.5). The case for pion decay as origin for the γ -ray emission is stronger for Tycho's SNR, given the recent detection with the *Veritas* TeV telescope (Acciari et al., 2011).

The apparent lack of evidence for a high cosmic ray acceleration efficiency for Cas A is also somewhat surprising, given the high magnetic field of Cas A, as argued in Sect. 11.2, which is suggestive of efficient cosmic-ray acceleration. It could be that a large part of the energy in cosmic rays has already escaped the SNR. Since Cas A evolves inside the wind of its progenitor, the background plasma that the escaped cosmic rays are in likely has a lower density than the SNR shell.

Indeed, several theories about non-linear cosmic ray acceleration point toward the importance of cosmic ray escape (Blasi et al., 2005; Vladimirov et al., 2008; Reville et al., 2009; Vink et al., 2010). Future very sensitive TeV telescopes like the Cherenkov Telescope Array (CTA, CTA Consortium, 2010) could in principle be used to search for "cosmic-ray haloes" around young SNRs. Hopefully, the improvement in sensitivity in TeV astronomy can be met with a similar improvement in sensitivity and spectral resolution in X-ray spectroscopy, which will help to detect thermal X-ray emission and provide temperatures for X-ray synchrotron emitting plasmas.

Interestingly enough, the case for a pion-decay origin of the γ -ray emission is most unambiguous for some of the mature SNRs that are interacting with or are near molecular clouds. An example is W44 (Abdo et al., 2010e, see also Sect. 10.3), for which it is argued that inverse Comp-

ton scattering, or bremsstrahlung do not provide an adequate description of the spectrum. But the γ -ray spectrum of this source steepens around 10 GeV, which is consistent with the idea that cosmic rays with energies above 10^{15} eV are present. This break in the spectrum could be evidence that cosmic rays with larger energies have already escaped the SNR in the past. This is also consistent with several SNRs that have γ -ray sources nearby, which could be caused by cosmic rays that escaped from the SNR and are now interacting with the high density medium of molecular clouds. The GeV/TeV sources associated with SNR W28 is an example for such an association (Aharonian et al., 2008b; Abdo et al., 2010b).³⁹

12 Concluding remarks

Our understanding of SNRs has greatly increased over the last decade due to the X-ray observatories *Chandra*, *XMM-Newton*, and *Suzaku*. The second half of this review essentially summarized the advances in SNR research made with these observatories. I think that a number of these results deserve more recognition outside the field of SNR research. I will summarize some of them here.

X-ray spectroscopy has proven to be a promising tool to separate young Type Ia (Sect. 8) from core collapse SNRs (Sect. 9.1). X-ray emission for Type Ia SNRs has given us important clues toward the nature of the progenitor systems: the progenitors did not produce fast winds, and delayed detonation models seem to explain the abundance patterns well. Type Ia SNRs are also well stratified, unlike core collapse SNRs.

An important question concerning core collapse supernovae is what drives the explosion (neutrino absorption, or other mechanisms?) and what types of massive stars produce neutron stars and what types make black holes. X-ray observations show that the core collapse process is chaotic, with pure metal plasma obtaining high velocities in seemingly random directions. But for one SNR, Cas A, there is evidence for an ejecta jet/counter jet. These are in Si-group material, not in Fe-rich material. With future observations we may learn more about rare elements, which may indicate the neutron content of the inner most ejecta. This may help us to identify the role of neutrino absorption in the explosion.

As for the question what determines the creation of a black hole. There is at least one SNR, G292.0+1.8, for which there is an indication that it produced a neutron star, but had nevertheless a progenitor mass above $30 M_{\odot}$ (Sect. 9.3). It is important to confirm this results with further X-ray studies, as a popular hypothesis is that stars above $25 M_{\odot}$ leave behind a black hole.

Another uncertainty in the theory of core collapse supernovae is how much iron they produce. The iron yield is greatly affected by the details of the explosion, such as explosion asymmetries and fall back on the neutron

star. There is evidence that the Cygnus Loop (Sect. 10.2) contains more iron than predicted by explosion models. Whereas for Cas A, iron seems to have obtained a higher velocity than predicted by explosion models.

One surprising result of X-ray imaging spectroscopy is that even mature SNRs still have regions with enhanced metal abundances. This is true for the Cygnus Loop (Sect. 10.2) and many mixed-morphology SNRs (Sect. 10.3). For the Vela SNR X-ray imaging spectroscopy confirmed that the bullets outside the main shock are indeed ejecta “shrapnels” that have enhanced abundances.

Finally, X-ray imaging spectroscopy has played an important role in increasing our understanding of cosmic-ray acceleration. A role it shared with the rapidly evolving fields of TeV astronomy with Cherenkov telescopes, and GeV astronomy with the *Fermi* satellite. In particular, X-ray detections of narrow width synchrotron filaments have provided evidence for magnetic-field amplification near SNR shocks (Sect. 11.2). This implies that SNRs are efficiently accelerating cosmic rays. However, the overall interpretation of both X-ray and γ -ray observations is still ambiguous, in particular concerning the total energy in cosmic-rays contained in young SNRs (Sect. 11.4).

As is clear from the above, our understanding of SNRs has greatly benefitted from the coming of age of X-ray imaging spectroscopy. The impact of high resolution X-ray spectroscopy has been more modest, as *Chandra* and *XMM-Newton* have grating spectrometers, which are not ideal for observations of extended sources as SNRs. Nevertheless, for bright sources of small angular extent important results have been obtained.

In the near future high resolution X-ray spectroscopy of SNRs will likely become much more important as microcalorimeters will become operational. These will have a spectral resolution of $\Delta E \approx 5$ eV at 6 keV ($R \approx 1200$) and also have some limited spatial resolution. The first opportunity to use them will start after the launch of *Astro-H*⁴⁰. After *Astro-H* the next step forward will hopefully be *ATHENA*, a mission concept for an European X-ray observatory that will offer a large effective area (> 1 m² at 1 keV) and a spatial resolution of $< 10''$, which should be compared to $1'$ for *Astro-H*.

The tantalizing glimpse of high resolution X-ray spectroscopy of SNRs offered by *Chandra* and *XMM-Newton*, shows that SNR research beyond 2014 will enter a new era.

acknowledgements

I am grateful to Eveline Helder and Sjors Broersen for carefully reading a draft version of this review. I also appreciate comments from Joke Claeys on section 2 and discussion with her, Alexandros Chiotellis, and Dani Maoz on Type Ia supernovae. I thank the editor of A&A Reviews, Thierry Courvoisier, for inviting me for this re-

³⁹<http://tevcat.uchicago.edu/> lists 6 SNRs/Molecular Cloud associations as TeV sources.

⁴⁰Formerly known as *Astro-H* (Takahashi et al., 2008).

view and the patience he showed for the completion of the manuscript.

I want to express my dissatisfaction that Utrecht University decided to close its astronomy department, which had a long and fruitful tradition of 370 yr.

We acknowledge the permission of the AAS for the reproduction of the figures 7,22, 28, 29,30,32,34 and 38, the permission of the Publications of the Astronomical Society of Japan for reproduction of figures 23 and 35, and the permission of Astronomy and Astrophysics for the figures 16, 21, 25, 27, 41. Figure 33 was taken from <http://www.mpe.mpg.de> and appears with permission from the Max-Planck-Institut für extraterrestrische Physik.

References

- Abdo AA, Ackermann M, Ajello M, Allafort A, et al. (2010a) Fermi Large Area Telescope First Source Catalog. *ApJS*188:405–436, 1002. 2280
- Abdo AA, Fermi LAT Collaboration (2011) Observations of the young supernova remnant RX J1713.7-3946 with the Fermi Large Area Telescope. *ArXiv e-prints* 1103. 5727
- Abdo AA, et al. (2009) Fermi LAT Discovery of Extended Gamma-Ray Emission in the Direction of Supernova Remnant W51C. *ApJ*706:L1–L6, 0910. 0908
- Abdo AA, et al. (2010b) Fermi Large Area Telescope Observations of the Supernova Remnant W28 (G6.4-0.1). *ApJ*718:348–356
- Abdo AA, et al. (2010c) Fermi-Lat Discovery of GeV Gamma-Ray Emission from the Young Supernova Remnant Cassiopeia A. *ApJ*710:L92–L97, 1001. 1419
- Abdo AA, et al. (2010d) Fermi-LAT Study of Gamma-ray Emission in the Direction of Supernova Remnant W49B. *ApJ*722:1303–1311
- Abdo AA, et al. (2010e) Gamma-Ray Emission from the Shell of Supernova Remnant W44 Revealed by the Fermi LAT. *Science* 327:1103–
- Abdo AA, et al. (2010f) Observation of Supernova Remnant IC 443 with the Fermi Large Area Telescope. *ApJ*712:459–468, 1002. 2198
- Acciari VA, Aliu E, Arlen T, Aune T, et al. (2011) Discovery of TeV Gamma-ray Emission from Tycho's Supernova Remnant. *ApJ*730:L20+, 1102. 3871
- Acerro F, Ballet J, Decourchelle A (2007) The gas density around SN 1006. *A&A*475:883–890, 0709. 0956
- Acerro F, Ballet J, Decourchelle A, Lemoine-Goumard M, et al. (2009) A joint spectro-imaging analysis of the XMM-Newton and HESS observations of the supernova remnant RX J1713.7-3946. *A&A*505:157–167, 0906. 1073
- Aharonian A F Akhperjanian, Barrio J, et al. (2001) Evidence for TeV gamma ray emission from Cassiopeia A. *A&A*370:112–120
- Aharonian F, Akhperjanian AG, Barres de Almeida U, et al. (2008a) HESS upper limits for Kepler's supernova remnant. *A&A*488:219–223, 0806. 3347
- Aharonian F, et al. (2007) Primary particle acceleration above 100 TeV in the shell-type supernova remnant RX J1713.7-3946 with deep HESS observations. *A&A*464:235–243
- Aharonian F, et al. (2008b) Discovery of very high energy gamma-ray emission coincident with molecular clouds in the W 28 (G6.4-0.1) field. *A&A*481:401–410, 0801. 3555
- Aharonian F, et al. (2009) Discovery of Gamma-Ray Emission From the Shell-Type Supernova Remnant RCW 86 With Hess. *ApJ*692:1500–1505, 0810. 2689
- Aharonian FA, Atoyan AM (1999) On the origin of TeV radiation of SN 1006. *A&A*351:330–340
- Aharonian FA, et al. (2004) High-energy particle acceleration in the shell of a supernova remnant. *Nat*432:75–77
- Ahmad I, Greene JP, Moore EF, Ghelberg S, et al. (2006) Improved measurement of the Ti44 half-life from a 14-year long study. *Phys. Rev. C*74(6):065 803–+
- Albert J, et al. (2007a) Discovery of Very High Energy Gamma Radiation from IC 443 with the MAGIC Telescope. *ApJ*664:L87–L90, 0705. 3119
- Albert J, et al. (2007b) Observation of VHE γ -rays from Cassiopeia A with the MAGIC telescope. *A&A*474:937–940, *arXiv*:0706. 4065
- Allen GE, Gotthelf EV, Petre R (1999) Evidence of 10-teV to 100-teV electrons in supernova remnants. in the proceedings of the 26th International Cosmic Ray Conference (astro-ph/9908209) *astro-ph/9908209*
- Allen GE, Houck JC, Sturmer SJ (2008) Evidence of a Curved Synchrotron Spectrum in the Supernova Remnant SN 1006. *ApJ*683:773–785, 0807. 1702
- Allen GE, et al. (1997) Evidence of X-Ray Synchrotron Emission from Electrons Accelerated to 40 TeV in the Supernova Remnant Cassiopeia A. *ApJ*487:L97–L100
- Allen MP, Horvath JE (2004) Influence of an Internal Magnetar on Supernova Remnant Expansion. *ApJ*616:346–356
- Arnett D (1996) *Supernovae and nucleosynthesis*. Princeton series in astrophysics, Princeton, NJ: Princeton University Press, —c1996
- Arnett WD, Bahcall JN, Kirshner RP, Woosley SE (1989) Supernova 1987A. *ARAA*27:629–700
- Arons J (2003) Magnetars in the Metagalaxy: An Origin for Ultra-High-Energy Cosmic Rays in the Nearby Universe. *ApJ*589:871–892, *astro-ph/0208444*
- Aschenbach B (1998) Discovery of a young nearby supernova remnant. *Nat*396:141–142
- Aschenbach B, Egger R, Trümper J (1995) Discovery of Explosion Fragments Outside the VELA Supernova Remnant Shock-Wave Boundary. *Nat*373:587–+
- Asvarov AI, Guseinov OH, Kasumov FK, Dogel' VA (1990) The hard X-ray emission of the young supernova remnants. *A&A*229:196–200
- Aubourg É, Tojeiro R, Jimenez R, Heavens A, et al. (2008) Evidence of short-lived SN Ia progenitors. *A&A*492:631–636, 0707. 1328
- Axford WI, Leer E, Skadron G (1977) The Acceleration of Cosmic Rays by Shock Waves. In: *International Cosmic*

- Ray Conference, vol. 11 of *International Cosmic Ray Conference*, pp. 132–+
- Badenes C (2010) X-ray studies of supernova remnants: A different view of supernova explosions. *Proceedings of the National Academy of Science* 107:7141–7146, 1002.0596
- Badenes C, Borkowski KJ, Bravo E (2005) Thermal X-Ray Emission from Shocked Ejecta in Type Ia Supernova Remnants. II. Parameters Affecting the Spectrum. *ApJ*624:198–212
- Badenes C, Borkowski KJ, Hughes JP, Hwang U, et al. (2006) Constraints on the Physics of Type Ia Supernovae from the X-Ray Spectrum of the Tycho Supernova Remnant. *ApJ*645:1373–1391, arXiv:astro-ph/0511140
- Badenes C, Bravo E, Borkowski KJ, Domínguez I (2003) Thermal X-Ray Emission from Shocked Ejecta in Type Ia Supernova Remnants: Prospects for Explosion Mechanism Identification. *ApJ*593:358–369
- Badenes C, Bravo E, Hughes JP (2008a) The End of Amnesia: A New Method for Measuring the Metallicity of Type Ia Supernova Progenitors Using Manganese Lines in Supernova Remnants. *ApJ*680:L33–L36, arXiv:0805.3344
- Badenes C, Hughes JP, Bravo E, Langer N (2007) Are the Models for Type Ia Supernova Progenitors Consistent with the Properties of Supernova Remnants? *ApJ*662:472–486, arXiv:astro-ph/0703321
- Badenes C, Hughes JP, Cassam-Chenaï G, Bravo E (2008b) The Persistence of Memory, or How the X-Ray Spectrum of SNR 0509-67.5 Reveals the Brightness of Its Parent Type Ia Supernova. *ApJ*680:1149–1157, 0801.4761
- Ballet J (2006) X-ray synchrotron emission from supernova remnants. *Advances in Space Research* 37:1902–1908, arXiv:astro-ph/0503309
- Bamba A, Koyama K, Tomida H (2000) Discovery of non-thermal X-rays from the shell of RCW 86. *PASJ*52:1157–1163
- Bamba A, Ueno M, Nakajima H, Koyama K (2004) Thermal and Nonthermal X-Rays from the Large Magellanic Cloud Superbubble 30 Doradus C. *ApJ*602:257–263
- Bamba A, Yamazaki R, Yoshida T, Terasawa T, et al. (2005) A Spatial and Spectral Study of Nonthermal Filaments in Historical Supernova Remnants: Observational Results with Chandra. *ApJ*621:793–802, arXiv:astro-ph/0411326
- Bandiera R (1987) The origin of Kepler’s supernova remnant. *ApJ*319:885–892
- Bandiera R, van den Bergh S (1991) Changes in the optical remnant of Kepler’s supernova during the period 1942-1989. *ApJ*374:186–201
- Becker RH, Szymkowiak AE, Boldt EA, Holt SS, et al. (1980) Is the remnant of SN 1006 Crablike. *ApJ*240:L33–L35
- Behar E, Rasmussen AP, Griffiths RG, Dennerl K, et al. (2001) High-resolution X-ray spectroscopy and imaging of supernova remnant N132D. *A&A*365:L242–L247
- Beiersdorfer P, Phillips T, Jacobs VL, Hill KW, et al. (1993) High-resolution measurements, line identification, and spectral modeling of K-alpha transitions in Fe XVIII-Fe XXV. *ApJ*409:846–859
- Bell AR (1978a) The acceleration of cosmic rays in shock fronts. I. *MNRAS*182:147–156
- Bell AR (1978b) The acceleration of cosmic rays in shock fronts. II. *MNRAS*182:443–455
- Bell AR (2004) Turbulent amplification of magnetic field and diffusive shock acceleration of cosmic rays. *MNRAS*353:550–558
- Bennett L, Ellison DC (1995) Investigation of intrinsic variability in one-dimensional parallel shocks using steady state hybrid simulations. *Journal of Geophysical Research*100:3439–3448
- Berezhko EG, Ellison DC (1999) A Simple Model of Non-linear Diffusive Shock Acceleration. *ApJ*526:385–399
- Berezhko EG, Ksenofontov LT, Völk HJ (2003) Confirmation of strong magnetic field amplification and nuclear cosmic ray acceleration in SN 1006. *A&A*412:L11–L14
- Berezhko EG, Völk HJ (2010) Nonthermal and thermal emission from the supernova remnant RX J1713.7-3946. *A&A*511:A34+, 0910.2094
- Bionta RM, Blewitt G, Bratton CB, Caspere D, et al. (1987) Observation of a neutrino burst in coincidence with supernova 1987A in the Large Magellanic Cloud. *Physical Review Letters* 58:1494–1496
- Blair WP (2005) Kepler’s Supernova Remnant: The View at 400 Years. In: 1604-2004: Supernovae as Cosmological Lighthouses (eds. Turatto M, Benetti S, Zampieri L, Shea W), vol. 342 of *Astronomical Society of the Pacific Conference Series*, pp. 416–+
- Blandford RD, Ostriker JP (1978) Particle acceleration by astrophysical shocks. *ApJ*221:L29–L32
- Blasi P, Gabici S, Vannoni G (2005) On the role of injection in kinetic approaches to non-linear particle acceleration at non-relativistic shock waves. *MNRAS*361:907–918, arXiv:astro-ph/0505351
- Bleeker JAM, et al. (2001) Cassiopeia A: On the origin of the hard X-ray continuum and the implication of the observed O VIII Ly- α / Ly- β distribution. *A&A*365:L225–L230
- Blondin JM, Mezzacappa A (2007) Pulsar spins from an instability in the accretion shock of supernovae. *Nat*445:58–60, arXiv:astro-ph/0611680
- Blondin JM, Mezzacappa A, DeMarino C (2003) Stability of Standing Accretion Shocks, with an Eye toward Core-Collapse Supernovae. *ApJ*584:971–980, arXiv:astro-ph/0210634
- Bocchino F, Miceli M, Troja E (2009) On the metal abundances inside mixed-morphology supernova remnants: the case of IC 443 and G166.0+4.3. *A&A*498:139–145, 0901.3228
- Bocchino F, Vink J, Favata F, Maggio A, et al. (2000) A BeppoSAX and ROSAT view of the RCW86 supernova

- remnant. *A&A*360:671–682
- Böhringer H, Werner N (2009) X-ray spectroscopy of galaxy clusters: studying astrophysical processes in the largest celestial laboratories. *A&A Rev.*:11–+
- Bookbinder J (2010) The International X-ray Observatory - RFI#1. ArXiv e-prints 1001.2329
- Borkowski KJ, Hendrick SP, Reynolds SP (2006) Dense, Fe-rich Ejecta in Supernova Remnants DEM L238 and DEM L249: A New Class of Type Ia Supernova? *ApJ*652:1259–1267, arXiv:astro-ph/0608297
- Borkowski KJ, Hendrick SP, Reynolds SP (2007) X-Ray-Emitting Ejecta of Supernova Remnant N132D. *ApJ*671:L45–L48, 0711.3140
- Borkowski KJ, Lyerly WJ, Reynolds SP (2001a) Supernova Remnants in the Sedov Expansion Phase: Thermal X-Ray Emission. *ApJ*548:820–835
- Borkowski KJ, Reynolds SP, Green DA, Hwang U, et al. (2010) Radioactive Scandium in the Youngest Galactic Supernova Remnant G1.9+0.3. *ApJ*724:L161–L165, 1006.3552
- Borkowski KJ, Rho J, Reynolds SP, Dyer KK (2001b) Thermal and nonthermal X-Ray emission in supernova remnant RCW 86. *ApJ*550:334–345
- Borkowski KJ, Sarazin CL, Blondin JM (1994) On the X-ray spectrum of Kepler’s supernova remnant. *ApJ*429:710–725
- Borkowski KJ, Szymkowiak AE (1997) X-Ray Emission from Dust in Hot Plasmas. *ApJ*477:L49+
- Boumis P, Meaburn J, López JA, Mavromatakis F, et al. (2004) The kinematics of the bi-lobal supernova remnant G 65.3+5.7. II. *A&A*424:583–588, arXiv:astro-ph/0405350
- Branch D, Buta R, Falk SW, McCall ML, et al. (1982) Interpretation of the maximum light spectrum of a Type I supernova. *ApJ*252:L61–L64
- Broersen S, Vink J, Raymond JC, Kaastra J (2011) xx. *A&A*1:1–5
- Brun F, de Naurois M, Hofmann W, Carrigan S, et al. (2011) Discovery of VHE gamma-ray emission from the W49 region with H.E.S.S. ArXiv e-prints 1104.5003
- Burrows A, Livne E, Dessart L, Ott CD, et al. (2007) Features of the Acoustic Mechanism of Core-Collapse Supernova Explosions. *ApJ*655:416–433
- Burrows CJ, Krist J, Hester JJ, Sahai R, et al. (1995) Hubble Space Telescope Observations of the SN 1987A Triple Ring Nebula. *ApJ*452:680–+
- Burrows DN, et al. (2000) The X-Ray Remnant of SN 1987A. *ApJ*543:L149–L152
- Bykov AM (2004) Shocks and particle acceleration in SNRs: theoretical aspects. *Advances in Space Research* 33:366–375
- Bykov AM, Chevalier RA, Ellison DC, Uvarov YA (2000) Nonthermal Emission from a Supernova Remnant in a Molecular Cloud. *ApJ*538:203–216, arXiv:astro-ph/0003235
- Bykov AM, Fleishman GD (1992) On non-thermal particle generation in superbubbles. *MNRAS*255:269–275
- Bykov AM, Paerels FBS, Petrosian V (2008a) Equilibration Processes in the Warm-Hot Intergalactic Medium. *Space Science Reviews* 134:141–153, 0801.1008
- Bykov AM, Uvarov YA (1999) Electron kinetics in collisionless shock waves. *Soviet Journal of Experimental and Theoretical Physics* 88:465–475
- Bykov AM, Uvarov YA, Ellison DC (2008b) Dots, Clumps, and Filaments: The Intermittent Images of Synchrotron Emission in Random Magnetic Fields of Young Supernova Remnants. *ApJ*689:L133–L136, 0811.2498
- Canizares CR, Flanagan KA, Davis DS, Dewey D, et al. (2001) High Resolution Spectroscopy of Two Oxygen-Rich SNRs with the Chandra HETG. In: *X-ray Astronomy 2000* (ed. R Giacconi, S Serio, & L Stella), vol. 234 of *Astronomical Society of the Pacific Conference Series*, pp. 173–+, arXiv:astro-ph/0105060
- Canizares CR, et al. (2005) The Chandra High-Energy Transmission Grating: Design, Fabrication, Ground Calibration, and 5 Years in Flight. *PASP*117:1144–1171, arXiv:astro-ph/0507035
- Caprioli D, Blasi P, Amato E, Vietri M (2008) Dynamical Effects of Self-Generated Magnetic Fields in Cosmic-Ray-modified Shocks. *ApJ*679:L139–L142, 0804.2884
- Cargill PJ, Papadopoulos K (1988) A mechanism for strong shock electron heating in supernova remnants. *ApJ*329:L29–L32
- Carlton AK, Borkowski KJ, Reynolds SP, Hwang U, et al. (2011) Expansion of the Youngest Galactic Supernova Remnant G1.9+0.3. ArXiv e-prints 1106.4498
- Cassam-Chenaï G, et al. (2004) XMM-Newton observation of Kepler’s supernova remnant. *A&A*414:545–558
- Cassam-Chenaï G, Hughes JP, Ballet J, Decourchelle A (2007) The Blast Wave of Tycho’s Supernova Remnant. *ApJ*665:315–340, arXiv:astro-ph/0703239
- Cassam-Chenaï G, Hughes JP, Reynoso EM, Badenes C, et al. (2008) Morphological Evidence for Azimuthal Variations of the Cosmic-Ray Ion Acceleration at the Blast Wave of SN 1006. *ApJ*680:1180–1197, 0803.0805
- Castro D, Slane P (2010) Fermi Large Area Telescope Observations of Supernova Remnants Interacting with Molecular Clouds. *ApJ*717:372–378, 1002.2738
- Charles PA, Kahn SM, McKee CF (1985) Einstein observations of selected regions of the Cygnus Loop. *ApJ*295:456–462
- Chen Y, Seward FD, Sun M, Li J (2008) The Thermal Composite Supernova Remnant Kesteven 27 as Viewed by Chandra: Shock Reflection from a Cavity Wall. *ApJ*676:1040–1049, 0711.0515
- Chevalier RA (1982) Self-similar solutions for the interaction of stellar ejecta with an external medium. *ApJ*258:790–797
- Chevalier RA (1990) *Supernovae*. Springer-Verlag Berlin Heidelberg New York.
- Chevalier RA (2005) Young Core-Collapse Supernova Remnants and Their Supernovae. *ApJ*619:839–855,

- arXiv:astro-ph/0409013
- Chevalier RA (2010) Neutron Stars in Supernovae and Their Remnants. ArXiv e-prints 1011.3731
- Chevalier RA, Kirshner RP, Raymond JC (1980) The optical emission from a fast shock wave with application to supernova remnants. *ApJ*235:186–195
- Chevalier RA, Oishi J (2003) Cassiopeia A and Its Clumpy Presupernova Wind. *ApJ*593:L23–L26
- Chieffi A, Limongi M (2004) Explosive Yields of Massive Stars from $Z = 0$ to $Z = Z_{\text{solar}}$. *ApJ*608:405–410, arXiv:astro-ph/0402625
- Chiotellis A, Schure KM, Vink J (2011) The imprint of a symbiotic binary progenitor on the properties of Kepler’s supernova remnant. (*A&A* in press), ArXiv e-prints 1103.5487
- Claussen MJ, Frail DA, Goss WM, Gaume RA (1997) Polarization Observations of 1720 MHz OH Masers toward the Three Supernova Remnants W28, W44, and IC 443. *ApJ*489:143–+, arXiv:astro-ph/9706067
- Clayton DD, Silk J (1969) Measuring the Rate of Nucleosynthesis with a Gamma-Ray Detector. *ApJ*158:L43–L48
- Cook WR, et al. (1988) An imaging observation of SN 1987A at gamma-ray energies. *ApJ*334:L87–L90
- Cowie LL, McKee CF (1977) The evaporation of spherical clouds in a hot gas. I - Classical and saturated mass loss rates. *ApJ*211:135–146
- Cox DP, Shelton RL, Maciejewski W, Smith RK, et al. (1999) Modeling W44 as a Supernova Remnant in a Density Gradient with a Partially Formed Dense Shell and Thermal Conduction in the Hot Interior. I. The Analytical Model. *ApJ*524:179–191
- Crotts APS, Kunkel WE, McCarthy PJ (1989) Light echoes and transient luminescence near SN 1987A. *ApJ*347:L61–L64
- CTA Consortium T (2010) Design Concepts for the Cherenkov Telescope Array. ArXiv e-prints 1008.3703
- Cui W, Cox DP (1992) Two-temperature models of old supernova remnants with ion and electron thermal conduction. *ApJ*401:206–219
- Davidson K, Humphreys RM (1997) Eta Carinae and Its Environment. *ARAA*35:1–32
- Davies B, Figer DF, Kudritzki R, Trombly C, et al. (2009) The Progenitor Mass of the Magnetar SGR1900+14. *ApJ*707:844–851, 0910.4859
- de Luca A (2008) Central Compact Objects in Supernova Remnants. In: 40 Years of Pulsars: Millisecond Pulsars, Magnetars and More (ed. C Bassa, Z Wang, A Cumming, & V M Kaspi), vol. 983 of *American Institute of Physics Conference Series*, pp. 311–319, 0712.2209
- De Luca A, Caraveo PA, Mereghetti S, Tiengo A, et al. (2006) A Long-Period, Violently Variable X-ray Source in a Young Supernova Remnant. *Science* 313:814–817, arXiv:astro-ph/0607173
- Decourchelle A, Ellison DC, Ballet J (2000) Thermal X-Ray emission and cosmic-ray production in young supernova remnants. *ApJ*543:L57–L60
- Decourchelle A, et al. (2001) XMM-Newton observation of the Tycho supernova remnant. *A&A*365:L218–L224
- Delaney T, Rudnick L (2003) The first measurement of Cassiopeia A’s forward shock expansion rate. *ApJ*589:818
- DeLaney T, Rudnick L, Stage MD, Smith JD, et al. (2010) The Three-dimensional Structure of Cassiopeia A. *ApJ*725:2038–2058, 1011.3858
- den Herder JW, et al. (2001) The Reflection Grating Spectrometer on board XMM-Newton. *A&A*365:L7–L17
- Dewey D (2002) Extended Source Analysis for Grating Spectrometers. In: High Resolution X-ray Spectroscopy with XMM-Newton and Chandra (ed. G Branduardi-Raymont)
- Dewey D, Delaney T, Lazendic JS (2007) Cas A: The Bright X-ray Knots and Oxygen Emission. In: *Revista Mexicana de Astronomia y Astrofisica Conference Series*, vol. 30 of *Revista Mexicana de Astronomia y Astrofisica Conference Series*, pp. 84–89
- Dewey D, Zhekov SA, McCray R, Canizares CR (2008) Chandra HETG Spectra of SN 1987A at 20 Years. *ApJ*676:L131–L134, 0802.2340
- Dickel JR, Sault R, Arendt RG, Korista KT, et al. (1988) The evolution of the radio emission from Kepler’s Supernova remnant. *ApJ*330:254–263
- Dieckmann ME, Bret A (2009) Particle-In-Cell Simulation of a Strong Double Layer in A Nonrelativistic Plasma Flow: Electron Acceleration to Ultrarelativistic Speeds. *ApJ*694:154–164
- Diehl R, Timmes FX (1998) Gamma-Ray Line Emission from Radioactive Isotopes in Stars and Galaxies. *PASP*110:637–659
- Dodson R, Legge D, Reynolds JE, McCulloch PM (2003) The Vela Pulsar’s Proper Motion and Parallax Derived from VLBI Observations. *ApJ*596:1137–1141, arXiv:astro-ph/0302374
- Dopita MA, Tuohy IR, Mathewson DS (1981) An oxygen-rich young supernova remnant in the Small Magellanic Cloud. *ApJ*248:L105–L108
- Dotani T, Hayashida K, Inoue H, Itoh M, et al. (1987) Discovery of an unusual hard X-ray source in the region of supernova 1987A. *Nat*330:230–+
- Drury L, Aharonian FA, Malyshev D, Gabici S (2009) On the plasma temperature in supernova remnants with cosmic-ray modified shocks. *A&A*496:1–6, 0811.3566
- Drury LO, Duffy P, Kirk JG (1996) Limits on diffusive shock acceleration in dense and incompletely ionised media. *A&A*309:1002–1010, astro-ph/9510066
- Dubner GM, Velázquez PF, Goss WM, Holdaway MA (2000) High-Resolution VLA Imaging of the Supernova Remnant W28 at 328 and 1415 MHz. *AJ*120:1933–1945
- Duncan RC, Thompson C (1992) Formation of very strongly magnetized neutron stars - Implications for gamma-ray bursts. *ApJ*392:L9–L13
- Durant M, van Kerkwijk MH (2006) Distances to Anomalous X-Ray Pulsars Using Red Clump Stars.

- ApJ650:1070–1081, arXiv:astro-ph/0606027
- Dwarkadas VV (2005) The Evolution of Supernovae in Circumstellar Wind-Blown Bubbles. I. Introduction and One-Dimensional Calculations. ApJ630:892–910
- Elias JH, Matthews K, Neugebauer G, Persson SE (1985) Type I supernovae in the infrared and their use as distance indicators. ApJ296:379–389
- Ellison DC, Patnaude DJ, Slane P, Raymond J (2010) Efficient Cosmic Ray Acceleration, Hydrodynamics, and Self-Consistent Thermal X-Ray Emission Applied to Supernova Remnant RX J1713.7-3946. ApJ712:287–293, 1001.1932
- Esposito JA, Hunter SD, Kanbach G, Sreekumar P (1996) EGRET Observations of Radio-bright Supernova Remnants. ApJ461:820–+
- Favata F, et al. (1997) The broad-band X-ray spectrum of the Cas A supernova remnant as seen by the BeppoSAX observatory. A&A324:L49–L52
- Feinstein F, Fiasson A, Gallant Y, Chaves RCG, et al. (2009) What do supernova remnants interacting with molecular clouds reveal? In: American Institute of Physics Conference Series (ed. D Bastieri & R Rando), vol. 1112 of *American Institute of Physics Conference Series*, pp. 54–62
- Ferrario L, Wickramasinghe D (2006) Modelling of isolated radio pulsars and magnetars on the fossil field hypothesis. MNRAS367:1323–1328
- Fesen RA, Hammell MC, Morse J, Chevalier RA, et al. (2006) The Expansion Asymmetry and Age of the Cassiopeia A Supernova Remnant. ApJ645:283–292, arXiv:astro-ph/0603371
- Figier DF, Najarro F, Geballe TR, Blum RD, et al. (2005) Massive Stars in the SGR 1806-20 Cluster. ApJ622:L49–L52, arXiv:astro-ph/0501560
- Fink M, Röpke FK, Hillebrandt W, Seitenzahl IR, et al. (2010) Double-detonation sub-Chandrasekhar supernovae: can minimum helium shell masses detonate the core? A&A514:A53+, 1002.2173
- Flanagan KA, Canizares CR, Dewey D, Houck JC, et al. (2004) Chandra High-Resolution X-Ray Spectrum of Supernova Remnant 1E 0102.2-7219. ApJ605:230–246
- Frail DA, Goss WM, Reynoso EM, Giacani EB, et al. (1996) A Survey for OH (1720 MHz) Maser Emission Toward Supernova Remnants. AJ111:1651–+
- Frail DA, Mitchell GF (1998) OH (1720 MHz) Masers as Signposts of Molecular Shocks. ApJ508:690–695, arXiv:astro-ph/9807011
- Fransson C, Björnsson CI (1998) Radio Emission and Particle Acceleration in SN 1993J. ApJ509:861–878, arXiv:astro-ph/9807030
- Fransson C, Cassatella A, Gilmozzi R, Kirshner RP, et al. (1989) Narrow ultraviolet emission lines from SN 1987A - Evidence for CNO processing in the progenitor. ApJ336:429–441
- Furuzawa A, Ueno D, Hayato A, Ozawa M, et al. (2009) Doppler-Broadened Iron X-Ray Lines From Tycho's Supernova Remnant. ApJ693:L61–L65, 0902.3049
- Gabriel AH, Jordan C (1969) Interpretation of solar helium-like ion line intensities. MNRAS145:241–+
- Gaensler BM, McClure-Griffiths NM, Oey MS, Haverkorn M, et al. (2005) A Stellar Wind Bubble Coincident with the Anomalous X-Ray Pulsar 1E 1048.1-5937: Are Magnetars Formed from Massive Progenitors? ApJ620:L95–L98, arXiv:astro-ph/0501563
- Gaensler BM, Slane PO (2006) The Evolution and Structure of Pulsar Wind Nebulae. ARAA44:17–47, arXiv:astro-ph/0601081
- Gaensler BM, Wallace BJ (2003) A Multifrequency Radio Study of Supernova Remnant G292.0+1.8 and Its Pulsar Wind Nebula. ApJ594:326–339
- Gaetz TJ, Butt YM, Edgar RJ, Eriksen KA, et al. (2000) Chandra X-Ray Observatory Arcsecond Imaging of the Young, Oxygen-rich Supernova Remnant 1E 0102.2-7219. ApJ534:L47–L50, arXiv:astro-ph/0003355
- Galama TJ, Vreeswijk PM, van Paradijs J, et al. (1998) An unusual supernova in the error box of the γ -ray burst of 25 April 1998. Nat395:670–672, arXiv:astro-ph/9806175
- Garmire GP, Pavlov GG, Garmire AB, Zavlin VE (2000) 1E 161348-5055. IAU Circ.7350:2–+
- Garnavich PM, et al. (1998) Supernova Limits on the Cosmic Equation of State. ApJ509:74–79, arXiv:astro-ph/9806396
- Gelfand JD, Gaensler BM (2007) The Compact X-Ray Source 1E 1547.0-5408 and the Radio Shell G327.24-0.13: A New Proposed Association between a Candidate Magnetar and a Candidate Supernova Remnant. ApJ667:1111–1118, 0706.1054
- Ghavamian P, Laming JM, Rakowski CE (2007) A Physical Relationship between Electron-Proton Temperature Equilibration and Mach Number in Fast Collisionless Shocks. ApJ654:L69–L72, arXiv:astro-ph/0611306
- Ghavamian P, Rakowski CE, Hughes JP, Williams TB (2003) The Physics of Supernova Blast Waves. I. Kinematics of DEM L71 in the Large Magellanic Cloud. ApJ590:833–845
- Ghavamian P, Raymond J, Smith RC, Hartigan P (2001) Balmer-dominated spectra of nonradiative shocks in the Cygnus Loop, RCW 86, and Tycho supernova remnants. ApJ547:995–1009
- Ghavamian P, Winkler PF, Raymond JC, Long KS (2002) The optical spectrum of the SN 1006 supernova remnant revisited. ApJ572:888–896
- Ginzburg VL, Syrovatskii SI (1965) Cosmic Magnetobremstrahlung (synchrotron Radiation). ARAA3:297–+
- Ginzburg VL, Syrovatskii SI (1969) The origin of cosmic rays. New York, Gordon and Breach, 1969
- Ginzburg VL, Syrovatskij SI (1967) Cosmic rays in the Galaxy (Introductory Report). In: Radio Astronomy and the Galactic System (ed. H van Woerden), vol. 31 of *IAU Symposium*, pp. 411–+
- Gonzalez M, Safi-Harb S (2003) New Constraints on the Energetics, Progenitor Mass, and Age of the Supernova Remnant G292.0+1.8 Containing PSR J1124-

5916. ApJ583:L91–L94
- Goss WM, Shaver PA, Zealey WJ, Murdin P, et al. (1979) Optical identification and spectrum of the supernova remnant G292.0+1.8. MNRAS188:357–363
- Gotthelf EV, Halpern JP (2007) Precise Timing of the X-ray Pulsar 1E 1207.4-5209: A Steady Neutron Star Weakly Magnetized at Birth. ApJ664:L35–L38, 0704.2255
- Gotthelf EV, Halpern JP (2008) CCO Pulsars as Anti-Magnetars: Evidence of Neutron Stars Weakly Magnetized at Birth. In: 40 Years of Pulsars: Millisecond Pulsars, Magnetars and More (ed. C Bassa, Z Wang, A Cumming, & V M Kaspi), vol. 983 of *American Institute of Physics Conference Series*, pp. 320–324, 0711.1554
- Gotthelf EV, Halpern JP (2009) Discovery of a 112 ms X-Ray Pulsar in Puppis A: Further Evidence of Neutron Stars Weakly Magnetized at Birth. ApJ695:L35–L39, 0902.3007
- Gotthelf EV, Halpern JP, Seward FD (2005) Discovery of a 105 ms X-Ray Pulsar in Kesteven 79: On the Nature of Compact Central Objects in Supernova Remnants. ApJ627:390–396, arXiv:astro-ph/0503424
- Gotthelf EV, Petre R, Vasisht G (1999) X-Ray Variability from the Compact Source in the Supernova Remnant RCW 103. ApJ514:L107–L110
- Gotthelf EV, et al. (2001) Chandra detection of the forward and reverse shocks in Cassiopeia A. ApJ552:L39–L43
- Green AJ, Frail DA, Goss WM, Otrupcek R (1997) Continuation of a survey of OH (1720 MHz) Maser Emission Towards Supernova Remnants. AJ114:2058–
- Hachisu I, Kato M, Nomoto K (1996) A New Model for Progenitor Systems of Type IA Supernovae. ApJ470:L97+
- Hachisu I, Kato M, Nomoto K (1999) A Wide Symbiotic Channel to Type IA Supernovae. ApJ522:487–503, arXiv:astro-ph/9902304
- Hamilton AJS, Chevalier RA, Sarazin CL (1983) X-ray line emission from supernova remnants. I - Models for adiabatic remnants. ApJS51:115–147
- Hamilton AJS, Fesen RA, Blair WP (2007) A high-resolution ultraviolet absorption spectrum of supernova ejecta in SN1006. MNRAS381:771–778, arXiv:astro-ph/0602553
- Hamilton AJS, Sarazin CL, Szymkowiak AE (1986) The X-ray spectrum of SN 1006. ApJ300:698–712
- Hamuy M, Phillips MM, Suntzeff NB, Maza J, et al. (2003) An asymptotic-giant-branch star in the progenitor system of a type Ia supernova. Nat424:651–654, arXiv:astro-ph/0306270
- Hasinger G, Aschenbach B, Truemper J (1996) The X-ray lightcurve of SN 1987A. A&A312:L9–L12, arXiv:astro-ph/9606149
- Hayato A, Yamaguchi H, Tamagawa T, Katsuda S, et al. (2010) Expansion Velocity of Ejecta in Tycho's Supernova Remnant Measured by Doppler Broadened X-ray Line Emission. ApJ725:894–903, 1009.6031
- Heger A, Fryer CL, Woosley SE, Langer N, et al. (2003) How Massive Single Stars End Their Life. ApJ591:288–300
- Heinke CO, Ho WCG (2010) Direct Observation of the Cooling of the Cassiopeia A Neutron Star. ApJ719:L167–L171, 1007.4719
- Helder EA, Kosenko D, Vink J (2010) Cosmic-ray Acceleration Efficiency versus Temperature Equilibration: The Case of SNR 0509-67.5. ApJ719:L140–L144, 1007.3138
- Helder EA, Vink J (2008) Characterizing the Nonthermal Emission of Cassiopeia A. ApJ686:1094–1102
- Helder EA, Vink J, Bassa CG (2011) Temperature Equilibration Behind the Shock Front: An Optical and X-Ray Study Of RCW 86. ApJ737:85–, 1106.0303
- Helder EA, et al. (2009) Cosmic-ray acceleration in a supernova remnant: a quantitative measurement of the efficiency. Science 325:719–722
- Helfand DJ, Becker RH (1984) Observation of stellar remnants from recent supernovae. Nat307:215–221
- Helfand DJ, Collins BF, Gotthelf EV (2003) Chandra X-Ray Imaging Spectroscopy of the Young Supernova Remnant Kesteven 75. ApJ582:783–792, arXiv:astro-ph/0209348
- Helfand DJ, Gotthelf EV, Halpern JP (2001) Vela Pulsar and Its Synchrotron Nebula. ApJ556:380–391, arXiv:astro-ph/0007310
- Hendrick SP, Borkowski KJ, Reynolds SP (2003) Ejecta Detection in Middle-Aged Large Magellanic Cloud Supernova Remnants 0548-70.4 and 0534-69.9. ApJ593:370–376
- Hendrick SP, Reynolds SP, Borkowski KJ (2005) An Fe-Ni Bubble in the Small Magellanic Cloud Supernova Remnant B0049-73.6. ApJ622:L117–L120
- Heng K (2010) Balmer-Dominated Shocks: A Concise Review. Publications of the Astronomical Society of Australia 27:23–44, 0908.4080
- Heng K, Haberl F, Aschenbach B, Hasinger G (2008) Probing Elemental Abundances in SNR 1987A using XMM-Newton. ApJ676:361–370, 0710.3682
- Hester JJ (2008) The Crab Nebula: An Astrophysical Chimera. ARAA46:127–155
- Hines DC, et al. (2004) Imaging of the Supernova Remnant Cassiopeia A with the Multiband Imaging Photometer for Spitzer (MIPS). ApJS154:290–295
- Hinton JA, Hofmann W (2009) Teraelectronvolt Astronomy. ARAA47:523–565
- Hiraga JS, Uchiyama Y, Takahashi T, Aharonian FA (2005) Spectral properties of nonthermal X-ray emission from the shell-type SNR RX J1713.7 3946 as revealed by XMM-Newton. A&A431:953–961, arXiv:astro-ph/0407401
- Hirata K, Kajita T, Koshihara M, Nakahata M, et al. (1987) Observation of a neutrino burst from the supernova SN1987A. Physical Review Letters 58:1490–1493
- Holt SS, Gotthelf EV, Tsunemi H, Negoro H (1994) ASCA observations of Cassiopeia A. PASJ46:L151–L155

- Hörandel JR (2008) Cosmic-ray composition and its relation to shock acceleration by supernova remnants. *Advances in Space Research* 41:442–463, arXiv:astro-ph/0702370
- Horvath JE, Allen MP (2011) The supernova remnant CTB 37B and its associated magnetar CXOU J171405.7-381031: evidence for a magnetar-driven remnant. ArXiv e-prints 1104.2875
- Huba JD (2002) NRL Plasma Formulary
- Hughes JP, Badenes C, Bamba A, Blair W, et al. (2009) Formation of the Elements. In: *astro2010: The Astronomy and Astrophysics Decadal Survey*, vol. 2010 of *Astronomy*, p. 136
- Hughes JP, Ghavamian P, Rakowski CE, Slane PO (2003a) Iron-rich Ejecta in the Supernova Remnant DEM L71. *ApJ*582:L95–L99
- Hughes JP, Hayashi I, Koyama K (1998) ASCA X-Ray Spectroscopy of Large Magellanic Cloud Supernova Remnants and the Metal Abundances of the Large Magellanic Cloud. *ApJ*505:732–748
- Hughes JP, Helfand DJ (1985) Self-consistent models for the X-ray emission from supernova remnants - an application to Kepler's remnant. *ApJ*291:544–560
- Hughes JP, Rakowski CE, Burrows DN, Slane PO (2000) Nucleosynthesis and Mixing in Cassiopeia A. *ApJ*528:L109–L113
- Hughes JP, Singh KP (1994) Elemental abundances of the supernova remnant G292.0+1.8: Evidence for a massive progenitor. *ApJ*422:126–135
- Hughes JP, Slane PO, Burrows DN, Garmire G, et al. (2001) A Pulsar Wind Nebula in the Oxygen-rich Supernova Remnant G292.0+1.8. *ApJ*559:L153–L156, arXiv:astro-ph/0106031
- Hughes JP, Slane PO, Park S, Roming PWA, et al. (2003b) An X-Ray Pulsar in the Oxygen-rich Supernova Remnant G292.0+1.8. *ApJ*591:L139–L142
- Hughes JP, et al. (1995) ASCA observations of the Large Magellanic Cloud supernova remnant sample: Typing supernovae from their remnants. *ApJ*444:L81–L84
- Hwang U, Decourchelle A, Holt SS, Petre R (2002) Thermal and Nonthermal X-Ray Emission from the Forward Shock in Tycho's Supernova Remnant. *ApJ*581:1101–1115
- Hwang U, Gotthelf EV (1997) X-Ray Emission-Line Imaging and Spectroscopy of Tycho's Supernova Remnant. *ApJ*475:665–
- Hwang U, Holt SS, Petre R (2000) Mapping the X-Ray-emitting Ejecta in Cassiopeia A with Chandra. *ApJ*537:L119–L122, arXiv:astro-ph/0005560
- Hwang U, Laming JM (2003) Where was the Iron Synthesized in Cassiopeia A? *ApJ*597:362–373
- Hwang U, Petre R, Flanagan KA (2008) X-Ray-emitting Ejecta in Puppis A Observed with Suzaku. *ApJ*676:378–389, 0712.3208
- Hwang U, Petre R, Holt SS, Szymkowiak AE (2001) The Thermal X-Ray-emitting Shell of Large Magellanic Cloud Supernova Remnant 0540-69.3. *ApJ*560:742–748, arXiv:astro-ph/0106415
- Hwang U, et al. (2004) A Million Second Chandra View of Cassiopeia A. *ApJ*615:L117–L120, astro-ph/0409760
- Itoh H (1977) Theoretical Spectra of the Thermal X-Rays from Young Supernova Remnants. *PASJ*29:813–830
- Itoh H (1978) Two-fluid blast-wave model for SNR. *PASJ*30:489–498
- Itoh H (1984) Temperature relaxation in supernova remnants, revisited. *ApJ*285:601–606
- Itoh H, Masai K (1989) The effect of a circumstellar medium on the X-ray emission of young remnants of Type II supernovae. *MNRAS*236:885–899
- Iwamoto K, et al. (1999) Nucleosynthesis in Chandrasekhar Mass Models for Type IA Supernovae and Constraints on Progenitor Systems and Burning-Front Propagation. *ApJ*5125:439–462
- Iyudin AF, Schonfelder V, Bennett K, Bloemen H, et al. (1998) Emission from ^{44}Ti associated with a previously unknown Galactic supernova. *Nat*396:142–144
- Iyudin AF, et al. (1994) COMPTEL observations of Ti-44 gamma-ray line emission from CAS A. *A&A*284:L1–L4
- Janka HT, Langanke K, Marek A, Martínez-Pinedo G, et al. (2007) Theory of core-collapse supernovae. *PhysRep*442:38–74, arXiv:astro-ph/0612072
- Jerkstrand A, Fransson C, Kozma C (2011) The ^{44}Ti -powered spectrum of SN 1987A. *A&A*530:A45+, 1103.3653
- Jones TW, Rudnick L, Jun B, Borkowski KJ, et al. (1998) 10^{51} Ergs: The Evolution of Shell Supernova Remnants. *PASP*110:125–151, arXiv:astro-ph/9710227
- Joyce RM, Birsá FB, Holt SS, Noordzy MP, et al. (1978) The Goddard Space Flight Center Solid State Spectrometer for the HEAO-B Mission. *IEEE Transactions on Nuclear Science* 25:453–458
- Kaastra JS, Jansen FA (1993) A spectral code for X-ray spectra of supernova remnants. *A&AS*97:873–885
- Kaastra JS, Mewe R (1995) Optical depth effects in the X-ray emission from supernova remnants. *A&A*302:L13+
- Kaastra JS, Mewe R, Raassen T (2003) New Results on X-Ray Models and Atomic Data. *Atomic Data for X-Ray Astronomy*, 25th meeting of the IAU, Joint Discussion 17, 22 July 2003, Sydney, Australia 17
- Kaastra JS, Paerels FBS, Durret F, Schindler S, et al. (2008) Thermal Radiation Processes. *Space Science Reviews* 134:155–190, 0801.1011
- Kahabka P, van den Heuvel EPJ (1997) Luminous Super-soft X-Ray Sources. *ARAA*35:69–100
- Kahn SM, Gorenstein P, Harnden FR Jr, Seward FD (1985) Einstein observations of the VELA supernova remnant - The spatial structure of the hot emitting gas. *ApJ*299:821–827
- Kalemci E, Boggs SE, Milne PA, Reynolds SP (2006) Searching for Annihilation Radiation from SN 1006 with SPI on INTEGRAL. *ApJ*640:L55–L57, arXiv:astro-ph/0602233
- Kallman TR, Palmeri P, Bautista MA, Mendoza C, et al.

- (2004) Photoionization Modeling and the K Lines of Iron. *ApJS*155:675–701, [arXiv:astro-ph/0405210](#)
- Kargaltsev O, Pavlov GG (2008) Pulsar Wind Nebulae in the Chandra Era. In: 40 Years of Pulsars: Millisecond Pulsars, Magnetars and More (eds. Bassa C, Wang Z, Cumming A, Kaspi VM), vol. 983 of *AIP Conf. Series*, pp. 171–185
- Kaspi VM (1998) Radio pulsar/supernova remnant associations. *Advances in Space Research* 21:167–176
- Katsuda S, Mori K, Tsunemi H, Park S, et al. (2008a) Discovery of Fast-Moving X-Ray-Emitting Ejecta Knots in the Oxygen-Rich Supernova Remnant Puppis A. *ApJ*678:297–302, 0805.1369
- Katsuda S, Petre R, Hughes JP, Hwang U, et al. (2010a) X-ray Measured Dynamics of Tycho’s Supernova Remnant. *ApJ*709:1387–1395, 1001.2484
- Katsuda S, Petre R, Long KS, Reynolds SP, et al. (2009) The First X-Ray Proper-Motion Measurements of the Forward Shock in the Northeastern Limb of SN 1006. *ApJ*692:L105–L108, 0901.0149
- Katsuda S, Petre R, Mori K, Reynolds SP, et al. (2010b) Steady X-ray Synchrotron Emission in the Northeastern Limb of SN 1006. *ApJ*723:383–392, 1009.0280
- Katsuda S, Tsunemi H (2005) Spatially Resolved Spectral Analysis of Vela Shrapnel D. *PASJ*57:621–628, [arXiv:astro-ph/0507344](#)
- Katsuda S, Tsunemi H (2006) Spatially Resolved X-Ray Spectroscopy of Vela Shrapnel A. *ApJ*642:917–922, [arXiv:astro-ph/0603454](#)
- Katsuda S, Tsunemi H, Kimura M, Mori K (2008b) Chandra Observations of the Northeastern Rim of the Cygnus Loop. *ApJ*680:1198–1205, 0806.4005
- Katsuda S, Tsunemi H, Mori K, Uchida H, et al. (2011) Possible Charge-exchange X-ray Emission in the Cygnus Loop Detected with Suzaku. *ApJ*730:24–, 1103.1669
- Katsuda S, Tsunemi H, Uchida H, Kimura M (2008c) Forward Shock Proper Motions of Kepler’s Supernova Remnant. *ApJ*689:225–230, 0812.0339
- Katz B, Waxman E (2008) In which shell-type SNRs should we look for gamma-rays and neutrinos from P-P collisions? *Journal of Cosmology and Astro-Particle Physics* 1:18–, 0706.3485
- Kawasaki M, Ozaki M, Nagase F, Inoue H, et al. (2005) Ionization States and Plasma Structures of Mixed-Morphology Supernova Remnants Observed with ASCA. *ApJ*631:935–946, [arXiv:astro-ph/0507348](#)
- Kawasaki MT, Ozaki M, Nagase F, Masai K, et al. (2002) ASCA Observations of the Supernova Remnant IC 443: Thermal Structure and Detection of Overionized Plasma. *ApJ*572:897–905, [arXiv:astro-ph/0202484](#)
- Kelly PL, Kirshner RP, Pahre M (2008) Long γ -Ray Bursts and Type Ic Core-Collapse Supernovae Have Similar Locations in Hosts. *ApJ*687:1201–1207, 0712.0430
- Khokhlov AM (1991) Delayed detonation model for type IA supernovae. *A&A*245:114–128
- Kifonidis K, Plewa T, Janka HT, Müller E (2003) Non-spherical core collapse supernovae. I. Neutrino-driven convection, Rayleigh-Taylor instabilities, and the formation and propagation of metal clumps. *A&A*408:621–649
- Kifonidis K, Plewa T, Scheck L, Janka H, et al. (2006) Non-spherical core collapse supernovae. II. The late-time evolution of globally anisotropic neutrino-driven explosions and their implications for SN 1987 A. *A&A*453:661–678, [arXiv:astro-ph/0511369](#)
- Kinugasa K, Tsunemi H (1999) ASCA Observation of Kepler’s Supernova Remnant. *PASJ*51:239–252
- Kirshner RP (2007) SN 1987A: Twenty Years of Serious Fun with IUE and HST. In: *Supernova 1987A: 20 Years After: Supernovae and Gamma-Ray Bursters* (ed. S Immler, K Weiler, & R McCray), vol. 937 of *American Institute of Physics Conference Series*, pp. 15–24
- Klein RI, McKee CF, Colella P (1994) On the hydrodynamic interaction of shock waves with interstellar clouds. 1: Nonradiative shocks in small clouds. *ApJ*420:213–236
- Koralesky B, Frail DA, Goss WM, Claussen MJ, et al. (1998a) Shock-excited Maser Emission from Supernova Remnants: G32.8-0.1, G337.8-0.1, G346.6-0.2, and the HB 3/W3 Complex. *AJ*116:1323–1331, [arXiv:astro-ph/9805371](#)
- Koralesky B, Rudnick L, Gotthelf EV, Keohane JW (1998b) The X-Ray Expansion of the Supernova Remnant Cassiopeia A. *ApJ*505:L27+, [arXiv:astro-ph/9806241](#)
- Kosenko D, Blinnikov SI, Vink J (2011) Modeling supernova remnants: effects of diffusive cosmic-ray acceleration on the evolution, application to observations. *ArXiv e-prints* 1105.5966
- Kosenko D, Helder EA, Vink J (2010) The kinematics and chemical stratification of the type Ia supernova remnant 0519-69.0. An XMM-Newton and Chandra study. *A&A*519:A11+, 1001.0983
- Kosenko D, Vink J, Blinnikov S, Rasmussen A (2008) XMM-Newton X-ray spectra of the SNR 0509-67.5: data and models. *A&A*490:223–230, 0807.0579
- Kosenko DI (2006) Inner-shell ionization, radiative losses and thermal conductivity in young SNRs. *MNRAS*369:1407–1410, [arXiv:astro-ph/0605349](#)
- Koyama K, Kinugasa K, Matsuzaki K, Nishiuchi M, et al. (1997) Discovery of non-thermal X-rays from the northwest shell of the new SNR RX J1713.7-3946. *PASJ*49:L7–L11
- Koyama K, et al. (1995) Evidence for Shock Acceleration of High-Energy Electrons in the Supernova Remnant SN 1006. *Nat*378:255–
- Krause J, Carmona E, Reichardt I, for the MAGIC Collaboration (2011) Probing proton acceleration in W51C with MAGIC. *ArXiv e-prints* 1111.0066
- Krause MO (1979) Atomic radiative and radiationless yields for K and L shells. *Journal of Physical and Chemical Reference Data* 8:307–327
- Krause O, Birkmann SM, Usuda T, Hattori T, et al.

- (2008a) The Cassiopeia A Supernova Was of Type IIb. *Science* 320:1195–, arXiv:0805.4557
- Krause O, Tanaka M, Usuda T, Hattori T, et al. (2008b) Tycho Brahe's 1572 supernova as a standard type Ia as revealed by its light-echo spectrum. *Nat*456:617–619, 0810.5106
- Krymskii GF (1977) A regular mechanism for the acceleration of charged particles on the front of a shock wave. *Soviet Physics Doklady* 22:327–+
- Kurfess JD, et al. (1992) Oriented Scintillation Spectrometer Experiment observations of Co-57 in SN 1987A. *ApJ*399:L137–L140
- Laming JM (2001a) Accelerated electrons in Cassiopeia A: An explanation for the hard X-ray tail. *ApJ*546:1149–1158
- Laming JM (2001b) Accelerated electrons in Cassiopeia A: Thermal and electromagnetic effects. *ApJ*563:828–841
- Laming JM, Hwang U, Radics B, Lekli G, et al. (2006) The Polar Regions of Cassiopeia A: The Aftermath of a Gamma-Ray Burst? *ApJ*644:260–273, astro-ph/0603434
- Lasker BM (1979) The shell nebulae in the Magellanic Clouds - A survey in forbidden S II, H-alpha, and forbidden O III. *PASP*91:153–157
- Lazendic JS, Dewey D, Schulz NS, Canizares CR (2006) The Kinematic and Plasma Properties of X-Ray Knots in Cassiopeia A from the Chandra HETGS. *ApJ*651:250–267, arXiv:astro-ph/0605078
- Lazendic JS, Slane PO (2006) Enhanced Abundances in Three Large-Diameter Mixed-Morphology Supernova Remnants. *ApJ*647:350–366, arXiv:astro-ph/0505498
- Lazendic JS, Wardle M, Burton MG, Yusef-Zadeh F, et al. (2002) Shocked molecular gas towards the supernova remnant G359.1-0.5 and the Snake. *MNRAS*331:537–544, arXiv:astro-ph/0112410
- Lee JJ, Park S, Hughes JP, Slane PO, et al. (2011) SNR 0104-72.3: A Remnant of a Type Ia Supernova in a Star-forming Region? *ApJ*731:L8+, 1012.5703
- Leising MD (2001) Prospects for X-Ray Studies of Supernova Electron Capture Radioactivity. *ApJ*563:185–190
- Leising MD (2006) X-ray astronomy of radioactivity in SN 1987A. *NewAR*50:557–560
- Leising MD, Share GH (1990) The gamma-ray light curves of SN 1987A. *ApJ*357:638–648
- Leonard PJT, Duncan MJ (1990) Runaway stars from young star clusters containing initial binaries. II - A mass spectrum and a binary energy spectrum. *AJ*99:608–616
- Levenson NA, Graham JR, Hester JJ, Petre R (1996) All Quiet on the Western Front? X-Ray and Optical Observations of a Prototypical Cloud-Blast Wave Interaction in the Cygnus Loop. *ApJ*468:323–+
- Levenson NA, Graham JR, Keller LD, Richter MJ (1998) Panoramic Views of the Cygnus Loop. *ApJS*118:541–561
- Levenson NA, Graham JR, Walters JL (2002) Shell Shock and Cloud Shock: Results from Spatially Resolved X-Ray Spectroscopy with Chandra in the Cygnus Loop. *ApJ*576:798–805, arXiv:astro-ph/0205191
- Lewis KT, Burrows DN, Hughes JP, Slane PO, et al. (2003) The Radial Structure of Supernova Remnant N103B. *ApJ*582:770–782, arXiv:astro-ph/0209280
- Li X, van den Heuvel EPJ (1997) Evolution of white dwarf binaries: supersoft X-ray sources and progenitors of type Ia supernovae. *A&A*322:L9–L12
- Liedahl DA (1999) The X-Ray Spectral Properties of Photoionized Plasma and Transient Plasmas. *Lecture Notes in Physics*, Berlin Springer Verlag 520:189–+
- Long KS, Reynolds SP, Raymond JC, Winkler PF, et al. (2003) Chandra CCD Imagery of the Northeast and Northwest Limbs of SN 1006. *ApJ*586:1162–1178
- Lopez LA, Ramirez-Ruiz E, Badenes C, Huppenkothen D, et al. (2009) Typing Supernova Remnants Using X-Ray Line Emission Morphologies. *ApJ*706:L106–L109, 0910.3208
- Lopez LA, Ramirez-Ruiz E, Huppenkothen D, Badenes C, et al. (2011) Using the X-ray Morphology of Young Supernova Remnants to Constrain Explosion Type, Ejecta Distribution, and Chemical Mixing. *ApJ*732:114–+, 1011.0731
- Lu FJ, Aschenbach B (2000) Spatially resolved X-ray spectroscopy of the Vela supernova remnant. *A&A*362:1083–1092
- Lynden-Bell D (1967) Statistical mechanics of violent relaxation in stellar systems. *MNRAS*136:101–+
- Maeda Y, Uchiyama Y, Bamba A, Kosugi H, et al. (2009) Suzaku X-Ray Imaging and Spectroscopy of Cassiopeia A. *PASJ*61:1217–, 0912.5020
- Mahoney WA, Varnell LS, Jacobson AS, Ling JC, et al. (1988) Gamma-ray observations of Co-56 in SN 1987A. *ApJ*334:L81–L85
- Malkov MA (1997) Analytic Solution for Nonlinear Shock Acceleration in the Bohm Limit. *ApJ*485:638–+, arXiv:astro-ph/9707152
- Malkov MA, Drury L (2001) Nonlinear theory of diffusive acceleration of particles by shock waves. *Reports of Progress in Physics* 64:429–481
- Mannucci F, Della Valle M, Panagia N (2006) Two populations of progenitors for Type Ia supernovae? *MNRAS*370:773–783, arXiv:astro-ph/0510315
- Marcaide JM, Martí-Vidal I, Alberdi A, Pérez-Torres MA, et al. (2009) A decade of SN 1993J: discovery of radio wavelength effects in the expansion rate. *A&A*505:927–945, 0903.3833
- Markert TH, Clark GW, Winkler PF, Canizares CR (1983) High-velocity, asymmetric Doppler shifts of the X-ray emission lines of Cassiopeia A. *ApJ*268:134–144
- Martin DC, Seibert M, Neill JD, Schiminovich D, et al. (2007) A turbulent wake as a tracer of 30,000 years of Mira's mass loss history. *Nat*448:780–783
- Martin P, Vink J, Jiraskova S, Jean P, et al. (2010) Annihilation emission from young supernova remnants. *A&A*519:A100+, 1006.2537

- Mathewson DS, Dopita MA, Tuohy IR, Ford VL (1980) A new oxygen-rich supernova remnant in the Large Magellanic Cloud. *ApJ*242:L73–L76
- Matsunaga K, et al. (2001) Detection of Eight Molecular Shells in the Southern Milky Way with Nanten. *PASJ*53:1003–1016
- Mazzali PA, Röpke FK, Benetti S, Hillebrandt W (2007) A Common Explosion Mechanism for Type Ia Supernovae. *Science* 315:825–, [arXiv:astro-ph/0702351](#)
- McCray R (2007) Supernova 1987A at Age 20. In: *Supernova 1987A: 20 Years After: Supernovae and Gamma-Ray Bursters* (ed. S Immler, K Weiler, & R McCray), vol. 937 of *American Institute of Physics Conference Series*, pp. 3–14
- McCray R, Snow TP Jr (1979) The violent interstellar medium. *ARAA*17:213–240
- McKee CF (1974) X-Ray Emission from an Inward-Propagating Shock in Young Supernova Remnants. *ApJ*188:335–340
- McKee CF, Hollenbach DJ (1980) Interstellar shock waves. *ARAA*18:219–262
- Mendoza C, Kallman TR, Bautista MA, Palmeri P (2004) Decay properties of K-vacancy states in Fe X-Fe XVII. *A&A*414:377–388, [arXiv:astro-ph/0306320](#)
- Mereghetti S (2008) The strongest cosmic magnets: soft gamma-ray repeaters and anomalous X-ray pulsars. *A&A Rev.*15:225–287, 0804.0250
- Mewe R (1999) *Atomic Physics of Hot Plasmas*. Lecture Notes in Physics, Berlin Springer Verlag 520:109–+
- Mewe R, Schrijver J (1978) Heliumlike Ion Line Intensities. II Non-stationary Plasmas. *A&A*65:115–+
- Miceli M, Bocchino F, Iakubovskiy D, Orlando S, et al. (2009) Thermal emission, shock modification, and X-ray emitting ejecta in SN 1006. *A&A*501:239–249, 0903.3392
- Miceli M, Bocchino F, Maggio A, Reale F (2005) Shock-cloud interaction in the Vela SNR observed with XMM-Newton. *A&A*442:513–525, [arXiv:astro-ph/0509911](#)
- Miceli M, Bocchino F, Reale F (2008) Physical and Chemical Inhomogeneities inside the Vela SNR Shell: Indications of Ejecta Shrapnels. *ApJ*676:1064–1072, 0712.3017
- Michael E, Zhekov S, McCray R, Hwang U, et al. (2002) The X-Ray Spectrum of Supernova Remnant 1987A. *ApJ*574:166–178
- Minkowski R (1941) Spectra of Supernovae. *PASP*53:224–+
- Miyata E, Katsuda S, Tsunemi H, Hughes JP, et al. (2007) Detection of Highly-Ionized Carbon and Nitrogen Emission Lines from the Cygnus Loop Supernova Remnant with the Suzaku Observatory. *PASJ*59:163–170
- Miyata E, Masai K, Hughes JP (2008) Evidence for Resonance Line Scattering in the Suzaku X-Ray Spectrum of the Cygnus Loop. *PASJ*60:521–, 0801.4418
- Miyata E, Tsunemi H (1999) The Radial Structure of the Cygnus Loop Supernova Remnant: Possible Evidence of a Cavity Explosion. *ApJ*525:305–317
- Miyata E, Tsunemi H, Aschenbach B, Mori K (2001) Chandra X-Ray Observatory Study of Vela Shrapnel A. *ApJ*559:L45–L48
- Miyata E, Tsunemi H, Pisarski R, Kissel SE (1994) The plasma structure of the north-east rim of the Cygnus Loop as observed with ASCA. *PASJ*46:L101–L104
- Mokiem MR, de Koter A, Vink JS, Puls J, et al. (2007) The empirical metallicity dependence of the mass-loss rate of O- and early B-type stars. *A&A*473:603–614, 0708.2042
- Morlino G, Blasi P, Vietri M (2007) On Particle Acceleration around Shocks. IV. Particle Spectrum as a Function of the Equation of State of the Shocked Plasma. *ApJ*662:980–987, [arXiv:astro-ph/0703555](#)
- Morris DJ, Bennett K, Bloemen H, Diehl R, et al. (1997) Reassessment of the ⁵⁶Co emission from SN 1991T. In: *AIP Conf. Proc.* 410: Proceedings of the Fourth Compton Symposium, pp. 1084–+
- Morris T, Podsiadlowski P (2007) The Triple-Ring Nebula Around SN 1987A: Fingerprint of a Binary Merger. *Science* 315:1103–, [arXiv:astro-ph/0703317](#)
- Morris T, Podsiadlowski P (2009) A binary merger model for the formation of the Supernova 1987A triple-ring nebula. *MNRAS*399:515–538
- Muno MP, Clark JS, Crowther PA, Dougherty SM, et al. (2006) A Neutron Star with a Massive Progenitor in Westerlund 1. *ApJ*636:L41–L44, [arXiv:astro-ph/0509408](#)
- Nagataki S, Hashimoto M, Sato K, Yamada S, et al. (1998) The High Ratio of ⁴⁴Ti/ ⁵⁶Ni in Cassiopeia A and the Axisymmetric Collapse-driven Supernova Explosion. *ApJ*492:L45+
- Nemes N, Tsunemi H, Miyata E (2008) XMM-Newton Observation of the Northeastern Limb of the Cygnus Loop. *ApJ*675:1293–1303
- Ng C, Gaensler BM, Staveley-Smith L, Manchester RN, et al. (2008) Fourier Modeling of the Radio Torus Surrounding SN 1987A. *ApJ*684:481–497, 0805.4195
- Nishiuchi M, Yokogawa J, Koyama K, Hughes JP (2001) ASCA Observations of the Twin Supernova Remnants in the Large Magellanic Cloud, DEM L316. *PASJ*53:99–104, [arXiv:astro-ph/0009318](#)
- Nomoto K (1982) Accreting white dwarf models for type I supernovae. I - Presupernova evolution and triggering mechanisms. *ApJ*253:798–810
- Nomoto K, Tanaka M, Tominaga N, Maeda K (2010) Hypernovae, gamma-ray bursts, and first stars. *NewAR*54:191–200
- Nomoto K, Thielemann FK, Yokoi K (1984) Accreting white dwarf models of Type I supernovae. III - Carbon deflagration supernovae. *ApJ*286:644–658
- Nugis T, Lamers HJGLM (2000) Mass-loss rates of Wolf-Rayet stars as a function of stellar parameters. *A&A*360:227–244
- Ohnishi T, Koyama K, Tsuru TG, Masai K, et al. (2011) X-Ray Spectrum of a Peculiar Supernova Remnant, G359.1-0.5. *PASJ*63:527–

- Olausen SA, Kaspi VM, Ng CY, Zhu WW, et al. (2011) On the Extended Emission around the Anomalous X-Ray Pulsar 1E 1547.0-5408. *ApJ*742:4, 1107. 2952
- Ott CD, Burrows A, Thompson TA, Livne E, et al. (2006) The Spin Periods and Rotational Profiles of Neutron Stars at Birth. *ApJS*164:130–155, astro-ph/0508462
- Ozawa M, Koyama K, Yamaguchi H, Masai K, et al. (2009) Suzaku Discovery of the Strong Radiative Recombination Continuum of Iron from the Supernova Remnant W49B. *ApJ*706:L71–L75, 0910.3302
- Palmeri P, Mendoza C, Kallman TR, Bautista MA, et al. (2003) Modeling of iron K lines: Radiative and Auger decay data for Fe II-Fe IX. *A&A*410:359–364, arXiv:astro-ph/0306321
- Pannuti TG, Allen GE, Filipović MD, De Horta A, et al. (2010a) Non-thermal X-ray Emission from the Northwestern Rim of the Galactic Supernova Remnant G266.2-1.2 (RX J0852.0-4622). *ApJ*721:1492–1508, 1008.1072
- Pannuti TG, Rho J, Borkowski KJ, Cameron PB (2010b) Mixed-morphology Supernova Remnants in X-rays: Isothermal Plasma in HB21 and Probable Oxygen-rich Ejecta in CTB 1. *AJ*140:1787–1805, 1009.3987
- Parizot E, Marcowith A, Ballet J, Gallant YA (2006) Observational constraints on energetic particle diffusion in young supernovae remnants: amplified magnetic field and maximum energy. *A&A*453:387–395, arXiv:astro-ph/0603723
- Parizot E, Marcowith A, van der Swaluw E, Bykov AM, et al. (2004) Superbubbles and energetic particles in the Galaxy. I. Collective effects of particle acceleration. *A&A*424:747–760, arXiv:astro-ph/0405531
- Park S, Hughes JP, Burrows DN, Slane PO, et al. (2003) 0103-72.6: A New Oxygen-rich Supernova Remnant in the Small Magellanic Cloud. *ApJ*598:L95–L98, arXiv:astro-ph/0309271
- Park S, Hughes JP, Slane PO, Burrows DN, et al. (2007) A Half-Megasecond Chandra Observation of the Oxygen-rich Supernova Remnant G292.0+1.8. *ApJ*670:L121–L124, 0710.2902
- Park S, Hughes JP, Slane PO, Mori K, et al. (2010) A Deep Chandra Observation of the Oxygen-Rich Supernova Remnant 0540-69.3 in the Large Magellanic Cloud. *ApJ*710:948–957, 0912.5177
- Park S, Lee J, Hughes JP, Slane PO, et al. (2009) Chandra Observation of the Galactic SNR G272.2-3.2. In: American Astronomical Society Meeting Abstracts 214, vol. 214 of *American Astronomical Society Meeting Abstracts*, pp. 426.04–
- Park S, Zhekov SA, Burrows DN, Garmire GP, et al. (2006) Evolutionary Status of SNR 1987A at the Age of Eighteen. *ApJ*646:1001–1008, arXiv:astro-ph/0604201
- Park S, Zhekov SA, Burrows DN, McCray R (2005) SNR 1987A: Opening the Future by Reaching the Past. *ApJ*634:L73–L76, arXiv:astro-ph/0510442
- Park S, et al. (2002) The Structure of the Oxygen-rich Supernova Remnant G292.0+1.8 from Chandra X-Ray Images: Shocked Ejecta and Circumstellar Medium. *ApJ*564:L39–L43
- Patnaude DJ, Fesen RA (2007) Small-Scale X-Ray Variability in the Cassiopeia A Supernova Remnant. *AJ*133:147–153, arXiv:astro-ph/0609412
- Patnaude DJ, Fesen RA (2009) Proper Motions and Brightness Variations of Nonthermal X-ray Filaments in the Cassiopeia A Supernova Remnant. *ApJ*697:535–543, 0808.0692
- Patnaude DJ, Fesen RA, Raymond JC, Levenson NA, et al. (2002) An Isolated, Recently Shocked ISM Cloud in the Cygnus Loop Supernova Remnant. *AJ*124:2118–2134, arXiv:astro-ph/0206492
- Patnaude DJ, Vink J, Laming JM, Fesen RA (2011) A Decline in the Nonthermal X-ray Emission from Cassiopeia A. *ApJ*729:L28+, 1012.0243
- Perlmutter S, et al. (1998) Discovery of a supernova explosion at half the age of the universe. *Nat*391:51–+, arXiv:astro-ph/9712212
- Petre R, Serlemitsos PJ, Marshall FE, Jahoda KA, et al. (1993) Highlights of the BBXRT mission. In: *UV and X-Ray Spectroscopy of Astrophysical and Laboratory Plasmas*, pp. 424–433
- Pfeffermann E, Aschenbach B (1996) ROSAT Observation of a New Supernova Remnant in the Constellation Scorpius. In: *Roentgenstrahlung from the Universe*, eds. Zimmermann, H.U., Trümper, and Yorke, H., pp. 267–268
- Phillips MM, et al. (1992) SN 1991T - Further evidence of the heterogeneous nature of type IA supernovae. *AJ*103:1632–1637
- Podsiadlowski P (1992) The progenitor of SN 1987 A. *PASP*104:717–729
- Podsiadlowski P, Hsu JLL, Joss PC, Ross RR (1993) The progenitor of supernova 1993J - A stripped supergiant in a binary system? *Nat*364:509–511
- Podsiadlowski P, Joss PC, Hsu JLL (1992) Presupernova evolution in massive interacting binaries. *ApJ*391:246–264
- Pohl M, Yan H, Lazarian A (2005) Magnetically Limited X-Ray Filaments in Young Supernova Remnants. *ApJ*626:L101–L104
- Porquet D, Dubau J, Grosso N (2010) He-like Ions as Practical Astrophysical Plasma Diagnostics: From Stellar Coronae to Active Galactic Nuclei. *SSRv*157:103–134, 1101.3184
- Porquet D, Mewe R, Dubau J, Raassen AJJ, et al. (2001) Line ratios for helium-like ions: Applications to collision-dominated plasmas. *A&A*376:1113–1122, arXiv:astro-ph/0107329
- Prantzos N (2011) Nucleosynthesis and gamma-ray lines. *ArXiv e-prints* 1101.2112
- Prantzos N, Boehm C, Bykov AM, Diehl R, et al. (2011) The 511 keV emission from positron annihilation in the Galaxy. *Reviews of Modern Physics* 83:1001–1056, 1009.4620
- Racusin JL, Park S, Zhekov S, Burrows DN, et al. (2009) X-ray Evolution of SNR 1987A: The Radial Expansion.

- ApJ703:1752–1759, 0908.2097
- Rakowski CE, Ghavamian P, Hughes JP (2003) The Physics of Supernova Remnant Blast Waves. II. Electron-Ion Equilibration in DEM L71 in the Large Magellanic Cloud. ApJ590:846–857
- Rakowski CE, Laming JM, Ghavamian P (2008) The Heating of Thermal Electrons in Fast Collisionless Shocks: The Integral Role of Cosmic Rays. ApJ684:348–357, 0805.3084
- Rasmussen AP, et al. (2001) The X-ray spectrum of the supernova remnant $\text{jASTROBJ}_{\text{I}}\text{E 0102.2-7219j}/\text{ASTROBJ}_{\text{I}}$. A&A365:L231–L236
- Raymond JC, Blair WP, Long KS (1995) Detection of Ultraviolet Emission Lines in SN 1006 with the Hopkins Ultraviolet Telescope. ApJ454:L31–L37
- Raymond JC, Vink J, Helder EA, de Laat A (2011) Effects of Neutral Hydrogen on Cosmic-ray Precursors in Supernova Remnant Shock Waves. ApJ731:L14+, 1103.3211
- Reach WT, Rho J, Jarrett TH (2005) Shocked Molecular Gas in the Supernova Remnants W28 and W44: Near-Infrared and Millimeter-Wave Observations. ApJ618:297–320, arXiv:astro-ph/0409414
- Reed JE, Hester JJ, Fabian AC, Winkler PF (1995) The three-dimensional structure of the Cassiopeia A supernova remnant. I. The spherical shell. ApJ440:706–721
- Renaud M, et al. (2006a) An INTEGRAL/IBIS view of young Galactic SNRs through the ^{44}Ti gamma-ray lines. New Astronomy Review 50:540–543, astro-ph/0602304
- Renaud M, et al. (2006b) The Signature of ^{44}Ti in Cassiopeia A Revealed by IBIS/ISGRI on INTEGRAL. ApJ647:L41–L44
- Rest A, et al. (2005) Light echoes from ancient supernovae in the Large Magellanic Cloud. Nat438:1132–1134, arXiv:astro-ph/0510738
- Rest A, et al. (2008) Spectral Identification of an Ancient Supernova Using Light Echoes in the Large Magellanic Cloud. ApJ680:1137–1148, 0801.4762
- Reville B, Kirk JG, Duffy P (2009) Steady-State Solutions in Nonlinear Diffusive Shock Acceleration. ApJ694:951–958, 0812.3993
- Reynolds SP (1998) Models of synchrotron X-rays from shell supernova remnants. ApJ493:375–
- Reynolds SP (2008) Supernova Remnants at High Energy. ARAA46:89–126
- Reynolds SP, Borkowski KJ, Green DA, Hwang U, et al. (2008) The Youngest Galactic Supernova Remnant: G1.9+0.3. ApJ680:L41–L44, 0803.1487
- Reynolds SP, Borkowski KJ, Hwang U, Hughes JP, et al. (2007) A Deep Chandra Observation of Kepler’s Supernova Remnant: A Type Ia Event with Circumstellar Interaction. ApJ668:L135–L138, arXiv:0708.3858
- Reynolds SP, Chevalier RA (1981) Nonthermal Radiation from Supernova Remnants in the Adiabatic Stage of Evolution. ApJ245:912–
- Reynolds SP, Ellison DC (1992) Electron acceleration in Tycho’s and Kepler’s supernova remnants - Spectral evidence of Fermi shock acceleration. ApJ399:L75–L78
- Reynoso EM, Dubner GM, Goss WM, Arnal EM (1995) VLA Observations of Neutral Hydrogen in the Direction of Puppis A. AJ110:318–
- Reynoso EM, Moffett DA, Goss WM, Dubner GM, et al. (1997) A VLA Study of the Expansion of Tycho’s Supernova Remnant. ApJ491:816–
- Rho J, Dyer KK, Borkowski KJ, Reynolds SP (2002) X-ray synchrotron-emitting Fe-rich ejecta in supernova remnant RCW 86. ApJ581:1116–1131
- Rho J, Petre R (1998) Mixed-Morphology Supernova Remnants. ApJ503:L167+
- Riess AG, et al. (2007) New Hubble Space Telescope Discoveries of Type Ia Supernovae at $z > 1$: Narrowing Constraints on the Early Behavior of Dark Energy. ApJ659:98–121, arXiv:astro-ph/0611572
- Riquelme MA, Spitkovsky A (2011) Electron Injection by Whistler Waves in Non-relativistic Shocks. ApJ733:63–+, 1009.3319
- Rosado M, Le Coarer E, Georgelin YP (1994) Kinematics of supernova remnants in the Small Magellanic Cloud I. The SNRs inside the nebular complex N 19, the SNR 0046-73.5 and the SNR 0050-72.8. A&A286:231–242
- Rothenflug R, et al. (2004) Geometry of the non-thermal emission in SN 1006. A&A425:121–131
- Ruiter AJ, Belczynski K, Fryer C (2009) Rates and Delay Times of Type Ia Supernovae. ApJ699:2026–2036, 0904.3108
- Rybicki GB, Lightman AP (1979) Radiative processes in astrophysics. New York, Wiley-Interscience, 1979
- Salvesen G, Raymond JC, Edgar RJ (2009) Shock Speed, Cosmic Ray Pressure, and Gas Temperature in the Cygnus Loop. ApJ702:327–339, 0812.2515
- Sandie WG, Nakano GH, Chase LF, Fishman GJ, et al. (1988) High-resolution observations of gamma-ray line emission from SN 1987A. ApJ334:L91–L94
- Sankrit R, Blair WP, Delaney T, Rudnick L, et al. (2005) HST/ACS imaging of a Balmer-dominated shock in Kepler’s supernova remnant. Advances in Space Research 35:1027–1030
- Schaefer BE (2008) a Problem with the Clustering of Recent Measures of the Distance to the Large Magellanic Cloud. AJ135:112–119, 0709.4531
- Schure KM, Achterberg A, Keppens R, Vink J (2010) Time-dependent particle acceleration in supernova remnants in different environments. MNRAS406:2633–2649, 1004.2766
- Schure KM, Kosenko D, Kaastra JS, Keppens R, et al. (2009) A new radiative cooling curve based on an up-to-date plasma emission code. A&A508:751–757, 0909.5204
- Schure KM, Vink J, García-Segura G, Achterberg A (2008) Jets as Diagnostics of the Circumstellar Medium and the Explosion Energetics of Supernovae: The Case of Cassiopeia A. ApJ686:399–407, 0806.4617
- Sedov LI (1959) Similarity and Dimensional Methods in Mechanics. Similarity and Dimensional Methods in Mechanics, New York: Academic Press, 1959

- Seward FD, Williams RM, Chu YH, Dickel JR, et al. (2006) Chandra Observation of the Magellanic Cloud Supernova Remnant 0454-67.2 in N9. *ApJ*640:327–334, arXiv:astro-ph/0511619
- Shelton RL, Cox DP, Maciejewski W, Smith RK, et al. (1999) Modeling W44 as a Supernova Remnant in a Density Gradient with a Partially Formed Dense Shell and Thermal Conduction in the Hot Interior. II. The Hydrodynamic Models. *ApJ*524:192–212, arXiv:astro-ph/9806090
- Shelton RL, Kuntz KD, Petre R (2004a) Chandra Observations and Models of the Mixed-Morphology Supernova Remnant W44: Global Trends. *ApJ*611:906–918, arXiv:astro-ph/0407026
- Shelton RL, Kuntz KD, Petre R (2004b) G65.2+5.7: A Thermal Composite Supernova Remnant with a Cool Shell. *ApJ*615:275–279, arXiv:astro-ph/0409692
- Shen KJ, Bildsten L (2007) Thermally Stable Nuclear Burning on Accreting White Dwarfs. *ApJ*660:1444–1450, arXiv:astro-ph/0702049
- Shimada N, Hoshino M (2000) Strong Electron Acceleration at High Mach Number Shock Waves: Simulation Study of Electron Dynamics. *ApJ*543:L67–L71
- Shull JM, van Steenberg M (1982) The ionization equilibrium of astrophysically abundant elements. *ApJS*48:95–107
- Slane P, Gaensler BM, Dame TM, Hughes JP, et al. (1999) Nonthermal X-Ray emission from the shell-type supernova remnant G347.3-0.5. *ApJ*525:357–367
- Slane P, Helfand DJ, van der Swaluw E, Murray SS (2004) New Constraints on the Structure and Evolution of the Pulsar Wind Nebula 3C 58. *ApJ*616:403–413, arXiv:astro-ph/0405380
- Slane P, Hughes JP, Edgar RJ, Plucinsky PP, et al. (2001) RX J0852.0-4622: Another nonthermal shell-type supernova remnant (G266.2-1.2). *ApJ*548:814–819
- Smartt SJ (2009) Progenitors of Core-Collapse Supernovae. *ARAA*47:63–106, 0908.0700
- Smith RC (1997) The discovery of Balmer-Filaments Encircling SNR RCW 86. *AJ*114:2664–
- Smith RC, Kirshner RP, Blair WP, Winkler PF (1991) Six Balmer-dominated supernova remnants. *ApJ*375:652–662
- Smith RK, Hughes JP (2010) Ionization Equilibrium Timescales in Collisional Plasmas. *ApJ*718:583–585, 1006.0254
- Sorokina EI, Blinnikov SI, Kosenko DI, Lundqvist P (2004) Dynamics and Radiation of Young Type-Ia Supernova Remnants: Important Physical Processes. *Astronomy Letters* 30:737–750, arXiv:astro-ph/0502026
- Spitzer L (1965) *Physics of Fully Ionized Gases*. New York: Interscience (2nd revised edition), 1965
- Stanek KZ, et al. (2003) Spectroscopic Discovery of the Supernova 2003dh Associated with GRB 030329. *ApJ*591:L17–L20
- Stephenson FR, Green DA (2002) *Historical supernovae and their remnants*. Oxford: Clarendon Press
- Strüder L, et al. (2001) The European Photon Imaging Camera on XMM-Newton: The pn-CCD camera. *A&A*365:L18–L26
- Strom R, Johnston HM, Verbunt F, Aschenbach B (1995) A radio-emitting X-ray "bullet" ejected by the Vela supernova. *Nat*373:590–592
- Sunyaev R, Kaniovsky A, Efremov V, Gilfanov M, et al. (1987) Discovery of hard X-ray emission from supernova 1987A. *Nat*330:227–229
- Sushch I, Hnatyk B, Neronov A (2011) Modeling of the Vela complex including the Vela supernova remnant, the binary system γ^2 Velorum, and the Gum nebula. *A&A*525:A154+, 1011.1177
- Takahashi T, Kelley R, Mitsuda K, Kunieda H, et al. (2008) The NeXT Mission. In: Society of Photo-Optical Instrumentation Engineers (SPIE) Conference Series, vol. 7011 of *Society of Photo-Optical Instrumentation Engineers (SPIE) Conference Series*
- Tamagawa T, Hayato A, Nakamura S, Terada Y, et al. (2009) Suzaku Observations of Tycho's Supernova Remnant. *PASJ*61:167–+, 0805.3377
- Tanaka Y, Inoue H, Holt SS (1994) The X-ray astronomy satellite ASCA. *PASJ*46:L37–L41
- Tatischeff V (2009) Radio emission and nonlinear diffusive shock acceleration of cosmic rays in the supernova SN 1993J. *A&A*499:191–213, 0903.2944
- Taylor G (1950) The Formation of a Blast Wave by a Very Intense Explosion. I. Theoretical Discussion. *Royal Society of London Proceedings Series A* 201:159–174
- Teegarden BJ, Barthelmy SD, Gehrels N, Tueller J, et al. (1989) Resolution of the 1,238-keV gamma-ray line from supernova 1987A. *Nat*339:122–+
- Tenorio-Tagle G, Rozyczka M, Franco J, Bodenheimer P (1991) On the evolution of supernova remnants. II - Two-dimensional calculations of explosions inside pre-existing wind-driven bubbles. *MNRAS*251:318–329
- The LS, et al. (1996) CGRO/OSSE observations of the Cassiopeia A SNR. *A&AS*120:C357+
- Theiling MF, Leising MD (2006) Investigation of ^{44}Ti decay X-ray lines in CasA. *NewAR*50:544–547
- Thielemann FK, Nomoto K, Hashimoto MA (1996) Core-Collapse Supernovae and Their Ejecta. *ApJ*460:408–+
- Thorstensen JR, Fesen RA, van den Bergh S (2001) The Expansion Center and Dynamical Age of the Galactic Supernova Remnant Cassiopeia A. *AJ*122:297–307
- Toledo-Roy JC, Velázquez PF, de Colle F, González RF, et al. (2009) Numerical model for the SNR DEM L316: simulated X-ray emission. *MNRAS*395:351–357
- Troja E, Bocchino F, Miceli M, Reale F (2008) XMM-Newton observations of the supernova remnant IC 443. II. Evidence of stellar ejecta in the inner regions. *A&A*485:777–785, 0804.1049
- Truelove JK, McKee CF (1999) Evolution of Nonradiative Supernova Remnants. *ApJS*120:299–326
- Tsunemi H, Katsuda S, Nemes N, Miller ED (2007) The Plasma Structure of the Cygnus Loop from the Northeastern Rim to the Southwestern Rim. *ApJ*671:1717–1725, 0710.1135

- Tsunemi H, Miyata E, Aschenbach B (1999) Spectroscopic Study of the Vela-Shrapnel. *PASJ*51:711–+, [arXiv:astro-ph/9909393](#)
- Tueller J, et al. (1990) Observations of gamma-ray line profiles from SN 1987A. *ApJ*351:L41–L44
- Tüllmann R, Long KS, Pannuti TG, Winkler PF, et al. (2009) Chandra ACIS Survey of M33 (ChASeM33): The Enigmatic X-Ray Emission from IC131. *ApJ*707:1361–1371, 0910.5666
- Tuohy IR, Burton WM, Clark DH (1982) The peculiar X-ray morphology of the supernova remnant G292.0+1.8 - Evidence for an asymmetric supernova explosion. *ApJ*260:L65–L68
- Turner MJL, et al. (2001) The European Photon Imaging Camera on XMM-Newton: The MOS cameras : The MOS cameras. *A&A*365:L27–L35
- Uchida H, Tsunemi H, Katsuda S, Kimura M (2008) The Plasma Structure of the Southwestern Region of the Cygnus Loop with the XMM-Newton Observatory. *ApJ*688:1102–1111, 0809.0594
- Uchida H, Tsunemi H, Katsuda S, Kimura M, et al. (2009) Line-of-Sight Shell Structure of the Cygnus Loop. *ApJ*705:1152–1159, 0910.3731
- Uchida H, Tsunemi H, Tominaga N, Katsuda S, et al. (2011) First Detection of Ar-K Line Emission from the Cygnus Loop. *ArXiv e-prints* 1102.1495
- Uchiyama Y, Aharonian FA (2008) Fast Variability of Nonthermal X-Ray Emission in Cassiopeia A: Probing Electron Acceleration in Reverse-Shocked Ejecta. *ApJ*677:L105–L108, 0803.3410
- Uchiyama Y, Aharonian FA, Tanaka T, Takahashi T, et al. (2007) Extremely fast acceleration of cosmic rays in a supernova remnant. *Nat*449:576–578
- Ueno M, Yamauchi S, Bamba A, Yamaguchi H, et al. (2006) Synchrotron X-Ray SNR Candidates Discovered in the ASCA Galactic Plane Survey. In: *Populations of High Energy Sources in Galaxies* (ed. E J A Meurs & G Fabbiano), vol. 230 of *IAU Symposium*, pp. 333–337
- van Adelsberg M, Heng K, McCray R, Raymond JC (2008) Spatial Structure and Collisionless Electron Heating in Balmer-dominated Shocks. *ApJ*689:1089–1104, 0803.2521
- van den Bergh S, Kamper KW (1977) The remnant of Kepler's supernova. *ApJ*218:617–619
- van der Heyden KJ, Behar E, Vink J, Rasmussen AP, et al. (2002a) High-Resolution X-ray imaging and spectroscopy of N 103B. *A&A*392:955–962
- van der Heyden KJ, Bleeker JAM, Kaastra JS (2004) Synoptic study of the SMC SNRs using XMM-Newton. *A&A*421:1031–1043, [arXiv:astro-ph/0309030](#)
- van der Heyden KJ, Bleeker JAM, Kaastra JS, Vink J (2003) High resolution spectroscopy and emission line imaging of DEM L 71 with XMM-Newton. *A&A*406:141–148
- van der Heyden KJ, Paerels F, Cottam J, Kaastra JS, et al. (2001) Detection of X-ray line emission from the shell of SNR B0540-69.3 with XMM-Newton RGS. *A&A*365:L254–L258, [arXiv:astro-ph/0011487](#)
- van der Heyden KJ, et al. (2002b) High-Resolution X-ray imaging and spectroscopy of N 103B. *A&A*392:955–962
- van der Laan H (1962) Expanding supernova remnants and galactic radio sources. *MNRAS*124:125–+
- van der Swaluw E, Wu Y (2001) Inferring Initial Spin Periods for Neutron Stars in Composite Remnants. *ApJ*555:L49–L53
- van Loon JT, Cioni M, Zijlstra AA, Loup C (2005) An empirical formula for the mass-loss rates of dust-enshrouded red supergiants and oxygen-rich Asymptotic Giant Branch stars. *A&A*438:273–289, [arXiv:astro-ph/0504379](#)
- van Veelen B, Langer N, Vink J, García-Segura G, et al. (2009) The hydrodynamics of the supernova remnant Cassiopeia A. The influence of the progenitor evolution on the velocity structure and clumping. *A&A*503:495–503, 0907.1197
- Velázquez PF, Martinell JJ, Raga AC, Giacani EB (2004) Effects of Thermal Conduction on the X-Ray and Synchrotron Emission from Supernova Remnants. *ApJ*601:885–895
- Vink J (2004a) High Resolution X-ray Spectroscopy of SN 1006. [astro-ph/0412447](#) [astro-ph/0412447](#)
- Vink J (2004b) X- and γ -ray studies of Cas A: exposing core collapse to the core. *New Astronomy Review* 48:61–67
- Vink J (2006) X-ray High Resolution and Imaging Spectroscopy of Supernova Remnants. In: *The X-ray Universe 2005*, ESA SP-604 Vol. 1, A. Wilson ed. (ESA, ESTEC, The Netherlands), p. 319
- Vink J (2008a) Multiwavelength Signatures of Cosmic Ray Acceleration by Young Supernova Remnants. In: *American Institute of Physics Conference Series*, vol. 1085 of *American Institute of Physics Conference Series*, pp. 169–180
- Vink J (2008b) Non-thermal bremsstrahlung from supernova remnants and the effect of Coulomb losses. *A&A*486:837–841, [arXiv:0806.4393](#)
- Vink J (2008c) The Kinematics of Kepler's Supernova Remnant as Revealed by Chandra. *ApJ*689:231–241, 0803.4011
- Vink J, Bamba A (2009) The discovery of a pulsar wind nebula around the magnetar candidate AXP 1E1547.0-5408. *ApJ*707:L148–L152, 0909.3843
- Vink J, Bleeker J, Kaastra JS, Rasmussen A (2004) High resolution X-ray spectroscopy of G292.0+1.8/MSH 11-54. *Nucl Phys B Proc Suppl* 132:62–65
- Vink J, Bleeker J, van der Heyden K, Bykov A, et al. (2006) The X-Ray Synchrotron Emission of RCW 86 and the Implications for Its Age. *ApJ*648:L33–L37
- Vink J, Bloemen H, Kaastra JS, Bleeker JAM (1998) The expansion of Cassiopeia A as seen in X-rays. *A&A*339:201–207
- Vink J, Kaastra JS, Bleeker JAM (1996) A new mass estimate and puzzling abundances of SNR Cassiopeia A. *A&A*307:L41–L44

- Vink J, Kaastra JS, Bleeker JAM (1997) X-ray spectroscopy of the supernova remnant RCW 86. A new challenge for modeling the emission from supernova remnants. *A&A*328:628–633
- Vink J, Kuiper L (2006) Supernova remnant energetics and magnetars: no evidence in favour of millisecond proto-neutron stars. *MNRAS*370:L14–L18, astro-ph/0604187
- Vink J, Laming JM (2003) On the magnetic fields and particle acceleration in Cassiopeia A. *ApJ*584:758–769
- Vink J, Laming JM, Gu MF, Rasmussen A, et al. (2003) Slow temperature equilibration behind the shock front of SN 1006. *ApJ* 587:31–34
- Vink J, Maccarone MC, Kaastra JS, Mineo T, et al. (1999) A comparison of the X-ray line and continuum morphology of Cassiopeia A. *A&A*344:289–294
- Vink J, Yamazaki R, Helder EA, Schure KM (2010) The Relation Between Post-shock Temperature, Cosmic-ray Pressure, and Cosmic-ray Escape for Non-relativistic Shocks. *ApJ*722:1727–1734, 1008. 4367
- Vink J, et al. (2001) Detection of the 67.9 and 78.4 keV lines associated with the radioactive decay of ^{44}Ti in Cassiopeia A. *ApJ*560:L79–L82
- Vladimirov AE, Bykov AM, Ellison DC (2008) Turbulence Dissipation and Particle Injection in Nonlinear Diffusive Shock Acceleration with Magnetic Field Amplification. *ApJ*688:1084–1101, 0807. 1321
- Völk HJ, Berezhko EG, Ksenofontov LT (2003) Variation of cosmic ray injection across supernova shocks. *A&A*409:563–571, arXiv:astro-ph/0306016
- Völk HJ, Berezhko EG, Ksenofontov LT (2005) Magnetic field amplification in Tycho and other shell-type supernova remnants. *A&A*433:229–240
- Wampler EJ, Wang L, Baade D, Banse K, et al. (1990) Observations of the nebulosities near SN 1987A. *ApJ*362:L13–L16
- Wang L, Howell DA, Höflich P, Wheeler JC (2001) Bipolar Supernova Explosions. *ApJ*550:1030–1035
- Warren JS, Hughes JP (2004) Raising the Dead: Clues to Type Ia Supernova Physics from the Remnant 0509-67.5. *ApJ*608:261–273
- Warren JS, et al. (2005) Cosmic-Ray Acceleration at the Forward Shock in Tycho's Supernova Remnant: Evidence from Chandra X-Ray Observations. *ApJ*634:376–389
- Weaver R, McCray R, Castor J, Shapiro P, et al. (1977) Interstellar bubbles. II - Structure and evolution. *ApJ*218:377–395
- Webber WR (1998) A New Estimate of the Local Interstellar Energy Density and Ionization Rate of Galactic Cosmic Rays. *ApJ*506:329–334
- Weiler KW, Panagia N (1978) Are Crab-type Supernova Remnants (Plerions) Short-lived? *A&A*70:419–
- Weiler KW, Panagia N, Sramek RA, van Dyk SD, et al. (2009) Radio Emission from Supernovae. In: *American Institute of Physics Conference Series* (ed. G Giobbi, A Tornambe, G Raimondo, M Limongi, L A Antonelli, N Menci, & E Brocato), vol. 1111 of *American Institute of Physics Conference Series*, pp. 440–447
- Weinberg NN, Quataert E (2008) Non-linear saturation of g-modes in proto-neutron stars: quieting the acoustic engine. *MNRAS*387:L64–L68, 0802. 1522
- Westerlund BE (1969) OB stars near the supernova remnant RCW 86. *AJ*74:879–881
- Wheeler JC, Meier DL, Wilson JR (2002) Asymmetric Supernovae from Magnetocentrifugal Jets. *ApJ*568:807–819, arXiv:astro-ph/0112020
- White RL, Long KS (1991) Supernova remnant evolution in an interstellar medium with evaporating clouds. *ApJ*373:543–555
- Williams BJ, Blair WP, Blondin JM, Borkowski KJ, et al. (2011) RCW 86: A Type Ia Supernova in a Wind-blown Bubble. *ApJ*741:96, 1108. 1207
- Williams RM, Chu YH (2005) Supernova Remnants in the Magellanic Clouds. VI. The DEM L316 Supernova Remnants. *ApJ*635:1077–1086, arXiv:astro-ph/0509696
- Willingale R, Bleeker JAM, van der Heyden KJ, Kaastra JS (2003) The mass and energy budget of Cassiopeia A. *A&A*398:1021–1028
- Willingale R, Bleeker JAM, van der Heyden KJ, Kaastra JS, et al. (2002) X-ray spectral imaging and Doppler mapping of Cassiopeia A. *A&A*381:1039–1048
- Willingale R, West RG, Pye JP, Stewart GC (1996) ROSAT PSPC observations of the remnant of SN 1006. *MNRAS*278:749–762
- Winkler PF, Clark GW, Markert TH, Petre R, et al. (1981) X-ray line emission from the Puppis A supernova remnant - Oxygen lines. *ApJ*245:574–580
- Woltjer L (1972) Supernova Remnants. *ARAA*10:129–
- Woosley S, Janka T (2005) The physics of core-collapse supernovae. *Nature Physics* 1:147–154, arXiv:astro-ph/0601261
- Woosley SE, Eastman RG, Weaver TA, Pinto PA (1994) SN 1993J: A Type IIb supernova. *ApJ*429:300–318
- Woosley SE, Kasen D, Blinnikov S, Sorokina E (2007) Type Ia Supernova Light Curves. *ApJ*662:487–503, arXiv:astro-ph/0609562
- Woosley SE, Weaver TA (1995) The Evolution and Explosion of Massive Stars. II. Explosive Hydrodynamics and Nucleosynthesis. *ApJS*101:181–
- Yamaguchi H, Koyama K, Katsuda S, Nakajima H, et al. (2007) X-Ray Spectroscopy of SN 1006 with Suzaku. *ArXiv e-prints* 706, 0706. 4146
- Yamaguchi H, Koyama K, Katsuda S, Nakajima H, et al. (2008) X-Ray Spectroscopy of SN 1006 with Suzaku. *PASJ*60:141–, 0706. 4146
- Yamaguchi H, Ozawa M, Koyama K, Masai K, et al. (2009) Discovery of Strong Radiative Recombination Continua from the Supernova Remnant IC 443 with Suzaku. *ApJ*705:L6–L9, 0909. 3848
- Yang X, Lu F, Chen L (2008) High Spatial Resolution X-Ray Spectroscopy of Cas A with Chandra. *Chinese Journal of Astronomy and Astrophysics* 8:439–450, 0712. 1071
- Yang XJ, Tsunemi H, Lu FJ, Chen L (2009) A Cr-K Emis-

- sion Line Survey in Young Supernova Remnants with Chandra. *ApJ*692:894–901, 0810.4687
- Young PA, et al. (2006) Constraints on the Progenitor of Cassiopeia A. *ApJ*640:891–900, arXiv:astro-ph/0511806
- Yusef-Zadeh F, Goss WM, Roberts DA, Robinson B, et al. (1999) Three New Supernova Remnant OH Masers Near the Galactic Center: Evidence for Large-Scale Maser Emission from Supernova Remnants. *ApJ*527:172–179, arXiv:astro-ph/9907370
- Yusef-Zadeh F, Roberts DA, Goss WM, Frail DA, et al. (1996) Detection of 1720 MHz Hydroxyl Masers at the Galactic Center: Evidence for Shock-excited Gas and Milligauss Fields. *ApJ*466:L25+
- Yusef-Zadeh F, Uchida KI, Roberts D (1995) Shock-Excited OH Maser Emission Outlining the Galactic Center Supernova Remnant G359.1-0.05. *Science* 270:1801–1804
- Zel'dovich Y, Raizer YP (1966) *Elements of Gasdynamics and the Classical Theory of Shock Waves*. New York: Academic Press, 1966, edited by Hayes, W.D.; Probstein, Ronald F.
- Zhekov SA, McCray R, Dewey D, Canizares CR, et al. (2009) High-Resolution X-Ray Spectroscopy of SNR 1987A: Chandra Letg and HETG Observations in 2007. *ApJ*692:1190–1204, 0810.5313
- Zhekov SA, Park S, McCray R, Racusin JL, et al. (2010) Evolution of the Chandra CCD spectra of SNR 1987A: probing the reflected-shock picture. *MNRAS*407:1157–1169, 1005.1037
- Zirakashvili VN, Aharonian F (2007) Analytical solutions for energy spectra of electrons accelerated by nonrelativistic shock-waves in shell type supernova remnants. *A&A*465:695–702, arXiv:astro-ph/0612717
- Zirakashvili VN, Aharonian FA (2010) Nonthermal Radiation of Young Supernova Remnants: The Case of RX J1713.7-3946. *ApJ*708:965–980, 0909.2285
- Zirakashvili VN, Ptuskin VS (2008) The influence of the Alfvénic drift on the shape of cosmic ray spectra in SNRs. In: *American Institute of Physics Conference Series* (ed. F A Aharonian, W Hofmann, & F Rieger), vol. 1085 of *American Institute of Physics Conference Series*, pp. 336–339